



**HAL**  
open science

# Development of new material systems for the ferroelectric control of Rashba spin-orbit coupling and spin-charge interconversion

Gaétan Verdierre

► **To cite this version:**

Gaétan Verdierre. Development of new material systems for the ferroelectric control of Rashba spin-orbit coupling and spin-charge interconversion. Materials Science [cond-mat.mtrl-sci]. Université Paris-Saclay, 2024. English. NNT : 2024UPASP018 . tel-04584801

**HAL Id: tel-04584801**

**<https://theses.hal.science/tel-04584801>**

Submitted on 23 May 2024

**HAL** is a multi-disciplinary open access archive for the deposit and dissemination of scientific research documents, whether they are published or not. The documents may come from teaching and research institutions in France or abroad, or from public or private research centers.

L'archive ouverte pluridisciplinaire **HAL**, est destinée au dépôt et à la diffusion de documents scientifiques de niveau recherche, publiés ou non, émanant des établissements d'enseignement et de recherche français ou étrangers, des laboratoires publics ou privés.

# Development of new material systems for the ferroelectric control of Rashba spin-orbit coupling and spin-charge interconversion

*Développement de nouveaux matériaux pour le  
contrôle ferroélectrique du couplage Rashba spin-orbit  
et de l'interconversion spin-charge*

**Thèse de doctorat de l'université Paris-Saclay**

École doctorale n° 564 Physique en Île-de-France (PIF)

Spécialité de doctorat : Physique

Graduate School : Physique. Référent : faculté des sciences d'Orsay

Thèse préparée dans l'unité de recherche **Laboratoire Albert Fert** (Université Paris-Saclay, CNRS, Thales), sous la direction de **Manuel BIBES**, Directeur de recherche, le co-encadrement de **Gertjan KOSTER**, Directeur de recherche

**Thèse soutenue à Paris-Saclay, le 25 mars 2024, par**

**Gaétan VERDIERRE**

## Composition du jury

Membres du jury avec voix délibérative

<b>Gervasi HERRANZ</b> Directeur de recherche, Institut de Ciencia de Materials de Barcelona	Président
<b>Houssny BOUYANFIF</b> Maître de conférences, HDR, Université de Picardie Jules Verne (UPJV)	Rapporteur & Examineur
<b>Ulrike LÜDERS</b> Directrice de recherche, CRISMAT, Université de Normandie	Rapporteuse & Examinatrice
<b>Sylvia MATZEN</b> Maîtresse de conférences, Université Paris-Saclay	Examinatrice

**Titre :** Développement de nouveaux matériaux pour le contrôle ferroélectrique du couplage Rashba spin-orbit et de l'interconversion spin-charge

**Mots clés :** Rashba, Oxydes, Ferroélectriques, Wurtzites

**Résumé :** Alors que la spintronique classique s'est traditionnellement appuyée sur les métaux ferromagnétiques comme générateurs et détecteurs de spin, les effets de couplage spin-orbite permettent désormais de générer et de détecter efficacement des courants de spin à partir de courants de charge dans des architectures exemptes de matériaux ferromagnétiques. Cependant, les systèmes existants capables d'obtenir cette interconversion spin/charge ne possèdent pas le caractère non volatil des matériaux ferromagnétiques. La non volatilité de l'état ferroïque est une condition nécessaire pour le stockage et le traitement de données. Les recherches présentées dans cette thèse visent à développer des systèmes dans lesquels il sera possible de combiner les avantages du couplage spin-orbite de type Rashba (RSOC) pour une interconversion efficace entre les courants de spin et de charge avec une autre famille de systèmes ferroïques, les ferroélectriques. Le RSOC apparaît dans les systèmes dont la symétrie d'inversion est brisée, et est plus fort en présence d'éléments lourds. Les ferroélectriques rompent intrinsèquement la symétrie d'inversion et pourraient donc abriter du RSOC. En prime, la commutation de la polarisation du ferroélectrique via un champ électrique devrait pouvoir changer le signe du RSOC, et ce faisant la polarité avec laquelle le matériau interconvertirait les courants de spin en courant de charge via l'effet Edelstein. De plus, les ferroélectriques peuvent accumuler (ou réduire) de très grandes densités de porteurs dans les matériaux adjacents et ainsi générer des champs électriques à l'interface qui dépendent de la direction de la polarisation du matériau ferroélectrique. En utilisant cet effet, il est donc possible de créer un RSOC interfacial qui devrait également être commutable par l'action d'un champ électrique, permettant ainsi un contrôle électrique et non volatil de l'interconversion spin/charge. Dans le cadre du travail mené durant cette thèse, nous avons conçu et caractérisé deux types d'hétérostructures de couches minces ferroélectriques dans le but d'observer à terme du RSOC commutable : (i) un matériau monophasé,  $\text{SrBiO}_3$ , dont nous avons prédit qu'il deviendrait ferroélectrique avec un RSOC commutable si il était soumis à une forte contrainte en compression; (ii) un système multicouches combinant un membre de la famille des wurtzites ferroélectriques, le  $(\text{Al,Sc})\text{N}$ , avec le  $\text{BiSb}$ , dont les propriétés pourraient être modulées à l'aide de la ferroélectricité.

**Title :** Development of new material systems for the ferroelectric control of Rashba spin-orbit coupling and spin-charge interconversion

**Keywords :** Rashba, Oxides, Ferroelectrics, Wurtzites

**Abstract :** While classical spintronics has traditionally relied on ferromagnetic metals as spin generators and spin detectors, spin-orbit effects now make it possible to efficiently generate and detect spin currents from charge currents in architectures free from ferromagnets. However, existing materials able to achieve this spin/charge interconversion do not possess the non-volatile character of ferromagnets required for non-volatile data storage and processing. In the work presented in this thesis, we tried to develop material systems in which it would be possible to combine the advantages of Rashba-type spin-orbit coupling (RSOC) for efficient interconversion between spin and charge currents with another family of ferroic systems, ferroelectrics. RSOC appears in systems with broken inversion symmetry, and is stronger in the presence of heavy elements. Ferroelectrics intrinsically break inversion symmetry and could thus harbour RSOC. As a bonus, switching the polarization of the ferroelectric with an electric field should switch

the sign of the RSOC and thus the polarity with which the material would interconvert spin into charge via the Edelstein effect. In addition, ferroelectrics can accumulate or deplete very large carrier densities in adjacent materials and thus generate interfacial electric fields that would depend on the ferroelectric polarization direction. This would result in an interfacial RSOC that should also be tunable, allowing for a non-volatile electrical control of spin/charge interconversion.

In the framework of this thesis, we investigated the growth and characterisation of two types of ferroelectric thin film heterostructures which should present switchable RSOC : (i) a single phase material,  $\text{SrBiO}_3$ , that we predicted to become ferroelectric with switchable RSOC at compressive strain; (ii) an interface system combining the novel family of ferroelectrics, the wurtzites  $(\text{Al,Sc})\text{N}$ , with  $\text{BiSb}$ , a topological insulator whose spin-charge interconversion properties could be modulated through the means of ferroelectricity.

*À ma famille et mes amis.  
To my family and friends.*





# Acknowledgements

Le travail présenté dans cette thèse n'aurait pas été possible sans l'aide que j'ai pu recevoir tout au long de ma thèse.

Je remercie tout d'abord le jury d'avoir accepté d'évaluer ce travail. Merci à Ulrike Luders et à Houssny Bouyanfif d'avoir pris le temps de rapporter cette thèse. Merci à Gervasi Herranz et à Sylvia Matzen d'avoir relu mon manuscrit et évalué ma soutenance. Ce fut un honneur de vous avoir tous les quatre dans mon jury. Merci enfin à Agnès, d'avoir assisté à ma soutenance, mais aussi pour toutes les discussions que nous avons pu avoir pendant ces trois années de thèse. C'est un véritable honneur pour moi d'avoir pu travailler dans le même groupe que toi.

First and foremost, I think the two individuals whom I owe the most gratitude to for this thesis are my two supervisors, Manuel and Gertjan. You designed this project together, based on your mutual expertise and with the aim of strengthening the collaboration between your two labs, or maybe I could say my labs. I had a blast working with the two of you and enjoyed having these two working environments. Thank you, Gertjan, for all the help you provided me with during my stays in Enschede, be it for numerous meetings we had when I was there, or for the help you provided me with logistics in the lab. You were very kind to me, and I will always remember that on my first day in Enschede, I was quarantined because of COVID, you came to my flat to give me some chocolate and goodies to make my time in quarantine feel less strenuous. Manu, ces trois années en tant que directeur de thèse officiel ont mis en avant à quel point tu es un encadrant génial, drôle et attentif au bien-être des gens avec qui tu travailles. Merci pour tout le temps que tu as pu prendre pour m'encadrer, que ça soit quand j'étais à Enschede ou à Paris. Merci d'avoir été bienveillant et positif quand le moral n'était pas au plus haut. Merci d'avoir partagé avec moi ces différentes passions que nous avons en commun, la musique, la kraft et la science. Merci enfin d'avoir fait attention à ma santé pendant la thèse et à mes perspectives de carrière après la thèse.

Je souhaite également remercier les personnes qui ont collaboré, de près ou de loin, à ce travail de thèse. Merci à Marta D. Rossel pour son aide sur les mesures de STEM, et pour votre réactivité. Merci à Nicolas Gauquelin et à Daen Jannis pour les nombreux échanges que nous avons pu avoir sur le STEM de mes couches d'oxydes.

Merci avant tout à ma famille, de m'avoir toujours soutenu et poussé, et ce malgré mon faible taux de réponse.

Faisant partie de deux laboratoires différents, j'ai bénéficié de l'expérience et de l'entraide d'énormément de personnes. Un très grand merci à Thomas, à Luis et à Anouk, avec qui j'ai pu travailler. Ce travail en équipe n'a duré que 6 mois, mais il représente pour moi beaucoup. Travailler avec vous a été un véritable plaisir, alors merci pour ça! Thank you Shu, Emma, Ellen and Iris for taking care of the old lady that COMAT is with me. I hope she won't drive you crazy in the future. Thank you, Yorick, you are one of the most knowledgeable people I know and I am glad for all the help you gave me. Thank you Frank and Dominic,

you are the ones running the lab from the backstage. Au laboratoire Albert Fert, merci Karim, pour ton aide précieuse, ta bonne humeur et ton humour acerbe. J'aimerais aussi remercier Stiff et Vincent, pour les nombreuses journées que l'on a pu passer ensemble sur mes échantillons défectueux. Merci Cécile pour ton aide sur les Xs, ainsi que Florian et Sophie pour toutes les croissances par pulvérisation. Merci enfin à Anne, Florence et Marion pour votre aide administrative.

J'aimerais également remercier toutes les personnes qui ont contribué à rendre mon quotidien au labo plus rigolo, certaines de ces personnes ayant déjà été mentionnées au-dessus, mais catégoriser c'est compliqué. I would like to thank the good friends I made in the Netherlands, the magic players in Daniel, Melvin, Marijn and Moritz, but also Tati for all the fun we had on Saturdays growing in the lab talking about cheese, and Eli. I wish I could have spent more time with you all. Un très grand merci à Pierre-Alexis, pour m'avoir dépanné quand je n'avais nulle part où dormir, et pour m'avoir soutenu à grand coup de longues pauses café clope et de soirée jeux/bières (...). Mes séjours aux Pays-Bas n'auraient certainement pas été les mêmes sans toi, alors merci. Merci aussi à tous mes co-bureaux d'avoir partagé mon quotidien. Merci MB pour ton tuto stalking' haha. Merci aux oxydes, à Julien, Sara, Sri et Lucia, qui étaient là quand je suis arrivé, à Dongxin et Luigi, à tronco Fer, à Hugo le fou du vélib, à Thomas le fou du vélo et à Gab pour le PAIN. Merci aux "vieux" doctorants. Merci à Aurélien pour les soirées jeux et longues discussions à propos de HK. Merci à Diane, j'espère qu'on pourra continuer à partager des apéros fromages, et à Paupau, ma collègue de galère, garde ta pêche monumentale. Merci à Yanis, pour ta bienveillance infinie. Merci enfin à Aya, on a enfin réussi à la finir cette thèse! J'espère qu'au moment où j'écris ces mots tu es en train de prendre des vacances à la plage !

Merci avant tout à tous ceux que je vais oublier de lister, car il y en aura forcément. Merci à tous mes amis avec qui j'ai pu partager un toit durant ces trois dernières années. Merci à Clément, qui m'a eu comme coloc bien malgré lui. Merci Nico, Emma et Bibi d'avoir partagé avec moi ce délicieux breuvage qu'est l'advocaat, à Arthur, Victor et Arnaud pour les nombreuses LAN et pour l'introduction à Jojoooo. Merci enfin à Martina, Blandine, Bastien et Annabelle pour la colo l'âge de glace dans laquelle nous vivons maintenant. Merci aussi à tous mes amis avec qui je n'ai pas vécu, que ça soit ceux avec qui j'ai pu manger (Apo, Albert, Marion, Héloïse ...), jouer (Gasch, Emile, Jacques, Arthur, Clem, Arnaud...) ou grimper (Magali, Tanel, Héloïse (bis héhé)). Merci à Sophie (et par extension à Wilfried) de m'avoir accueilli sur ton (votre) divan pendant de nombreuses heures, et à Nolwenn pour nos nombreuses heures de marche. Merci Cécile pour les sessions de télétravail avec de délicieuses galettes. Noémie, merci d'avoir partagé avec moi tes nombreuses passions, sources d'épanouissement sans cesse renouvelées. J'espère que tu sauras continuer à chercher ton bonheur.

Suzanne, merci d'avoir partagé tous mes dimanches matins et mercredi midi dans le but d'atteindre des objectifs bien trop ambitieux. Espérons qu'on puisse y arriver bientôt, dans un tout nouveau cadre (hihi).

Matthieu et Marie, je ne vous ai bien entendu pas oubliés. Merci à vous deux d'avoir partagé avec moi ces trois années de thèse, du début à la (presque) fin. Merci de m'avoir toujours écouté et soutenu, je sais que je pourrai toujours compter sur vous. Je vous souhaite tout le bonheur du monde.

Enfin, merci à Francisco, tu es mon ami de plus longue date et une constante de ma vie, dont l'importance n'est plus à démontrer. En espérant te retrouver bientôt dans des contrées plus méridionales.

Partager ces trois dernières années avec vous tous fut un plaisir. J'ai pu apprendre et vivre à vos côtés. Je suis fier de ce que j'ai pu devenir grâce à vous, alors merci pour tout.

# Contents

<b>1 Background</b>	<b>5</b>
1.1 Spintronics and spin-orbitronics	5
1.1.1 Basis of spintronics	5
1.1.1.1 The electron beyond its charge	5
1.1.1.2 Spin and charge currents	6
1.1.1.3 Spin-orbit coupling	8
1.1.2 Rashba Spin-orbit Coupling	9
1.1.3 The normal and inverse Edelstein effects and spin to charge interconversion	11
1.2 The MESO and FESO devices	14
1.3 Ferroelectricity	17
1.3.1 Ferroic orders	17
1.3.2 Ferroelectrics	17
1.4 Rashba systems	21
1.4.1 Overview	21
1.4.2 Two dimensional Electron Gases	21
1.4.3 Topological insulators	24
1.4.4 Ferroelectric control of the Rashba effect	25
1.4.4.1 Ferroelectric control of the Rashba effect: Functionalisation of the 2DEG	25
1.4.4.2 Heterostructures	25
1.4.4.3 FerroElectric Rashba SemiConductors	27
1.5 Bismuthates	31
1.5.1 Generalities about perovskite oxides	31
1.5.2 Structure of bismuthates	31
1.5.2.1 Generalities	31

1.5.2.2	Hole-doped bismuthates	32
1.5.3	Physical properties of bulk bismuthates	33
1.5.4	Two dimensional conductive states at bismuthates' edges	36
1.5.5	Bismuthates thin films, hetero-structures and interfaces	37
1.6	wurtzite and fluorites	40
1.6.1	History	40
1.6.1.1	Fluorites	40
1.6.1.2	wurtzites	40
1.6.2	Ferroelectricity in Wurtzites: properties and mechanism	41
1.6.3	Growth conditions overview	43
1.6.4	AlN based hetero structures: one possible approach.	43
<b>2</b>	<b>Experimental techniques</b>	<b>45</b>
2.1	Surface preparation	45
2.2	Growth techniques	46
2.2.1	Pulsed Laser Deposition	46
2.2.1.1	Growth parameters	46
2.2.1.2	Growth kinetics	47
2.2.1.3	<i>In-situ</i> monitoring: Reflection High Energy Electron Diffraction	48
2.2.2	Magnetron Sputtering	49
2.3	Crystal quality control characterisation methods	51
2.3.1	X-Ray Photo Emission Spectroscopy	51
2.3.1.1	Notes about quantitative XPS	51
2.3.2	X-Ray Diffraction	52
2.3.2.1	Symmetric scans	53
2.3.2.2	Reciprocal space maps	53
2.3.3	Scanning Transmission Electron Microscopy	54
2.3.3.1	Data analysis	54
2.3.4	Atomic Force Microscopy	54
2.3.5	Electrical characterisation of ferroelectrics	57
<b>3</b>	<b>Growth optimisation of SrBiO<sub>3</sub></b>	<b>59</b>
3.1	Introduction	59

<b>3.2 Growth optimisation</b>	60
<b>3.2.1 Initial conditions</b>	60
<b>3.2.2 Stability of B-site bismuth perovskites</b>	60
<b>3.2.3 Capping</b>	61
<b>3.2.4 Growth optimisation</b>	62
<b>3.2.5 Post-annealing</b>	63
<b>3.2.6 SBO strain state on STO</b>	65
<b>3.3 Substrate study</b>	65
<b>3.3.1 Strain state on different substrates</b>	65
<b>3.3.2 Scanning Transmission Electron Microscopy</b>	66
<b>3.3.2.1 Tetragonality and strain mapping</b>	67
<b>3.4 Conclusion</b>	70
<b>4 Ferroelectricity in SrBiO<sub>3</sub></b>	<b>73</b>
<b>4.1 Electrodes optimisation for the growth of ferroelectric SBO</b>	73
<b>4.1.1 Ba<sub>x</sub>Sr<sub>1-x</sub>RuO<sub>3</sub></b>	73
<b>4.1.2 La<sub>x</sub>Ba<sub>1-x</sub>SnO<sub>3</sub></b>	74
<b>4.2 Ferroelectricity in SrBiO<sub>3</sub></b>	76
<b>4.2.1 SrBiO<sub>3</sub> electrical properties</b>	76
<b>4.2.2 (SrTiO<sub>3</sub>)<sub>(8)</sub>/SrBiO<sub>3</sub>/Ba<sub>0.5</sub>Sr<sub>0.5</sub>RuO<sub>3</sub>/NdScO<sub>3</sub></b>	77
<b>4.2.3 (SrTiO<sub>3</sub>)<sub>(8)</sub>/SrBiO<sub>3</sub>/La<sub>0.07</sub>Ba<sub>0.97</sub>SnO<sub>3</sub>/substrate</b>	77
<b>4.3 Origin of ferroelectricity in STO<sub>8</sub>/SBO/LBSO/NSO</b>	80
<b>4.3.1 Probing polarization by STEM</b>	81
<b>4.3.2 Correlations between tetragonality and polarization</b>	84
<b>4.4 Conclusion</b>	85
<b>5 Development of heterostructures based on (Al,Sc)N</b>	<b>87</b>
<b>5.1 (Al,Sc)N growth optimisation</b>	87
<b>5.2 Plasma stability</b>	87
<b>5.3 AlScN ferroelectric properties</b>	91
<b>5.4 Interfacing BiSb and (Al,Sc)N</b>	96
<b>5.5 Conclusion</b>	99
<b>6 General conclusions and perspectives</b>	<b>101</b>

**A Résumé de la thèse en français**

**131**

# Introduction

Information technologies play an ever-growing role in our daily lives. The numerous sub-fields within this sector depend on microelectronic devices for advancement and success. The forthcoming significant advancements in the information sector include *the internet of things* and *machine learning*. However, achieving progress in both these technological areas necessitates substantial improvements at the smallest scale of electronics. Since the 1980s, the cornerstone of electronics has been Complementary Metal Oxide Semiconductors (CMOS) Transistors. Enhancing them through miniaturization and band engineering has been a focal point for both industrial and academic efforts. As transistor technology progressed, an empirical law known as Moore's Law [1] emerged. This law gauges the evolution of the component industry, asserting that the number of transistors per unit area on state-of-the-art commercial chips should double every 18-24 months. However, as transistors approach sizes below 10 nm, Moore's Law is reaching its limit, necessitating a new paradigm for components. Further size reduction poses increasing challenges, primarily due to various physical limitations.

First and foremost, the switching voltage of transistors is limited due to the so called "Boltzmann tyranny", which puts a limit to the current control in a transistor channel (60 mV for every change in current by a factor of 10 at room temperature). In addition, the equipment used to fabricate devices will soon reach its resolution size, in the form of the diffraction limit. The gate lengths of the last commercial devices produced by TSMC and Intel are as small as 2 nm. However, if we were to follow Moore's law in terms of scalability, devices on commercial chip in 6 years should be 10 times smaller. This is not achievable with the current fabrication technologies available to the industry. Finally, a functioning transistor dissipates heat, which can damage and reduce its efficiency and lifetime [2]. Cooling of the basic components of electronic architecture is crucial but energy-consuming. Fig 1 presents the total energy consumption of the Information and Communication Technology (ICT) sector, with data centers accounting for a large proportion of the chart [3]. In fact, up to 50% of the energy consumed in data centers is used for cooling systems [4].

In a context of sobriety, it is essential to develop better, ideally passive and targeted, cooling technologies, as well as less energy-intensive and more efficient components, in order to reduce the overall energy consumption of the ICT sector. The current CMOS paradigm is reaching its limit, clearly calling for a change of paradigm. The end of Moore's law is a great opportunity in that regard.

An avenue towards reducing the energy footprint of computing lies in changing the architecture of electronic devices. In modern computing devices, memory and processing components are physically separated, meaning that every operation requires an exchange between the two units. This architecture is better known as the Von Neumann architecture. *In-memory computing* would enable circumvention of the problems inherent to the Von Neumann architecture. In the search of new *in-memory computing* compatible components, industrial players have been investigating electronic devices with technologies that operates at lower energies, and which might potentially have better scalability than CMOS devices. Such devices are known as "beyond-CMOS devices".

A number of "beyond-CMOS devices" have been proposed to meet this need, and a methodology to

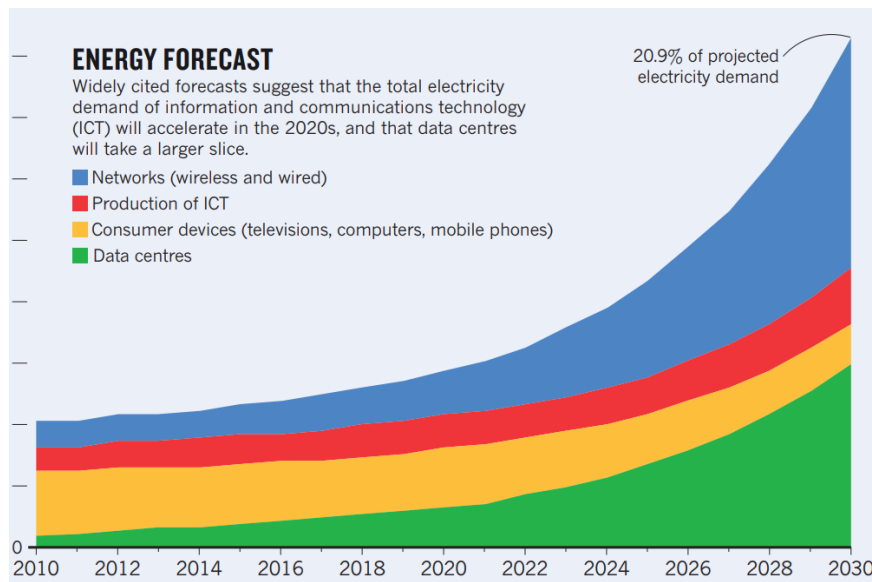


**Figure 1:** Total energy consumption of ICTs. Data centres represent an increasing percentage of the total consumption.

quantify their performance was established [5]. Among all the devices analysed, spintronic devices were highlighted as interesting for their low standby power [6]. In the frame of this approach to conceptualise a "beyond CMOS device", the vector that propagates the information is the spin, which allows for manipulation of the information at low energies. In parallel, another approach to develop better information devices, based on the use of collective state switching, has been developed. Architectures relying on this principle operate by switching an order parameter from  $\Theta$  to  $-\Theta$ , providing a non volatile, Boltzmann tyranny free, building block for electronics. Amongst collective state switching devices, ferroelectric and multiferroic based architectures were highlighted as promising [5], with the issue that a transistor free read out was, at that time, strenuous. Nonetheless, recent advancements in spin to charge conversion allowed for the conceptualisation of efficient devices based on the interplay of ferroic orders and spintronics. The so-called FESO technology makes use of the the spin as the information vector and ferroelectricity as the switchable collective state that stores the information. This device is *in-memory computing* compatible, as the polarization of the ferroelectric serves two purposes: it both encodes the information and modulates the spin-current. Ferroelectrics are well-known and widely used as memory devices. The ferroelectric control of the spin degree of freedom, on the other hand, is still a hot research topic and of great interest for both academic and industrial players. The existence of ferroelectricity can be used to influence the spin-orbit coupling and the resulting spin textures at heterostructure interfaces. The interplay of ferroelectricity and spintronics can go down a number of routes: either through the use of interfaces, heterostructures or materials which have both interesting spinorbitronic and ferroic properties.

Building on the expertise around spin-orbitronics and oxides acquired in the Oxitronics group in Unite Mixte de Physique CNRS, Thales, Universite Paris Saclay (UMPhy), as well as the expertise in Oxide growth and characterisation in the Inorganic Material Science group, University of Twente (IMS) we will focus in this thesis on the investigation of candidate homo- and heterostructures towards the ultimate goal of ferroelectric control of the spin transport properties in said structures.

In Chapter 1, we will (re)introduce some basic knowledge on the fields of spintronics and ferroelectrics. We will then introduce a review on the two class of materials which were investigated during this thesis: the bismuthates which were proposed as a possible homostructure toward the ferroelectric control of the Rashba

effect, and the wurtzites, which are trendy CMOS compatible ferroelectrics and may serve as one of the elements of an heterostructure with both spintronic and ferroelectric properties.

In Chapter 2, we will be introducing the different set ups and techniques used during this thesis.

In Chapter 3, we will be presenting the growth investigation of  $\text{SrBiO}_3$ , which was proposed as a candidate ferroelectric Rashba semiconductor. Structural characterisation of SBO thin films will be presented in Chapter 3, whereas the investigation of its ferroelectric properties will be presented in Chapter 4.

Finally, in Chapter 5, we will present a preliminary work which was carried out to synthesise and characterise  $(\text{Al,Sc})\text{N}$  thin films, as well as a preliminary characterisation study of wurtzites based heterostructures that may be of interest to interface spintronics and ferroelectricity.



# Chapter 1

## Background

In this chapter, we provide key concepts and an overview of the literature to give the reader a better understanding of this thesis. We will first discuss spin transport and spin-to-charge conversion. We will then progress to introducing the collective state switching of ferroic orders as physical components for beyond CMOS devices. This will lead us to introduce two classes of materials that are promising towards such applications. First, we will review a not widely known class of materials, called bismuthates, which take a prominent part in this thesis. Lastly, we will be giving an overview of a novel class of ferroelectric, the Wurtzites, which were optimised and characterised during this thesis with the ultimate goal of building CMOS compatible heterostructures.

### 1.1 Spintronics and spin-orbitronics

Spintronics traces its origins back to the discovery of giant magneto resistance in 1988 by Albert Fert and Peter Grünberg. Since then, research aimed at controlling, propagating, and utilizing the spin degree of freedom has gained increasing attention. Referred to as spintronics, this subfield of solid-state physics has historically utilized ferromagnets to influence and detect spin currents. A focal point of recent progress in spintronics involves the manipulation of spin currents in non magnetic materials by using spin-orbit coupling, which links the spin degree of freedom of electrons to the orbital landscape of the medium in which they propagate. This emerging subfield, collectively known as spinorbitronics<sup>[7]</sup>, is focused on the efficient spin-charge interconversion in magnet-free systems.

In this section, we will provide the reader with key concepts related to spintronics, spinorbitronics, and charge interconversion, which play a critical role in the motivations of this thesis.

#### 1.1.1 Basis of spintronics

Electronics, as we commonly know it, is mainly based on the electron's fundamental property of charge  $q_e = -e$ , and its subsequent transport. However, the electron has a multitude of other noteworthy properties.

##### 1.1.1.1 The electron beyond its charge

Carrying a charge is not the only property the free electron possesses; it also has a mass  $m_e$ , which plays an integral role in the transport process. As the electron is a fermion, it has a spin of  $\pm\frac{1}{2}$  and a quantized spin

angular momentum  $S = \frac{\hbar}{2}\sigma$ , where  $\sigma$  is the vector of Pauli matrices. When the spin angular momentum is projected on an arbitrary axis  $\mathbf{u}_z$ ,  $S$  takes the value  $S_z = \pm \frac{\hbar}{2}$ , which are commonly referred to as "spin-up" and "spin-down". The spin-angular momentum also results in a magnetic moment:

$$\mu_{spin} = -g_e \frac{e}{2m_e} S = -g_s \frac{\mu_B}{\hbar} S \quad (1.1)$$

where  $g_s = |g_e|$  is the dimensionless electron  $g$ -factor and  $\mu_B$  is a measure of magnetic moment and is called the Bohr magneton.

In addition, electrons in solid state systems are interacting with their environment, be it with the lattice in which they exist or with the other electrons present in the system. In this situation, because of the accumulation of many electrons and the Pauli exclusion principle, each material will have a specific band structure, which will be influenced by intrinsic properties (atomic composition, cristal structure, doping, coupling with the lattice, ... ) and the environment ( temperature, strain ... ). This band structure, which relates the electrons' wave vectors to their energies, dictates along which directions and at which energy electrons can propagate in a crystal. To incorporate all the interactions the electrons are subjected to, the concept of the effective mass  $m^* = \alpha \cdot m_e$  of electrons in a solid state system was introduced. By its very nature, the effective mass depends on the propagation direction of the electrons and on the energy at which they propagate.

Finally, while the modern electronics transport of information relies mainly on the propagation of the charge information of the electrons, storage and readout of information have been vigorously utilizing other degrees of freedom, particularly ones that allow nonvolatile storage of the information. Magnetic properties were particularly exploited in memory devices. The discovery of the Giant Magneto Resistance (GMR) around 25 years ago spawned the field of spintronics. This technology is now widely used in storage devices. Nowadays, new paradigms have emerged, proposing to use spin, angular orbital and angular momentum as a medium to store, read, and propagate information[8].

### 1.1.1.2 Spin and charge currents

As we start to consider using electrons as an information vector, we can introduce the notions of charge carrier density  $n$  and spin density  $s$ . It is also helpful to associate these two quantities with the density of carriers for a spin-up  $n_\uparrow$  or a spin-down  $n_\downarrow$  orientation along a fixed quantization axis  $\mathbf{u}_s$ .

$$n = n_\uparrow + n_\downarrow \quad (1.2)$$

$$s = n_\uparrow - n_\downarrow \quad (1.3)$$

We also define the carrier spin polarization  $\mathbf{P}$  which is defined as the ratio between the spin density over the total carrier density:

$$\mathbf{P} = \frac{s}{n} \mathbf{u}_s \quad (1.4)$$

To illustrate the concept of spin transport, let us revisit some basic concepts related to charge transport. Consider a volume  $V$  enclosed by an oriented surface  $\Omega$ , with a given charge density  $\rho = nq$ , with  $q$  the charge of a single carrier. As per charge conservation, any variation of the carrier density must be produced

by a charge current density  $\mathbf{j}_c$  passing through  $\Omega$ . This can be written as

$$\iiint_V \frac{\partial \rho}{\partial t} dV = - \oiint_{\Omega} \mathbf{j}_c \cdot d\Omega \quad (1.5)$$

Using the divergence and by changing variable, we get that

$$\frac{\partial \rho}{\partial t} = -\nabla \cdot \mathbf{j}_c \quad (1.6)$$

Equation [1.6](#) is known as the conservation equation of the charge. In addition, by definition, the charge current is the time derivative of the product between the charge and a position variable  $j_c = \frac{\partial}{\partial t}(\rho \mathbf{r})$ , where  $\mathbf{r}$  is the position vector of the carriers, and because the charge must remain conserved, *i.e.* the time derivative of  $\rho$  is zero, we have  $j_c = nq\mathbf{v}$ . Finally, a charge current ( but this is applicable to any current ) can be induced by either an external conjugated field, here an external electric field  $\mathbf{E}$ , or by a density gradient, here of carriers,  $\nabla n$ . This can be written as

$$\mathbf{j}_c = \mathbf{j}_{drift} + \mathbf{j}_{diffusion} = q(n\mu\mathbf{E} + D\nabla n) \quad (1.7)$$

with  $\mathbf{v} = \frac{\partial \mathbf{r}}{\partial t}$  being the velocity of the carriers,  $\mu$  being their mobility,  $\mathbf{E}$  the electric field and  $D$  the diffusion coefficient. Equation [1.7](#) as a typical drift-diffusion equation form, the quantity considered here being the charge. These equations ([1.6](#) and [1.7](#)) are transposable to other quantities (*e.g.*: wave physics, probabilities ...) such as spins, or a well chosen subpart of the total carrier density  $n_\sigma$ , for example a spin population  $\sigma = \uparrow (\downarrow)$ . However, the spin angular momentum is non conservative. There is a probability  $p_f$  that a carrier's spin flips from  $\sigma$  to  $-\sigma$  within the time  $\tau$  such that the spin flip rate is  $p_f/\tau$ . For one given spin population, this equivalent to adding a creation and an annihilation term to the conservation equation. This can be written as:

$$\frac{\partial n_\sigma}{\partial t} = -\frac{\nabla \cdot \mathbf{j}_\sigma}{q} - p_f(n_\sigma - n_{-\sigma}) \quad (1.8)$$

The drift diffusion equation can be written as:

$$\mathbf{j}_\sigma = q(n_\sigma \mu \mathbf{E} + D \nabla n_\sigma) \quad (1.9)$$

In the same way we defined charge and spin densities, it is interesting to define charge and spin currents as:

$$\mathbf{j}_c = \mathbf{j}_\uparrow + \mathbf{j}_\downarrow = q(n_\uparrow \mathbf{v}_\uparrow + n_\downarrow \mathbf{v}_\downarrow) \quad (1.10)$$

$$\mathbf{j}_s = \mathbf{j}_\uparrow - \mathbf{j}_\downarrow = q(n_\uparrow \mathbf{v}_\uparrow - n_\downarrow \mathbf{v}_\downarrow) \quad (1.11)$$

Which then permits the definition of a current polarization:

$$P_j = \frac{j_s}{j_c} \quad (1.12)$$

With this notation, it is easy to picture the different propagation scenarios: a system in which there is charge current but no net spin current ( $\mathbf{j}_\uparrow = \mathbf{j}_\downarrow \neq 0$  such that  $\mathbf{j}_s = 0$  and  $\mathbf{j}_c \neq 0$ ),  $P_j = 0$ . There is also the possibility of having a net charge current and a net spin current, in which case  $P_j \neq 0$ . We can also imagine the extreme case in which there is spin current with a no net charge current ( $\mathbf{j}_\uparrow = -\mathbf{j}_\downarrow \neq 0$ ). This scenario is known as the scenario of *pure spin current*, and displays the major advantage of requiring no net displacement of charges, hence getting rid of dissipation, which is an appealing feature for low-power devices. We note that we defined the velocities of two spin population independently, which do not necessarily have to be identical.

Finally, we saw that we can deduce a conservation and a drift diffusion equation for the spin in the same way we did for the charge. We get that

$$\frac{\partial s}{\partial t} = -\frac{\nabla \cdot \mathbf{j}_s}{q} - \frac{s}{\tau_{sf}} \quad (1.13)$$

where  $\tau_{sf} = 1/2p_f$  is the spin relaxation time and

$$\mathbf{j}_s = q(s\mu\mathbf{E} + D\nabla s) \quad (1.14)$$

In the particular case in which we neglect the drift term, which means that the electrons are not subjected to an external electric field, if we consider one dimensional transport only and assume a spin density at  $t=0$  all concentrated locally at  $x=0$ , the general solution of the spin diffusion equation becomes:

$$s(x, t) = \frac{s_0}{\sqrt{4\pi Dt}} e^{x^2/4Dt} e^{-t/\tau_{sf}} \quad (1.15)$$

the two exponential terms of this equation are responsible respectively for the spatial spin diffusion and the spin relaxation. From this equation we introduce the spin diffusion length:

$$\lambda_s = \sqrt{D\tau_{sf}} \quad (1.16)$$

$\lambda_s$  is the typical distance over which a spin relaxes, and thus the distance over which the information encoded into a spin current is lost. As such,  $\lambda_s$  is a critical parameter when trying to build a spintronic devices.

### 1.1.1.3 Spin-orbit coupling

So far, we have treated the spin and charge currents as two independent variables. However, the spin and angular momentum of electrons are decorrelated, and thus an electron moving in a lattice will see its spin affected by the orbital landscape in which it is travelling.

Spin-orbit Coupling (SOC) couples the spin with the orbital landscape, providing a link between the spin space and the crystal lattice. SOC enabled major breakthrough in condensed matter physics, allowing for the comprehension numerous physical phenomena including the Dzyaloshinskii-Moriya interaction and the magnetocrystalline anisotropy. To better understand the origins of SOC, let's consider an electron rotating around a nucleus. It is subjected to a radial electric field originating from this nucleus. We can express this electric field as

$$E_r = \left| \frac{E}{r} \right| \mathbf{r} \quad (1.17)$$

We can then express the electric field as the gradient of the potential  $V$ . By making the assumption that the field has a spherical symmetry, we can write

$$|E| = \frac{\partial V}{\partial r} \quad (1.18)$$

Using Maxwell's equations, we can deduce that in the referential of the electron, it is subjected to an effective magnetic field  $B_e$ , given by

$$B_e = \frac{\mathbf{r} \wedge \mathbf{v}}{c^2} \left| \frac{E}{r} \right| \quad (1.19)$$

By replacing  $E$  by the expression [1.18](#) and by introducing  $\mathbf{L}$ , the angular momentum, as the cross product of  $\mathbf{r} \wedge \mathbf{p}$  and  $m_e$  as the mass of the electron, we then get

$$B_e = \frac{1}{m_e c^2} \frac{1}{r} \frac{\partial V}{\partial r} \mathbf{L} \quad (1.20)$$

What we introduced here is an effective magnetic field to which the electron is subjected, which depends on  $\mathbf{L}$ , the orbital torque of the system. The electron has a non zero spin, and thus interacts with this magnetic field. The energy of this interaction is given by

$$H_{SO} = -\mu_m \cdot B_e \quad (1.21)$$

With  $\mu_m$  the magnetic moment,

$$\mu = -\frac{g_s \mu_B}{\hbar} \boldsymbol{\sigma} \quad (1.22)$$

Where  $\boldsymbol{\sigma}$  is the spin matrix,  $\mu_B$  the Bohr magneton and  $g_s$  the spin factor. By substituting expression [1.20](#) into the energy [1.21](#) we finally get

$$H_{SO} = \frac{g_s \mu_B}{\hbar m_e c^2} \frac{1}{r} \frac{\partial V}{\partial r} (\boldsymbol{\sigma} \cdot \mathbf{L}) \quad (1.23)$$

This interaction energy depends on the dot product of  $\boldsymbol{\sigma}$  and  $\mathbf{L}$ , and is thus commonly referred to as spin-orbit coupling. Considering atomic spin-orbit coupling only, the general trend is that SOC is stronger for heavier compounds.

## 1.1.2 Rashba Spin-orbit Coupling

### The Rashba Hamiltonian

The electron we considered so far was only subjected to an interaction with the nucleus it is revolving around. Let's now consider an electron subjected to an external electric field  $\mathbf{E} = E_0 \mathbf{z}$  and in the presence of SOC. We can rewrite [1.23](#) as

$$H_{SO} = \frac{g_s \mu_B}{\hbar} \frac{1}{m_e c^2} (\mathbf{p} \wedge \mathbf{E}) \cdot \boldsymbol{\sigma} \quad (1.24)$$

By permuting the cross product and introducing the Rashba coefficient  $\alpha_R$  we obtain:

$$H_{Rashba} = \alpha_R (\boldsymbol{\sigma} \wedge \mathbf{p}) \cdot \mathbf{z} \quad (1.25)$$

with

$$\alpha_R = \frac{g_s \mu_B E_0}{\hbar m_e c^2} \quad (1.26)$$

$\alpha_R$  is proportional to the magnitude of the external electric field  $E_0$  and can thus be tuned and even reversed by controlling the external field.

### Dispersion relation

By finding the eigenvalues of the total Hamiltonian  $H = H_0 + H_{Rashba}$ , it can be shown that the Rashba effects lifts the spin-degeneracy and the otherwise spin-degenerate band of free electron of mass  $m^*$  with momentum  $k$  splits into two bands. The respective dispersion relation for the two branches of opposite spin polarization (+ or -) is given by the eigenvalues of the Hamiltonian H:

$$E_{\pm} = \frac{\hbar^2 k^2}{2m^*} \pm \alpha_R k \quad (1.27)$$

with eigenvectors:

$$\Psi_{\pm} = \frac{e^{i\mathbf{k}\cdot\mathbf{r}}}{\sqrt{2}} \begin{pmatrix} 1 \\ \mp i e^{i\xi r} \end{pmatrix} \quad (1.28)$$

Where  $\mathbf{k} = k(\cos(\xi), \sin(\xi))$ . The Rashba momentum, defined as  $k_R = |m^*| \alpha_R / \hbar^2$ , quantifies the mutual shift of the splits bands. A schematic representation in  $k$  space of the band separation with the dispersion relation given by [1.27](#) is presented on figure [1.1](#) (a). To discuss spin transport, it is interesting to look at the Fermi surface of such a system.

### Spin texture of the Fermi surface

After the application of the electric field, the Fermi surface is not a paraboloid of revolution anymore but the surface delimited by the 2 Fermi discs of opposite polarization (as illustrated by figure [1.1](#) (b)). The radius of the two disks can be computed by imposing that the total electron density of the system is constant, and by solving the system without SOC, for both eigen states. We get that

$$k_{F\pm} \sim k_F \mp \frac{m_e^* \alpha_R}{\hbar^2} = k_F (1 \mp \eta) \quad (1.29)$$

in order to get an insight on the spin texture of the Fermi surface, we compute the spin expectation value of the eigenvectors of the Rashba Hamiltonian that we derived in [1.28](#)

$$\sigma_{\pm, k} = \langle \Psi_{\pm, k} | \sigma | \Psi_{\pm, k} \rangle = \frac{1}{k} \begin{pmatrix} k_x \\ k_y \end{pmatrix} = \begin{pmatrix} \pm \sin(\xi) \\ \mp \cos(\xi) \end{pmatrix} \quad (1.30)$$

This expectation value tells us that the spin polarization direction is locked to the momentum direction, and along any given  $k$  direction the spin will be of opposite sign on one band with respect to the other. This is illustrated on figure 1.1 (b).

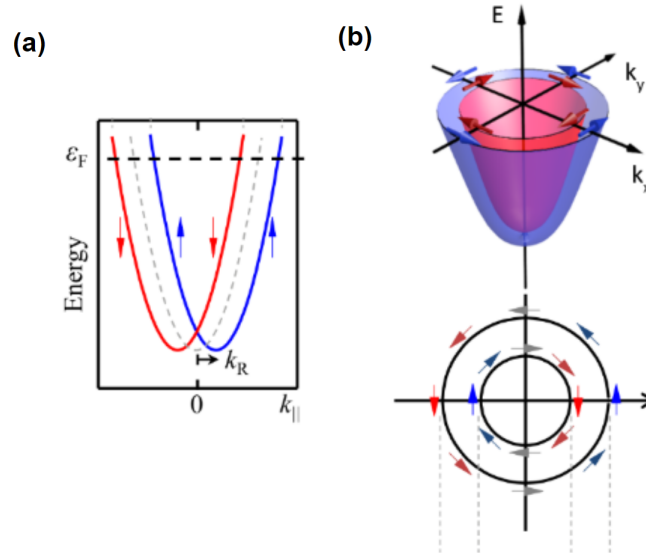


**Figure 1.1:** Schematic of the band splitting occurring in the presence of the Rashba effect. The degenerated parabolic band split into two  $k$ -splitted parabolic bands of opposite polarities separated by a factor of  $\alpha_R$ , the Rashba coefficient

### Conclusion

To conclude, we saw that the Rashba effect requires two main ingredients: strong spin-orbit coupling, and an external electric field perpendicular to the direction in which the electrons propagate. The nature of this electric field can vary in between different Rashba systems, whereas the SOC origin always lies in the presence of an atom with large orbitals. The Rashba effect will result in spin degeneracy being lifted and in a spin textured Fermi surface.

As stated above, by using the unique spin texture onset by the Rashba effect, one can achieve charge to spin conversion (Direct Edelstein Effect) and spin to charge conversion (Inverse Edelstein Effect).

### 1.1.3 The normal and inverse Edelstein effects and spin to charge interconversion

#### The direct Edelstein effect

We consider the Fermi contour of a single parabolic Rashba system. As aforementioned, in the  $k$  space it is represented by two  $k$  splitted parabolic bands of opposite polarities. Introducing a charge current into such a system is equivalent to populating a specific area of the  $k$  space. We chose the  $x$  axis so that the current introduced is purely along it. This is akin to introducing an in plane electric field  $E_{//}$ , or a shift of  $k$ ,  $\Delta k_x = \frac{qm^*}{\hbar^2 k} E_{//}$ . Shifting both bands by  $\Delta k_x$  yields two excess spin populations for the two contours, as illustrated on figure 1.2 (a). The two spin populations of opposite polarization generated this way are non equivalent because the Fermi surfaces considered are not. This results in a net spin density which can be estimated as [9][10]:

$$\langle \delta \sigma \rangle = \langle \delta \sigma \rangle_+ - \langle \delta \sigma \rangle_- = \frac{\alpha_R m^*}{2\pi \hbar} \Delta k_x \mathbf{y} \quad (1.31)$$

This highlights that a charge current can induce a spin current through the creation of two non equivalent populations of spins of opposite polarities in a Rashba-Edelstein system. This is commonly known as the direct Edelstein Effect (DEE).

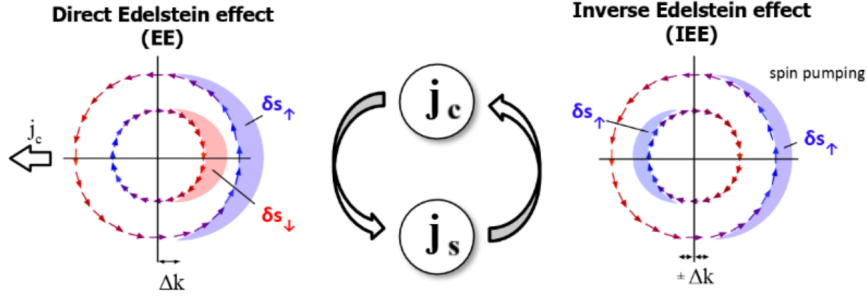


**Figure 1.2:** The Edelstein and Inverse Edelstein effects. Through the Rashba effect, a charge current can induce a spin current, and the inverse is also true.

### The inverse Edelstein effect

The reciprocal effect, the Inverse Edelstein effect (IEE), can also be deduced from relation [1.31](#) and was first experimentally observed by Rojas-Sanchez *et al.* [\[11\]](#). The injection of a pure spin current into a Rashba system (through spin injection, spin pumping, etc...) results in uncompensated currents in opposite  $\pm k_x$  directions as illustrated on figure [1.2](#) (b). There are more state to populate on the outer contour and they are of higher  $k$  values which, in the end, results in a net charge current [\[11\]](#) :

$$j_c = j_{c+} + j_{c-} = \frac{q\alpha_R}{\hbar} \langle \delta\sigma \rangle \mathbf{x} \quad (1.32)$$

Relation [1.31](#) and [1.32](#) demonstrate that Rashba systems are suitable for the investigation of spin-charge interconversion.

### Efficiency of the conversion: the figure of merit

It is convenient to introduce a figure of merit that relates the spin currents and charge currents for both DEE and IEE. Such a figure of merit is a direct measure of the spin to charge interconversion efficiency in Rashba systems. We define  $\lambda_{IEE}$  as:

$$j_c = \lambda_{IEE} j_s \quad (1.33)$$

Finally, we note that we can also show that in spin pumping experiments  $j_s$  is related to the total non equilibrium spin density [\[11\]](#) by

$$\frac{j_s}{e} = \frac{\langle \delta\sigma \rangle}{\tau^*_s} \quad (1.34)$$

where  $\tau_s$  is the spin relaxation time. By combining equations [1.32](#) and [1.34](#), we get the expression of the figure of merit as a function of the Rashba coefficient

$$\lambda_{IEE} = \frac{\alpha_r \tau^*_s}{\hbar} \quad (1.35)$$

Increasing the Rashba coefficient of such systems and expanding the lifetime of spins is thus of critical importance to design efficient spin to charge converters using the Rashba effect.

## 1.2 The MESO and FESO devices

The fields of spintronics and spin-orbitronics, which we just introduced, have been highlighted as particularly promising for the conception of *In-memory computing* beyond CMOS devices [5]. In parallel, important research and industrial developments on new types of non-volatile memories based on the interplay of ferroic orders (be it with ferromagnets [8], antiferromagnets [12] or ferroelectrics [13][14][15]...) and spin-orbitronics have seen important attention. Thorough efforts have been made to make such technologies compatible with large scale fabrication processes and the current semiconductor industry.

In 2018, Intel proposed its new architecture for a beyond CMOS device [8]. The proposed structure uses the magnetoelectric effect to switch a ferromagnet that stores the information. The information is read out using spin-orbit coupling. Hence the name Magneto Electric Spin-orbit (MESO) device. Changing the sign of the incoming current reverses the polarity of the ferromagnet through the magnetoelectric effect, which in turns changes the sign of the spin pumped in the spin-orbit layer which results in a current switch at the exit of the device. The proposed architecture is presented in figure 1.3.

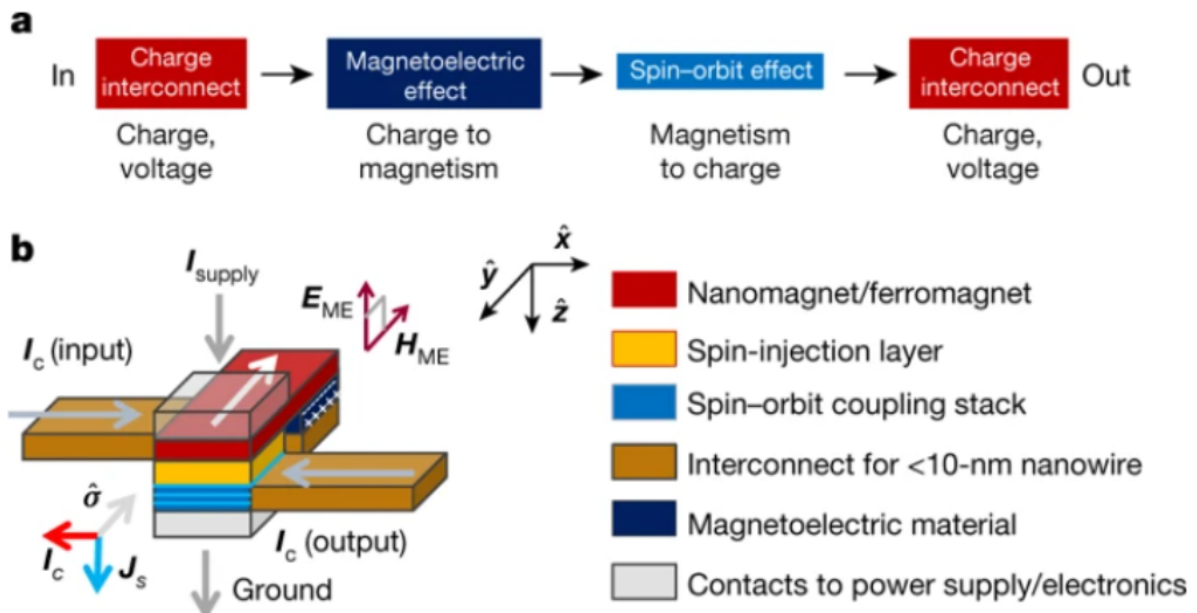


**Figure 1.3:** The MESO device proposed by Maniputrani et al. [8]. The input current is converted into a ferromagnetic information through the use of the magnetoelectric effect. The read out is performed through a spin to charge conversion heterostructure consisting of a spin injection layer and a spin-orbit coupling layer.

This device has a number of advantages compared to other beyond CMOS technologies. Due to the favorable scaling of spin to charge conversion, it is highly compatible with progressive miniaturisation of devices. As a result, the MESO energy scales to the cube with size. The authors of the MESO paper also claim that the interconnects necessary to build complex architectures have relatively low requirements. The device supports high resistivity ( $>1 \text{ m}\Omega \text{ cm}$ ) and capacitance ( $>10 \text{ fF } \mu\text{m}^{-1}$ ), both requirements being up to 100 % less strict than for other "beyond CMOS-devices" designs. It supports relatively long electrical interconnects while preserving switching time, in stark contrast with pure spintronic devices, that have to use spin interconnects which are strongly limited by the spin flip time, which we previously introduced. According to simulation ran by the authors, this device has superior energy switching, lower switching voltage and higher logic density compared to state of the art CMOS technology [8].

Nonetheless, the control of magnetoelectrics (MEs) with low energy remains difficult and represents a

bottleneck towards developing the MESO device. The target switching voltage for a MESO device compatible magnetoelectric component is of 100 mV. In 2019, the year the MESO device was first introduced on, state of the art switching voltages of MEs were one order of magnitude higher than the target value, in the range of 1 V [8]. At the date of this manuscript redaction, in the span of only 5 years, state of the art MESO devices have made consequent progress and can now operate at switching voltages which are on the range of 100 mV [16]. Such progresses were made attainable through the use of La doped  $\text{BiFeO}_3$  [17]. However, such devices yield relatively low reliability: Vaz *et al.* demonstrated the reversability of the magnetisation of  $\text{La}_x\text{Bi}_{1-x}\text{FeO}_3/\text{CoFe}$  by an electric field but highlighted the lack of control of the phenomena [16]. More work is still needed to attain devices competitive with existing architectures.

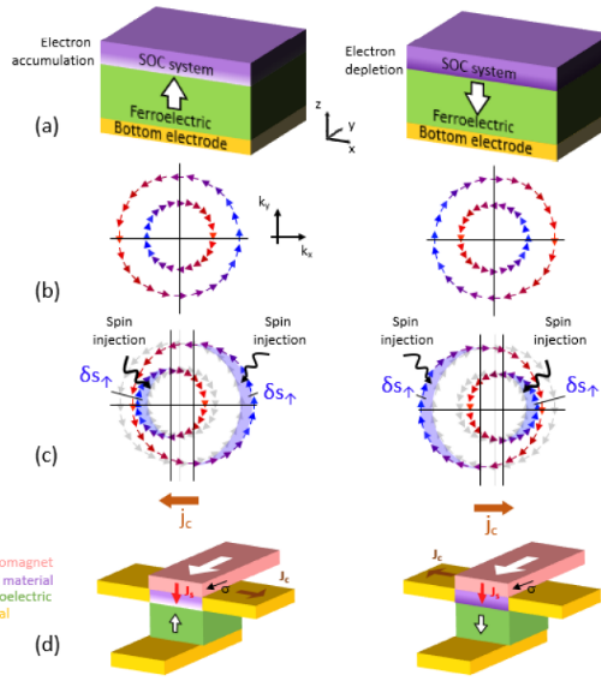


**Figure 1.4:** The FESO device proposed by Noel *et al.* [18]. In this device, the information stored in the ferromagnet is modulated through the ferroelectric control of spin-orbit coupling. This device does not need a magnetoelectric material. Reproduced from Noel *et al.* [18]

In addressing the difficulties linked to the utilization of magnetoelectrics, an alternative design was suggested by Noel *et al.* in 2020. In the proposed architecture, the spin-orbit coupling stack would be interfaced not with a magneto electric, but with a ferroelectric [18]. As previously highlighted, a sizeable atomic spin-orbit coupling coexisting with any symmetry breaking field would result in a Rashba environment, with all the subsequent effects concerning spin degeneracy, spin momentum locking and spin-to-charge interconversion that were highlighted in the preceding section. Several theoretical works highlighted the possibility of harnessing the polar character of ferroelectrics coupled with large intrinsic spin-orbit coupling material to achieve electric control of the spin-charge conversion [19]. This is precisely the role the magnetoelectrics is fulfilling in the MESO device.

Ferroelectrics have the advantage of presenting a ferroic order switchable by an electric field. The energy cost associated with this operation is 1000 times smaller than the one associated with switching the magnetisation of a ferromagnet [5]. We can imagine several designs based on the interplay of ferroelectricity and SOC. Lets for example consider an heterostructure composed of a ferroelectric and of a SOC. At the interface of the ferroelectric, electrons are accumulated or depleted depending on the polarization direction. This will in turn locally modify the electric field at the interface, ideally reversing it. If a Rashba state is present in

the SOC system at the interface with the ferroelectric, the modulation of the electric field will influence the spin texture, and consequently the spin-charge interconversion properties of the stack. In the extreme case in which the field changes direction, the injection of a spin current will produce a charge current whose sign will be fully determined by the polarization state of the ferroelectric[18]. Devices based on this principle were first introduced by Noel *et al.* in 2020 and are known as FESO devices. A schematic of such a device is presented in figure 1.4. The FESO device presents all the advantages of the MESO device in terms of energy efficiency, non volatility of the information stored as well as scalability. It also incorporates in a very similar way in modern electronic architectures. FESO based logic gates were proposed in a similar fashion as the one that were proposed for the MESO device[20][21].

In the following section, we will present fundamental concepts of ferroelectricity. Subsequently, we will introduce various Rashba systems and explore the potential of integrating them with ferroelectricity to achieve non-volatile ferroelectric control of the Rashba coefficient. Our ultimate objective is to incorporate these systems into devices resembling FESO for enhanced functionality, which is beyond the scope of this thesis alone.

## 1.3 Ferroelectricity

Ferroelectricity is a collective state which characterises a class of material, the ferroelectrics. It is one of the four known ferroic orders.

### 1.3.1 Ferroic orders

Ferroic materials are characterized by a phase transition upon which a spontaneous long-range ordering of some physical property emerges. The collective switching of this physical property, commonly referred to as the order parameter, is usually triggered by a lowering of the point group symmetry of the ferroic material crystal. This occurs at the temperature of the phase transition. The temperature of the phase transition is named the Curie temperature and denoted  $T_c$ . The order parameter, will have at least two low-energy states, typically degenerated in energy. An energy cost, associated with overcoming a barrier during the switching process from one energy state to another, is incurred. As a result, the low-energy states are usually remanent: if left under no influence, they remain in the state they were switched on. Exploited for their technological prospects, these remanent states find applications in memory devices. To minimize their internal energy, ferroic systems tend to form ferroic domains, where a long-range uniform ordering of the order parameter appears. These domains can be controlled through the application of an external conjugate field. However, switching from one state to the other requires the field to overcome the aforementioned energy barrier associated with collective switching. As a result, the sweeping of the order parameter by its conjugate field is a hysteretic process.

The emergence of the order parameter may cause a breaking of either or both the time reversal and space inversion symmetries. Based on this consideration, four classes of ferroic materials, classified according to the symmetry breaking induced by the onset of their order parameter, have been predicted and investigated. The four ferroic orders are as follows:

- Ferroelasticity: Space and time symmetries are preserved, allowing for spontaneous and cyclable strain under the application of stress.
- Ferroelectricity: Time symmetry is preserved, but space inversion is broken, resulting in spontaneous and cyclable electric polarization under the application of an electric field.
- Ferromagnetism: Space inversion is preserved, while time reversal symmetry is broken, leading to spontaneous and cyclable magnetic dipoles under the application of a magnetic field.
- Ferrotoroidicity: Both space and time reversal symmetries are broken, causing spontaneous ferrotoroidic order under the application of the ferrotoroidic field (see [22]).

Recently, multiferroics, in which the co existence of multiple order parameter exists, have been highlighted as potential key components for the elaboration of beyond CMOS devices[5].

### 1.3.2 Ferroelectrics

#### Generalities

Ferroelectrics are ferroics in which time reversal symmetry is conserved, but space inversion symmetry is broken. They are characterized by the presence of an internal remanent electric polarization  $\mathbf{P}$ , caused by the spontaneous ordering of electrical dipole moments. Dipolar moments result from polar displacements—specifically,

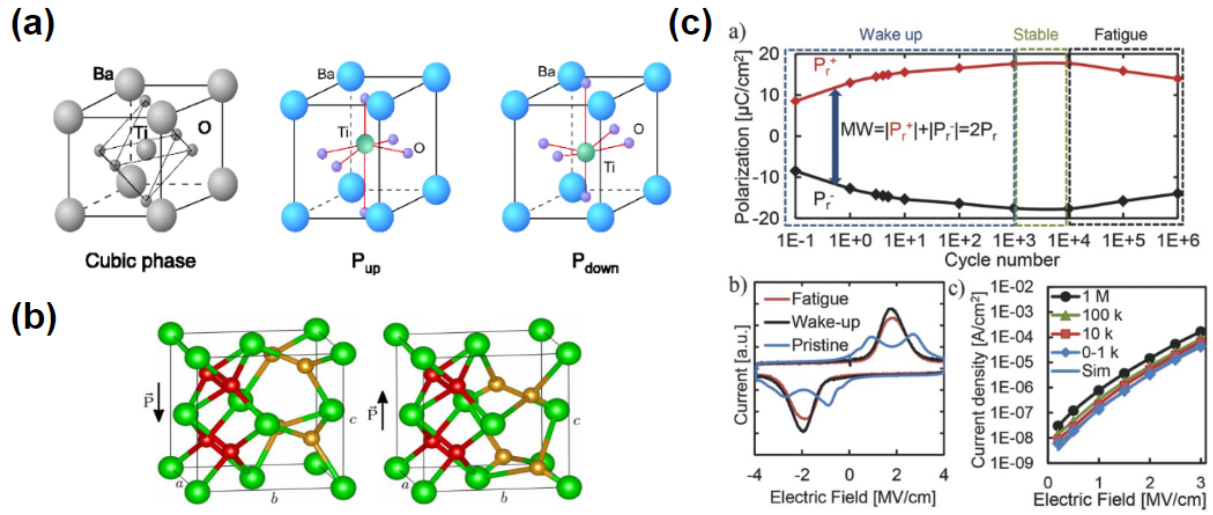


**Figure 1.5:** Prototypical ferroelectrics and wake-up effect: (a) perovskite-structure ferroelectric,  $\text{BaTiO}_3$  and (b) fluorite-structure,  $\text{HfO}_2$  polarization states; and (c) wake-up and fatigue effects in  $\text{HfO}_2$  capacitors. (a) adapted from [23], (b) adapted from [24], (c) adapted from [25].

the displacement of cations (positively charged) relative to anions (negatively charged). This displacement leads to a net electrical dipole moment at the scale of the unit cell. For this to occur, the crystal structure must be non-centrosymmetric. This justifies that, during the phase transition, the point group symmetry of the system is lowered in order to achieve a ferroelectric phase. A proper ferroelectric should display spontaneously ordered electrical dipole moments, even without external electric field application, resulting in a macroscopic polarization  $\mathbf{P}$ . An illustration of the crystal structure in the two degenerate polarization states of two prototypical oxide ferroelectrics is presented in panels (a) and (b) of Figure 1.5

However, the long-range ordering of dipolar electric moments is not a sufficient condition to characterize a ferroelectric material. As aforementioned, in a ferroic material, the order parameter has to be switchable by its conjugate field. In the case of ferroelectricity, the polarization has to be switchable by an electric field. Other polar materials lack the particular property of switchability of the order parameter by its conjugate field. This is the case for piezoelectrics and pyroelectrics, in which the polarization can be switched under the application of pressure and temperature changes, respectively. Ferroelectrics will always exhibit piezoelectric and pyroelectric behaviors, but the inverse is not true. As such, ferroelectrics are characterized by their hysteretic response to the cyclic application of an electric field. A lower order of polarization switching, such as piezo- or pyroelectricity, can still indicate premises of a ferroelectric order.

Ferroelectrics can be characterized by a number of figures of merit. These figures include the magnitude of the order parameter (*i.e.*, the polarization, in  $\mu\text{C cm}^{-2}$ ), their Curie temperature (in K), their band gap (in eV), their endurance (*i.e.*, the number of times the ferroelectric can be cycled before the ferroelectric properties vanish because of fatigue, in cycles), and their coercive field (in  $\text{kV cm}^{-1}$ ). The coercive field, in particular, needs to be compared to the breakdown field, which is an intrinsic property of the crystal structure. Perhaps the most famous oxide ferroelectric is  $\text{PbZr}_x\text{Ti}_{1-x}\text{O}_3$  (PZT). PZT typically has a polarization of  $40 \mu\text{C cm}^{-2}$  at  $x=0.52$ , a Curie temperature  $T_c \sim 400$  K, an endurance of up to  $10^{15}$  cycles, and a coercive field of  $40\text{-}50 \text{ kV cm}^{-1}$  (which needs to be compared to a breakdown field of  $\sim 1400 \text{ kV cm}^{-1}$ ) [26] [27]. A comprehensive summary of the ferroelectric properties of the most extensively studied ferroelectric families is presented in Figure 1.6 covering all the key figure of merits.

It is worth mentioning that not all ferroelectrics are perfect. Some ferroelectric materials may present weak

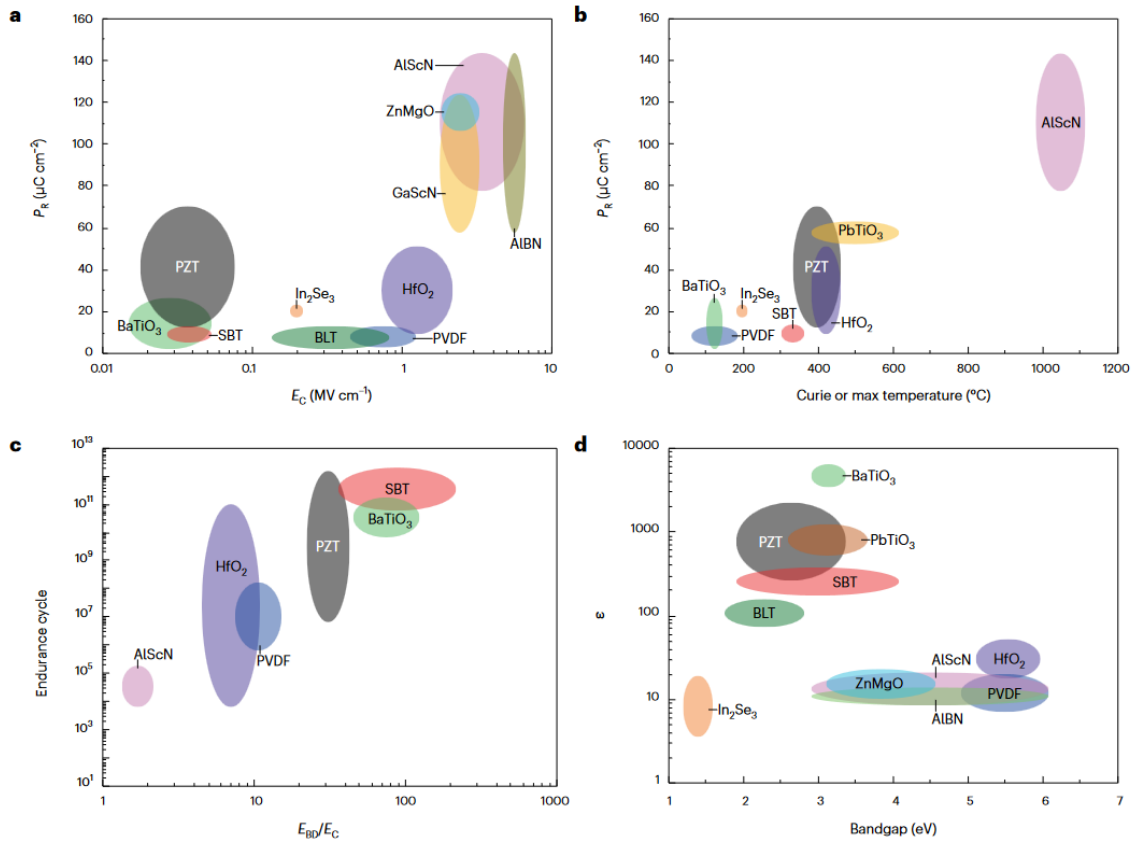


**Figure 1.6:** Overview of state art ferroelectric properties of popular ferroelectrics, reproduced from [?].

to no natural polarization in their pristine state. However, they may still have remanent, stable ferroelectric domains along with the typical  $\mathbf{P}(E)$  ferroelectric loops when forcibly activated through the application of an external electric field. This effect is usually referred to as the wake-up effect and was observed in perovskite-structure ferroelectrics[28]. The number of cycles needed to stabilize the ferroelectric properties must be compared to the endurance of the ferroelectric. Fortunately, commercially available perovskite-structure ferroelectrics interfaced with oxide electrodes show negligible wake-up effect[29]. However, it is not (yet) the case for the next generation of ferroelectrics such as fluorites[30] or Wurtzites[31] ferroelectrics. The wake-up and fatigue effects in fluorite HfO<sub>2</sub> are illustrated in panel (c) of Figure 1.5.

### Formalism

To explain the phase transition from the paraelectric to the ferroelectric phase at the Curie temperature, Landau introduced a theoretical model in 1937, which was further developed by Devonshire in the early 50s. This model is nowadays widely known as the Landau-Ginzburg-Devonshire (LGD) theory of phase transition[32]. At the vicinity of the Curie temperature, the free-energy of a crystal structure can be expanded into even powers of the polarization. We consider the simplest 1D case. In this framework, the Taylor expansion of the free-energy translates as:

$$\Phi = \Phi_0 + \frac{\alpha}{2}P^2 + \frac{\beta}{4}P^4 - EP(\beta > 0) \quad (1.36)$$

with

$$\alpha = \alpha_0(T - T_0) \quad (1.37)$$

where  $\Phi_0$ ,  $\alpha$ ,  $\beta$ , and  $E$  denote the temperature and polarization-independent free-energy, temperature-dependant coefficient, temperature-independent coefficient and external electric field, respectively. When considering this particular expansion of the free-energy,  $\beta$  is necessarily strictly positive. The stable states of the system are characterized by the conditions at which the first derivative of the free energy is equal to zero. This can be written as:

$$\frac{\partial \Phi}{\partial P} = 0 \rightarrow E = \alpha P + \beta P^3 \quad (1.38)$$

For alpha positive, *i.e.* for  $T > T_0$ , the only possible extremum of the free-energy is a minimum at zero polarization: the crystal is paraelectric. For alpha negative, *i.e.* for  $T < T_0$ , the free energy will have three possible extrema. A local maximum at  $P=0$ , which accounts for a metastable unpolarised state. In addition, the free energy will be minimal at two opposite polarization values, with magnitude  $P = \pm \sqrt{-\frac{\alpha}{\beta}}$ , resulting into two stable polarization states. Switching the polarization from one state to the other requires overcoming the energy barrier height  $\Phi_c = \frac{\alpha^2}{4\beta}$ .

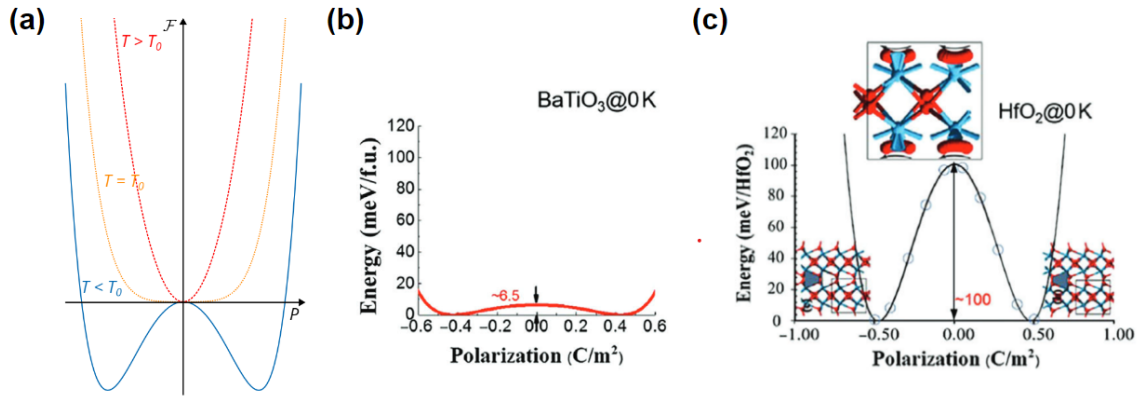


**Figure 1.7:** LGD theory of phase transition and energy landscapes of prototypical ferroelectrics (a) Schematic potential landscape of a system passing through a paraelectric-ferroelectric phase transition around the temperature  $T_c$ , and energy landscapes of two prototypical ferroelectrics: (b)  $\text{BaTiO}_3$  at 0 K and (c)  $\text{HfO}_2$  at 0 K. (b) adapted from [30], (c) adapted from [24].

Using this approach we can explain the hysteretic behavior of the polarization with respect to the external electric field: when cycling the field, the system reaches a local minimum of the internal field, which can only be reversed when the external field provides enough energy to overcome the energy barrier previously introduced, at which point the internal field switches. This operation causes the internal electric field to be stable at positive bias smaller than the coercive voltage. This results in the characteristic  $\mathbf{P}(E)$  hysteretic loop. A schematic of the energy landscape across the ferroelectric phase transition is represented on panel (a) of figure 1.7, along with the energy landscapes of two prototypical ferroelectric systems.

Finally, we note that the Landau theory can be pushed to the sixth order to account for the different orders of the phase transition. The order of the phase transition will be encoded in the sign of  $\beta$ . Other LGD extensions can also include more components to take into account strain and long-range interactions. Strain in particular can play an essential role in ferroelectricity, as will be illustrated later in this manuscript.

## 1.4 Rashba systems

It was strongly emphasised that the Rashba effect requires the co-existence of two components: spin-orbit coupling and an external symmetry breaking electric field perpendicular to the direction of the flow of electrons. Different mechanisms were proposed and exploited as the origin of the electric field. In this section we will be classifying and describing different Rashba systems, each family emerging from a different nature of the electric field responsible for the symmetry breaking.

### 1.4.1 Overview

#### Semiconductor heterostructures

The first Rashba systems to be investigated were quantum wells created with heterostructures of Zinc Blende semiconductors, such as InAlAs/InGaAs [33] or GaSb/InAs [34]. These systems involve sandwiching a metallic layer between an insulating hole-doped layer and an undoped insulating layer, creating a conduction channel subjected to an electric field perpendicular to the carrier flow. The electric field experienced by the confined carriers can be modulated by using a gate voltage. In InGaAs/InAlAs heterostructures, the analysis of Shubnikov-de Haas oscillations and spin precession yields a Rashba parameter of approximately  $0.67 \times 10^{-1} \text{ eV} \cdot \text{\AA}$  [33].

#### Heavy metal surfaces

Shortly after, surfaces of heavy metals and alloys (e.g.: surfaces of Au(111) [35], Ir(111) [36], Bi(111) [37], BiAg(111) alloys [38]...) were investigated by angle resolved photo emission spectroscopy (ARPES). The structural inversion asymmetry provided by the surface coupled with the large intrinsic spin-orbit coupling enabled by the heavy-metal related orbitals was proven to result in relatively large Rashba band splittings, two orders of magnitude larger than that of semiconductor heterostructures (e.g.:  $\alpha_R = 3.05 \text{ eV} \cdot \text{\AA}$  for BiAg(111) alloys surfaces [38]).

#### Two dimensional Electron Gases, topological insulators and FERSCs

The discovery of 2DEGs at the interface of insulating perovskite oxides in 2004 as well as the recent investigation of topological insulators (TIs) proved to be interesting for the Rashba community. The Rashba effect was indeed observed and characterised in both 2DEGs (e.g.:  $\alpha_R = 20 \text{ meV} \cdot \text{\AA}$  in LAO/STO [39]) and TIs (e.g.:  $\alpha_R = 4 \text{ eV} \cdot \text{\AA}$  in Bi<sub>2</sub>Se<sub>3</sub> [40]). Finally, structures that present inversion symmetry coming from their polar character were also investigated for their Rashba properties (e.g.:  $\alpha_R = 4.8 \text{ eV} \cdot \text{\AA}$  in GeTe [41]). A more detailed overview of the mechanism at play within these three systems ( 2DEGs, TIs and polar materials, which includes ferroelectric Rashba semiconductors) will be given in the next sections.

### 1.4.2 Two dimensional Electron Gases

Two dimensional Electron Gases (2DEGs) were first investigated experimentally in 2004 at the interface of LaAlO<sub>3</sub> (LAO) grown by PLD on SrTiO<sub>3</sub> (STO) by Ohtomo & Hwang [42]. LAO and STO are both insulators, making the apparition of this interfacial conductive state all the more intriguing.

#### Generalities

The formation of this so called 2DEGs was at first attributed to the polar catastrophe scenario, which is the result of a polar discontinuity at the interface. LAO(001) is a sequence of alternating layers of (LaO)<sup>+1</sup>

and  $(\text{AlO}_2)^{-1}$ . STO, on the other hand, is non polar along the (001) axis, *i.e.* it is a sequence of alternating uncharged layers. Given that no electronic transfer occur, as the thickness of LAO increases, an interfacial electric field should build up. This electric field will in turn lead to an electrical potential that will diverge with the LAO thickness. This can be avoided by the transfer of half an electron at the interface, to compensate for the polar discontinuity. This phenomena can explain the apparition of an interfacial conductive state<sup>[43]</sup>. This theory is corroborated by the existence of a critical LAO thickness under which the formation of a 2DEG can not occur: if the potential is not divergent enough, the electronic transfer does not occur. This critical thickness was experimentally determined to be of 4 unit cells of LAO<sup>[44]</sup>. The polar catastrophe concept is illustrated on panels (a) and (b) of figure 1.8.

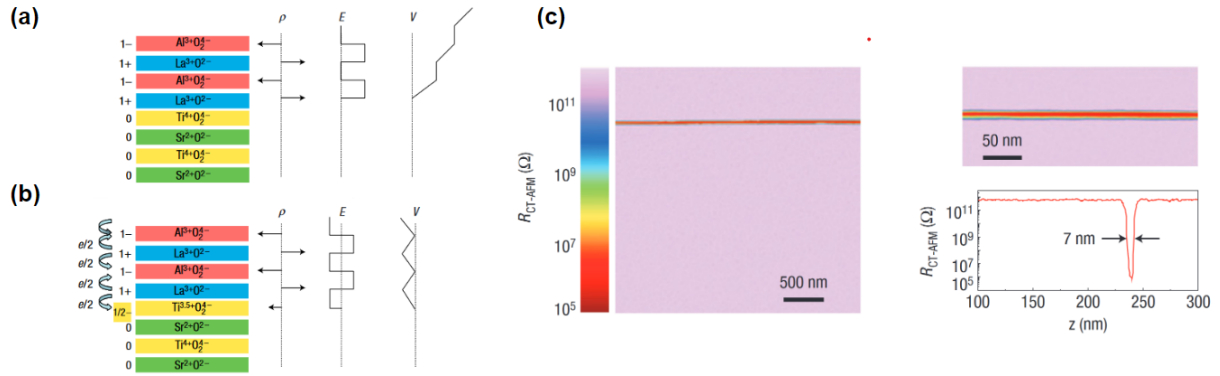


**Figure 1.8:** Experimental evidence of a 2DEG at the LAO/STO interface and its origin (a) Depicts the polar catastrophe scenario in which the electrical potential diverges with the thickness, which can be avoided by the transfer of half an electron, from LAO to STO when STO is  $\text{TiO}_2$  terminated, as depicted in (b). (c) CT-AFM resistance mapping of an LAO/STO interface. The conductive 2DEG is confined within 7 nm at the interface, sandwiched in between the insulating perovskites. (a) and (b) were adapted from <sup>[43]</sup> and (c) was adapted from <sup>[45]</sup>.

Later studies demonstrated other methods to obtain a 2DEG at the surface of STO, *via* deposition of other insulating perovskites such as  $\text{LaTiO}_3$  or  $\text{LaVO}_3$ , or by deposition of amorphous materials like the spinel  $\gamma\text{-Al}_2\text{O}_3$ <sup>[46]</sup>. Bare surfaces of STO were also made conductive through proper surface treatments<sup>[47]</sup>. This particular approach enabled the characterisation of 2DEGs by surface methods, such as Angle Resolved PhotoEmission Spectroscopy (ARPES), but has to be performed under ultra high vacuum. However, the formation of 2DEGs *via* the aforementioned methods, be it through the formation of a secondary or ternary compound or the use of complex surface treatments, is not cost efficient and hardly scalable.

Of interest for us, another approach recently emerged to generate 2DEGs at interfaces of oxide perovskites<sup>[48]</sup><sup>[49]</sup>. By depositing a thin layer of metal on top of an oxide perovskite, a 2DEG is generated at the interface. The formation mechanism of such 2DEGs lies in the reduction of one of the sub-oxide specie of the oxide perovskite by the metal (e.g.:  $\text{Me}^0 + \text{Ti}^{\text{IV}}\text{O}_x \rightarrow \text{Me}^0 + \text{Ti}^{\text{III}}\text{O}_{x-1}$  in the case of STO), coupled with a charge transfer from the cation (: e.g.: Ti) to the oxygen, and the interdiffusion of oxygen across length scales larger than a monolayer. Up to a critical metal thickness (e.g.: 2 nm of Al for STO/Al<sup>[48]</sup>) the metal is pumping the oxygens from the perovskite, which results in the creation of interfacial oxygen deficiencies. This, combined with a charge transfer from one of the cations, results in a 2D conductive state confined at the interface, in the oxide perovskite. The metal deposited at the interface will be oxidised into an insulating interfacial layer (e.g.:  $\text{Al}_2\text{O}_3$ ). As a result, the conductive state is sandwiched in-between two insulating (non equivalent) layers (e.g.: STO on one side,  $\text{Al}_2\text{O}_3$  on the other). Examples of suitable metals to deposit on perovskites to induce a 2DEG include Al, Ta, Y<sup>[50]</sup>, Gd<sup>[51]</sup> and Eu<sup>[52]</sup>. Magnetotransport and XPS confirmed the reduction of Ti by Al<sup>[53]</sup>. The characterisation of interfaces at which such 2DEGs appear by XPS was made possible

by the low deposition thickness required to create a 2DEG with this method: the critical thickness of metal which has to be deposited to reduce the perovskite is thinner than the penetration depth of the X-Rays used in a typical XPS experiment. The creation of 2DEGs *via* deposition of aluminium thin films on STO and KTO was optimised by Vicente-Arche *et al.* [50] [53].

We would like to highlight that this approach is systematic, scalable and highly reproducible. It constitutes a toolbox that could allow for the investigation of 2DEGs at the interface of any insulating oxides, given that the right metal is deposited on top. This toolbox which allows the engineering of metallic topological states on perovskite is of the utmost interest to probe the electronic properties that maybe induced in insulating oxides with exotic physical properties (e.g.: ferroic properties). This approach has been exploited to create functional 2DEGs at interfaces of ferroelectrics [48] [54], multiferroics [55] and superconductors [56].

### 2DEGs as Rashba materials

In the systems aforementioned, an intrinsic symmetry breaking electric field is present at the interface at which the 2DEG is formed. If, in addition, one of the two insulators in between which the 2DEG is confined contains a high spin-orbit component, they would be perfect candidates to probe the Rashba effect [39] [57]. In fact, the Rashba spin splitting at the LaO/STO interfaces was predicted [58] and measured by both weak antilocalisation (WAL) [39] [59] and bilinear magnetoResistance (BMR) [60] to be of the order of magnitude  $\alpha_r \sim 20 \text{ meV \AA}$ . We note that the electrons of the 2DEG created at such an interface are subjected to both a linear and a cubic Rashba effect. The linear/cubic Rashba effect ratio can be tuned by a gate voltage [61].

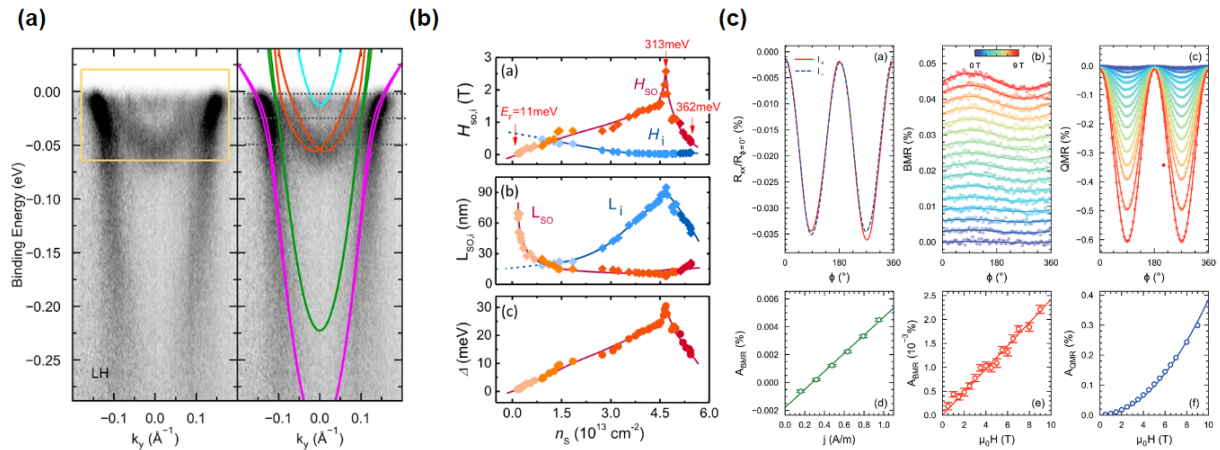


**Figure 1.9:** Experimental observation of Rashba spin splitting occurring in a KTO based-2DEG: (a) Band dispersion of Al/KTO(001) surface measured by ARPES. The tight-binding fits are overlaid to the data in the right panel. A specific color is associated to each pair of bands. (b) experimental variations of the spin-orbit and dephasing fields and lengths, as well as the spin-orbit splitting  $\Delta$  for different carrier densities in illuminated KTO 2DEG samples and (c) BMR acquired on a KTO 2DEG. (a) reused from [62], (b) reused from [63] and (c) reused from [64]

To design 2DEGs with enhanced Rashba properties, the fabrication of 2DEGs on  $\text{KTAO}_3$  was thoroughly investigated. The creation of a 2DEG was demonstrated by a cleaving method [65], by growth of polar oxides [66] [67] [68] or by deposition of Al [64]. The larger SOC of tantalum ( $Z=73$ ) compared to titanium ( $Z=22$ ) enhances the band splitting caused by the Rashba effect. The fabrication of KTO based 2DEGs enabled the direct visualisation of the Rashba splitting by ARPES measurements [62]. In another work performed in Laboratoire Albert Fert, the Rashba coefficient was extracted to be  $\alpha_R \sim 70 \text{ meV \AA}$  to  $280 \text{ meV \AA}$  *via* BMR measurements [64], in good agreement with the values measured by ARPES [62] and extracted by WAL [63].

### 1.4.3 Topological insulators

The initial predictions for topological insulators focused on 2D systems, specifically graphene<sup>[69]</sup> and HgTe/CeTe<sup>[70]</sup> quantum wells. The concept of TIs originated from the quantum hall effect. When a magnetic field perpendicular to the plane of a 2D material influences its electrons, they exhibit circular orbital motion with a cyclotron frequency given by:

$$\omega_{cyclotron} = \frac{qB}{m^*} \quad (1.39)$$

This explains the overall insulating behavior of the material. However, the circular orbit is impeded at the outermost edges, resembling scattering by a magnetic impurity. This interference causes the electron to deviate from its orbit and propagate along the edge in a specific direction. Consequently, under the influence of a strong perpendicular magnetic field, these so-called 2D quantum hall insulators exhibit 1D conductive edge states, while the bulk remains insulating. As mentioned earlier, spin-orbit coupling can induce a magnetic-like effect without an external magnetic field. In the presence of spin-orbit coupling, it might happen that one valence band is energetically lifted with respect to the other because of the SOC, potentially surpassing the lowest conduction band. In this case, a gap reopens, but the conduction and valence bands' nature is inverted compared to a trivial insulator. Topology dictates that at the interface between a non-trivial insulator (*i.e.*:with a reversed band structure at one point in the Brillouin Zone) and a trivial insulator(*e.g.*:air), the gap should close to reopen in either band order on each side. This leads to the emergence of 1D conduction channels at the edges of the topological insulator, which can also be referred to as a quantum spin hall insulator, even in the absence of a magnetic field. The mechanisms at play in the creation of spin hall edge states are illustrated on panel (a) of figure <sup>[1.10]</sup>

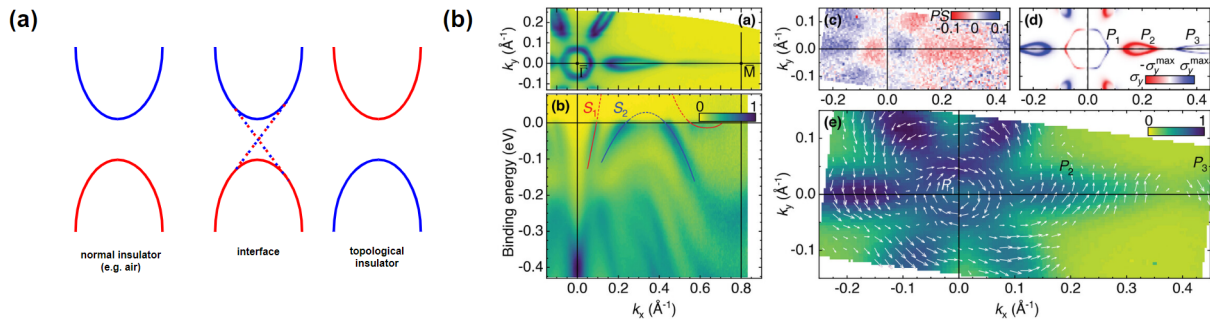


**Figure 1.10:** *Topological insulators. (a) schematic of the band structure of an interface of a quantum spin hall insulator with a trivial insulator and (b) band structure acquired by ARPES of Bi<sub>0.85</sub>Sb<sub>0.15</sub>. (b) reproduced from [71]*

The absence of a requirement for a perpendicular magnetic field in a specific direction indicates that the material is no longer confined to being 2D. Three-dimensional TIs represent an extension of quantum spin hall insulators, where spin-orbit coupling plays a crucial role in creating 2D topologically conductive edge states. In comparison to their 2D counterparts, these materials offer the advantage of not only presenting spin-locked 1D channels but also a surface state characterized by a Rashba spin texture. This phenomenon has been confirmed through Angle-Resolved Photoemission Spectroscopy (ARPES)<sup>[71]</sup>. The band structure of Bi<sub>0.85</sub>Sb<sub>0.15</sub> is reproduced on panel (c) of figure <sup>[1.10]</sup>. Examples of such materials include Bi<sub>2</sub>Se<sub>3</sub>, Bi<sub>2</sub>Te<sub>3</sub> as well as Bi<sub>x</sub>Sb<sub>1-x</sub><sup>[72]</sup>. In a recent work from Laboratoire Fert, the spin-to-charge conversion was recently demonstrated by making use of the Rashba spin-texture characterising the surface state of Bi<sub>0.85</sub>Sb<sub>0.15</sub><sup>[71]</sup>.

### 1.4.4 Ferroelectric control of the Rashba effect

#### 1.4.4.1 Ferroelectric control of the Rashba effect: Functionalisation of the 2DEG

Functionalising the insulating perovskite on which the metal is deposited may result in a Rashba 2DEG with added features. The idea is to use a perovskite with an exotic property (*e.g.*: collective switching) and to try to propagate this property to a 2DEG created at one of its interfaces (*e.g.*: at the interface with a sputtered metal). Ferrioc 2DEGs were recently demonstrated by using this method. In 2020, Noel *et al.* [18] successfully stabilised a ferroelectric 2DEG on STO. STO undergoes a temperature and electric field driven phase transition to a field-induced ferroelectric state. By applying a strong voltage loop to STO, it becomes a ferroelectric with a  $T_c$  of 50 K. Using this approach, the authors were able to measure a ferroelectric 2DEG at the interface with sputtered aluminium. The key results of this study are reported on figure 1.11. In an even more recent study, Brehin *et al.* investigated 2DEGs grown on ferroelectric calcium doped STO (Ca-STO) [54]. The authors demonstrated that a 2DEG grown on a ferroelectric substrate could itself become ferroelectric. They obtained a ferroelectric 2DEG with  $T_c = 25$  K. By changing the electric field applied to the system, they were able to modulate and even reverse the sign of the Rashba coefficient, hence opening up the way towards FESO like devices using ferroelectric 2DEGs.

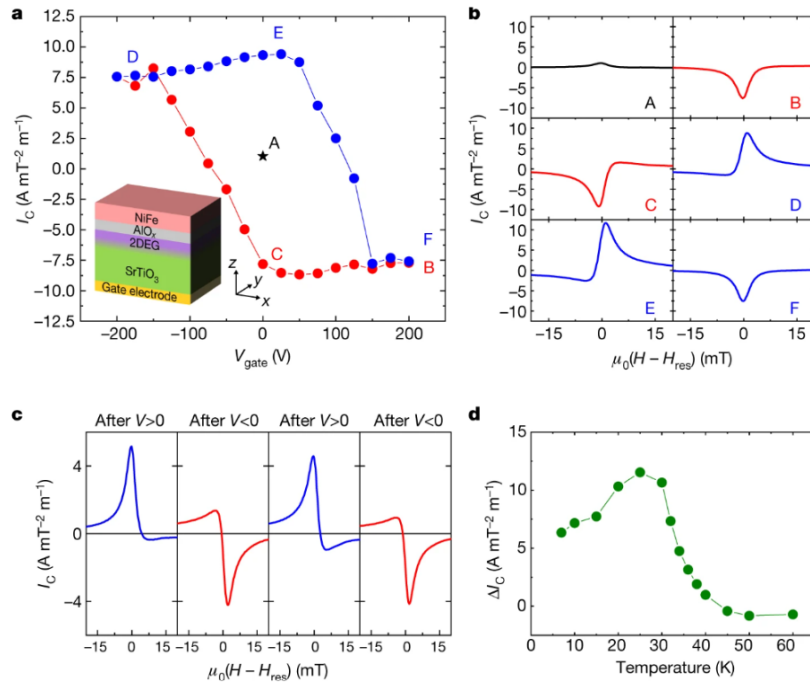


**Figure 1.11:** *Electrical control of spin-charge conversion. (a) Gate-voltage dependence of the charge current acquired after injecting spins through spin pumping. (b) Magnetic-field dependence of the current produced in spin pumping experiment, (c) charge current at electrical remanence and (d) temperature dependence of the difference between the two current states defined on panel (a). Reproduced from [18].*

#### 1.4.4.2 Heterostructures

An other approach towards the electric control of spin-to-charge interconversion comes in the form of heterostructures. Heterostructures comprised of a ferroelectric layer interfaced with a spin-orbit coupling layer should have all the necessary ingredients to be the medium of the electrical control of spin to charge conversion.

##### Full oxide Heterostructures

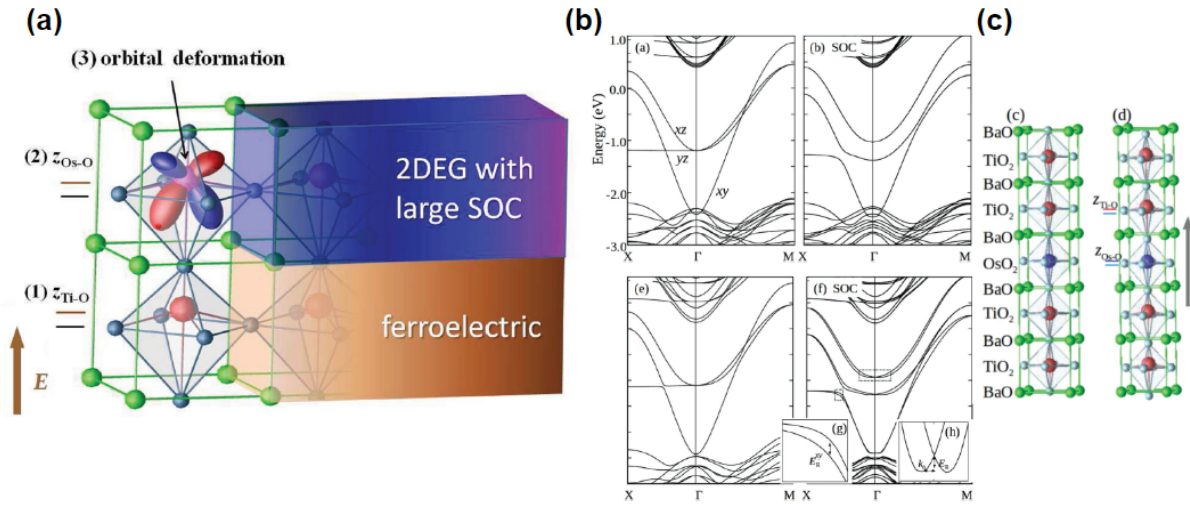


**Figure 1.12:** Oxides as FERSCs (a) Schematic of the oxide heterostructure. One of the layers is a ferroelectric while the other one provides strong spin-orbit coupling. (b) Band structure in the presence and in the absence of an out-of-plane electric field. The bands split when the electric field is applied and (c) a schematic of the atomic displacements induced in the BOO by the atomic displacements in BTO. Adapted from [73]

In 2015, different heterostructures composed of different oxides with the same perovskite crystal structure and a good lattice match were proposed as a suitable candidates for the observation of a giant switchable Rashba effect [73]. In a  $(\text{BaTiO}_3)_4/(\text{BaOsO}_3)_1$  ( $\text{BTO}_4/\text{BOO}_1$ ) heterostructure, the BTO plays the role of the ferroelectric while the two dimensional electron gas (2DEG) confined in the BOO layer is affected by the strong SO coupling coming from the heavy osmium ( $Z=76$ ) atoms. The ferroelectricity in BTO is caused by a Ti-O displacement of  $0.14 \text{ \AA}$ , which in turn induces an Os-O displacement of  $0.05 \text{ \AA}$ , hence breaking the symmetry in the BOO layer. As a result, a switchable Rashba spin splitting (RSS) with a Rashba coefficient of  $\alpha_R = 0.186 \text{ eV \AA}$  was predicted in this heterostructure. The authors computed the Rashba coefficients of the broader family  $(\text{BaTiO}_3)/(\text{Ba}(\text{Os, Ir, Ru})\text{O}_3)$  (see table 1.1). A scheme of the considered heterostructure along with the DFT calculations of the band structure with and without ferroelectricity are presented on figure 1.12.

In a more recent proposal, bismuth based hetero-structures with generic formula  $\text{BiMO}_3/\text{PbTiO}_3$ , ( $M=\text{Se, Y, La, Al, Ga, In}$ ) were proposed [74] as a family of compounds in which the RSS can be controlled through ferroelectricity. Compared to the systems we just mentioned, the heterostructure was chosen so that the RSS occurs at the conduction band minimum (CBM). In this proposition, the ferroelectric breaking the inversion symmetry is  $\text{PbTiO}_3$ , while the adjacent perovskite contains bismuth, which will be responsible for the strong SOC.

### Metal oxide hybrid heterostructures

Hybrid systems comprised of oxides and sputtered metals were also demonstrated as candidates to harbour the ferroelectric control of spin-orbit coupling. In a remarkable study, Fang *et al.* demonstrated that by switching the polarization of  $\text{PbZr}_{0.2}\text{Ti}_{0.8}\text{O}_3$  (PZT) interfaced with platinum (111) oriented, the degree of charge-spin conversion in the platinum could be modulated [75]. They attributed this effect to the onset of a Rashba coupling in the platinum in the  $P_\uparrow$  configuration of PZT, with a Rashba coefficient of  $\alpha_R = -152 \text{ meV \AA}$ , and no Rashba effect in the  $P_\downarrow$  configuration of PZT. As a result, they demonstrated the feasibility of using an electric field to modulate the Rashba effect in such structures, which should consequently modulate the spin-charge conversion. Xu *et al.* also reported the ferroelectric control of spin-orbit effects in a

Material formula	polarization ( $\mu\text{Ccm}^{-2}$ )	Rashba coefficient (eV $\text{\AA}$ )	Ref
BaTiO <sub>3</sub> /BaOsO <sub>3</sub>	$\sim 30$	0.186	[77] [73]
PbTiO <sub>3</sub> /BiInO <sub>3</sub>	$\sim 60$	0.5	[78] [74]
BaTiO <sub>3</sub> /Bi(111)	$\sim 30$	1.45	[77] [79]
PbZr <sub>0.2</sub> Ti <sub>0.8</sub> O <sub>3</sub> /Pt(111)	80	0.152	[75]
PbTiO <sub>3</sub> /Pt(111)	$\sim 60$	-	[80]
PbTiO <sub>3</sub> /Pd(111)	$\sim 60$	-	[80]

**Table 1.1:** Predicted ferroelectric Rashba heterostructures as well as typical measures of their ferroelectric and Rashba properties.

similar heterostructure [76]. The authors also proposed alternative heterostructures in which they anticipated a comparable trend, albeit with a more modest impact.

Table 1.1 highlights some heterostructures examples which were predicted or measured to present a RSS tunable by ferroelectricity.

#### 1.4.4.3 FerroElectric Rashba SemiConductors

Another approach to trigger the Rashba effect consists in making use of the electric field which arises from the symmetry breaking induced by the presence of ferroelectricity in a material in which a strong SOC is also present. Such materials are commonly referred to FerroElectric Rashba Semi Conductors (FERSCs).

##### GeTe and related compounds

FERSCs were first introduced in 2012 by DiSante *et al.* [41] [13]. The authors predicted that ferroelectricity and SOC should coexist in GeTe. Below 720 K, Ge and Te ions are displaced from their ideal rock salt positions along the (111) direction, resulting in a net polarization reversible by the application of an electric field. DiSante *et al.* predicted a Rashba splitting of the bands in the direction perpendicular to the polarization. Moreover, reversing the polarization, *i.e.* switching the ferroelectric, induces a spin texture reversal, demonstrating the possibility to electrically control the Rashba parameter in such systems. Results showing RSS in GeTe are presented on figure 1.13. By assuming k-linear dispersion, the authors computed the Rashba coefficient:

$$\alpha_R = \frac{2E_R}{k_R} \quad (1.40)$$

and found an  $\alpha_R$  value of 4.8 eV  $\text{\AA}$ . This value is one order of magnitude higher than the values observed for typical Rashba systems at interfaces [73] [75]. The main issue lying in GeTe as a FERSC lies in its semiconducting nature, specially in its small gap value (0.65 eV [41]). The high density of electrically active Ge vacancies in the crystal lattice results in the screening of the external electric field by the large density of holes carriers. The control of the polarization is impeded by the leakage currents created this way. GeTe is thus considered a weak, rather leaky ferroelectric, more akin to a polar metal than a proper ferroelectric. This makes it considerably harder to experimentally observe ferroelectricity and to probe the Rashba effect. Nonetheless, ferroelectric control of the Rashba effect in GeTe was recently experimentally demonstrated through the use of ultrashort electric field switches and PiezoForceMicroscopy probing of the resulting GeTe polarization [81] [82]. This, however, required complex experimental methods, making GeTe rather unpractical for industrial applications.

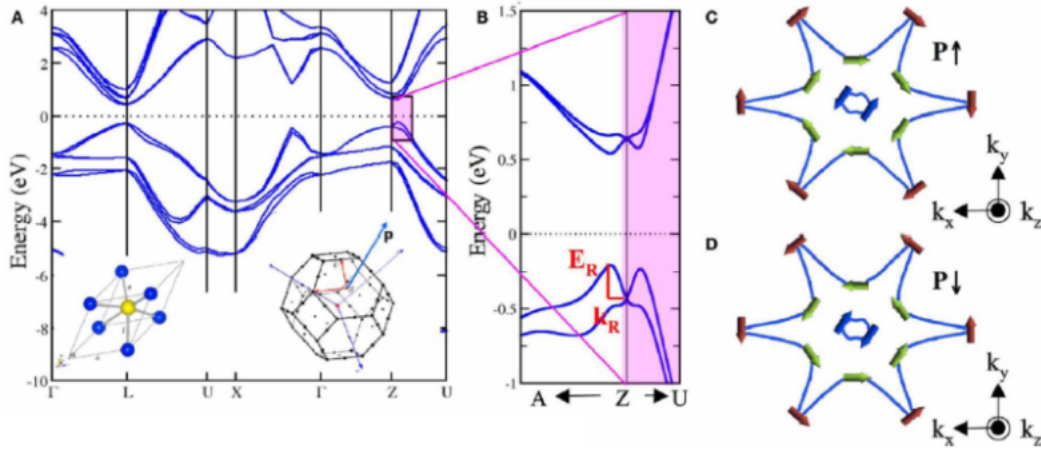


**Figure 1.13:** *GeTe*, a novel FERSC (a) Band structure of the *GeTe* subjected to an electric field. The CBM splits into two bands of opposite polarities, whose sign depends on the direction of the applied field as illustrated in (b) and (c) [41]. Reproduced from [13]

We note that members of the same family such as BiTeI and BiTeBr, which are polar metals and not ferroelectrics, were also investigated in the early 2010's as candidate systems in which the Rashba spin texture might be reversible through the application of an external electric field. However, they yield slightly lower Rashba coefficient compared to *GeTe* and suffer from the same kind of drawbacks [13] [83] [84] [85].

The seminal prediction of the coexistence of ferroelectricity and spin-orbit coupling in *GeTe* stimulated the research for other FERSCs, specially in the oxide family. However, a number of candidate FERSCs are not suitable for applications due to the position of the Rashba splitted band with respect to the Fermi level. If the Rashba bands are not located at the CBM or at the VBM, non Rashba bands will dominantly contribute to transport and consequently decrease the spin-charge conversion efficiency. The ideal case of a pure spin current can only be achieved when the RSS occurs at the conduction band minimum (CBM) if the carriers are electrons or at the valence band maximum (VBM) in the presence of holes. Based on this observation, recent research on FERSCs have been trying to focus on materials in which the band splitting occurs preferably at the CBM or VBM.

### Oxide FERSCs

Several oxides were proposed as FERSCs in the years which followed the DFT finding of the group of S. Picozzi *et al.*. In 2016, BiAlO<sub>3</sub> (BAO) was predicted to present ferroelectricity in two of its stable phases [86]. The rather large polarization values computed by the authors (79.38  $\mu\text{C cm}^{-2}$  and 90.46  $\mu\text{C cm}^{-2}$  for the rhombohedral and the tetragonal phases, respectively) highlight better overall ferroelectric properties compared to *GeTe*. In addition, the gap of both phases (1.49 eV and 2.57 eV) is large enough to ensure that leakages should not be detrimental to the observation of the Rashba effect. Last but not least, the RSS occurs close to the CBM for both investigated phases. However, according to the authors BAO does have its own issues. The Rashba parameters computed in the case of BAO are of 0.39 and 0.75 eV  $\text{\AA}$  for the rhombohedral and the tetragonal phases respectively, which is almost one order of magnitude lower than the computed value for *GeTe*. KTaO<sub>3</sub> (KTO) was also predicted to present ferroelectric properties when strained [87]. Tantalum presents the advantage of having huge d orbitals and is thus of prime interest when trying to induce spin-orbit coupling. Tao *et al.* predicted that under a -3% level of strain, substantial ferroelectricity will appear in KTO and will cause the onset of the Rashba effect with a Rashba coefficient of  $\alpha_R = 0.04 \text{ eV \AA}$ , two orders of magnitude lower than the  $\alpha_R$  of *GeTe*. In 2019, Arras *et al.* investigated the RSS of the bands located at

the CBM of  $\text{PbTiO}_3$  [88]. The authors predicted that the nature of the band at the CBM in  $\text{PbTiO}_3$  (PTO) could be engineered by using strain. When strain is applied to PBO, the band order is modified. Under sufficiently high strain, the band responsible for the CBM are originating from the heavy metallic  $E_g$  orbitals degenerated with the oxygen 2p orbitals. Incidentally, these bands are the ones which are submitted to the Rashba effect. Nonetheless, the computed Rashba coefficient of strained PTO ( $\alpha_R=0.3 \text{ eV}\text{\AA}$  [88]) remains one order of magnitude smaller than the one of GeTe.

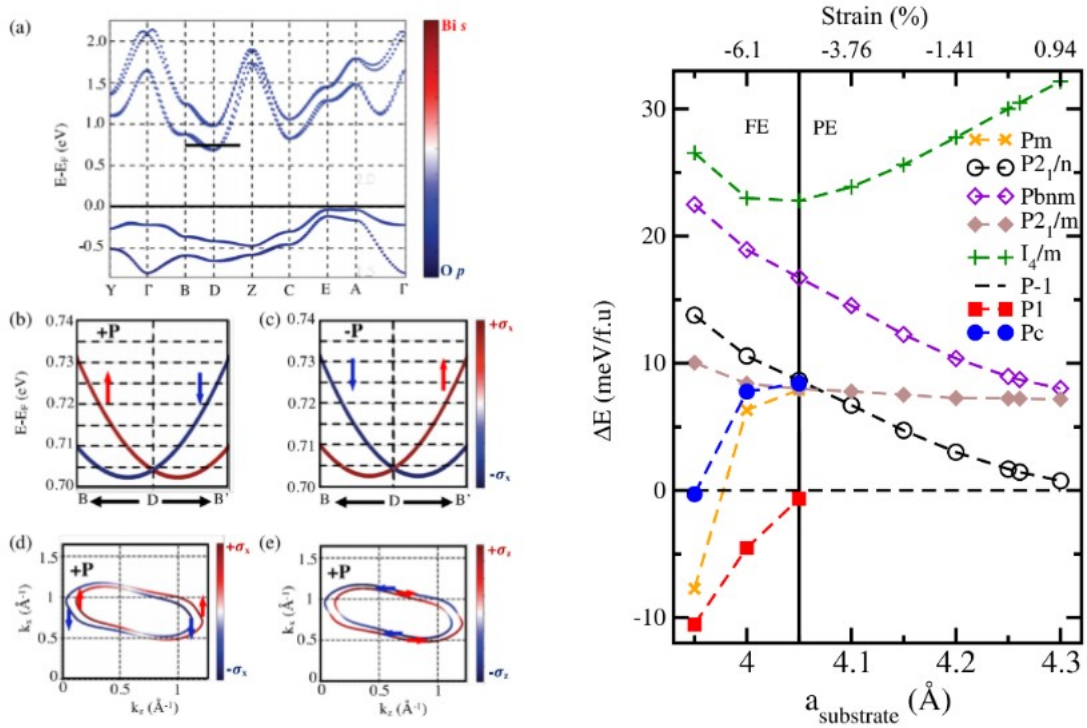


**Figure 1.14:** Rashba effect in SBO. On the right the band splitting and on the left the phase diagram. If sufficiently strained, SBO undergoes a strain driven phase transition to a P1 non centro symmetric phase, in which it is predicted that SBO is ferroelectric.

Around the same time, Djani *et al.* argued that pseudocubic perovskite oxides were not ideal FERSCs candidates as they were very likely to present Rashba splitted bands not located close to the Fermi level [89]. They proposed oxides with the Aurivilius (layered perovskites) structure as ideal candidate FERSCs. They argued that the RSS driving mechanism in perovskites lies in the hybridisation between the heavy metallic orbitals  $E_g$  and the 2p orbitals of the oxygen. For practical applications the Rashba band, which should be located at the CBM or at the VBM, has to have an hybridised 3d-2p orbital character. According to the authors calculations, this can not be the case for simple perovskites, but should be the case for layered perovskites. Such structures were predicted to have Rashba coefficient as large as  $1.28 \text{ eV}\text{\AA}$ .

### $\text{SrBiO}_3$

Yet, it was recently predicted that under a compressive strain of at least 5%  $\text{SrBiO}_3$  becomes ferroelectric and displays a RSS with a Rashba coefficient  $\alpha_R = 1.68 \text{ eV}\text{\AA}$ , when the tilting degree of the oxygen octahedra is optimised [90]. These results are presented on figure 1.14. The onset of ferroelectricity is the result of a strain driven phase transition under which the SBO unit cell adopts a P1 symmetry, which is non centro symmetric. In addition, as it usually is the case for oxide perovskite, SBO holds large internal electric dipoles. Hence, the inversion symmetry breaking results in the apparition of ferroelectricity, with a predicted polarization of  $12.65 \mu\text{C cm}^{-2}$  [90]. This result is the main motivation of the work which will be presented in chapters 3 and 4.

Material formula	polarization ( $\mu\text{C} \cdot \text{cm}^{-2}$ )	Rashba coefficient ( $\text{eV} \cdot \text{\AA}$ )	Ref
1MI-AgBiP <sub>2</sub> X <sub>6</sub> (X = S, Se and Te)	-	6.5	[91] [15]
1MI-AIBi	6.88??	2.74	[15]
BiTeI	polar semi-conductor	3.8	[85]
BiTeBr	polar semi-conductor	$\sim 2$	[83] [84]
GeTe*	-	4.8	[41] [82]
Pb <sub>1-x</sub> Ge <sub>x</sub> Te*	-	2	[92]
NaZnSb	49	2.58	[93]
(FA)SnI <sub>3</sub>	5.35	1.10	[94]
CsPbBr <sub>3</sub>	-	0.2	[95]
CsPbF <sub>3</sub>	34	1.05	[96]
LaWN <sub>3</sub>	61	2.7	[97]
HfO <sub>2</sub>	73	0.578	[98]
KTaO <sub>3</sub>	40	0.04	[87]
BiAlO <sub>3</sub>	79.38	0.39	[86]
	90.46	0.75	[86]
BiInO <sub>3</sub>	33.6	1.91	[99]
PbTiO <sub>3</sub>	90-120	0.3	[88]
Bi <sub>2</sub> WO <sub>6</sub>	$\sim 50$	1.28	[89]
SrBiO <sub>3</sub>	12.65	1.68	[90]

**Table 1.2:** Predicted FERSCs as well as typical measures of their ferroelectric and Rashba properties. Among the ferroelectric FERSCs, SBO is promising as it was predicted to presented a high Rashba coefficient that will translate into the spin to charge conversion properties. \* were confirmed experimentally to be FERSCs.

Table 1.2 lists all predicted FERSCs to date, to the best of the author knowledge, along with their predicted, or measured when available, ferroelectric properties and Rashba spin splitting. We note that a number of predictions concerning monolayers and bilayers of different compounds have started to emerge in the literature. We list a couple of these compounds at the very top of the table, but this list is not exhaustive.

Let us finally note that recently other interesting oxide candidates were highlighted as candidate ferroelectrics. It was proposed the BaSrBi<sub>2</sub>O<sub>6</sub> could be ferroelectric, without the need to induce strain [100]. The growth of thin films of such a material is even more challenging than growing SrBiO<sub>3</sub>, due to the fact that both A site atoms of the double perovskite structure are occupied by rather volatile atoms. Finally, it was also proposed that Ba<sub>1-x</sub>K<sub>x</sub>BiO<sub>3</sub> might be non centro symmetric under specific conditions [101]. The possibility to observe ferroelectricity was nor studied nor mentioned, but both core conditions for FE (non centro symmetry and presence of strong internal dipoles) are present in this material. In addition, due to the presence of bismuth, a strong SOC should be observed. As such, BKBO could be a candidate FERSCs. It could also be a good candidate to study the interplay between the Rashba effect and superconductivity.

In the framework of this thesis, we will be focusing on two different takes on the ferroelectric control of the Rashba effect. The first one relies on the investigation of the candidate FERSC SrBiO<sub>3</sub>. In the next section, we will be giving an overview of the available literature on SBO, and more generally on the bigger family it is part of, the bismuthates. The other approach we will introduce later involves using heterostructures based on (Al,Sc)N.

## 1.5 Bismuthates

Bismuthates are transition metal oxides which were first studied in the 70's for their superconducting properties. They have the general perovskite formula  $ABO_3$  with a bismuth atom occupying the B cation site.

### 1.5.1 Generalities about perovskite oxides

Transition metal oxides with the perovskite structure have been widely studied in the past 20-30 years. The ideal  $ABO_3$  perovskite structure is cubic with perfect octahedral coordination for the M cation and a coordination number (CN) of 12 for the A cation.  $SrTiO_3$ , for example, adopts a cubic perovskite phase at room temperature with  $Ti^{4+}$  ions occupying the centre of an  $O^{2-}$  octahedra, while the  $Sr^{2+}$  occupies the A site of the perovskite structure, surrounded by 12 oxygen atoms. Nonetheless, actual sizes of the A and B cations are such that this condition is rarely satisfied. A good idea of the crystalline structure adopted by a non-ideal perovskite can be deduced from the Goldschmidt's tolerance factor, which is a dimensionless number calculated from the ratio of the ionic radii:

$$t = \frac{r_A + r_O}{\sqrt{2}(r_B + r_O)} \quad (1.41)$$

In an ideal cubic perovskite structure  $t$  is equal to one. This is the case of STO at room temperature. If  $t$  is greater than one, the structure will usually adopt a tetragonal or an hexagonal structure. This is for example the case of the prototypical ferroelectric BTO, which we already introduced. Nonetheless, for most perovskite  $t$  is smaller than 1. If  $0.71 > t > 0.9$ , the structure will become orthorhombic, rhombohedral or tetragonal. This is for example the case of  $CaTiO_3$ , the original perovskite, at room temperature. Owing to other effect present in perovskite lattices, the crystal structure will deviate from the one predicted by the Goldschmidt's tolerance factor at finite temperatures. As a matter of fact, most perovskites eventually relax into the ideal cubic structure at high temperatures. STO, for example, is tetragonal with a  $I_{4/m}^{\bar{c}}$  structure at low temperature and only adopts a cubic  $Pm\bar{3}m$  above 105 K [102] [103].

### 1.5.2 Structure of bismuthates

#### 1.5.2.1 Generalities

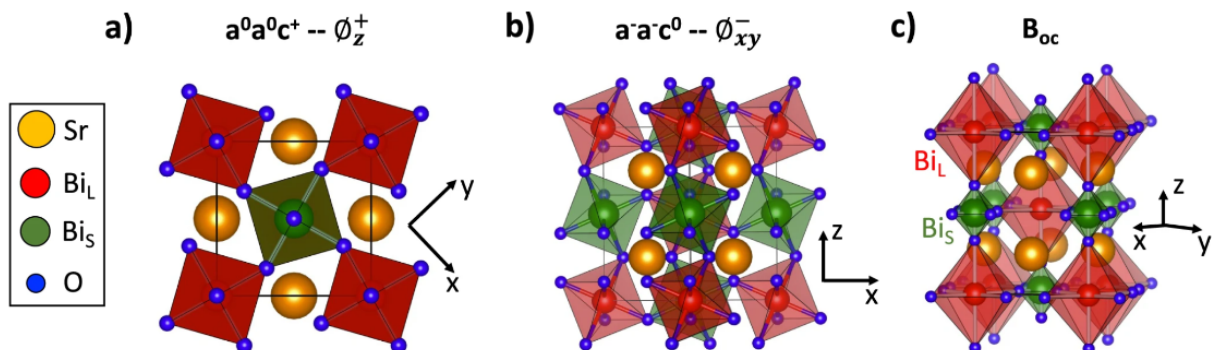


**Figure 1.15:** Structure of SBO: SBO crystallises in the  $P21/n$  symmetry characterised by several octahedral rotations: (a) In phase rotation around the z axis (b) Anti-phase rotation around the x and y axes and (c) breathing distortion  $B-oc$  splitting B sites into two different sites. Adapted from [104]

Bismuthates deviate from the ideal cubic perovskite phase, as they crystallise in a monoclinic phase at room temperature. In bulk, SBO and BBO adopt a monoclinic  $P21/n$  symmetry at 0 K. This structure is characterised by the two rotation modes of the oxygen octahedra  $a^0a^0c^+$  ( $\Phi_z$ ) and  $a^-a^-c^0$  ( $\Phi_{xy}$ ) in Glazer's notation (see figure 1.15 panels (a) and (b)). These rotational degrees of freedom are induced by the large size mismatch between the A and B cations of the  $ABO_3$  structure, characterised by a Goldschmidt tolerance factor of  $t=0.84$  in the case of SBO. The addition of the two rotations alone to the cubic symmetry would result in a  $Pbnm$  orthorhombic structure. The  $P21/n$  symmetry can be understood by the appearance of a breathing distortion  $B_{oc}$  of the oxygen octahedra, which itself is equivalent to a dimerisation of the material along the (111) cubic direction. This mode results in a rock salt pattern of large and compressed  $O_6$  octahedra, splitting the bismuth cations into two distinct populations:  $Bi_L$  and  $Bi_S$ , respectively. This breathing mode is associated with a charge disproportionation of the unstable  $Bi^{4+}-6s^1$  into the more stable cations  $Bi^{3+}-6s^2$   $Bi^{5+}-6s^0$  in the  $P21/n$  insulating phase. The charge disproportionation should result in the localisation of spin paired electron and holes on the  $Bi_L^{3+}$  and  $Bi_S^{5+}$  respectively. However, the occurrence of negative charge transfer caused by O anions supplying electrons to the depleted  $Bi_S^{5+}$  results in the formation of two (ligand) holes around the oxygen atoms [104]. The result is two populations of similarly charged bismuth cations in different local environment [105]. Hence, the charge disproportionation translates into a bond disproportionation.

It is worth noting that charge disproportionation was predicted and observed in several oxide systems presenting exotic properties such as superconductivity or metal to insulator transitions. In addition, antimonates (Ba, K)SbO<sub>3</sub> were recently highlighted as candidates high T<sub>c</sub> superconductors [106] [107]. ReNiO<sub>3</sub> [108] and CaFeO<sub>3</sub> [109] are also subjected to charge disproportionation [110].

At higher temperatures, the Sr-O bond length increases, while the Bi-O distance remains relatively constant. As a result the cubic symmetry becomes energetically favorable with increasing temperature. In the case of BaBiO<sub>3</sub>, the structure remains monoclinic up to 140 K, then transitions to a rhombohedral phase in space group R3 up to 820 K and finally becomes cubic above 830 K. SrBiO<sub>3</sub> has not been as studied as much as BBO, and a detailed phase diagram could not be found in the literature. However, we expect SBO to have similarities to BBO, owing to their rather close chemical compositions. BBO has a Goldschmidt's tolerance factor closer to unity than SBO ( $t_{BBO}=0.91$ ,  $t_{SBO}=0.84$ ). As we such, we expect the phase transitions of SBO to occur at higher temperatures compared to BBO.

### 1.5.2.2 Hole-doped bismuthates

Hole-doped bismuthates are well known type II high T<sub>c</sub> superconductors. As such, the phase diagram of  $Ba_{1-x}K_xBiO_3$  and  $BaK_xBi_{1-x}O_3$  were investigated and represent an important tool in the study of bismuthates.

Concerning potassium doped bismuthates, it is instructive to look at the fully doped compound. KBiO<sub>3</sub> adopts a  $Pm3m$  cubic lattice structure, owing to a Goldschmidt's tolerance factor closer to 1 compared to SBO and BBO ( $t_{KBiO_3}=1.01$ ). Potassium has a bigger atomic radius than both barium and strontium. It is empirically known that potassium doping of (Sr,Ba)BiO<sub>3</sub> results in a (Sr,Ba)<sub>1-x</sub>K<sub>x</sub>BiO<sub>3</sub> single phase with a  $P21/n$  lattice structure, up to the solubility limits at which two non miscible phases appear, a  $P21/n$  phase of (Sr,Ba)BiO<sub>3</sub> and a  $Pm3m$  phase of KBiO<sub>3</sub>. In the case of SrBiO<sub>3</sub>, the solubility limit is reached for  $x=0.6$ , whereas the solubility limit of BBO is of  $x=0.5$ . This difference stems from the difference in size of the A cation of the perovskite structure: Ba is larger than Sr and thus the BaBiO<sub>3</sub> unit cell is more susceptible to K doping than its parent compound SrBiO<sub>3</sub> [104]. Up to the solubility limit, doping with potassium should increase the  $t$  factor of the structure and lower the temperatures of the monoclinic to rhombohedral and rhombohedral to cubic phase transitions.

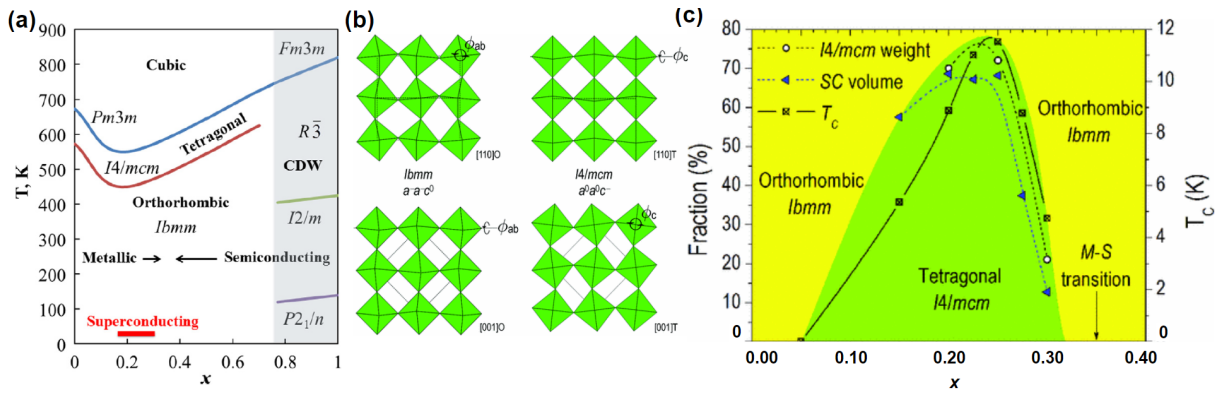


**Figure 1.16:** Phase diagram of  $BaPb_{1-x}Bi_xO_3$ . (a) phase diagram of  $BaPb_{1-x}Bi_xO_3$  as a function of temperature and the lead fraction, (b) most common configurations of the perovskite structure of  $BaPb_{1-x}Bi_xO_3$  in the superconducting regime and (c) phase diagram BBO in the vicinity of the superconducting region, highlighted in red on (a). (a) reproduced from [111], (b) and (c) adapted from [112]

Regarding  $BaPb_{1-x}Bi_xO_3$ ,  $BaPbO_3$  is orthorhombic at 0 K and at room temperature, in the  $Ibmm$  space group. It becomes tetragonal above 573 K and cubic above 673 K [113]. There is no solubility limit, and the perovskite structure prevails at all values of  $x$ . Bismuth being larger than lead,  $t$  decreases with doping content. The temperature of the aforementioned phase transitions should thus increase with  $x$ . Cubic symmetry is obtained at 673 K for  $x=0.0$  but not until 820 K for  $x=1.0$ . Surprisingly, a minimum appears at about  $x=0.2$ . This minimum is caused by an entropy driven factor in the free energy. The entropy inherent to a solid solution lowers the transition temperature down to a minimum at  $x=0.2$ . It increases as expected with further doping due to the destabilisation of the cubic phase caused by a larger mismatch in ionic radii of the A and B cation of the perovskite structure [111]. The phase diagram of BPBO is reproduced on panel (a) of figure 1.16. At low temperatures and for the doping ratios at which superconductivity occurs ( $x=0.1-0.3$ ), a metastable tetragonal phase appears [112]. The stabilization of the tetragonal phase at temperatures lower than that indicated by the monoclinic/ tetragonal phase transition is still poorly understood at this time. It is possible that the tetragonal phase is not metastable at room temperature and lower temperatures. What we do know is that only a fraction of the material stays tetragonal at these doping ratios. Hence, crystals are composed of a mix of monoclinic and tetragonal phases. However, only the tetragonal phase is superconducting and the maximum superconducting  $T_c$  (13K) of BPBO was observed at the doping ratios at which the tetragonal/monoclinic ratio is maximal. The relationship between the phase intermixing and superconductivity is illustrated on panel (c) of figure 1.16.

### 1.5.3 Physical properties of bulk bismuthates

In their undoped states, BBO and SBO are insulating. BBO has a band-gap estimated between 0.2 and 0.8 eV [114] [115], and SBO a band-gap estimated between 0.3 and 0.5 eV [90] [104]. The bismuth bond disproportionation has an effect on the band structure. Namely, the hybrid metal oxygen s-p band associated to the small oxygen octahedra is emptied, creating a ligand hole band. Regarding the large octahedra, the coupling with the ligand hole is weaker. This effectively pushes the holes to higher energies and the electrons to lower energies, eventually opening a gap [105]. In this picture, the electrons populating the VBM (CBM) will always be related to the large (small) octahedra.

Upon hole doping, bismuthates become superconducting. The first electrical characterisation results on doped BBO were published in 1975 [114]. It was reported for the first time that in  $BaPb_{1-x}Bi_xO_3$  samples with

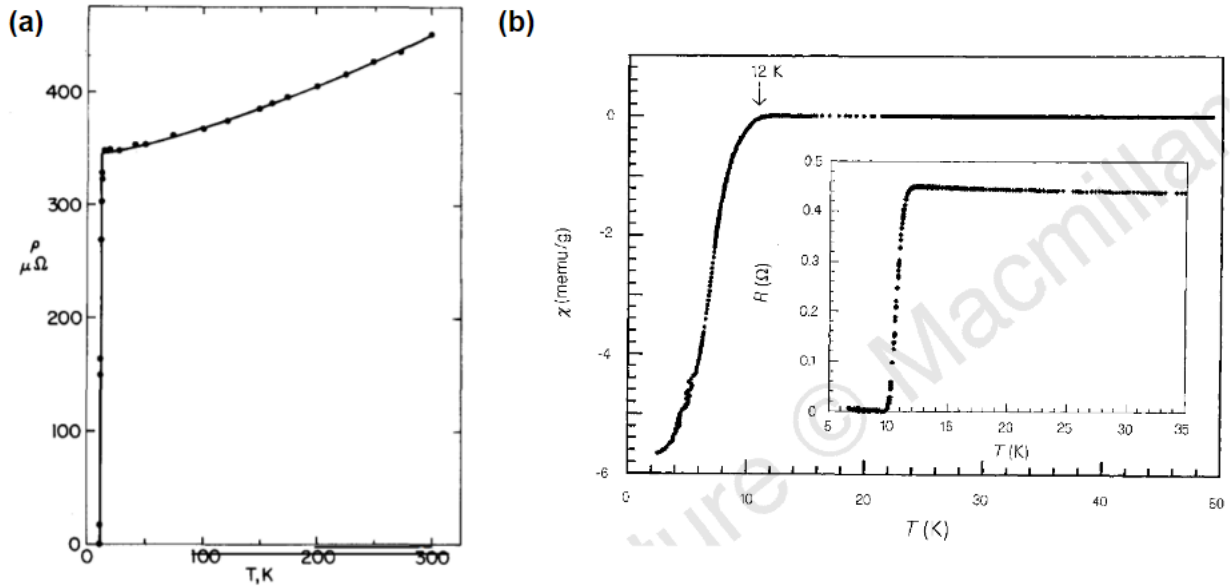


**Figure 1.17:** Superconductivity in bismuthates: (a) BBO doped with lead is superconductive with a  $T_c$  as high as 32K for  $x=0.45$  and (b) SBO doped with potassium is superconductive as high as 12K for  $x=0.6$ . Adapted from [116] and [114]

$x \in [0.05 - 0.3]$  superconductivity appeared with a  $T_c$  of 13 K. However, it was also reported that the density of states at Fermi level was relatively low. As a result, the idea of doping the electronically inactive barium donor sites instead of the bismuth sites emerged. This should result in the observation superconductivity with a higher  $T_c$ . Indeed, it led to the discovery in 1988 of superconductivity in the  $\text{Ba}_{1-x}\text{K}_x\text{BiO}_3$  system with a  $T_c$  of 30 K for  $x=0.4$  [117]. The key observation of superconductivity in bismuthates are presented in figure 1.17. This stimulated research for superconducting materials of the same family. In 1997, superconductivity was reported for the first time in  $\text{Sr}_{1-x}\text{K}_x\text{BiO}_3$  for potassium doping contents of  $x \in [0.45 - 0.6]$  and  $\text{Sr}_{1-x}\text{Rb}_x\text{BiO}_3$  with a Rubidium doping content of  $x=0.5$  [116]. The mechanisms at play in superconductive A-site doped bismuthates is still debated. Two pictures have emerged to explain it.

- The first scenario assumes the local formation of Cooper pairs. The previously mentioned bond disproportionation causes electron pairs to preferentially occupy one sub-lattice, giving rise to insulating Charge Density Waves (CDWs). With increasing doping, the charge disproportionation weakens and eventually disappears. Nevertheless, some electron pairs may persist and form Cooper pairs, ultimately leading to the onset of superconductivity [118].
- The other, more recent, picture posits that superconductivity in bismuthates is caused by strong electron phonon couplings. If long range Coulomb interactions are taken into account, the computed value for the electron-phonon coupling constant are in the range of  $\lambda \sim 1$  [119], in good accordance with the experimental value  $\lambda = 1.3 \pm 0.2$ , measured by ARPES [120]. It was proposed that  $\lambda$  is modulated by correlations and by the oxygen octahedral rotations [121]. In fact, it was recently suggested that most of the physics of bismuthates is caused by the modulation of the octahedral mode  $B_{oc}$ , which itself depends on the  $\Phi_z$  and  $\Phi_{xy}$  rotational modes. [104] Similarly to what happens in rare earth nickelates  $\text{RNiO}_3$ , whose physics is close to the physics of bismuthates owing to the fact that they also fall in the negative charge transfer insulator regime with similar lattice structure and bond disproportionation, Mercy *et al.* stated that  $B_{oc}$ ,  $\Phi_z$  and  $\Phi_{xy}$  are linked through the lattice mode couplings allowed in the

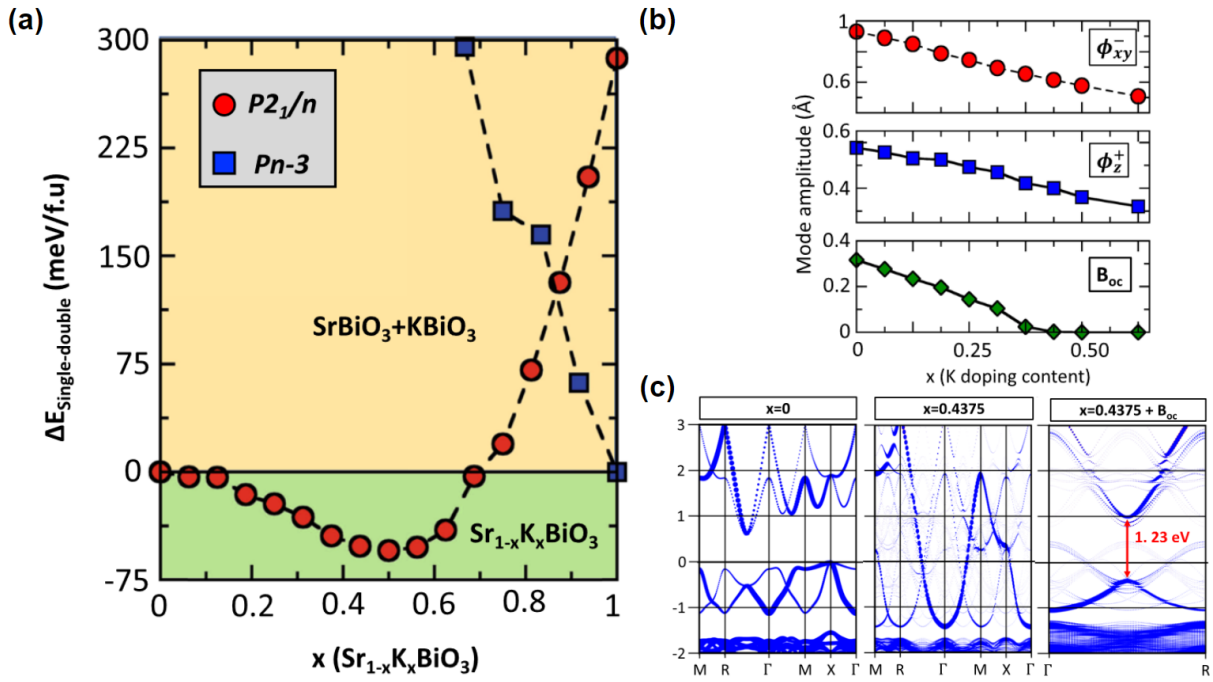


**Figure 1.18:** Influence of K doping on SrBiO<sub>3</sub> (a) Formation enthalpie of doped SBO with different crystal structures. The miscibility limit is reached around 70% doping, after which two distinct phases of SBO and KBO form. (b) behavior of  $\Phi_{xy}, \Phi_z$  and  $B_{oc}$  with K content. Upon reaching the superconducting phase, we observe the total suppression of the  $B_{oc}$  mode. (c) band structure of un-doped SBO, doped superconductive SBO and of doped SBO in which the  $B_{oc}$  mode is forced to remain at its undoped intensity, in which case the gap does not close and superconductivity is suppressed. Adapted from [104].

free-energy expansion F:

$$F = aQ_{B_{oc}}^2 + bQ_{B_{oc}}^2 Q_{\Phi_{xy}}^2 + cQ_{B_{oc}}^2 Q_{\Phi_z}^2 \propto (a + bQ_{\Phi_{xy}}^2 + cQ_{\Phi_z}^2) Q_{B_{oc}}^2 = a_{eff} Q_{B_{oc}}^2 \quad (1.42)$$

conditioning the appearance of  $B_{oc}$  to the sign of  $a_{eff}$ . Julien Varignon recently demonstrated that for low doping content,  $a_{eff}$  rises with doping content until it ultimately becomes positive [104]. As the amplitude of  $B_{oc}$  diminishes, reduced semi conducting states appear in the gap, in strict accordance with experimental data. As  $B_{oc}$  vanishes, the valence band and conduction band merge into a single parabola at the  $\Gamma$  point of the Brillouin Zone. This band is dispersing over a large energy range, for all K content higher than the critical one until the solubility limit of K in SBO is reached. This clearly suggests that the breathing mode  $B_{oc}$  is the main factor behind superconductivity. In this picture, it appears that the role of doping in bismuthates is simply steric: it diminishes the rotations amplitudes and in turn the breathing mode stabilisation. This is coherent with thin film and interfaces studies in which superconductivity is predicted to be induced by steric effects rather than substitution (e.g. by making use of the epitaxial relationship between the oxygen octahedras of two thin films at the interface [122]). Figure 1.18 illustrates the link between  $B_{oc}$  and the onset of superconductivity in potassium doped SBO.

This take on the origin of superconductivity in A-site doped bismuthates may also relate to the fact that superconductivity only appears in tetragonal phases of BPBO.

### 1.5.4 Two dimensional conductive states at bismuthates' edges

To harness the exotic properties of insulating bismuthates, specially ferroelectricity, being able to measure conductive state at their edges could be crucial. To do so, one could either make use of topological edge state or try to create a 2DEG at a bismuthate interface.

#### 2DEGs

Being able to create a 2DEG at the surface of an insulating phase can be seen as a way to investigate the electronic properties of said insulator. Ferroelectric are by their very nature insulators, and as such could highly benefit from this investigation method.

Almost a decade ago, Vildosola et al. [123] predicted the existence of two-dimensional electron gases (2DEGs) at the edges of thin films made of BaBiO<sub>3</sub> (BBO). According to their findings, in BiO<sub>2</sub> terminated BBO thin films the bismuth atoms of the outermost layer have an incomplete oxygen octahedral environment. This results in the disruption of the charge disproportionation and the breathing mode -which are together responsible for the gap opening in BBO- in the two outermost layers. As a result, these layers turn cubic and the band gap energy is reduced, thus creating a 2DEG confined to the two topmost BBO layers. The termination of BBO was previously verified to be BiO<sub>2</sub> [124]. An experimental study of the conductivity of surfaces of single-oriented and multi-oriented BBO thin films highlighted that single oriented films surfaces presented lower resistance than their multi-oriented counterparts [125] [126]. However, no 2DEG was measured at the surface of BBO. Such 2DEGs were also investigated by *in-situ* ARPES [127]. While this study did not confirm the presence of a 2DEG, it did reveal that surface bands existed below the Fermi level, aligning with predictions by Vildosola *et al.*. This suggests the potential existence of metallic surface states. Nevertheless, as of the writing of this thesis, no experimental measurements confirming the presence of such a 2DEG have been published [128].

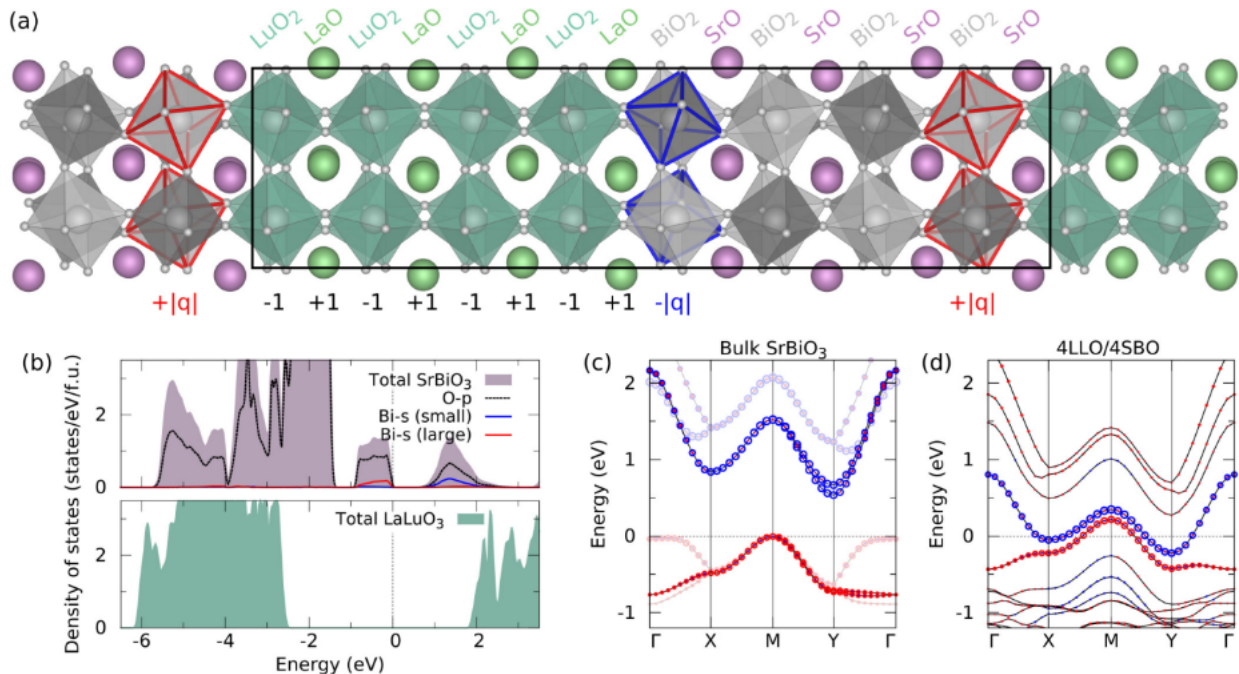


**Figure 1.19:** Heterostructures of SrBiO<sub>3</sub> and LaLuO<sub>3</sub> (a) schematic representation of an 4/4 SBO LLO heterostructure, (b) density of state close to the fermi level showing that the state at the VBM (CBM) have a Bi<sub>i</sub> (Bi<sub>s</sub>) nature, (c) band diagram of SBO and (d) of the heterostructure, which presents an electron (hole) pocket at the M (Y) point of the Brillouin zone. Reproduced from [129].

Due to the strong interplay between oxygen octahedral rotations and the electronic properties of bismuthates, through strong electron-phonon couplings, BBO was predicted to present conductive states when interfaced with the right material [122]. For example, it has been shown that interfacing BBO with BPO can lead to the creation of a 2DEG at the interface [122]. Because of epitaxial steric effects, oxygen octahedra at the interface are twinned, drastically reducing the influence of one of the phononic mode. This in turn forces the gap to close and induces a 2D state at the surface of BBO.

Regarding SBO, a recent study highlighted the possibility to observe a 2DEG as well as a two dimensional hole gas (2DHG) at the LaLuO<sub>3</sub>/SrBiO<sub>3</sub> interfaces [129]. Both gases could co exist in an hetero-structure of SBO/LLO, each one of them appearing at a different termination of SBO. The driving mechanism for the creation of such gases lies in the polarity of LLO coupled with the bond disproportionation of SBO. Depending on the termination of both layers, the charge transfer results in an electron gas at one interface and an hole gas at the other. These 2D gases are predicted to be highly stable because they are separated in both the direct and k space, owing to the fact in the Bi<sup>3+</sup>Bi<sup>5+</sup>O<sub>4</sub> layers, holes will be populating the Bi<sub>L</sub> octahedras and the electrons the Bi<sub>s</sub> octahedras. This will be giving rise to an hole and an electron pocket at the M and Y point of the Brillouin zone, respectively. These results are presented in figure 1.19. Such interfaces could enable the investigation of SrBiO<sub>3</sub> carriers, provided that the LaLuO<sub>3</sub> could be grown epitaxially on SBO. Finally, we can also infer that the mechanism that causes the apparition of conducting edge states at the surface and interfaces of BBO should also be relevant in SBO, as the gap of SBO also originates from the bond B<sub>oc</sub> and the bismuth charge disproportionation [104]. BaPbO<sub>3</sub> would not work as well as an interfacial oxygen octahedra engineering tool for SBO as it does for BBO due to the larger lattice mismatch [122] (-2.6% between SBO and BPO, -0.23% between BBO and BPO), and SrPbO<sub>3</sub> is semi-conducting [130], which is not ideal when trying to induce a 2DEG at an interface. However, pristine surfaces of SBO, SBO/EuO interfaces, or other SBO/MOx interfaces (e.g. M=Al or Ta) could be interesting to investigate SBO based 2DEGs that would carry on the possible Rashba properties of the bismuthate thin film.

### Topological conductive edge states

Another way of creating surfaces conductive edge state lies in topology. A<sup>III</sup>BiO<sub>3</sub> (A<sup>III</sup>= Al, Ga, In, Sc, Y and La) as well as A<sup>I</sup>BiO<sub>3</sub> (A<sup>I</sup>=Na, K, Rb, Cs) and A<sup>II</sup>BiO<sub>3</sub> (A<sup>II</sup>=Mg, Ca, Sr, Ba) in a cubic *Pm* $\bar{3}$ *m* perovskite-structure were predicted to present topologically protected conducting edge states [131] [132] [133] [134]. The origin of the topological edge states can be of two sorts: it is either caused by SOC or by orbital hybridisation with oxygen E<sub>g</sub> states. However, when considering such predictions one should be cautious. Indeed, it has been reported that in the case of A<sup>III</sup>BiO<sub>3</sub>, in their relaxed, stable structure, which in most case is a GdFeO<sub>3</sub> like *Pnma* structure, they are more likely to be trivial insulators [133]. Regarding A<sup>I</sup>BiO<sub>3</sub> and A<sup>II</sup>BiO<sub>3</sub>, some of them do indeed crystallise in a *Pm* $\bar{3}$ *m* (e.g. KBiO<sub>3</sub>) while others do not (e.g. BaBiO<sub>3</sub>). Nonetheless, in the particular case of BBO the authors investigated the resilience of the topological behavior with the addition of the breathing mode of distortion and concluded that it should be robust [134]. As of the writing of this thesis, there are no experimental evidences of the existence of such topological states.

### 1.5.5 Bismuthates thin films, hetero-structures and interfaces

Bismuthates thin films were barely studied and synthesised until rather recently. Their huge unit cell parameters makes it difficult to find proper candidate substrates for good epitaxial quality. In addition, bismuth is rather volatile, incorporating it on the B site of a perovskite can prove quite challenging.

Only a few reports dealing with BaBiO<sub>3</sub> can be found in the literature. MBE growth was investigated in the late 90s [136], while PLD growth only saw a couple of studies in the early 2000s [137] [138] [124]. We do

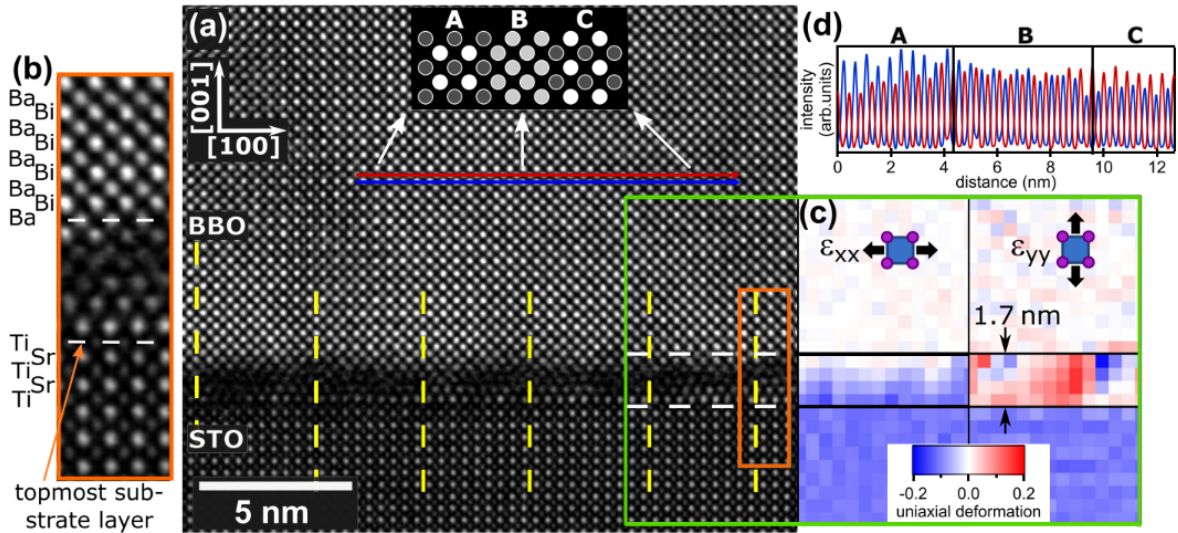


**Figure 1.20:** BBO epitaxial relationship with its substrate: (a) STEM image of a BBO thin film grown on STO. (b) Zoom on the STO/BBO interface. Two epitaxial layers of SrO are forming at the interface to better accommodate the strain. (c) and (d) rotation domains. Reproduced from [135]

note that one of these studies succeeded in the fabrication of superconducting thin films of BKBO by using the interval deposition technique [137]. However, in all the studies considered above the films were grown thick and relaxed. The prediction of a 2DEG at the surface of BBO as well as the prediction of topological edge states reinvigorated the interest in bismuthates. As a result, the behavior of their surfaces [126] [125] and interfaces [135] [139] [140] was intensively investigated in the last decade. The strainability of BBO was first studied in 2018 by Zapf *et al.*. Zapf *et al.* grew BBO thin films and studied the interaction between the film and its growth substrate [135]. In this study, the authors highlighted that at the interface with the SrTiO<sub>3</sub> substrate they observed the formation of dislocations arranged into a regular pattern. To have a perfect match in between 9 u.c. of BBO and 10 u.c. of STO, dislocations form every 10 u.c. of BBO. Above these so called misfit dislocations, BBO grows relaxed with the expected  $a = 4.35 \text{ \AA}$  lattice parameter [139] [140]. In addition, due to its large lattice parameter BBO can be used as a buffer layer for the growth of other large oxides of interest such as YBiO<sub>3</sub> [139].

Regarding SBO, as of the start of this thesis, and despite the exotic properties predicted for this particular structure [116] [134] [14] [104], only a single report dealing with SBO thin films could be found in the literature. In 2019, Fengmao Li *et al.* grew SBO thin films on STO by MBE [141]. The films were grown thick and relaxed, although the author argue that some level of strain should be present at the bottom interface. They investigated the in-plane lattice parameter as a function of thickness through *in-situ* RHEED monitoring. Although the level of strain at the interface estimated by RHEED should be high enough to observe ferroelectricity, the authors did not investigate it.

## Conclusion

We can summarize this section as follows. Bismuthates are perovskites structures in which a plethora of exotic properties were predicted, but very little experimental data is available. The challenges associated with their growth, with the chemical stabilisation of their surfaces and with the measurements of their exotic properties has so far been limiting the interest around this peculiar class of material. In this picture, we chose to investigate the growth and characterisation of one of the better known yet very little investigated member of this family, SrBiO<sub>3</sub>. In chapter 3 we will describe the growth investigation of SBO thin films by PLD and

in chapter 4 we investigate its physical properties, and in particular its ferroelectric properties.

## 1.6 wurtzite and fluorites

The materials we have been describing up until this point are primarily perovskites. When considering the ferroelectric control of the Rashba spin splitting in heterostructures, it is feasible to envision perovskite heterostructures, possibly based on BTO or PZT, which have been extensively studied for their ferroelectric properties. Investigation on PZT based heterostructures have actually already started [75]. We note that these perovskites are also compatible with the 2D approach toward the electric control of the Rashba coefficient: a 2DEG created on such perovskites (e.g. with  $\text{MO}_x$ ) could inherit their ferroelectric properties.

Going one step further, it would be intriguing to consider the development of such heterostructures embedded in a CMOS-compatible framework. Fortunately, the ferroelectric community has recently reported several CMOS-compatible ferroelectric materials. Assuming they can be integrated with a spin-orbit coupling stack, these materials hold significant promise for the development of CMOS-compatible FESO devices. In this section, we will review the latest advancements in CMOS-compatible ferroelectrics and propose a CMOS-compatible FESO device based on these materials.

### 1.6.1 History

#### 1.6.1.1 Fluorites

The first experimental observation of CMOS compatible ferroelectricity dates back to 2006, when  $\text{HfO}_2$  was characterised as ferroelectric. The exact mechanism of ferroelectricity in  $\text{HfO}_2$  is still debated, but it is admitted its origin lies in the stabilisation of one of its ferroelectric phases, either the rhombohedral or the orthorhombic phase, through a post-annealing step at  $>400^\circ\text{C}$ . The growth conditions of this ferroelectric fluoride are Back End Of Line compatible, making them particularly attractive for device applications.

Their ferroelectric properties are not yet on par with the perovskite ferroelectric, but are promising, to say the least. They present nice data retention, up to  $10^5$ - $10^6$  s at room temperature, and present modest remnant polarization of  $10$ - $50 \mu\text{C cm}^{-2}$ . This is an important feature to consider when trying to elaborate a ferroelectric random access memory (FE-RAM) or ferroelectric tunnel junction (FTJ). However, their main feature of interest, beyond their CMOS compatibility, lies in their *c*-axis down-scalability of the ferroelectricity, as sub 10 nm thin films were proven to retain similar ferroelectric properties to their thicker counterpart. In addition, the relatively large band-gap ( $\sim 5.3$  eV) of  $\text{HfO}_2$  contributes to the suppression of leakage current in thin ( $<10$  nm) samples. The conjunction of these advantages have allowed for the aggressive down scaling of  $\text{HfO}_2$  based FE devices, and as a result has attracted a lot of interest.

In 2019, another class of CMOS compatible materials were demonstrated to present ferroelectricity, the Wurtzites materials, in particular members of the AlN family.

#### 1.6.1.2 wurtzites

Aluminium Nitride and related doped compounds piezoelectric properties are very well known in the electronic industry. AlN stability at high temperatures and the high acoustic velocity measured in it [142] [143] makes it an ideal material for thin film based surface acoustic waves devices, which have numerous applications in electronics. As such, AlN related compounds are broadly used as acoustic band pass filters in 4G/5G antennas [143] [144]. They have been optimised and grown on a wafer scale by using processes which are CMOS compatible. Indeed, AlN can be epitaxially grown on silicon wafers by PVD at  $300$ - $350^\circ\text{C}$ . As such, they are

compatible with Back End of the Line processes (BEOL) of CMOS. Hopes are high that doped compounds of interest can rather easily be transferred to industrial application with minimal growth scalability optimisation needed.

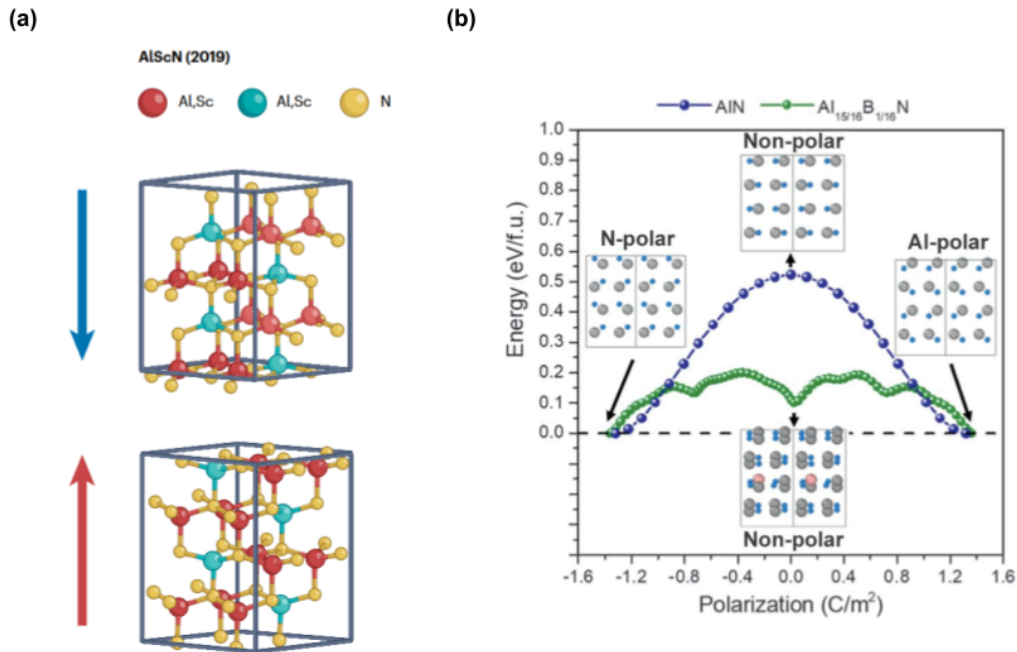


**Figure 1.21:** Structure and energy landscapes of Wurtzites perovskites: (a) Structure of  $(Al,Sc)N$  in its two polarization states and (b) the energy landscapes of doped and un-doped AlN computed by Calderon et al. [145]. It can be seen in the case of the undoped compounds, the only two stable states are the fully polarised states, and the non-polar state is metastable. When doped, the energy barrier associated to the switching operation is lowered, and stable intermediary states are created. Both of these mechanism are contributing to easing off the switching operation. Adapted from [?] and [145]

Until 2019, there were no reports of polarization switching in AlN based compounds. The polarization states of AlN are very stable, and the field that would be needed to reverse the polarization,  $E_c$ , is stronger than the field at which the material breaks down,  $E_{Br}$ . However, it was found that scandium substitution of the aluminium reduces the switching energy, down to the limit at which  $E_c$  becomes smaller than  $E_{Br}$ , making it possible to switch the polarization. This limit is reached for a doping content of 27% Sc [146] [147]. We note that spurred on by the  $Al_{1-x}Sc_xN$  research, ferroelectricity in other Wurtzites-structured N based materials such as  $Al_{1-x}B_xN$  [148] and  $Ga_{1-x}Sc_xN$  [149] has recently been investigated. In this manuscript, we chose to focus on  $Al_{1-x}Sc_xN$ , and will be only discussing this material. Nonetheless, the physical concepts at stake in the case of  $Al_{1-x}Sc_xN$  are expandable to the ferroelectric nitride Wurtzites family as a whole.

In the next section we will be detailing the Wurtzites structure, and the origin of the ferroelectric properties of doped compounds.

## 1.6.2 Ferroelectricity in Wurtzites: properties and mechanism

AlN adopts a Wurtzites ( $P6_3mc$ ) structure, which is part of the hexagonal crystal system, illustrated on panel(a) of figure 1.21. Compared to an ideal layered hexagonal structure, the Wurtzites structure presents two distinct non-equivalent atomic sub-planes, one cationic and one anionic. This results in a net-non zero polarization whose sign depends on the relative ordering of the planes. In the same manner as we introduced

the Goldschmidt's tolerance factor in the case of perovskite oxide as a measure of the deviation from the ideal, higher symmetry, cubic structure, and argued on its effect on the physics of bismuthates, we can introduce an internal parameter  $u$ , which can be defined as the  $c$ -axis projected distance between the cation and the anion, with respect to the lattice parameter. In the case of a non polar layered hexagonal structure  $u=0.5$ , whereas (Al,Sc)N Wurtzites are expected to have a  $u \sim 0.38$ . [150]

We note that this should be reminiscent of the physics of bismuthates in which the internal parameter of interest is the oxygen octahedra tilt, which can be tuned through different steric effects, be it chemical substitution, epitaxial strain or thickness modifications. We also note that the polarization in (Al,Sc)N is already rather stable, and that the aim of material engineering is to make switching possible. This can also be viewed as destabilising the two polarization states. Thus, when trying to engineer  $u$ , the aim is to approach the non-polar layered hexagonal state. As a result, the strain would have to be tensile by nature, with the aim of reducing the  $c/a$  ratio of the material and by doing so the out-of-plane polarization.

The switching process in ferroelectric (Al,Sc)N can be seen as the reorientation of the cation-anion planes to the opposite relative order. This can also be understood as the reorientation of the cation-anion tetrahedra along the  $c$ -axis. An intermediate, metastable and non-polar, layered hexagonal state is expected to briefly exist during the switching process. The energy cost associated with this transition is on the order of magnitude of the energy associated with the breakdown of the crystalline structure.

In the case of undoped AlN, the energy barrier associated with this operation is too high for the material to support. To lower the switching barrier and enable polarization switching, one can vary the internal parameter  $u$ , which can be done by chemical strain ( e.g. substitution of Al by Sc or B [148]), epitaxial strain ( e.g. growth on an electrode which can induce strain such as W(110) [151] [152]) or by thickness modification.

The polarization switching mechanism has been investigated at the atomic scale with scanning transmission electron microscopy [145]. This study confirmed that the polarization switching of doped compounds goes through the formation of a transient, metastable, non polar geometry, which is not permitted in AlN. The chemical and structural disorder in doped-compounds leads to a flat energy landscapes that facilitates switching. The authors also computed the energy barrier as a function of the polarization in the case of doped and undoped compounds. This is presented on figure 1.21

The energy landscapes is flatter in the case of doped compounds and presents a number of intermediate stable states, including the flat layered hexagonal structure which is metastable in the case of undoped compounds. The appearance of these intermediary states is critical to explain the switching mechanism of ferroelectric Wurtzites. The trend of  $E_C$  with scandium doping in  $Al_{1-x}Sc_xN$  was measured to be  $E_c(x) = -15x + 8.35$  ( $MV\ cm^{-1}$ ) for  $x \in [0, 0.43]$ . This high  $E_c$  results is advantageous for long term data retention and large memory windows, but it comes with the disadvantage of high switching voltages and relatively weak endurance [146] [153].

It should be noted that in addition to lowering the switching energy barrier, scandium doping also introduces disorder which will put a strain on the lattice, eventually causing more N vacancies which are detrimental to ferroelectricity as they lead to the apparition of higher leakage currents. Increasing the scandium content thus has both the effect of reducing the polarization switching energy, which is critical to observe ferroelectricity, and increasing the leakage currents which are detrimental to ferroelectricity. A middle ground has to be found and typical values are of a doping content of 25-35%.

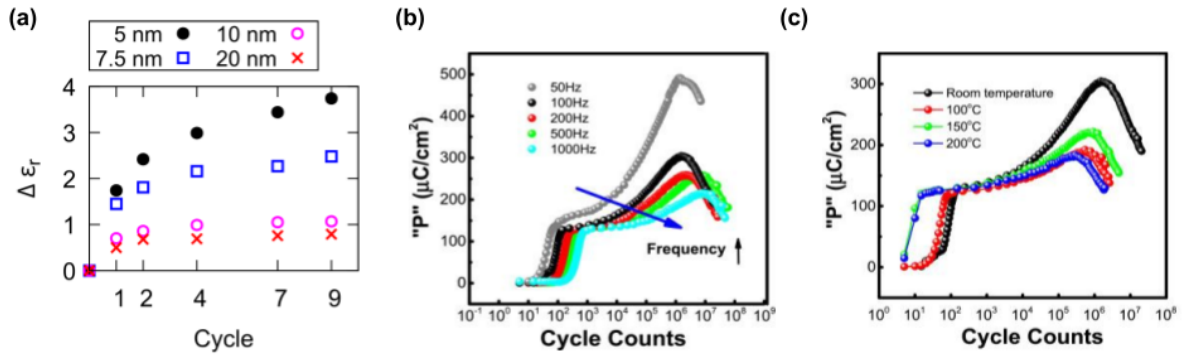


**Figure 1.22:** Wake-up and fatigue in Wurtzites ferroelectrics (a) wake-up effect investigation in (Al,Sc)N as a function of thickness, (b) and (c) wake-up and fatigue effects as a function of frequency and temperature, respectively. In all cases, endurance remains low compared to the values required to be competitive with existing technologies ( $\sim 10^{15}$  cycles), as illustrated in figure 1.5 (a) adapted from [31], (b) and (c) adapted from [153]

### 1.6.3 Growth conditions overview

Epitaxial growth of (Al,Sc)N has been demonstrated by magnetron sputtering at relatively low temperatures on c-sapphire, and electrodes of TiN, W(110) and Pt (111). Pt(111) has the advantage of having a good epitaxial match with (Al,Sc)N. As such, it is considered the easiest electrode to optimise the growth of the Wurtzites compounds. W(110) induces moderate tensile strain on the Wurtzites, improving its ferroelectric properties [151].

Growth is typically performed at 300-400 °C, under a mix atmosphere of Ar/N<sub>2</sub>. Introducing 25% of Ar was demonstrated to improve the c-axis orientation of the Wurtzites and thus its piezo- and ferroelectric properties [143].

We note that wurtzites have been investigated through different epitaxial methods, be it by MBE [154] [155], MO-CVD [156], ALD [157] or sputtering [158]. Thus far, the best results both in terms of ferroelectric properties, scalability and BEOL compatibility have been obtained by sputtering [?][?]. In addition, most industrial processes are based on sputtering. In the framework of the study we carried out during this thesis, we chose to optimise the growth of (Al,Sc)N by co-sputtering.

### 1.6.4 AlN based hetero structures: one possible approach.

To achieve ferroelectric control of the spin to charge inter-conversion, we propose to grow Wurtzites based hetero-structures. The spin momentum locked Rashba spin texture could be provided by a three-dimensional topological insulator.

$\text{Bi}_{1-x}\text{Sb}_x$  grows in a hexagonal lattice. Provided that it can be epitaxially grown on (Al,Sc)N, the conductive Rashba edge states may be controlled through the use of ferroelectricity. The lattice mismatch between the two structures is rather important ( $c_{(\text{Al,Sc})\text{N}} \sim 3.2 \text{ \AA}$ ,  $c_{\text{BiSb}} \sim 4.3 \text{ \AA}$ ,  $\sigma \sim 25\%$ ). Nonetheless, Singh and Romero predicted that BiSb might form misfit dislocations to accommodate the strain, in which case the strain is reduced to 1.3% [159]. The resulting heterostructure is predicted to have a Rashba parameter of 1.5 eV  $\text{\AA}$ , and should in theory be modulable by switching the polarization of the ferroelectric. We note that we do not expect a total reversal of the spin texture, as the asymmetry field involved in the Rashba effect here has two components: the polar contribution and the topological confinement.

We can summarize this section as follows. (Al,Sc)N Wurtzites are promising CMOS compatible ferroelectrics which have started to harness attention from the spintronic community. We believe they might become an important building block for the ferroelectric control of the Rashba effect as part of heterostructures, for example with BiSb. We optimized the growth of (Al,Sc)N and characterised its ferroelectric properties. Finally, we conceptualised a CMOS compatible ferroelectric Rashba heterostructure in which (Al,Sc)N plays the role of the ferroelectric. Chapter [A](#) will be centered around the work carried out on the Wurtzites in the framework of this thesis.

## Chapter 2

# Experimental techniques

Having shown the interest of growing bismuthate and wurtzite thin films, we will now detail the experimental process through which these thin films can be grown and characterised. The bismuthate thin films that are presented in this manuscript were grown by Pulsed Laser Deposition (PLD), while the wurtzite thin films were grown by magnetron sputtering. The films stoichiometry and crystal quality were then characterised using Reflection High Energy Electron Diffraction (RHEED), X Ray Spectroscopy (XPS), X Ray Diffraction (XRD), Atomic Force Microscopy (AFM) and Transmission Electron Microscopy (TEM). In this chapter, we will be detailing these characterisation methods to give the reader all the tools necessary to understand this work.

### 2.1 Surface preparation

For the purpose of this thesis, we used single crystal oxides substrates commercially available. They were cut to the desired size and polished by the crystal manufacturer CrysTec. Prior to deposition, the surface of the different substrates were cleaned, etched and terminated. Cleaning was done by standard procedure, using acetone, ethanol and isopropanol.

The (001) SrTiO<sub>3</sub> substrates were then prepared by a wet etching step in a buffered hydrogen fluoride (BHF) solution, followed by a 1.5 hour annealing step at 950 °C in a tube furnace with a flow of pure oxygen gas [160]. This results in TiO<sub>2</sub> terminated STO substrates. In the case of AScO<sub>3</sub> scandates (A = Nd, Dy, Gd), two preparation methods were used depending on the wanted termination. For an AO termination, the scandate substrates were prepared by a 4 hours annealing step at 1000 °C, in a flow of oxygen, followed by two subsequent etching steps in buffered HF and sodium hydroxide [161]. For an ScO<sub>2</sub> termination, the substrates were annealed at 1050°C for 90 minutes [162]. Proper single-termination of the substrates is critical to induce a good epitaxial relationship between the substrate and the film. AFM images of single-terminated substrates obtained by the different methods presented in this paragraph are presented on figure 2.1

Most of the growth performed for the purpose of this thesis were conducted in the COMAT (Complex Oxide MATerial) system depicted on figure 2.2. The growth chamber is equipped with a RHEED gun and CCD camera coupled to an electron screen, which permits the in-situ time resolved measurement of the RHEED pattern of the surface of the thin film. RHEED will be detailed in the next section. In addition, the deposition chamber is connected to a transfer chamber which is itself connected to an XPS system.

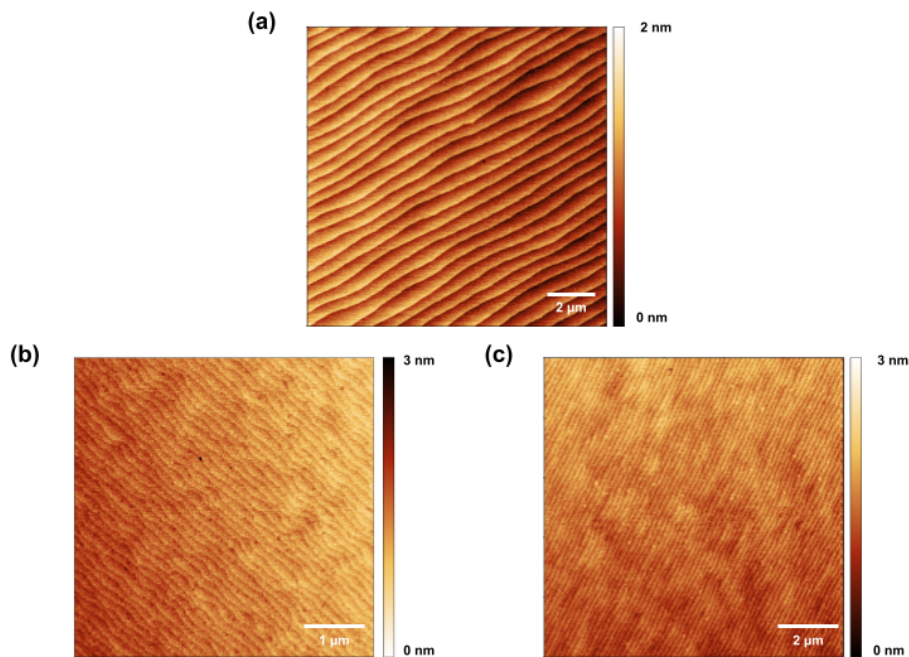


**Figure 2.1:** Surface preparation of substrates. (a) Single terminated STO after annealing and etching. Single terminated  $AScO_3$  terminated with an AO and  $ScO_2$  layer are presented on panels (c) and (d), respectively

## 2.2 Growth techniques

### 2.2.1 Pulsed Laser Deposition

During a Pulsed Laser Deposition (PLD) experiment, a target, either a single crystal target or a ceramic target for compounds which are not available as single crystals, is ablated by a laser. Particles are ejected from the surface of the target in the direction of a substrate, on which, under optimised conditions, they adsorb and reconfigure to epitaxially grow a thin film. PLD, compared to other epitaxial methods, allows for different control parameters, and supposedly better cation stoichiometry while remaining relatively affordable [163] [164]. In this section, the main growth parameters of PLD will be discussed. In addition, we will introduce an important in-situ characterisation method, Reflection High Energy Electron Diffraction (RHEED).

#### 2.2.1.1 Growth parameters

As aforementioned, during a PLD experiment the material that will deposit and grow thin films epitaxially comes from a target which is ablated by using a laser. After the particles are ejected from the target, they are transported towards the substrate. The transport in the space between the target and the substrate depends on several parameters such as: the initial energy distribution of the particles, their initial angular distribution, pressure and particle scattering during transport.

A critical parameter to consider when discussing transport of matter is the mean free path of said particles. In a PLD experiment at room temperature, the mean free path is of the order of magnitude  $l \simeq 0.063\text{mm}/p$ , with  $p$  being the background pressure, in mbar. PLD operates in the pressure range  $10^0 - 10^{-1}\text{mbar}$ , the mean free path is of the same order of magnitude as the distance between the target and the substrate, *i.e.*

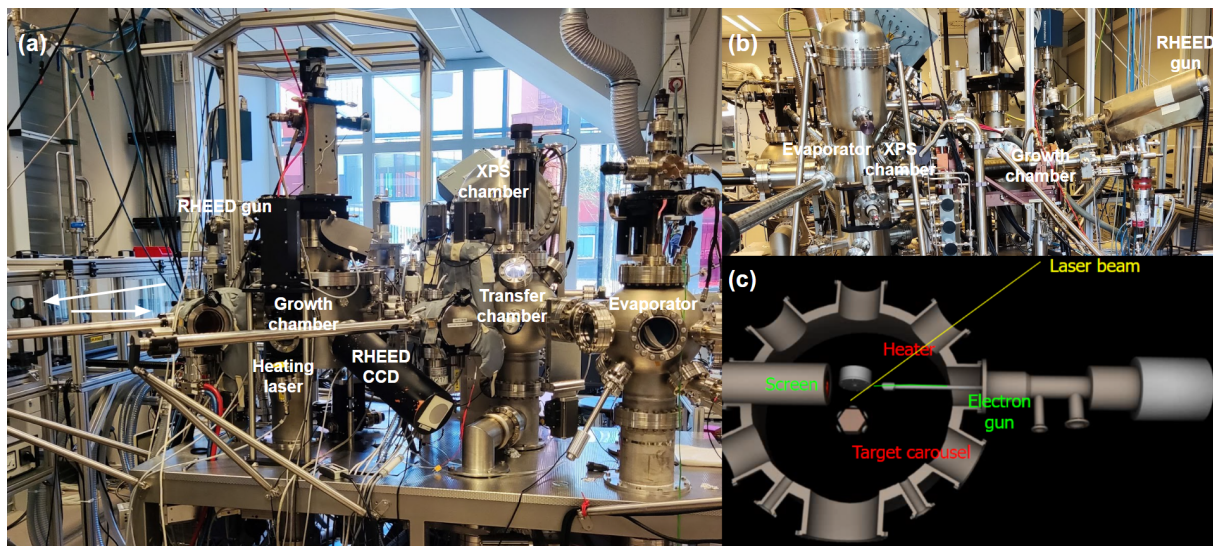


**Figure 2.2:** The COMAT system seen (a) from the front, (b) from the rear and a (c) schematic of the growth chamber.

a few centimeters.

As a result, the plasma diffuses towards the substrate. However, particle scattering during transport can cause energy reduction, which can in turn cause angle and stoichiometry modifications. In addition, some chemical species may oxidise the plasma. The  $O_2$  concentration is also a critical parameter. Through the acquisition of XRD data of STO grown on STO, it was shown that with partial Oxygen pressure lower than 0.06 mbar, bulk growth is observed [165]. In addition, if the partial Oxygen pressure is too high, no growth is observed as the reactants can not even reach the substrate. Finally, it was highlighted that the amount of Oxygen supplied for the growth of the different layers may change as a function of time during the growth. This happens because the Oxygen sources may have multiple origins: the target, the background and the substrate. This has to be taken into account when optimising a growth process [165].

### 2.2.1.2 Growth kinetics

As aforementioned, understanding growth kinetics is critical when trying to improve the growth quality. Epitaxy goes through several steps: first, when the precursors come into contact with the surface, (i) they may stick to it. They will then (ii) diffuse on the surface, and will either (iii) contribute to the growth or (iv) detach from the surface before having a chance to do so. These four steps are commonly referred to as (i) *adsorption*, (ii) *diffusion*, (iii) *reaction* and (iv) *desorption*. They have an influence on the nature of the material grown. The contact time between the precursor and the substrate, which corresponds to the time between the adsorption and the desorption events, is called  $\tau$ , the residence time.

The film grown epitaxially can take different forms. Growth occurs around a nucleation site, which can be of two types: a step or nucleus. Islands will form around the nucleation site, and may then coalesce into a new layer. If growth only occurs at step edges, the epitaxial growth mode is commonly referred to as *step-flow growth*. If the precursors do not encounter any edges during their residence time, they may still form a nucleus on the surface. Then, two growth modes may occur. If the lateral growth of the thin film is fast with respect to the nucleation process, layer-by-layer growth will be observed. However, if nucleation is favored compared to the lateral growth of the film, a new nucleus may form on top of an unfinished layer, resulting in an unwanted island growth pattern. Under a thermodynamic equilibrium these two distinct modes

are commonly referred to as the *Van der Merwe* and the *Volmer Weber* epitaxial modes, respectively. The different growth modes are illustrated on panels (a) and (b) of figure 2.3

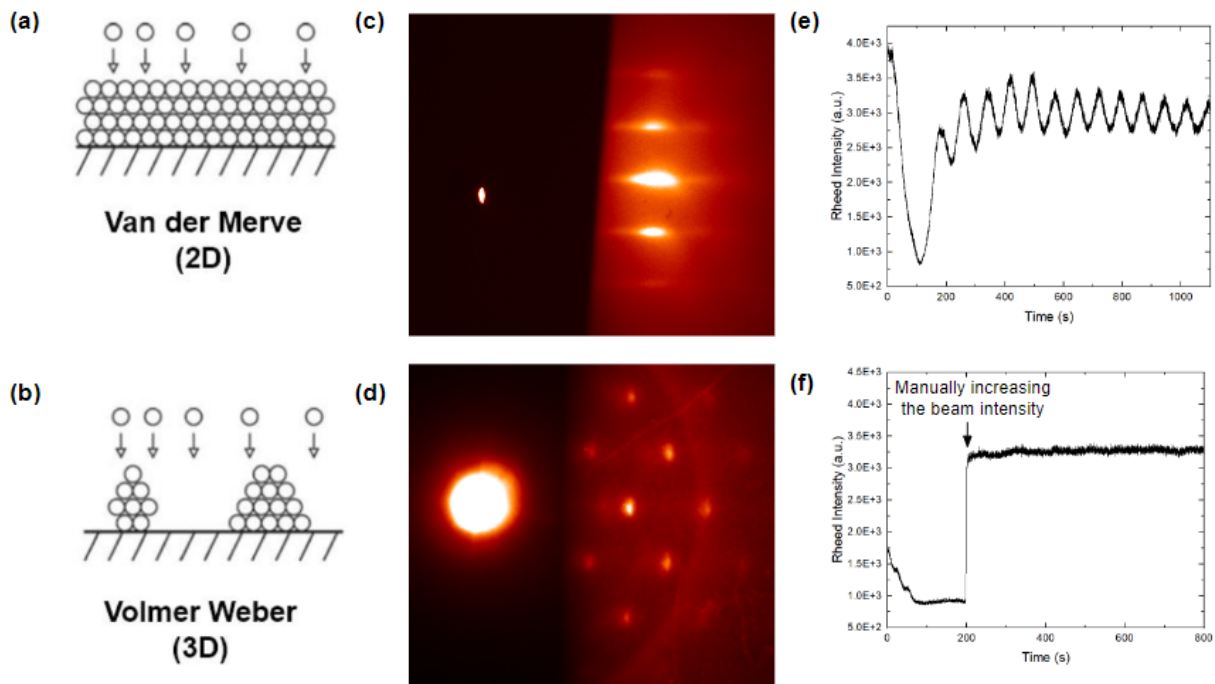


**Figure 2.3:** Growth kinetics monitoring by RHEED. (a) and (b) present 2D and 3D growth modes and their respective associated RHEED pattern are presented on (c) and (d). On the RHEED vs time intensity patterns presented on panel (e) we observe oscillations with no intensity drop, which is characteristic of perfect 2D growth. The RHEED vs time intensity patterns presented in (f) shows no oscillations and only a background intensity shift, which is characteristic of 3D growth.

Parameters that influence the growth mode during PLD include: the temperature of the substrate, the energy of the laser, which influences both the composition and the shape of the plasma as well as the adsorption probability, the total and partial oxygen pressures and the residence time. To be able to better understand the growth parameters and how they influence the growth kinetics, one may be interested in looking at the growth kinetics *in-situ*. The main investigation method available to monitor growth as it occurs is *in-situ* RHEED.

### 2.2.1.3 *In-situ* monitoring: Reflection High Energy Electron Diffraction

In a RHEED experiment, electrons are accelerated and propagated towards the film through the use of an electron gun. These electrons reach the film with a low incident angle. Momentum conservation imposes that refracted electrons interfere constructively only when the reciprocal lattice intersects the Ewald sphere. As a result, the pattern observed on the electron screen will be characteristic of the surface of the observed sample.

To get an idea of the kinetics of the reaction, we follow the growth of the material over time by looking at the intensity of the RHEED diffraction spots. If the growth is following a Van der Merwe growth mode, the RHEED intensity will evolve as follows. When the intensity is high, the surface of the material is highly crystalline: a new layer has just been created. The intensity then goes down as precursors are depositing on the surface. They will then contribute to the formation of a new layer and RHEED intensity will increase again. A typical RHEED intensity signal as a function of time in the case of growth occurring under the Van der Merwe growth mode is presented on figure 2.3 (e). Each maximum of the RHEED intensity corresponds

to the formation of a new layer. On the other hand, if the growth is going through the formation of islands, *i.e.* the growth is at least partially *Volmer Weber* like, the surface roughness will not vary, thus resulting in a RHEED signal presenting no oscillations. Such a RHEED intensity as a function of time is presented on panel (f) of figure 2.3. If the growth follows the step-flow growth mode, the surface morphology will remain unchanged throughout the growth process, resulting in a flat line RHEED intensity signal as a function of time.

Finally, we note that in the case of perfectly flat substrate, the additional straight lines originating from the first order diffraction pattern can be related to properties of the film below its surface. These features are called Kikuchi lines and characteristic of the inelastic scattering of electrons.

### 2.2.2 Magnetron Sputtering

Magnetron sputtering is widely used to perform depositions of different materials. It has the advantage of offering relatively high deposition rates as well as rather good uniformity over large growth areas, which can be harder to achieve with a method such as PLD.

Sputtering depositions are typically performed under a mix of inert and reactive gases atmospheres (Ar, N<sub>2</sub>, O<sub>2</sub>, etc ...) and under low pressure (typically 10<sup>-4</sup>-10<sup>-2</sup> mbar). In a similar fashion to PLD, one or more target(s) will be used to form of a plasma which will be propagated towards the substrate. This will in turn result in a deposition on the surface of said substrate. The mechanism at the origin of the plasma differs from the one of PLD: in a DC-sputtering experiment, a large negative voltage is applied between the target and the substrate plate. Beyond a certain voltage threshold, corresponding to the gas breakdown voltage, electrons start to escape from the cathode (target side) towards the anode (substrate side). This will cause the ionization of target atoms, which will in turn cause more electrons to flow towards the anode. This process is self-sustained, ensuing the formation of a plasma. Ionized positive atoms located close to the target will "feel" the electric field and will be accelerated towards the target. The collisions of these ions with the target species will result in the ejection of target atoms. They will then typically propagate ballistically towards the substrate.

In addition, a magnetic field is introduced by placing magnets behind the cathode. The magnets are placed so that the magnetic field will bend the path of the electrons in order to maximise their time of flight near the target. By doing so, the plasma is confined to the vicinity of the target. This will cause more collisions to occur, *i.e.* more target atoms will propagate towards the substrate. The introduction of magnets thus results in a better efficiency of the whole sputtering process. The addition of the magnetic field gives its full name to the experimental technique, magnetron sputtering. The principle of magnetron sputtering is illustrated on figure 2.4. We note that due to the plasma formation mechanism, DC-sputtering is particularly useful when trying to grow metal thin films, but is rather inefficient when trying to deposit insulators. This issue can be solved through the use of an RF source typically operating in the MHz range. The high frequency oscillations of the electric field will ensure that Ar ions follow their usual behaviour as they are too slow to follow the electric field. This typically comes at the cost of the growth rate, but allows for the deposition of a broad range of materials by sputtering.

In a similar fashion as PLD, a whole range of parameters can be explored to tune the growth modes. Parameters include the substrate temperature, the background pressure, the RF or DC power applied to the target, or the target-substrate distance. To ensure reproducibility, systematic pre-sputtering was performed before every growth.

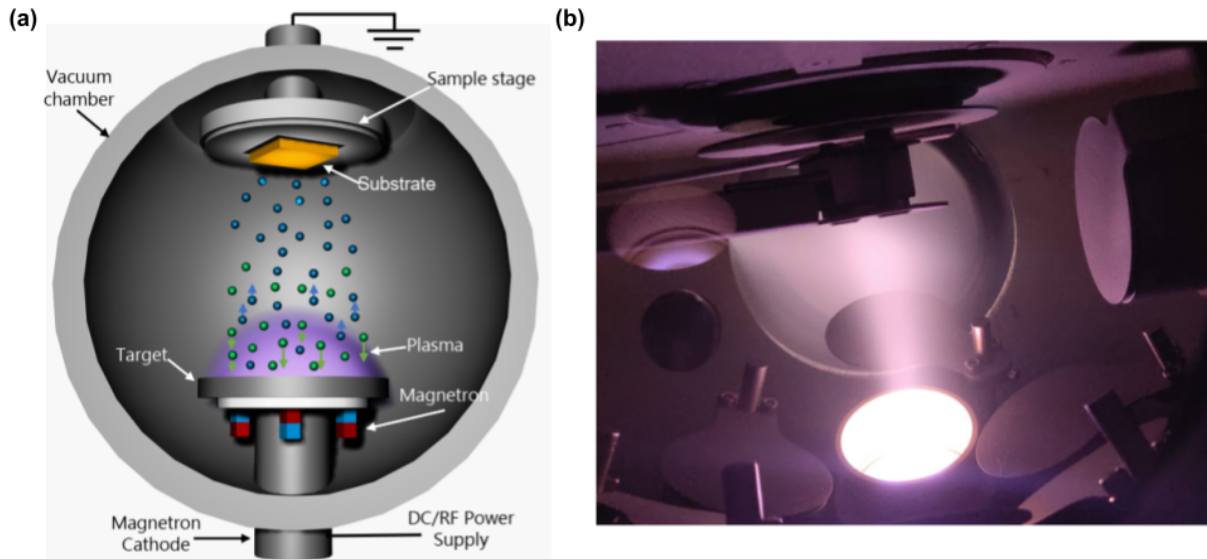


**Figure 2.4:** *Sputtering: (a) Schematic of a sputtering deposition experiment, reproduced from [64] with permission and (b) one of the confocal growth chambers used in the framework of this thesis.*

The depositions of samples that will be mentioned in this thesis were performed in two different Plassys MP450S standard magnetron sputtering chamber with a base pressure of about  $8.5 \times 10^{-9}$  mbar, with the option to have either DC or RF sources, and under a range of temperatures and pressures. These two set-ups may later be referred to as CONF and PLAS.

## 2.3 Crystal quality control characterisation methods

In the framework of this thesis, a wide variety of characterisation methods were used to control the thin films quality. Some of them, such as atomic force microscopy and X-Ray Photo Emission Spectroscopy, provide information about the top surface of the thin films, and others, such as Scanning Transmission Electronic Microscopy and X-Ray Diffraction, are critical in probing the crystal quality of thin films and their epitaxial relationship with their growth substrates.

### 2.3.1 X-Ray Photo Emission Spectroscopy

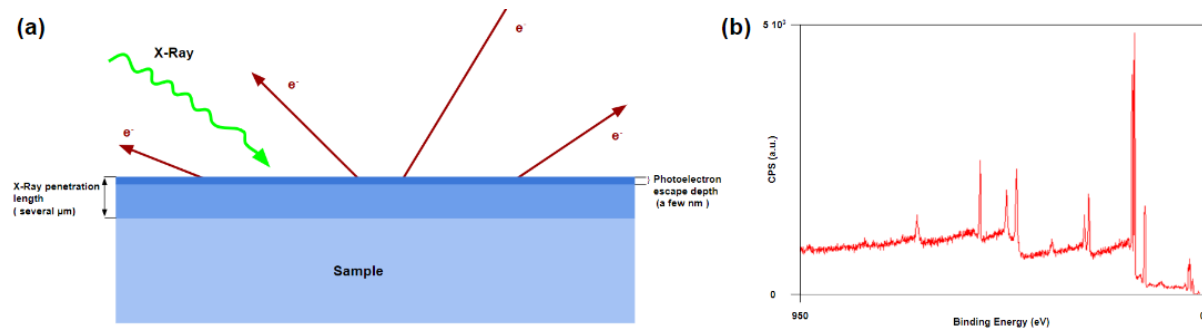


**Figure 2.5:** XPS: (a) Schematic of an XPS experiment and (b) survey scan of an SBO thin film.

In a X-Ray Photo emission Spectroscopy experiment (XPS), an X-Ray source, usually a fixed monochromatized Al or Mg anode emitting in the soft X-Ray range with energies of 1486.6 eV (Al  $K_{\alpha}$ ) or 1253.6 eV (Mg  $K_{\alpha}$ ) respectively, is used to excite the core electrons of the different atomic species of a material. The relaxation of the electrons from their excited states to their binding energy results in a photo-emission signal, which can be acquired. Thus, each peak appearing in a XPS spectrum should give rather detailed information about the chemical species present in the sample as well as their environment and their oxidation state. Peaks and artefacts may disturb the analysis (Fluorescence, emission of Auger electrons, satellites, energy loss lines due to plasmon excitation in metals, charging effect for insulators ...) which should be accounted for in the analysis to obtain proper values of the peaks' area. In addition, one should note that XPS is surface sensitive. A typical XPS set-up has a penetration depth of 5nm. We note that the penetration depth depends on the material, the angle of incidence and the energy of the X-Rays used. A schematic of an XPS experiment along with a typical XPS survey scan are presented on figure [2.5](#)

The photo emission spectroscopy set-ups used in the framework of this thesis are directly connected through a transfer chamber to the PLD and sputtering chambers. The samples investigated were sensitive to air exposure. Being able to easily transfer them from the growth chamber to an XPS set-up under high-vacuum played a huge role in the optimisation process of the different materials grown.

Finally, we note that XPS can also, in a certain measure, be used to quantitatively estimate the surface composition of a thin film.

#### 2.3.1.1 Notes about quantitative XPS

The photo ionization cross section,  $\sigma_{sc}$ , is the primary fundamental parameter determining XPS peak intensities. It represents the probability of a photon, of a given energy, causing an electron to ionize from a given

orbital of a given atom. Absolute  $\sigma_{sc}$  values have been calculated from theory for all atomic orbitals by John H. Scofield and normalised to the  $C_{1S}$ . Using these so called Relative Sensitivity Factors (RSFs) we can deduce the stoichiometric ratio of the different atomic species. However, recent reports trying to experimentally determine the RSFs values highlighted a sizeable difference between experimentally determined  $\sigma_{sc}$  and the theoretical values, especially for heavy atoms. The Scofield  $\sigma_{sc}$  values are accurate within  $\pm 5\%$  for elements of the elements of the first row of the periodic table, making it especially useful for quantification of organic compounds[166]. However, in the case of heavier atoms, quantification are believed to be precise within a  $\pm 10\%$  precision range, and should be evaluated as such[167].

### 2.3.2 X-Ray Diffraction

X-Ray Diffraction (XRD) is a widely used technique when it comes to characterising thin films. Crystals can be seen as a regular, periodic, arrangement of atomic planes separated by an interplanar distance,  $d$ . When an incident X-ray radiation of wavelength  $\lambda$  arrives at the surface with an angle  $\Theta$ , the diffracted beams will interfere with each other. The optical path difference between the two diffracted X-ray beams is such that the interference is constructive only if

$$2d_{hkl}\sin(\Theta) = n\lambda \quad (2.1)$$

Where  $n$  is the order of the reflection and  $d_{hkl}$  is the inter-planar distance between two adjacent (hkl) planes with  $k, k$  and  $l$  the Miller indices. This equation is commonly known as Bragg's Law.

In a XRD experiment, the incident angle of the X-Ray beam will be varied, leading to positive interference at different outgoing angles. In practice, we can have two different configurations for an XRD-set up. On one hand, we can fix the sample and move the source and the detector around it. This set-up main perks lies in the fact that it stabilises the sample: it can be laid on a stage with no need to fix it with tape or vacuum. One of the XRD systems used in the framework of this thesis was one of these so called  $\Theta$ - $\Theta$  set-up. In the other configuration, the source is fixed and the sample and the detector are moving. This enables the access to more "out-of-plane" peaks but requires the sample to be fixed to the stage with tape or with a vacuum system. The other XRD set-up used in the framework of this thesis was one of these  $\Theta$ - $2\Theta$  set-ups.

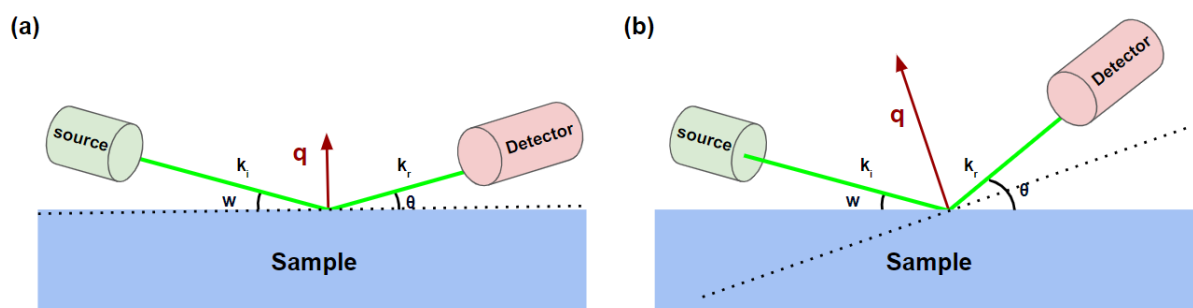


**Figure 2.6:** XRD working principle. Schematics of (a) a symmetric scan and (b) an asymmetric scan. The dotted lines indicate the diffraction planes. Note that in the case of a symmetric scan, the diffraction plane is not perfectly horizontal: substrates are slightly miscut.

### 2.3.2.1 Symmetric scans

In the referential of the substrate, we can consider that the source and the detector are in a symmetric configuration, *i.e.* they both form an angle  $\Theta$  with the crystal (hence the name, symmetric scan). The scattering vector  $\mathbf{q}$  is approximately perpendicular to the surface (the miscut angle needs to be accounted for during the alignment).  $\mathbf{q}$  is defined as the difference between  $\mathbf{k}_i$  and  $\mathbf{k}_r$ , the vectors of the incident and the reflected beams, respectively. During a  $2\Theta$ - $\omega$  scan, in the referential of the system the source and the detector move simultaneously over a range of  $\Theta$  angles so that  $\mathbf{q}$  stays perpendicular to the surface but its value changes. A peak of intensity will be detected when  $\Theta$  verifies Bragg's law, *i.e.* when  $q = \frac{1}{d_{00n}}$ , with  $n$  the order of the reflection. From this measurement we can deduce the value of the out-of-plane interplanar value. A schematic of such an experiment is represented on figure 2.6 (a).

### 2.3.2.2 Reciprocal space maps

To get an insight on the in-plane lattice parameter, which is representative of the epitaxial relationship between the substrate and the film, it is common to perform Reciprocal Space Maps (RSMs). During such an experiment, in the referential of the sample, the source and the detector are placed asymmetrically such that  $\mathbf{q}$  is tilted out of the plane perpendicular to the orientation of the substrate (*e.g.* if we neglect the miscut angle, out of the perpendicular plane). More precisely, to perform a reciprocal space map we fix the position of the detector and perform a sweep over the position of the source. We then increment the position of the detector and repeat the source sweep procedure over a range of  $2\theta$  values. The result are plotted as a map of the intensity of the signal acquired by the detector as a function of  $Q_{x,y}$ , the in-plane projection of  $\mathbf{q}$ , and  $Q_z$ , the out-of-plane projection of  $\mathbf{q}$ . We can express  $Q$  as

$$Q_{x,y} = \frac{4\pi}{\lambda} |\sin(\theta) \cdot \sin(\theta - \omega)| \quad (2.2)$$

$$Q_z = \frac{4\pi}{\lambda} |\sin(\theta) \cdot \cos(\theta - \omega)| \quad (2.3)$$

In addition, Bragg's law dictates that we only get constructive interference for values of  $Q$  which matches the inverse of an interplanar distance between two adjacent  $(h,k,l)$  planes such that

$$Q_{i[h,k,l]} = \frac{\lambda}{2} (ha_i^* + kb_i^* + lc_i^*) \quad (2.4)$$

with  $a_i^*$ ,  $b_i^*$  and  $c_i^*$  the components of the lattice vector in the reciprocal space, where  $i$  stands for  $x, y$  and  $z$ . From there, we can deduce the  $\mathbf{a}$ ,  $\mathbf{b}$  and  $\mathbf{c}$  real space lattice parameters by using

$$\mathbf{a}^* = 2\pi \frac{\mathbf{b} \times \mathbf{c}}{V} \quad (2.5)$$

$$\mathbf{b}^* = 2\pi \frac{\mathbf{c} \times \mathbf{a}}{V} \quad (2.6)$$

$$\mathbf{c}^* = 2\pi \frac{\mathbf{a} \times \mathbf{b}}{V} \quad (2.7)$$

A schematic of a 2D Reciprocal Space Map experiment is represented on panel (b) figure 2.6

### 2.3.3 Scanning Transmission Electron Microscopy

Scanning Transmission Electron Microscopy (STEM) permits the investigation of crystal quality at the atomic scale. During a STEM experiment, a beam of accelerated electrons is focused, through the use of electromagnetic lenses, on an ultra thin slice of sample preemptively prepared by focused ion beam (FIB). The incident electrons interact with the sample, and the outgoing transmitted signal is characteristic of the slab it went through. The transmitted signal is collected and refocused (once again using an electromagnetic optical path composed of several lenses, that will not be detailed here) to form a real space image of the sample. The contrast of the obtained image depends on the density and the atomic-numbers of the atoms which compose the thin-film. A STEM image thus contains information about the crystallinity and the stoichiometry of a thin film at the atomic scale. Depending on the incident angle and the energy of the incident electrons, they may be more sensitive to either heavy or light atoms. High Angle Annular Dark Field (HAADF) and Annular Bright Field (ABF) STEM modes are sensible to heavy and light atoms, respectively. Electron Energy Loss Spectroscopy (EELS) is commonly used to measure an atomic specie content as a function of depth and is also critical in understanding the interfaces in between different materials.

The STEM images presented in this thesis were the result of a collaboration with Nicolas Gauquelin and Daen Jannis. The samples were prepared in Antwerp by Nicolas Gauquelin by focused ion beam (FIB), and were then imaged by STEM.

#### 2.3.3.1 Data analysis

Proper treatment of STEM data can be time-consuming as the sheer amount of information contained in a STEM image is quite rich, and distortions inherent to the experiment have to be taken into account by a post experimental treatment. Python scripts for STEM analysis have been the subject of a number of recent papers [168] [169] [170]. In the framework of this thesis, we used the atomap library [170], which was tailored made for the purpose of tracking atomic positions in perovskites. It includes functionalities which help track the Oxygens' atomic positions on the ABF images. We complemented it with an homemade script developed to meet the specific needs related to this work, in particular to investigate polarization, strain and their correlations in specific areas of the samples. The data treatment presented in this work was performed by D. Jannis and G. Verdierre.

### 2.3.4 Atomic Force Microscopy

The surface topography is mapped by the means of atomic force microscopy (AFM). In a tapping-probe AFM experiment, a tip oscillating at its resonant frequency is approached towards a surface. The tip will feel an attractive/repulsive force which is directly related to the distance between the surface and the tip. This force will modify the oscillation amplitude of the tip plus cantilever system, which can be seen as a spring. The amplitude of the oscillation is implemented in a feedback loop to keep it constant. Hence, the feedback that has to be applied to the loop can directly be related to the topography of the surface. Other AFM methods require the use of the "contact mode" in which the tip has to be contacted to the surface. This is for example the case for conductive tip AFM (ct-AFM) which can be used to locally probe the resistive state of a surface. It is also the case for Piezo Force Microscopy (PFM), which can be used to characterise the local piezoelectric properties of thin films.

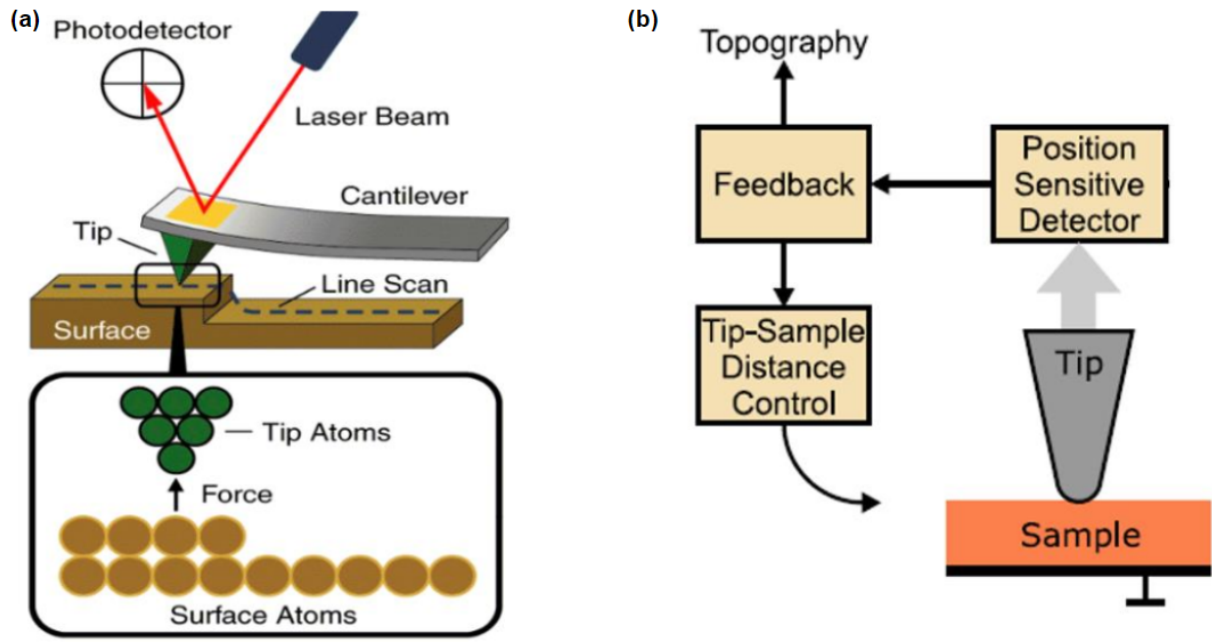


Figure 2.7: AFM working principle. Adapted from [171] and [172]

### Piezoresponse Force Microscopy

Piezoresponse Force Microscopy (PFM) is based on the inverse piezoelectric effect, which results from an elastic deformation of a piezo electric material under the application of an external electric field. If we consider a material polarised along an arbitrary axis  $\mathbf{u}_p$ , and we apply an electric field along the same axis, if the material has a positive (negative) piezoelectric coefficient, it will expand (shrink). If the electric field is applied along  $-\mathbf{u}_p$ , the material will shrink (expand). We can define a size difference,  $\Delta_z$ , along the  $\mathbf{u}_p$  axis. This difference is described by the evolution of the stress  $\eta$  as a function of the electric field:

$$\eta = d_{ij}E \quad (2.8)$$

where  $d_{ij}$  is the piezoelectric tensor,  $i$  denotes the direction along which the polarization is applied and  $j$  the direction in which the material expands/shrinks. The tensor term which has seen the most interest (because it is the easiest to measure in a PFM) is the  $d_{33}$ . It corresponds to an excitation along the out-of-plane axis and a response along the same axis. It is directly related to the voltage applied to the material by the relation

$$d_{33} = V\Delta_z \quad (2.9)$$

Hence, measuring  $\Delta_z$  gives us a direct measure of  $d_{33}$ . In practice, in a PFM experiment a thin film is scanned by an AFM probe connected to an electric circuit. The film has to be interfaced with a bottom electrode. By applying an oscillating electric field in between the back electrode and the AFM tip, one can cause a polar material to oscillate in or out-of phase with the AC voltage. Hence, PFM can provide insights into the presence of polar domains in a material, offering an initial indication of the material's potential ferroelectric properties. The piezoelectric signal for a material exhibiting a purely out-of-plane polarization, is of the form

$$\Delta_z = |d_{33}|V_{AC}\cos(\omega t + \phi(d_{33})) \quad (2.10)$$

Lock-in amplifiers are coupled to a standard PFM probe to access the deflection signal. The lock-in outputs are the amplitude and the phase of the PFM signal. Opposite polarizations will result in a  $180^\circ$  phase shift with the AC excitation phase: up domains will be in phase with the AC excitation whereas down domains will be anti-phased with the AC excitation. In our PFM set-up, we apply a  $90^\circ$  phase offsets to the lock-in, which results in a  $\pm 90^\circ$  for the down and up polarization, respectively. Hence, up polarization will appear as dark on the PFM scans, whereas down polarization will be characterised by a bright signal.

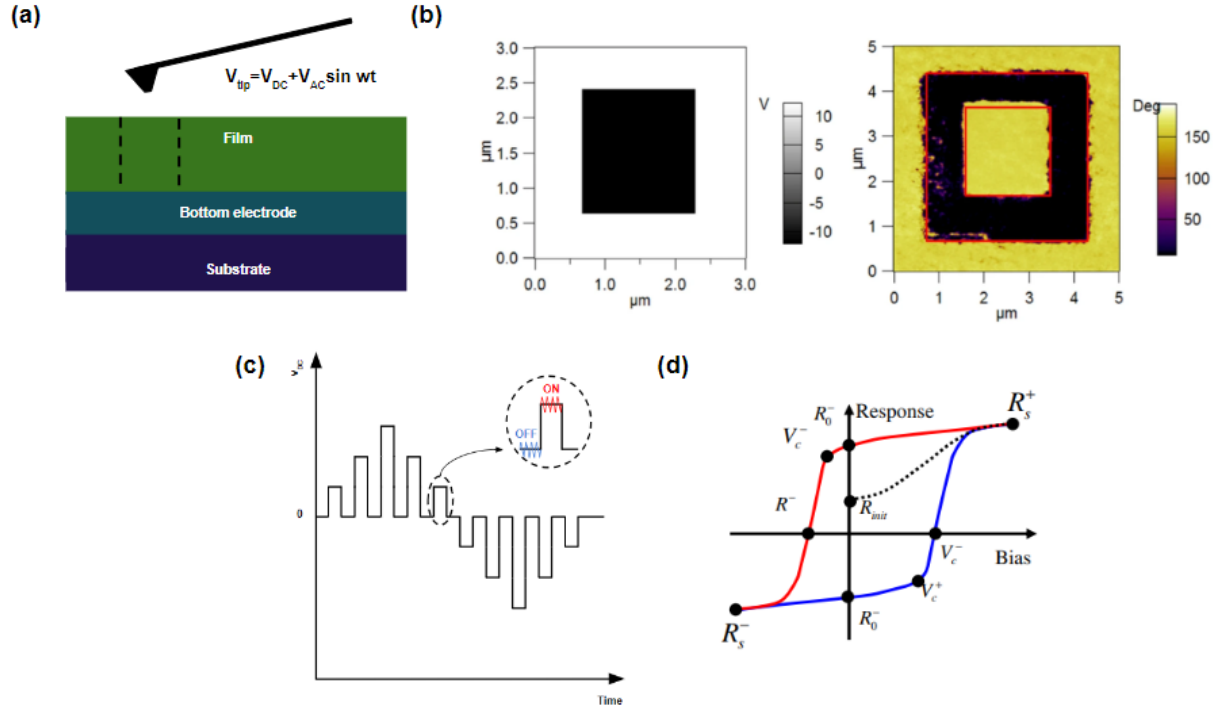


**Figure 2.8:** PFM working principle. (a) Schematic of a PFM experiment. A voltage is applied between the tip and the back electrode, (b) a "box in a box" experiment during which the polarization is written using a voltage mask (first figure) and the output polarization is read by PFM (second figure), (c) typical voltage applied to the tip during a polarization loop experiment by PFM and (d) the expected hysteretic polarization output of a ferroelectric sample to which the field is applied. Adapted from [173] and [174]

It is important to note that the polarization may not be purely out of plane, but also may have an in-plane component. The in plane polarization is detected through the torsion of the cantilever rather than its deflection. The reflected laser spot will then oscillate on the horizontal axis of the four quadrant photo-diode, indicating the presence of an in-plane polarization. The signal is processed by a separate lock-in amplifier. In the set-up used in framework of this thesis, if the polarization is pointing to the left (right), the contrast will be bright (dark). Both in-plane and out-of-plane PFM signals are recorded simultaneously. We note that in the case of weak ferroelectrics, the natural polarization may be unoriented. In this case, a voltage can be applied to the film to force the orientation of the polarization in one or the other direction. An example of such an experiment is presented on panel (b) of figure 2.8.

Finally, using PFM it is possible to acquire the P(E) response of a film interfaced with a back electrode. A pulse triangular waveform such as the one presented on figure 2.8 (c) is applied to the material. Piezoresponse Force Spectroscopy measurements can be acquired in bias-on and bias-off regimes. For a standard ferroelectric, the  $\Delta_z$  phase polarization loop should be hysteretic with two plateaus, as previously described. The  $d_{33}$  loop is built from the  $\Delta_z$  amplitude and phase signals. An example of the response of the polarization to a voltage sweep is presented on figure 2.8 (d). This method, compared to the one which will be presented in the next section, is harder to implement and does not permit the investigation of endurance due to the time necessary

to acquire a single loop, but enables the investigation of samples without a top electrode.

### 2.3.5 Electrical characterisation of ferroelectrics

The observation of polarization domains by PFM is one of the broadly used method to investigate the polarization states of candidate ferroelectrics. However, as aforementioned, ferroelectrics are characterised by their polarization response to the cyclic application of an electric field. In this subsection, we describe the electric measurements associated with macroscopic polarization switching. A typical set-up for characterizing a dielectric sample involves the use of the Sawyer-Tower circuit [175]. In this setup, a voltage is applied to one electrode and swept cyclically, often employing a signal with triangular shape. The current flowing from the top electrode to the grounded bottom electrode is measured or directly integrated over time, typically utilizing a reference capacitor. The dielectric samples which are analysed may be imperfect insulators. Hence, three different terms may contribute to the  $I(V)$  response of a dielectric.

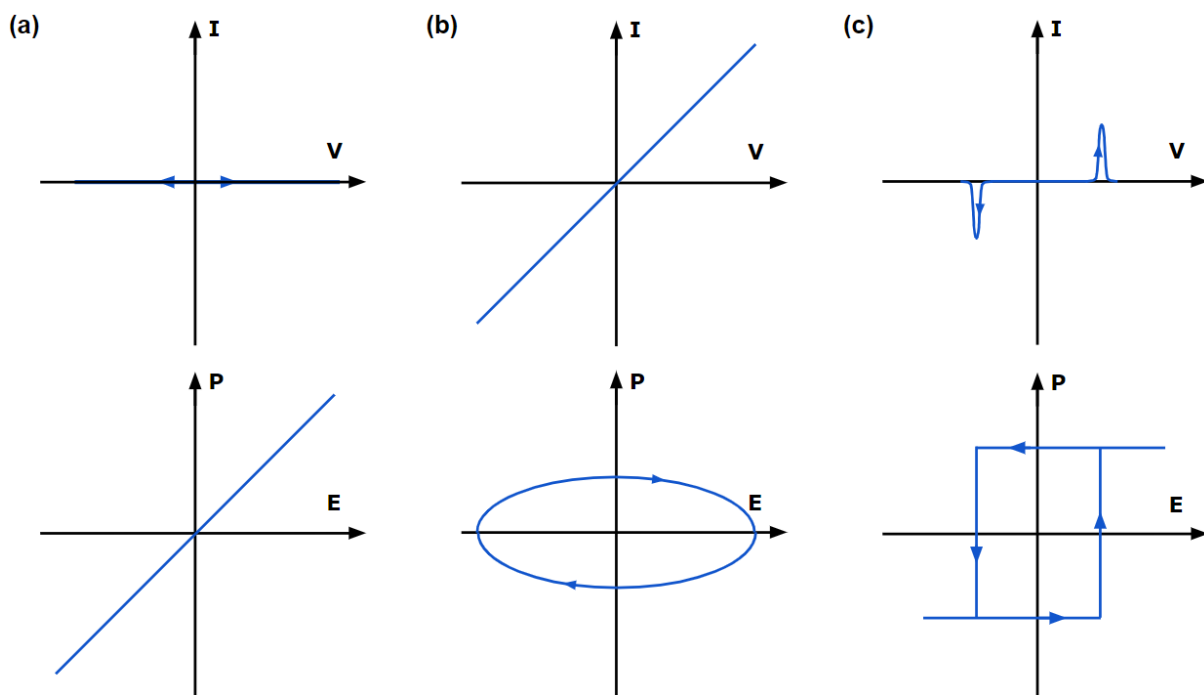


**Figure 2.9:** Contributions to the  $I(V)$  plot from (a) a capacitor, (b) a resistance and (c) an ideal ferroelectric.

- Capacitance contribution: in the case of a perfect insulator with no ferroelectric properties,  $P = \epsilon_0 \chi E$ , which results in the well known capacitor  $I(V)$  equation:  $I = C \frac{dV(t)}{dt}$  with  $C = \frac{\epsilon_0 \chi}{d}$ , with  $C$  the capacitance of the sample and  $d$  its thickness such that  $E = \frac{V}{d}$ . For a triangular voltage signal, the current response of the system is simply a constant, and the polarization (integrated current) will be linear with the electric field.
- Resistive/diode contribution: in the case of a resistance, Ohm's law dictates that  $I = \frac{V(t)}{R}$ . As a result, for a triangular voltage signal, the current response will be linear, and the resulting "polarization" (which has no physical meaning here, it is simply the variable defined as the integrated value of the intensity) will take the form of a close loop. It should not be mistaken for a ferroelectric loop as it presents no hysteretic behavior [176] [177].
- Ferroelectric contribution: In the case of a uniformly polarized ferroelectric, two characteristic current

peaks with opposite sign occur at well defined values of the electric field. These current peaks are associated to the polarization switching event. Because we simply have  $E = \frac{V}{d}$ , we can infer the apparition of two peaks at well defined polarization voltages. In other terms, upon polarization switching, a switching current propagates in the ferroelectric such that  $j_p = \frac{\partial P}{\partial t}$ . Otherwise, the sample behaves as a simple dielectric.

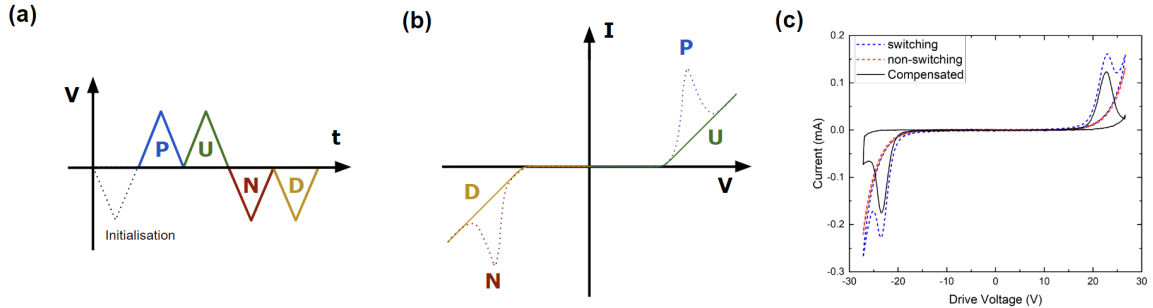


**Figure 2.10:** A PUND experiment (a) wave form of the voltage signal applied to the sample, (b) schematic of the current acquired on a ferroelectric sample with an additional diode behavior, which can typically be caused by leakage currents. (c) PUND data acquired on an (Al,Sc)N ferroelectric thin film.

The different contributions to the total current are represented on figure 2.9. To summarize, we may model the system as a parallel resistor/ capacitor with the addition of the polarization switching:

$$I(t) = C \frac{dV}{dt} + \frac{V(t)}{R} + A \frac{dP}{dt} \quad (2.11)$$

where A is the area of the sample. However, our focus lies solely on the polarization contribution. To isolate this polarization contribution, one may opt for a PUND sequence [31]. This sequence leverages the fact that once a ferroelectric is fully switched into one of its polarization states, sweeping the field in this direction effectively scans the capacitor and resistive features of the sample without interference from polarization switching currents. Subtracting this contribution from the original data yields the I(V) curve specifically associated with polarization switching. In a PUND experiment, a preset negative pulse with a voltage higher than the critical switching voltage is applied to initialize the polarization in the "down" state. Subsequently, a positive (P) triangular pulse switches the polarization up, eliciting responses from all three contributions to the voltage sweep. With the system on its up (U) state, the same positive voltage is applied, triggering only the responses unrelated to polarization switching. This current will later be subtracted from the previously acquired data, leaving only the intended polarization switching contribution. The same steps are repeated with negative (N) and down (D) pulses. The resulting data can be integrated to reconstruct the full polarization loop. This technique remains effective as long as the polarization switching current is not entirely overshadowed by ohmic contributions. PUND is illustrated on figure 2.10

# Chapter 3

## Growth optimisation of SrBiO<sub>3</sub>

### 3.1 Introduction

One of the fundamental parameters of crystalline material is its lattice parameters. Paradoxically, it is also among the most challenging to control. Bulk crystals can not handle more than 0.1% of hydro-static strain. The use of "chemical pressure" [178], *i.e.* tuning a bulk material lattice parameter through isovalent cation substitution, provides a route towards high levels of strain at the cost of disorder and potentially local distortions. Nonetheless, the solution towards tuning the lattice parameter of a material at the smallest of scales may well lie in epitaxial strain, which enables tuning of the biaxial strain degree of freedom at levels that would have been unfathomable before the advent of modern epitaxy techniques. In addition, the costs associated with epitaxial strain are very small, if not nonexistent. Strain levels of  $\pm 3\%$  are common [179][180], with the record being held by a whopping 6.6% level of compressive strain, enabled by a strain driven phase transition [181][182][178].

In this context, research for strain induced properties in materials has been booming in the material science community. For example, strain engineering played a huge role in enhancing the ferroelectric properties of already well known ferroelectrics, such as BaTiO<sub>3</sub> [183][184] and PbTiO<sub>3</sub> [185][186]. Shifts in ferroelectric Curie Temperatures are of the order of magnitude of 300K per percent biaxial strain. In addition, a strain driven phase transition in BiFeO<sub>3</sub> enabled the investigation of the multiferroic orders to make considerable progress [187]. EuTiO<sub>3</sub>, which is antiferromagnetic and paraelectric when grown relaxed, was transitioned to a multiferroic through the use of tensile strain. The driving mechanism of the strain induced phase transition lies in the softening of a phonon mode. In the continuity of these results, *ab initio* computations have been trying to find new ferroelectric phases that would be stabilised by strain. Ideally, such structures could have additional exotic functionalities, such as an other ferroic order or spin-orbit coupling. In this context, and as already introduced in chapter 2, it was proposed that SrBiO<sub>3</sub> (SBO) would undergo a strain driven phase transition to a ferroelectric phase. The addition of large spin-orbit coupling (SOC) induced by the Bi *d*-orbitals would result in a FerroElectric Rashba SemiConductor (FERSC) with an electrically switchable Rashba coefficient of  $\alpha_R = 1.68 \text{ eV}\cdot\text{\AA}$  [90].

In this chapter, we will describe the different step of growth optimisation of candidate FERSC SBO by PLD, as well as the investigation of its strainability through substrate engineering.

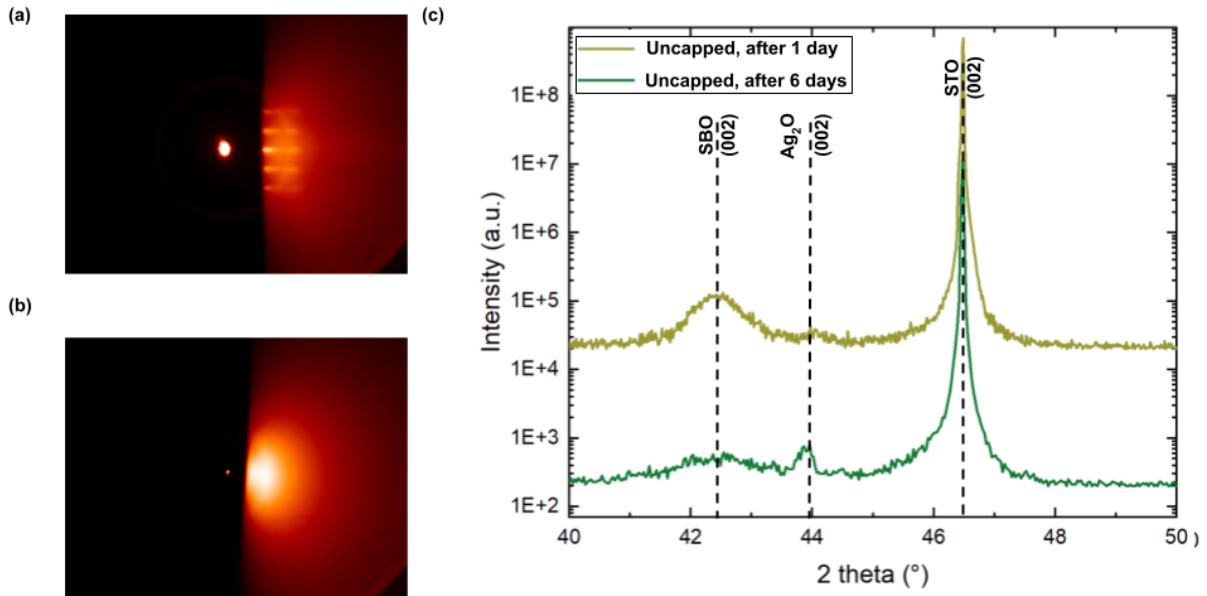


**Figure 3.1:** *Unstability of uncapped unoptimised thin films. (a) RHEED signal of a sample at the end of growth, after cooling it down and (b) RHEED signal acquired on the same sample after leaving it in a nitrogen box for a week. (c) XRD signal of said sample one day and six days after growth. The peak characteristic of SBO disappears over the course of a week. The peak at 44° is associated to silver paste, which we used to fix the samples during growth.*

## 3.2 Growth optimisation

A stoichiometric target of Sr-Bi-O (Toshiba, purity 99.99 %) was used for the PLD growth with a KrF laser (Coherent, 25 ns). The target-substrate distance was kept constant at 50 mm. This is a parameter which is fixed in COMAT (see section [2.2.1](#)).

### 3.2.1 Initial conditions

The starting point of our growth investigation were the growth conditions of  $\text{BaBiO}_3$  (BBO). BBO was optimised in COMAT by Luca Bouwmeester during her PhD [\[139\]](#). The reason for this choice lies in the fact that bismuth based perovskite main growth challenges are associated to the high volatility of bismuth. In addition, bismuthates have a tendency to form oxygen vacancies. This is a direct consequence of the bond disproportionation, which can be accommodated by the formation of oxygen vacancies [\[111\]](#). Thus, this effect is linked to the presence of bismuth on the B cation site of the perovskite structure. We inferred that changing the chemical nature of the A site cation should not have too much of an effect on the challenges usually associated with the growth of bismuthates. A repetition rate of 1 Hz was used throughout the growth optimisation. After an ablation test, we decided to settle for a fluency of  $1.9 \text{ J cm}^{-2}$ . The ablation test is presented in the supplementary materials.

### 3.2.2 Stability of B-site bismuth perovskites

With growth conditions similar to the one used for BBO, RHEED oscillations and diffraction patterns characteristic of a 2D thin film were acquired. However, XRD diffraction patterns did not present any film diffraction

peaks. We attributed this to the relatively low stability of B-site bismuth based perovskites[111]. We reintroduced the thin films in the chamber after the XRD measurements, and obtained a RHEED signal characteristic of an amorphous surface.

In addition, the XRD spectra of a film acquired right after growth and after a week in a nitrogen box under low vacuum is presented on 3.1. We observe a disappearance, over the course of a week, of the diffraction peaks characteristic of a 4.25 Å (001) oriented perovskite. We decided to cap our samples to increase their stability.

### 3.2.3 Capping

The material constituting the capping layer should meet a number of criteria. First, the growth conditions of the capping layer should leave the SBO untouched. This means that it should grow at similar or lower temperatures compared to SBO, and at pressure  $>10^{-2}$  mbar. Under these conditions, we infer that the SBO thin film should not form additional oxygen vacancies during the growth of the protection layer[111]. Finally, being transparent to XRD would be a plus for the capping layer. It would facilitate the XRD peak identification during the growth optimisation. With these requirements in mind, we identified two candidate capping layers: amorphous  $\text{Al}_2\text{O}_3$  and crystalline  $\text{SrTiO}_3$ .

Concerning  $\text{Al}_2\text{O}_3$ , it grows at room temperature under a high oxygen content ( $2 \cdot 10^{-2}$  mbar). Two hundred pulses of  $\text{Al}_2\text{O}_3$  were deposited as a capping layer. Growth was performed at a frequency of 2 Hz and with a fluency of  $1.5 \text{ J cm}^{-2}$ . This yielded a 4 nm homogeneous capping layer.  $\text{Al}_2\text{O}_3$  is amorphous and as such does not appear in the XRD spectra.

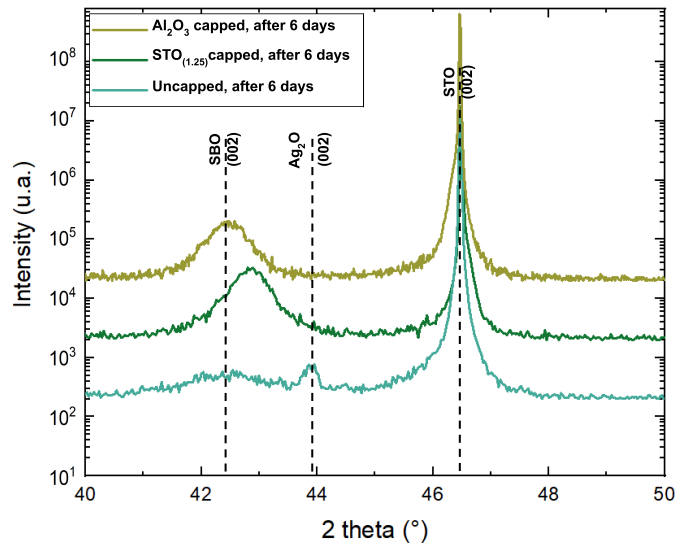


**Figure 3.2:** Stabilisation of SBO thin films through the use of different capping layers.

Regarding  $\text{SrTiO}_3$ , it is relatively easy to grow by PLD: it accommodates a variety of growth conditions[188]. In addition, in the vicinity of the growth conditions of SBO, it grows rather quickly (20 pulses per atomic layer). Given that we started the optimisation of SBO thin films on STO substrates, it also has the added benefit of not adding an extra peak on the XRD spectra. Indeed, the capping layer and substrate peaks should perfectly overlap provided that the capping layer is grown with a good enough quality. Finally, given that thin films of STO can be grown epitaxially on SBO, it may also reproduce the morphology of the bismuthate thin film, thus enabling the indirect investigation of the morphology of SBO by AFM. We also note that there is a

possibility that the STO capping layer may induce some level of compressive strain to the upper layers of SBO, further strengthening the overall strain applied to the bismuthate thin film. We discussed in section 1.5.5 how steric effects that may occur at bismuthate interfaces might affect the properties of SBO. Growth of the STO capping layer was performed at the same growth temperatures and pressures than that of SBO (which varied during the growth optimisation), at a frequency of 1 Hz and with a fluency of  $1.9 \text{ J cm}^{-2}$ . The XRD spectra of an  $\text{Al}_2\text{O}_3$  capped sample and of a STO capped sample are presented on figure 3.2. It demonstrates the efficiency of both capping layers. Regarding the STO capped sample, we note that the capping layer peak is overlapping with the substrate peak, which we interpret as an indication a good epitaxial quality of the capping layer [188]. We also note that the (002) perovskite peak of SBO seems to shift to higher angles when capped with STO. We expect the SBO to grow relaxed on STO because of the huge lattice parameter mismatch ( $> 8\%$  lattice mismatch). A smaller lattice parameter on a relaxed film may be related to a smaller amount of oxygen vacancies. We thus infer that the STO capping may enhance oxygen trapping in the film compared to the  $\text{Al}_2\text{O}_3$  capping. Motivated by this result as well as the possible benefits regarding strain aforementioned, we decided to proceed with our growth optimisation with an STO capping layer.

### 3.2.4 Growth optimisation

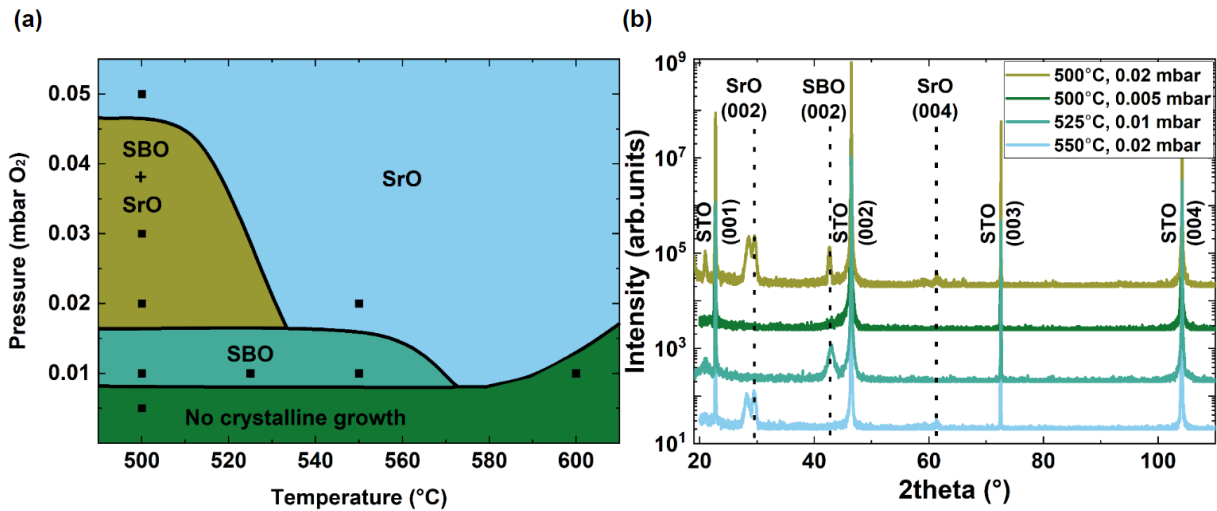


**Figure 3.3:** (a) SBO phase diagram established for the growth of SBO. (b) XRD spectra acquired in the different zones shown in (a). It is worth noting that the oxygen growth pressure is the most critical parameter to optimise when trying to grow bismuthates.

The capping layer being settled upon, a phase diagram as a function of temperature and pressure was established. The growths were performed on STO substrates treated as described on section 2.1 with a laser frequency of 1 Hz and a laser fluency of  $1.9 \text{ J cm}^{-2}$ . The phase diagram is represented on panel (a) of figure 3.3. Changing the pressure and temperature influences the nature of the crystal grown, with two crystal structures dominating the phase diagram. We infer that the critical parameter in differentiating which phase grows predominantly is the sticking of bismuth. If the bismuth does not stick, the main phase grown is (111)-oriented rocksalt strontium oxide with a lattice parameter of  $\sim 3.65 \text{ \AA}$  [189]. If the bismuth does stick, the main phase grown is a (001)-oriented perovskite with a  $\sim 4.25 \text{ \AA}$  lattice parameter, which is in good agreement with literature concerning  $\text{SrBiO}_3$  [116] [141]. The XRD spectra of the different regions of the phase diagram are represented on panel (b) of figure 3.3. We note that the oxygen pressure window in which a single-phase SBO perovskite can be grown epitaxially is relatively narrow. Thus, we infer that the oxygen partial pressure is the most critical parameter to optimize when trying to reproduce these growth [190].

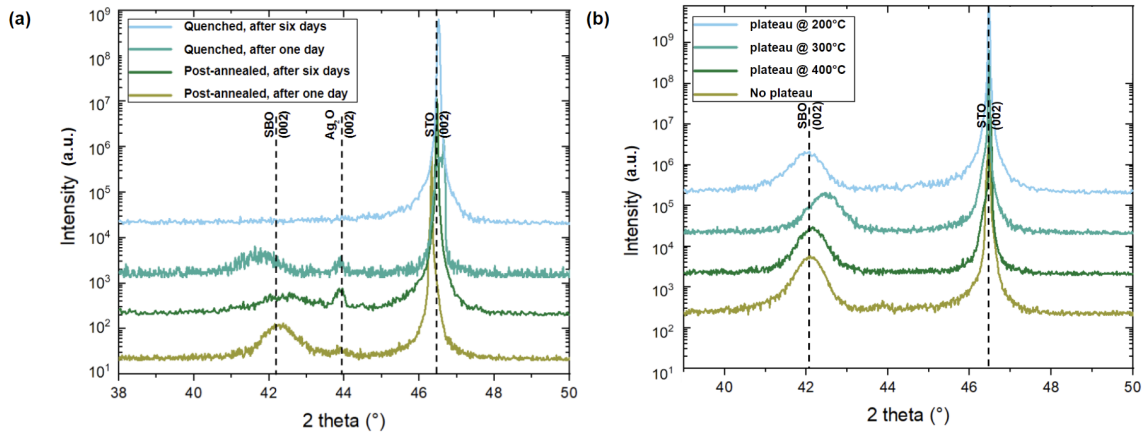


**Figure 3.4:** Fine-tuning post annealing to maximise the oxygen content in the SBO matrix (a) Evolution of the XRD spectra of two uncapped samples. The post annealed sample is more stable than the quenched one. (b) XRD of capped samples after different post annealing procedure. The peak shifting to higher angles in the case of the 300°C post annealed sample is indicative of a thin film of higher crystalline quality.

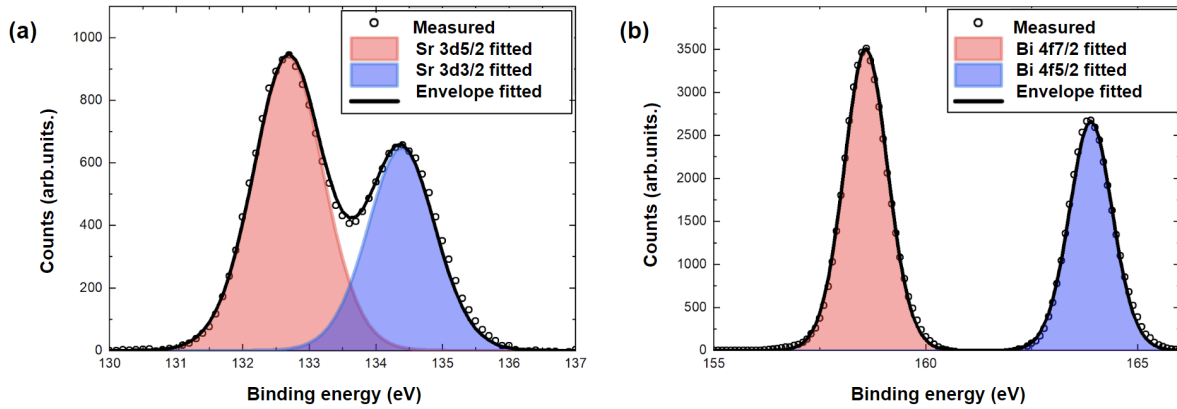


**Figure 3.5:** In-situ XPS characterisation of SBO thin films. strontium and bismuth valency are respectively 2+ and 4+, as expected. The stoichiometry computed from XPS is confirmed to be  $\text{SrBiO}_3 \pm 5\%$ .

This first growth optimization was carried out using a laser spotsize of  $1.787 \text{ mm}^2$ . Growing with such a spotsize resulted in growths of SBO at a speed of 6-7 pulses per unit cell. This one pulse uncertainty on the growth rate of SBO results in a  $\sim 16\%$  error on the thickness of the thin film. Controlling the thickness of our films is of critical importance, because we expect the strain to relax with thickness. In addition, it may however so slightly change the nature of the SBO termination, which could be critical, for example if we want to induce a 2D conductive state at the top interface<sup>[129]</sup>. Thus, we decided to reduce the spotsize to  $0.589 \text{ mm}^2$  by changing the size of the mask which is put in the laser path (up until now we were using a  $3 \times 15 \text{ mm}^2$  mask, which was replaced with a  $1 \times 15 \text{ mm}^2$  mask). This had the effect of slowing the speed of the growth to  $\sim 20$ -21 pulses per unit cell, allowing for a better control of the thickness (and we infer the termination of the topmost layer, though we can not directly check this) of the SBO thin films.

### 3.2.5 Post-annealing

Growth being relatively well optimised at this point, different post annealing procedures were investigated to maximise the oxygen loading content of the SBO thin films. The different post annealing procedures that were investigated are (i) optimizing the oxygen partial pressure during the post annealing procedure, (i) quenching,

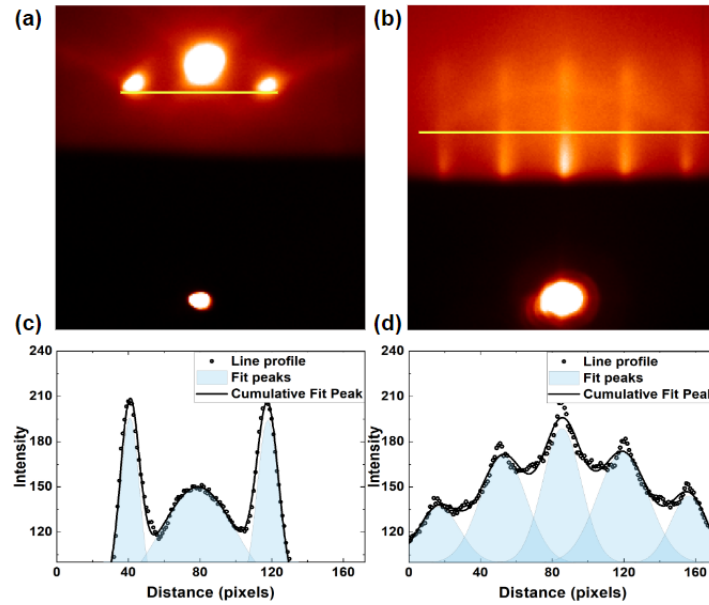


**Figure 3.6:** *In-situ RHEED signal acquired at room temperature on (a) an STO substrate prior to the growth of (b) an uncapped SBO thin film grown on said STO. The in-plane lattice parameter is computed to be  $4.3 \pm 0.05 \text{ \AA}$  from the RHEED intensity profiles (c) and (d), acquired along the yellow solid lines.*

*i.e.* cooling the samples down as fast as possible under a high oxygen background pressure (determined to be of 100 mbar from step (i)), and (iii) the introduction of a temperature plateau, under a 100 mbar oxygen background pressure. The aim of the post annealing step is to maximise the oxygen content in the bismuthate films. The result of this study are presented on figure 3.4. On panel (a), we highlight the fact that (i) quenched samples degrade quicker than post-annealed samples. The investigation regarding the (iii) introduction of a temperature plateau is summarized on panel (b) of figure 3.4. The SBO peaks are symmetric, indicative of an homogeneous strain state in the thin film. Considering the relatively large lattice parameter mismatch between STO and SBO, we suppose the films are unstrained. Taking into account this assumption, the over all shift of the (002) peak towards high angles is indicative of films of higher quality. Indeed, oxygen vacancies are bigger than oxygen atoms, and thus tend to increase the lattice parameter of the film. The relative position of the (002) SBO peak of the sample annealed at 300 °C for 20 minutes under a high oxygen pressure background indicates that the sample benefits from the introduction of this plateau.

The electronic structure and chemical composition of the optimised SBO films were investigated using *in situ* XPS. The Sr 3*d* and Bi 4*f* core-level spectra of a 75 nm thick SBO film are presented on panels (a) and (b) of figure 3.5. By this measurement, we confirm the valency of Sr to be 2+, and the valency of Bi to be nominally 4+. After subtraction of a Shirley background, the peaks were fitted to a Gaussian-Lorentzian function, with a 70% Lorentzian character. The FWHM of the different peaks of a given element was enforced to be the same, and the ratio of the peaks was enforced to be 0.66 for Sr3*d* and 0.75 for Bi4*f*. The stoichiometry of the film at the surface can be estimated from the area of the XPS peaks, weighted by a sensitivity factor, as described in section 2.3.1. The estimation results in a Sr:Bi:O ratio of  $21:26:52 \pm 5\%$  [167]. This is within a reasonable margin of uncertainty for XPS quantification of stoichiometric SBO. This is also in good agreement with previous XPS measurements performed on stoichiometric bismuthates [139] [166].

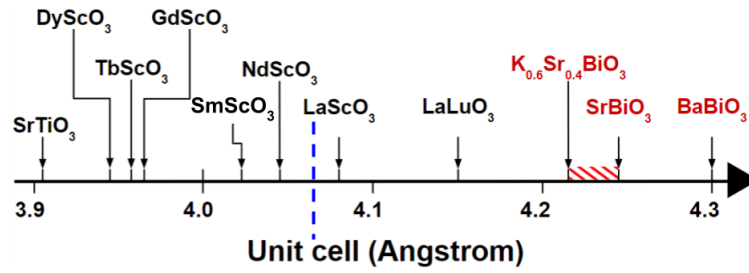


**Figure 3.7:** Available substrate to induce epitaxial strain on SBO. The blue dashed line delimits the theoretical limit from which SBO should be sufficiently strained to undergo a phase transition to a non-centrosymmetric ferroelectric phase.

### 3.2.6 SBO strain state on STO

This far, we have been discussing the growth of SBO thin films, regardless of their strain state. The out-of-plane lattice parameter of our optimised thin films grown on STO can be computed to be  $4.26 \text{ \AA}$ , from the symmetric XRD scan presented on panel (b) of figure 3.3. This is in good agreement with previously reported values for the lattice parameter of SBO [141] [116]. From the *in-situ* RHEED intensity signal, we can compute the in-plane lattice parameter of the SBO thin film grown on STO. A RHEED intensity pattern acquired on such films is presented on figure 3.6. We deduce an in-plane lattice parameter of  $4.3 \text{ \AA}$ . This result was confirmed by RSM, as will be illustrated in the next section. This is rather surprising, as it implies that our SBO films grown on STO are subjected to tensile strain. To better understand this result, we decided to grow thin films on different substrates to try to induce different strain states.

## 3.3 Substrate study

To investigate epitaxial strain, we decided to use different growth substrates. The substrates available to us, as well as the strain value they would induce to SBO, are presented on figure 3.7.  $\text{NdScO}_3$  (NSO),  $\text{LaScO}_3$  and  $\text{LaLuO}_3$  (LLO) lie close to the critical strain value at which the SBO should theoretically undergo a strain driven phase transition.  $\text{NdScO}_3$  is commercially available (at Crystec).  $\text{LaLuO}_3$  is not commercially available but it was optimised as a buffer layer by Pauline Dufour during the course of her PhD [191]. However, it was not available to us during our growth optimisation. Characterisation of LLO/SBO heterostructures would make for an interesting follow up to the work presented in this study.

### 3.3.1 Strain state on different substrates

We grew SBO thin films on NSO and STO substrates and acquired symmetric scans and 2D reciprocal space maps of such films. The XRD spectra are presented on panels (c), (d) and (e) of figure 3.8. Using the methodology presented in section 2.3.2 we compute the in-plane and out-of-plane lattice parameters of the SBO thin films. The different lattice parameters are presented in table 3.1. The in-plane lattice parameter of thick ( $\sim 75 \text{ nm}$ ) SBO films varies with the growth substrate. SBO appears to grow relatively relaxed on NSO.

Surprisingly, on STO, we observe the onset of tensile strain. This goes against our predictions, as STO has a smaller lattice parameter compared to SBO.

Furthermore, AFM highlights a striking difference between these films. Thin films grown on NSO exhibit

**Table 3.1:** Lattice parameters of  $\text{SrBiO}_3$  grown on different substrates

Substrate	Expected compressive strain (%)	SBO $\perp$ lattice parameter ( $\text{\AA}$ )	SBO $\parallel$ lattice parameter ( $\text{\AA}$ )	Measured Strain
$\text{SrTiO}_3$	8.8	4.26	4.31	+1.2% (tensile)
$\text{NdScO}_3$	6.0	4.26	4.26	0% (none)

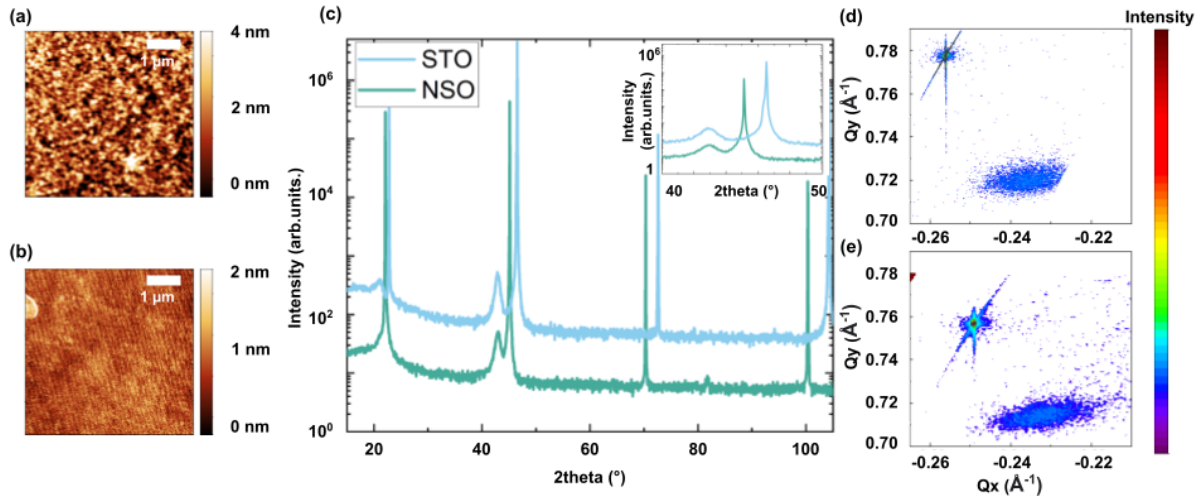


**Figure 3.8:** Effect of the substrate on the growth of SBO thin films: (a) and (b) AFM of the surface of the films grown on STO and NSO, respectively. (c) Symmetric XRD spectra of the films grown on STO and NSO. (d) and (e) Reciprocal space map of the (103) peak of SBO grown on STO and NSO, respectively. The spectra are characteristic of a single-phase perovskite.

atomic step features, characteristic of highly epitaxial thin films. Conversely, films based on STO are relatively flat, providing limited information about the epitaxial relationship between the film and its substrates. Nevertheless, this difference is notably distinct from what is observed on NSO [190]. This is highlighted on panels (a) and (b) of figure 3.8. To gain a deeper understanding of the epitaxial relationship between SBO and its various growth substrates, we conducted a detailed investigation of the different interfaces by STEM.

### 3.3.2 Scanning Transmission Electron Microscopy

An STEM image of an SBO film grown on STO is presented on figure 3.9. It appears the SBO is relaxing through two different mechanisms. The first strain relaxation mechanism lies in the formation of two interfacial rock-salt layers of SrO. Immediately above these two layers we observe the appearance of periodic dislocations. They form every 9/10 u.c. of SBO which will correspond to 10/11 u.c. of STO. Domain matching is conditioned by a perfect x to y lattice match. In our case, SBO has to accommodate some level of tensile strain to compensate for the domain matching mismatch. The 1.2% tensile strain measured by XRD in the case of STO/SBO results in  $\frac{a_{\text{film}}}{a_{\text{substrate}}}$  of 1.104, which lies right in between  $\frac{10}{9} = 1.110$  and  $\frac{11}{10} = 1.100$ . The tensile strain measured by XRD is coherent with the formation of misfit dislocations. These two relaxation

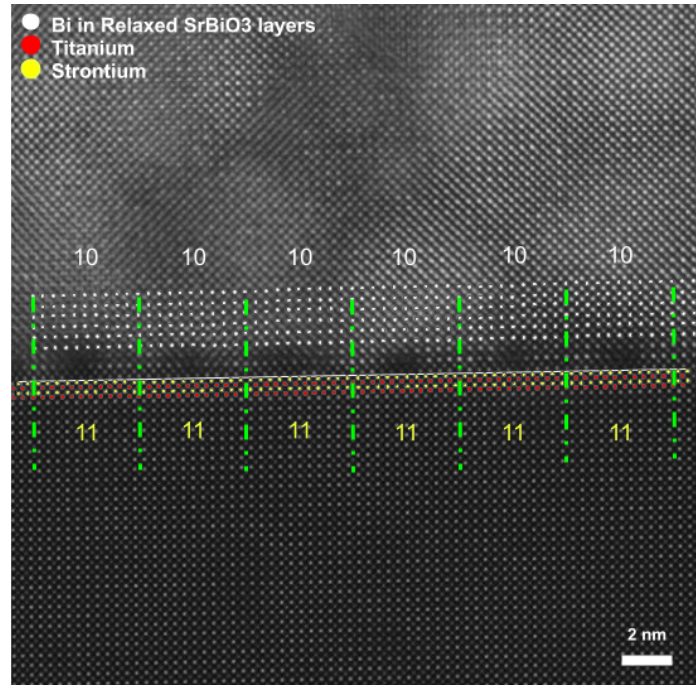


**Figure 3.9:** STEM HAADF image of an SBO thin film grown on STO.

mechanisms were similarly observed in BBO grown on STO [135] [139] [140]. It comes as no surprise that SBO behaves in a similar manner to its parent compound when grown in a similar fashion on a similar substrate.

An SBO thin film grown on NSO imaged by STEM is presented on figure 3.10. When compared to the STO/SBO sample, we notice a number of differences. First and foremost, there are no SrO buffer layers appearing at the interface between the NSO substrate and the SBO thin film. STO may favor the formation of such buffer layers, because STO itself is composed of alternating  $\text{TiO}_2$  and SrO atomic planes. In addition, we observe the formation of an interfacial, potentially strained, layer of perovskite  $\text{SrBiO}_3$ , above which dislocations form and relax the film. The interfacial slab is 3 to 5 layers thick. Using an homemade python code, which makes use of the atomap library [170], we track the position of each individual atom to extract the strain information.

### 3.3.2.1 Tetragonality and strain mapping

We define the tetragonality of a unit cell as

$$tetra = \frac{c}{a} \quad (3.1)$$

with  $c$  and  $a$  the out-of-plane and in-plane lattice parameter of a unit cell, respectively. Plotting tetragonality instead of strain is relevant as every variable necessary for the computation of tetragonality can be directly measured from an STEM image:  $a$  and  $c$  are the distance from an atom to its closest upper and right neighbours, respectively. Provided that the volume of a unit cell is conserved and the volume variation is small with respect to the volume of a unit cell (*i.e.* that strain values are small with respect to 1), the relationship between tetragonality and strain can be demonstrated to be linear. Indeed, strain is commonly defined as:

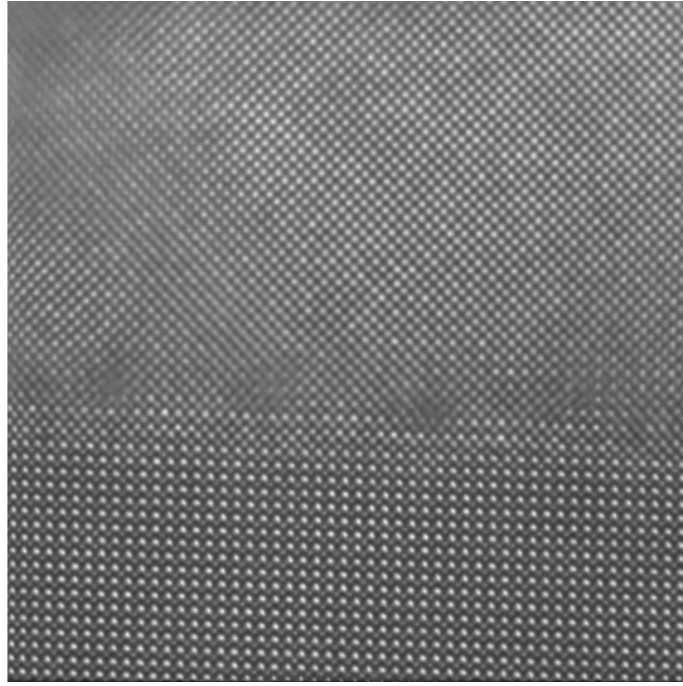


**Figure 3.10:** STEM HAADF image of an SBO thin film grown on NSO.

$$1 + \sigma = \frac{a_s}{a_0} \quad (3.2)$$

With  $\sigma$  the biaxial strain,  $a_s$  the strained unit cell parameter and  $a_0$  its unstrained value. Volume conservation enforces that  $\frac{a_s^3}{a_0^3} = \frac{c}{a_s}$ . Provided that the elongation is small compared to the initial size of the unit cell, we can write:

$$1 - tetra \sim \frac{1}{3} * \sigma \quad (3.3)$$

Mapping  $1 - \frac{c}{a}$  is thus equivalent, in first approximation, to mapping the strain.

Tetragonality maps of both samples are presented on figure 3.11 and 3.12. As expected, tetragonality on the sample grown on STO is uniform except close to the interface. It appears to be rather high at the interface. As aforementioned, two rocksalt layers of SrO form at the interface in the same way it does in BBO [135] [139]. These layers are coinciding exactly with the zone of high tetragonality. The "relaxation region", composed of the two rocksalt layers of SrO and the dislocation layers, is highlighted in purple in both the ADF image and in the lattice parameters vs depths panel (panels (a) and (b) of figure 3.11). The SBO above this region is subjected to a uniform level of tensile strain over the whole depth imaged. This is indicated by the in-plane lattice parameter being uniformly bigger than the out-of-plane lattice parameter. It is highlighted on panels (b) and (c) of figure 3.12.

The FFT presented on panel (d) of figure 3.11 further highlights that SBO grows almost cubic on STO. We can see that the (001) and (100)s axis of both crystals are perfectly aligned (the (100) and (001) axis are interchangeable). A zoom on the (101) axis should highlight that the (101)s peaks of SBO lie slightly out of the axis due to the tensile strain. However, the shift is extremely small and can barely be seen. Nonetheless, the tensile strain nature of this sample makes no doubt, as highlighted by panels (b) and (c).

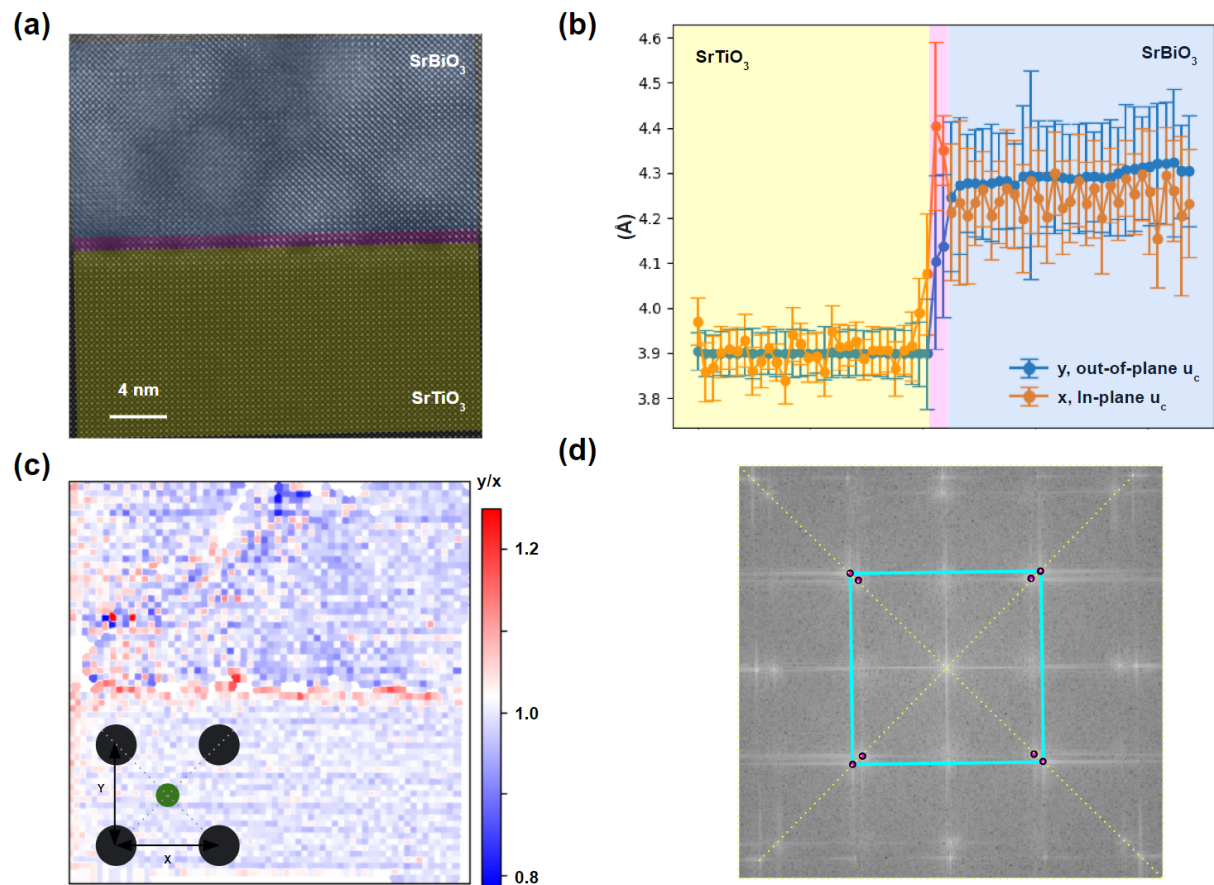


**Figure 3.11:** STEM analysis of a STO/SBO thin film. (a) ADF image of the sample, (b) Evolution of the lattice parameter as a function of the depth. The yellow highlighted region corresponds to the STO substrate and the blue region to SBO. The purple region contains the two rocksalt SrO layers as well as two layers in which the average lattice parameter is harder to define due to the formation of periodic dislocations. (c) tetragonality map of the sample. From both (b) and (c) we deduce that tetragonality is uniform in SBO, with  $c/a < 1$ . This further confirms the tensile strained nature of the film. (d) Fast Fourier Transform of the ADF image.

On NSO, the story changes completely. We observe the appearance of regions presenting a highly tetragonal character. Most of these regions are mainly located close to the interface with the substrate, right below the dislocations. Additional clusters of tetragonal regions are appearing on the leftmost part of the image presented on panel (a) of figure 3.12. The tetragonal interfacial region corresponds to the area highlighted in green on panels (a) and (b) of figure 3.12. In addition, interestingly enough, the SBO thin film is not cubic. This is highlighted by the fact that the FFT signal of the SBO thin film (in orange) is not square, though the one of NSO is (in light blue). The (110) axis of SBO, however, does perfectly align with the (001) pseudo-cubic axis of (110)<sub>o</sub> NSO.

The appearance of strained, non-cubic, regions in a matrix of cubic SBO constitutes an encouraging observation. The unit cells located closer to the interface with NSO are strained to the substrate, which accounts for a strain level of 4.99%. According to DFT computations<sup>[90]</sup>, such a level of strain should be sufficient to turn SBO into a ferroelectric. Thin enough SBO films could thus be ferroelectric. This presupposes that a good enough electrode can be grown on NSO, in order to have SBO reproduce the behavior observed on NSO. The growth of adequate electrodes will be discussed in the next chapter of this manuscript. The strained region appears to be 3 to 5 unit cells thick, as demonstrated by the unit cell parameters as a function of depths profiles presented on panel (b) of figure 3.12.

## 3.4 Conclusion

To conclude, growth of candidate FERSC  $\text{SrBiO}_3$  on different substrates was optimised. After characterising our thin films by XRD, XPS, AFM and TEM we conclude that crystalline  $\text{SrBiO}_3$  was grown with some level of tensile strain on  $\text{SrTiO}_3$ . It may serve as a negative test to probe ferroelectricity in bismuthates. Relaxed  $\text{SrBiO}_3$  thin films were grown on  $\text{NdScO}_3$ . An intensive TEM study was carried out to better understand the relaxation mechanisms between SBO and its different growth substrates. This study highlighted the possible existence of a thin interfacial layer of SBO which may be subjected to compressive strain in the case of films grown on NSO. The next step in the investigation of ferroelectric rashba SBO is to investigate ferroelectricity in strained and unstrained  $\text{SrBiO}_3$  films. This, however, presupposes the growth optimisation of electrodes which have a good lattice mismatch with the different substrate.

In the next chapter, we will be looking at the growth optimisation of candidate electrodes that have a proper lattice match with SBO and the different substrates of interest. We will also be detailing the ferroelectric characterisation of SBO based hetero structures through the means of piezo force microscopy.

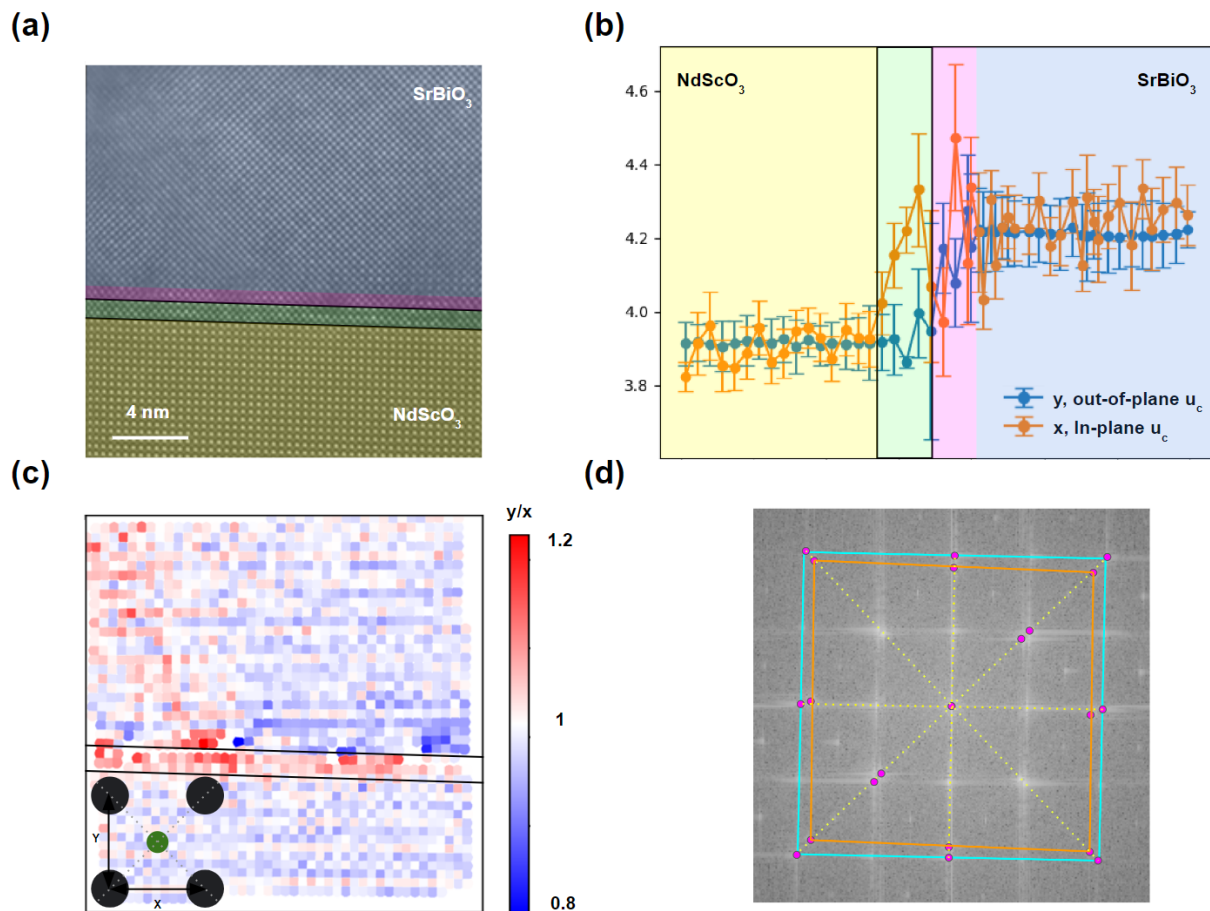


**Figure 3.12:** STEM analysis of a NSO/SBO thin film. (a) ADF image of the sample, (b) Evolution of the lattice parameter as a function of the depth. The yellow highlighted region corresponds to the NSO substrate and the blue region to SBO. In the region in green, the in-plane lattice parameter is constrained to the one of the substrate. The volume of the unit cell as a function of depth is non homogeneous. In the purple region, the apparition of dislocations relaxes the stress. (c) tetragonality map of the sample. The interface layers are subjected to some strain, which can also be observed on the left of the image. The two hard lines delimit the green highlighted region aforementioned. (d) Fast Fourier Transform of the ADF image.



# Chapter 4

## Ferroelectricity in $\text{SrBiO}_3$

### 4.1 Electrodes optimisation for the growth of ferroelectric SBO

In order to probe ferroelectricity by PFM, a bottom electrode has to be introduced in between the substrate and the thin film. Due to the huge lattice parameter of SBO, electrodes satisfying our needs are scarce. We identified two candidate electrodes:  $\text{Ba}_x\text{Sr}_{1-x}\text{RuO}_3$  and  $\text{La}_x\text{Ba}_{1-x}\text{SnO}_3$ . In this section we will be giving a quick overview of the literature and the growth optimisation of both of these electrodes.

#### 4.1.1 $\text{Ba}_x\text{Sr}_{1-x}\text{RuO}_3$

##### Generalities

The metal-oxide perovskite  $\text{SrRuO}_3$  has been extensively studied in the past 50 years. It presents a number of exotic properties, which we will not detail here but have been extensively reviewed in the literature [192] [193]. By far, its most dominant use is as the prototypical electrode for the elaboration of epitaxial oxide heterostructures. There are several reasons that makes it the predominantly used oxide electrode. First, it has a good lattice match with a variety of complex oxide (its pseudocubic lattice parameter is  $a_{\text{SRO}} = 3.93 \text{ \AA}$ ) including STO, which is often used as a growth substrate. In addition, it has high chemical stability and follows a nearly perfect step-flow growth mode over a wide range of growth conditions [192]. In the framework of this thesis, the thin film we want to interface with an electrode has a relatively large lattice mismatch with SRO (7.7 %). In order to lower the lattice mismatch, SRO is commonly doped with barium on the A site of the perovskite structure.  $\text{Ba}_{0.5}\text{Sr}_{0.5}\text{RuO}_3$  (BSRO) has a lattice parameter of  $3.97 \text{ \AA}$  (6.6% mismatch with SBO) [194].

##### Experimental

The growth optimisation of BSRO was optimised starting from the growth conditions of SRO [191]. The BSRO electrode used in the framework of this thesis was grown in the TURF PLD set-up at  $720 \text{ }^\circ\text{C}$ , with a frequency of 2 Hz, a fluency of  $1.8 \text{ J cm}^{-2}$  and under an oxygen background pressure of 0.16 mbar (120 mTorr). Under these conditions, BSRO grows epitaxially under a layer by layer growth mode, as illustrated by the RHEED intensity pattern at the end of growth and the RHEED versus time plot, both depicted on panels (a) and (b) of figure 4.1

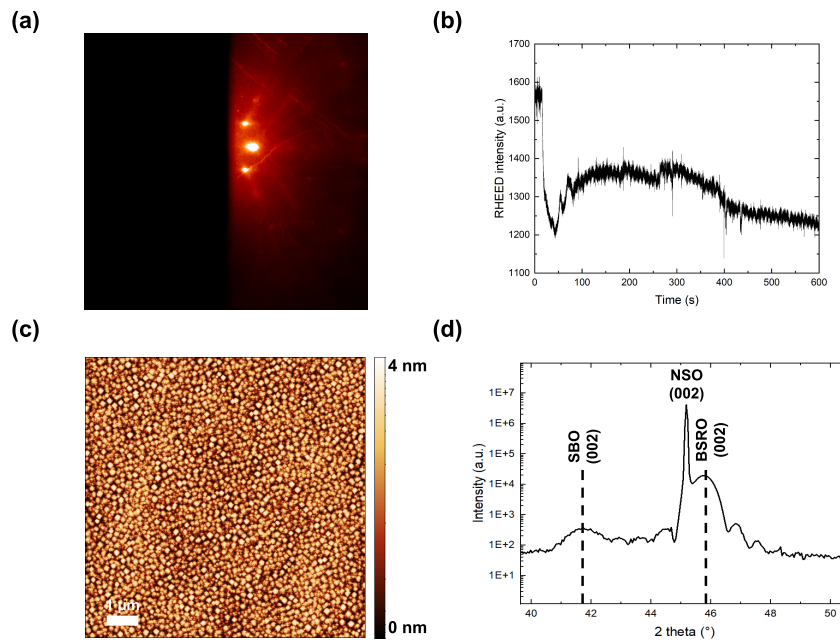


**Figure 4.1:** BSRO electrode grown on NSO (a) RHEED signal acquired on a BSRO thin film at the end of growth, and (b) RHEED vs time signal acquired during the growth of a BSRO thin film. The film grows perfectly 2D with a growth rate  $\sim 8$  pulses per layer, (c) AFM image of a BSRO electrode. The electrode is flat with no particles nor islands. (d) XRD spectrum of a BSRO electrode grown on NSO. The SBO thin film was grown ex-situ and will be discussed later.

#### 4.1.2 $\text{La}_x\text{Ba}_{1-x}\text{SnO}_3$

Transparent Conductive Oxides (TCOs) are in increasing demand in the burgeoning field of opto-electronics. Sn-doped  $\text{In}_2\text{O}_3$  (ITO) has been thoroughly studied in the last decade due to its transparency and high conductivity [195] [196]. However, indium shortages are pushing the field to develop indium free materials. In addition, a TCO perovskite could have the added benefits of high interfaciability with other functional perovskite, e.g. a light harvesting perovskite in the case of solar cells. In this framework, La-doped  $\text{BaSnO}_3$  has received a lot of interest due to its high mobility at room temperature, its transparency and its chemical stability [197] [198].

##### Generalities

$\text{BaSnO}_3$  is a perovskite with lattice constant  $4.11 \text{ \AA}$  [195] which can be doped with lanthanum. The partial replacement of  $\text{Ba}^{2+}$  atoms with  $\text{La}^{3+}$  atoms modifies the average charge of the Sn-sites. This has the effect of changing the Fermi energy from the top of the highly dispersive p-oxygen band, which is located at the valence band minimum, to the hybridised Sn-O s-p bands which are contributing to conduction [199]. It has a carrier concentration of  $\sim 10^{20}$ - $10^{21} \text{ cm}^{-3}$  [200]. This is relatively low compared to other perovskite electrodes such as  $\text{SrRuO}_3$  or  $\text{LaNiO}_3$  which have carrier concentrations in the range of  $10^{22} \text{ cm}^{-3}$  [192] [201]. Its main perks lies in its optical properties and its compatibility with large perovskite, as it is one of the only perovskite electrode with lattice parameter  $> 4.1 \text{ \AA}$ .

We note that  $\text{BaPbO}_3$  is another metallic oxide perovskite candidate, but it has to be grown in a lead dedicated chamber and its growth has not yet been reported. This material is beyond the scope of the research presented in this work.

##### Experimental

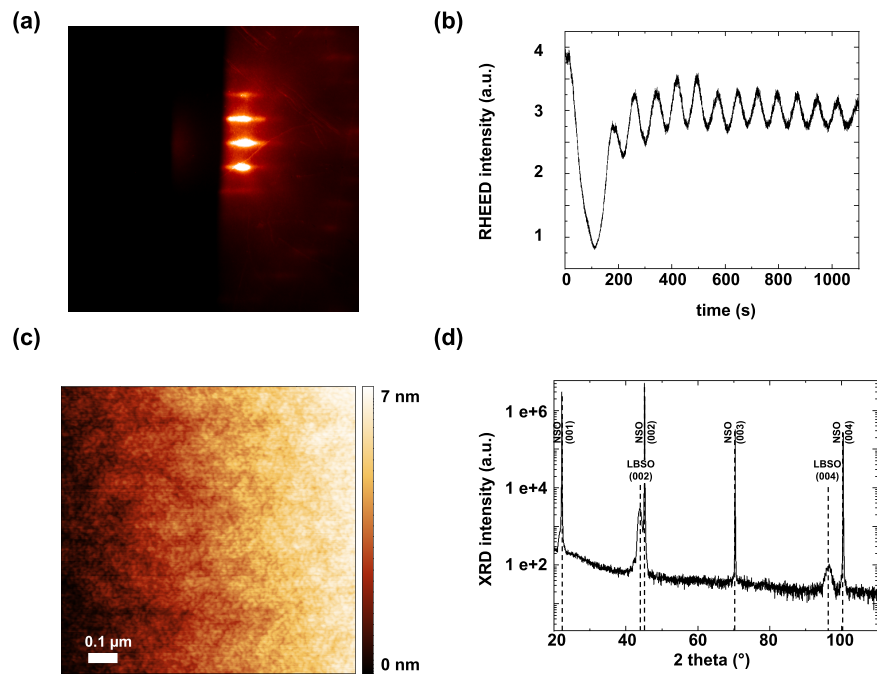


**Figure 4.2:** LBSO electrode grown on NSO (a) RHEED signal acquired on an LBSO thin film at the end of growth, and (b) RHEED vs time signal acquired during the growth of an LBSO thin film. The film grows perfectly 2D with a growth rate  $\sim 60$  pulses per layer, (c) AFM image of an LBSO electrode. The electrode is perfectly flat with no particles nor islands. (d) XRD spectrum of an LBSO electrode grown on NSO.

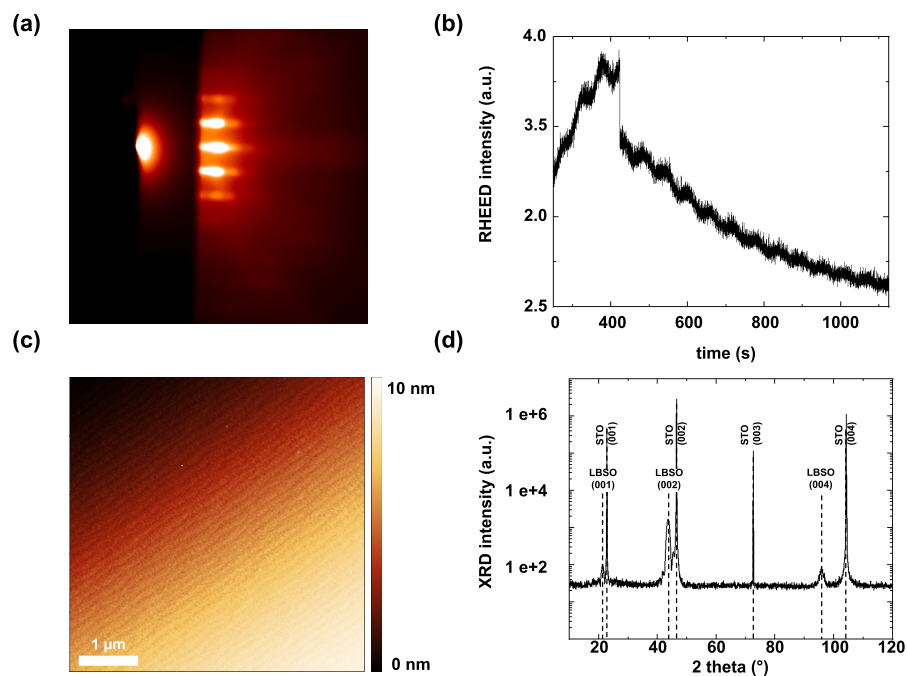


**Figure 4.3:** LBSO electrode grown on STO (a) RHEED signal acquired on an LBSO thin film at the end of growth, and (b) RHEED vs time signal acquired during the growth of an LBSO thin film. The film grows perfectly 2D with a growth rate  $\sim 60$  pulses per layer, (c) AFM image of an LBSO electrode. The electrode is perfectly flat with no particles nor islands. (d) XRD spectrum of an LBSO electrode grown on STO.

A stoichiometric target of  $\text{La}_{0.07}\text{Ba}_{0.93}\text{SnO}_3$  (Toshiba, purity 99.99 %) was used for the PLD growth with a KrF laser (Coherent, 25 ns). The distance between the target and substrate was kept constant at 50 mm. A repetition rate of 1 Hz was used. LBSO was previously optimised, in the same PLD chamber in which we optimised the growth of SBO, by Jun Wang during his P.h.D [200]. Due to a number of technical changes on the PLD optical path in between his growth optimisation and this work, growth conditions had to be re-optimised. Nonetheless, this served as a good starting point for the growth optimisation. LBSO electrodes were grown at 830°C and under a  $1.3 \cdot 10^{-1}$  mbar oxygen background pressure. The spotsize was kept at 0.589 mm<sup>2</sup>. Increasing the fluency from  $1.3 \text{ J cm}^{-2}$  to  $1.6 \text{ J cm}^{-2}$  with respect to the previously optimised growth conditions greatly improved the morphology of the electrode surface. LBSO electrodes were grown on NSO and STO and characterisation of such electrodes are presented on figure 4.2 and 4.3. Electrodes are epitaxial and partially strained. Strain relaxes as thickness increases, as highlighted by the lattice parameters computed on table 4.1. The lattice parameters computed are in good agreement with the literature [202] [200]. LBSO electrodes grown on STO are of exceptionally good crystalline quality, as highlighted by the presence of Laue fringes in the XRD spectra and by the atomic steps features that can be observed by AFM.

We note that due to some technical issues, halfway through the course of this work the morphology of the LBSO electrodes grown on NSO deviated from the one presented on panel (a) of figure 4.2. The apparition of island was then reproduced onto the subsequent layers, *i.e.* SBO and STO, and altered the properties of the heterostructure. More details about these issues and the different leads that were investigated to solve said issues are presented in appendix . These issues were a hassle towards further characterisation of ferroelectric SBO, as will be discussed in an upcoming section.

## 4.2 Ferroelectricity in $\text{SrBiO}_3$

### 4.2.1 $\text{SrBiO}_3$ electrical properties

In order to probe ferroelectricity in SBO, it needs to be insulating. Two probe electrical measurements indicated that SBO grown on NSO and STO substrates is indeed insulating. In addition, we used Nb-STO (0.5 % doping) as a back electrode substrate to probe the electric properties of SBO without the need to grow a bottom electrode. Nb-STO substrates were prepared in a similar fashion as STO substrates (see section 2.1).

A "thick" ( $\sim 70$  nm) film of SBO was grown on the Nb-STO substrates by using the optimised growth procedure for the growth of SBO on STO, as described in chapter 3. XRD of such a sample is presented on panel (a) of figure 4.4. Panels (b) presents conductive AFM scans of one of this samples. Surface conductivity was acquired using a custom conductive-tip AFM set-up, with a platinum tip, and under negative bias. We observe an insulating behavior from the SBO slab down to the Nb-STO substrate, with no current leaks, demonstrating the insulating nature of the SBO thin films. We retrieve a conductive signal after digging through the  $\sim 70$  nm of SBO (by applying a strong pressure with the AFM tip), as illustrated by panels (c), (d) and (e).

Having demonstrated the growth of conductive electrodes with adequate lattice mismatch with SBO, as well as the insulating nature of the SBO thin films, we proceeded to investigate the ferroelectric properties of SBO.

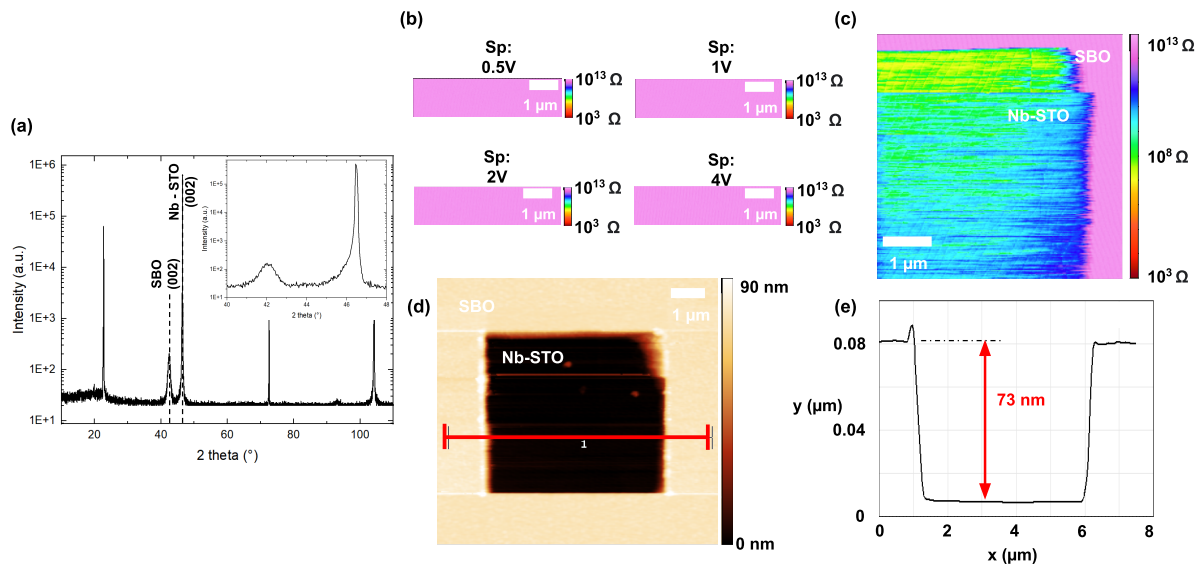


**Figure 4.4:** Electrical properties of  $\text{SrBiO}_3$ . (a) XRD spectrum confirming the growth of perovskite SBO on the Nb-STO substrates. (b) AFM scan on different areas of the sample and under different bias. The sample is insulating under all conditions. (c), (d) and (e): after digging through the insulating SBO we contact the cAFM tip to the substrate, confirming the insulating nature of the SBO thin film and the conductive nature of the Nb-STO substrates.

#### 4.2.2 $(\text{SrTiO}_3)_{(8)}/\text{SrBiO}_3/\text{Ba}_{0.5}\text{Sr}_{0.5}\text{RuO}_3/\text{NdScO}_3$

A thin film of  $\text{SrBiO}_3$  was grown on the  $\text{Ba}_{0.5}\text{Sr}_{0.5}\text{RuO}_3$  electrode. As aforementioned, the growth of the BSRO electrode was optimised at laboratoire Albert Fert whereas the growth of SBO was optimised at IMS. The electrodes thus had to be transferred from one chamber to the other in between the growths of the two films. XRD and AFM characterisations of such an heterostructure are presented on panels (a) and (b) figure 4.5. Due to the large lattice mismatch between BSRO and SBO, SBO grows with some level of tensile strain on the BSRO electrode. The in-plane and out-of-plane lattice parameters extracted from the symmetric scans and the reciprocal space maps are given in table 4.1. We note that the volume of a unit cell of SBO ( $V_{\text{cell}} = a_{\perp} * a_{\parallel}^2$ ) is larger than that of a film directly grown on the STO substrate, which is indicative of a worse crystal quality.

Such a sample was probed by PFM at laboratoire Albert Fert. As highlighted by panels (d), (e) and (f) of figure 4.5, it does not present any piezoelectric behavior, and by extension we determine it is not ferroelectric. Theoretical works and literature predict that SBO subjected to either tensile or no strain is an insulating paraelectric [116] [90]. Hence, we conclude the the PFM measurements presented here are in good accordance with the predictions.

#### 4.2.3 $(\text{SrTiO}_3)_{(8)}/\text{SrBiO}_3/\text{La}_{0.07}\text{Ba}_{0.97}\text{SnO}_3/\text{substrate}$

SBO thin films were grown *in-situ* on the LBSO electrodes aforementioned. Structural characterisations by XRD and AFM of such heterostructures are presented on figure 4.6. We note that despite the very nice morphology of the LBSO electrodes, SBO thin films grown on top of LBSO electrodes are by far less stable

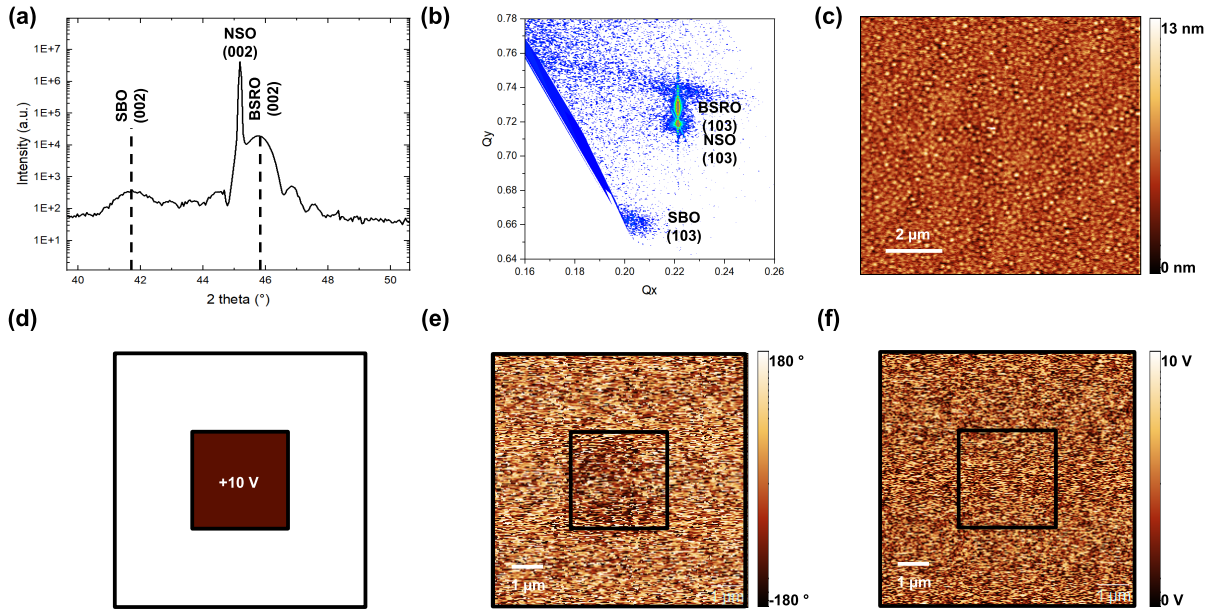


**Figure 4.5:** Characterisation of an  $(\text{SrTiO}_3)_8/\text{SrBiO}_3/\text{Ba}_{0.5}\text{Sr}_{0.5}\text{RuO}_3/\text{NdScO}_3$  heterostructure (a) XRD spectrum of the heterostructure and (b) Reciprocal space map acquired around the (103) peak of SBO. (c) AFM of the surface of the heterostructure. (d) writing mask used during the PFM experiment, and (e) the phase and (f) intensity images acquired by PFM after writing.

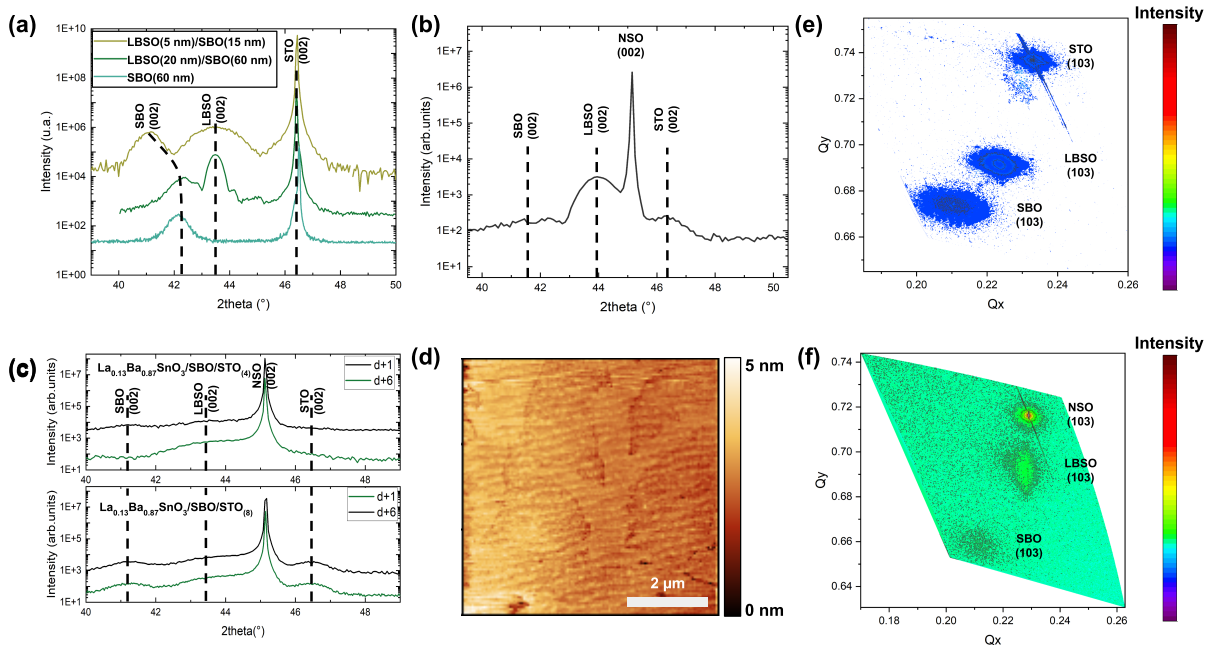


**Figure 4.6:** SBO growth on the LBSO electrode. (a) XRD spectra of  $\text{STO}_8/\text{SBO}/\text{LBSO}/\text{STO}$  thin films; (b) XRD spectrum of  $\text{STO}_8/\text{SBO}/\text{LBSO}/\text{NSO}$  sample, (c) demonstration of the need of a thicker STO capping, (d) AFM scan of a  $\text{STO}_8/\text{SBO}/\text{LBSO}/\text{NSO}$  sample, and RSM of the (103) peaks of (e) a  $\text{STO}_8/\text{SBO}/\text{LBSO}/\text{STO}$  sample and of (f) a  $\text{STO}_8/\text{SBO}/\text{LBSO}/\text{NSO}$  sample.

**Table 4.1:** Lattice parameters of  $\text{SrBiO}_3$  grown on different electrodes

Heterostructure	electrode $\perp$ ( $\text{\AA}$ )	electrode $//$ ( $\text{\AA}$ )	SBO $\perp$ ( $\text{\AA}$ )	SBO $//$ ( $\text{\AA}$ )	Measured Strain
SBO (60 nm)/LBSO (20 nm)/STO	4.13	4.07	4.25	4.25	0%
SBO (15 nm)/LBSO (5 nm)/NSO	4.15	4.02	4.32	4.27	-1.2%
SBO (15 nm)/BSRO (20 nm)/ NSO	3.96	4.01	4.31	4.34	+0.7%

than SBO thin films grown on either NSO or STO substrates. The origin of the weaker stability may stem from either a higher level of effective strain which may destabilise the thin film, a worse interface state, or interdiffusion of atoms at the electrode/film interface. Further STEM characterisation would have to be performed on these interfaces to better understand their relative instability when compared to the unconnected samples. To compensate for the destabilisation of the SBO thin films, the thickness of the STO capping layer had to be increased to no less than 8 units cells. Such a thick capping layer may be detrimental to the PFM measurements, as stoichiometric STO in its unstrained state is a paraelectric insulator with a dielectric constant of  $\sim 300$  [203]. As a result, it will absorb part of the applied electric field and dampen the relative deformation.

Interestingly enough, the asymmetrical nature of the SBO  $2\theta-\omega$  peak hints at some level of inhomogeneous strain in the film. The film peak asymmetry is more pronounced in these films than it was in film grown on NSO. In addition, the out-of-plane XRD peak is shifted towards lower angles when the electrode is grown thinner than 10 nm, as highlighted on panel (a) of figure 4.6. The lattice mismatch between SBO and LBSO is smaller than the one of SBO/NSO. This may result in a better interfacial strain state, *i.e.* less structural defects (such as dislocations) participating in strain relaxation. In addition, we note that the intensity of the (103) peak characteristic of SBO on the reciprocal space map of the heterostructure is weak, which is also strikingly different from what could be observed on samples without electrodes. We attribute this to some level of inhomogeneous strain state at the interface, thus resulting in a more diffuse XRD signal. From the analysis of the RSMs acquired around the (103) diffraction peaks of an SBO thin film grown on a relaxed LBSO (panel (e)) and on a strained LBSO electrode (panel (f)) we compute the in-plane and out-of-plane lattice parameters presented on table 4.1. The SBO thin film grown on a LBSO electrode with a rather large in-plane lattice parameter is unstrained (line 1 of table 4.1). On the contrary, the SBO thin film grown on a LBSO electrode presenting a higher level of strain seems to present some level of compressive strain. This is evidenced by the lattice parameters computed for the LBSO electrode and the SBO thin film in the case of the SBO (15 nm)/LBSO (5 nm)/NSO sample, presented on the second line of table 4.1. Finally, if the lattice mismatch between the thin film and the electrode is even more important, the strain eventually becomes tensile, as evidenced by the position of the (103) diffraction peak of the SBO thin film grown on a BSRO electrode. As discussed in chapter 3, this is indicative of the formation of misfit dislocations. Signs of compressive strain in SBO thin films are encouraging, especially considering that samples that were identified as fully relaxed by XRD were already determined to have an interfacial strained slab by STEM (see chapter 3).

We performed PFM measurements on such samples and the results of this experiment are presented of figure 4.7. We demonstrate that by applying a positive voltage of 10 V, we can induce, or write, "up" polarization domains, which can be switched to "down" polarization domains by applying a 5 V negative bias. From the intensity map, we observe that both domains have equal polarization amplitude. In addition, the amplitude goes to 0 V at the domains boundaries where domain walls appear. This is a good indication of the existence of two opposite polarization states fully switchable by the application of an electric field [204]. To confirm the ferroelectric nature of the heterostructure, piezo response polarization loops were acquired on

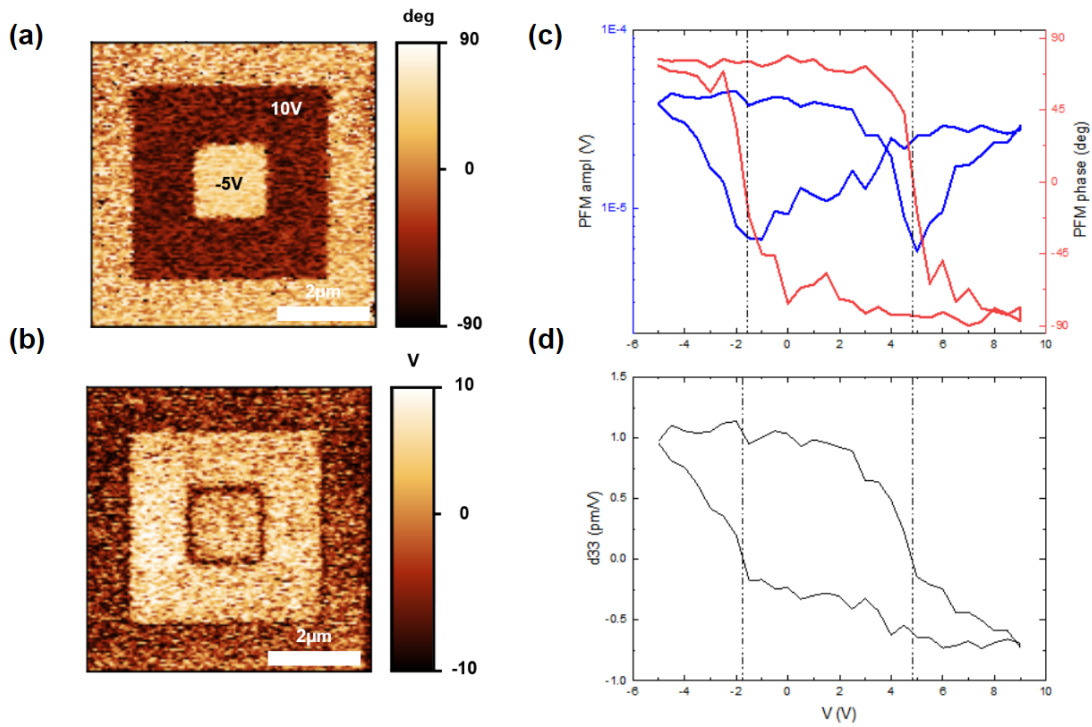


**Figure 4.7:** Ferroelectricity in NSO/LBSO/SBO/STO thin films. (a) phase and (b) amplitude mapping of the PFM signal after "writing" polarization states. (c) polarization hysteresis loop acquired by using the afm tip as a top electrode. We observe a ferroelectric behavior with a strong imprint. From the ferroelectric loop we deduce the (d)  $d_{33}$  parameter.

this sample. The PFM tip was used as the top electrode. The hysteresis loop presented on panel (c) are characteristic of a ferroelectric behavior with coercive voltages at -2 V and 5 V. The combination of the PFM images indicating polarization switching combined with the hysteretic polarization loops is indicative that the heterostructure is ferroelectric. However, we note that the stability over time of the polarization could be improved, as illustrated on panels (a) and (b) of figure 4.8. We expect this may be an effect of a combination of the relatively large imprint which can be observed in our sample and of the voltage amplitude necessary to "read" the ferroelectric state. Indeed, because the ferroelectric response coming from our samples is weak, we have to use a tip bias of 1.5 V peak to peak to read the ferroelectric domains we previously wrote. The coercive voltages being of -2 V and 5V, the read out is actively participating in the destruction of the written states. This reasoning is illustrated on panel (c) of figure 4.8. As will be further explained in the next section, we attribute the relatively small ferroelectric response coming from our sample to the co existence of a ferroelectric phase and a paraelectric phase which are probed at the same time by the PFM tip. This effectively results in a weak ferroelectric response. This line of reasoning is schematised on panel (d) of figure 4.8.

In this section, we highlighted the ferroelectric behavior of  $(\text{SrTiO}_3)_8/\text{SrBiO}_3/\text{La}_{0.07}\text{Ba}_{0.93}\text{SnO}_3/\text{NdScO}_3$  heterostructures grown on NSO substrates using a LBSO bottom electrode. In the next section, we will discuss the possible origins of ferroelectricity in such heterostructures.

### 4.3 Origin of ferroelectricity in $\text{STO}_8/\text{SBO}/\text{LBSO}/\text{NSO}$

When investigating the ferroelectric properties of an heterostructure, all layers are probed at the same time. As a result, a ferroelectric response coming from an heterostructure may be induced by one or multiple

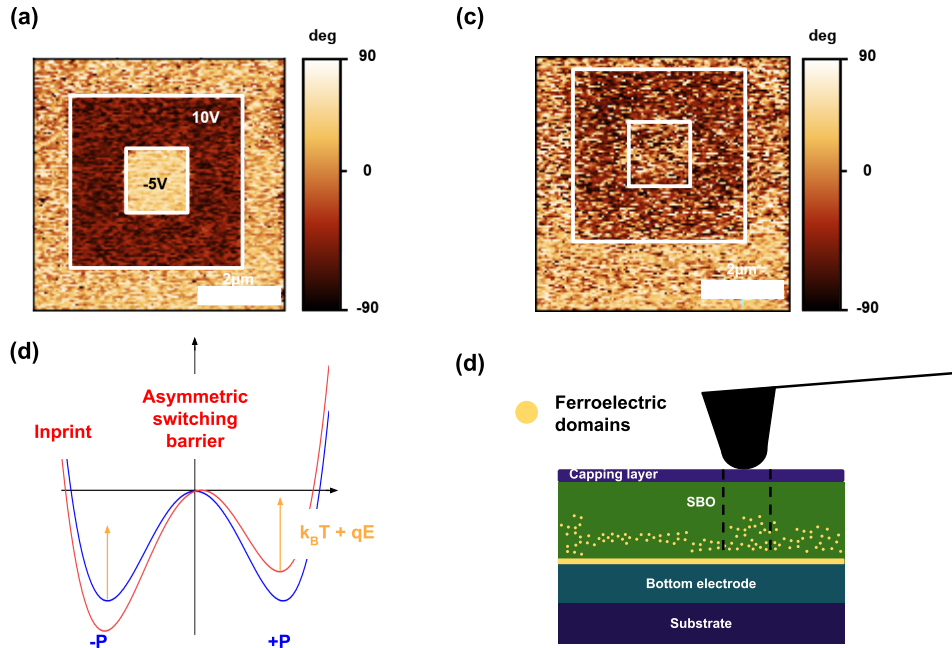


**Figure 4.8:** (a) PFM image acquired right after domain writing and (b) PFM image of the same zone acquired 16 hours later. (c) Schematic of the energy landscape of a ferroelectric with an imprint. The orange arrows represent the energy supplied to the ferroelectric system. (d) Schematic of a PFM experiment on an heterostructure presenting a mix of ferroelectric and non ferroelectric phases, the ferroelectric phases being smaller than the resolution of the PFM.

layers composing said heterostructure. In our case, LBSO is conducting at room temperature. Thus, the ferroelectric like response we observe can not come from this layer. It may hence originate from one or a combination of two possible sources: the STO capping layer, the SBO thin film, or both. Ferroelectricity at room temperature in  $\text{SrTiO}_3$  has been demonstrated by several groups. Tetragonal STO was demonstrated to be ferroelectric [205]. The formation of this particular STO crystal structure can be favored through the use of chemical or epitaxial strain, or by a 'wake-up' process [206]. In this study, owing to the lattice mismatch between SBO and STO, the strain applied to the STO thin capping film should be tensile. This might, according to literature, induce some level of in-plane polarization, but no out-of-plane polarization. Using XRD, we compute the lattice parameter of our STO capping film. As highlighted by panels (a) and (b) of figure 4.6, the peak attributed to the STO capping layer is perfectly overlapping with the STO substrate peak in the case of  $(\text{SrTiO}_3)_8/\text{SrBiO}_3/\text{La}_{0.07}\text{Ba}_{0.93}\text{SnO}_3/\text{NdScO}_3$  heterostructures. In addition, in the case of heterostructures grown on NSO, the (002) peak at  $46.46^\circ$  is characteristic of an unstrained STO thin film [206]. Hence, we confirm that our STO capping layer is unstrained. STO under these conditions is a well known paraelectric insulator [207]. As a result, we infer that the more likely scenario is that ferroelectricity comes from the SBO thin film. To further confirm this hypothesis, we speculate that fine analysis of the STEM images acquired of NSO/SBO stacks can help confirm the possible origin of this ferroelectric like behavior.

### 4.3.1 Probing polarization by STEM

The main requirement for ferroelectricity is the apparition of a polar displacements in the unit cell of the candidate ferroelectric. The polarization on an atomic scale can be deduced from HAADF images. In this section, we will be discussing the HAADF images of the  $\text{SrBiO}_3$  thin film grown on NSO we previously presented

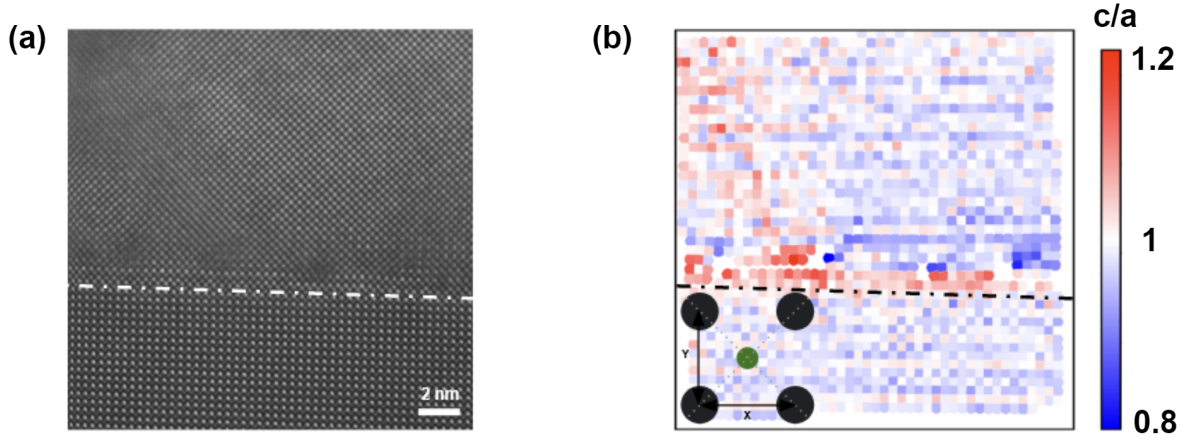


**Figure 4.9:** Tetragonality mapping of a NSO/SBO sample. (a) TEM image of a SBO thin film grown on NSO and (b) the tetragonality mapped on the image.

in chapter 3. The polarization in  $\text{SrBiO}_3$  is the result of the displacement of a bismuth atom with respect to the oxygen cage [104].

In principles, with high resolution TEM we should be able to image the rotations of the oxygen octahedra rotations using angular bright field images [208]. However, in our case we can locate the oxygens in the substrate and in the film far away from the interface, but not in the defect region. The reasons for this can be quite complex, ranging from thickness to high strain in these regions. As a result, probing the oxygen octahedra tilt and rotation at the interface is unfortunately not possible in our situation. Hence, to investigate the polarization, we decided to track the displacement of the strontium atoms with respect to the bismuth cage. Even though this displacement is not exactly equivalent to the polarization, as it is induced by the displacement of the anion octahedra with respect to the cationic cage, this is a commonly used method that gives a good indication of the polarization state of the material [?]. The movement of the B cation with respect to the A cations should be directly linked to the oxygen displacement with respect to the center of the cationic cage. To do so we identify all A cations in the HAADF image, subtract the lattice from the signal and identify the B atoms. We then create the matrix of the unit cells. An element of these matrix is a (5,1) vector composed of the position of an A atom,  $\mathbf{A}_0$ , the relative position of its closest neighbours along  $x$  and  $y$ ,  $\mathbf{A}_1$  and  $\mathbf{A}_2$ , respectively, and the relative position of the B atom which is at the center of the A cation cage,  $\mathbf{B}_0$ . We introduce  $\mathbf{A}_3$  and  $\mathbf{B}_{nopol}$  such that:

$$\mathbf{A}_0\mathbf{A}_3 = \mathbf{A}_0\mathbf{A}_1 + \mathbf{A}_0\mathbf{A}_2 \quad (4.1)$$

and

$$\mathbf{A}_0\mathbf{B}_{nopol} = \frac{1}{2}\mathbf{A}_0\mathbf{A}_3 \quad (4.2)$$

The polarization can then computed as:

$$P = \begin{pmatrix} (\mathbf{A}_0\mathbf{B}_0 - \mathbf{B}_{nopol}) \cdot \mathbf{A}_0\mathbf{A}_1 \\ (\mathbf{A}_0\mathbf{B}_0 - \mathbf{B}_{nopol}) \cdot \mathbf{A}_0\mathbf{A}_2 \end{pmatrix} \quad (4.3)$$

In this formalism, we can define the tetragonality as

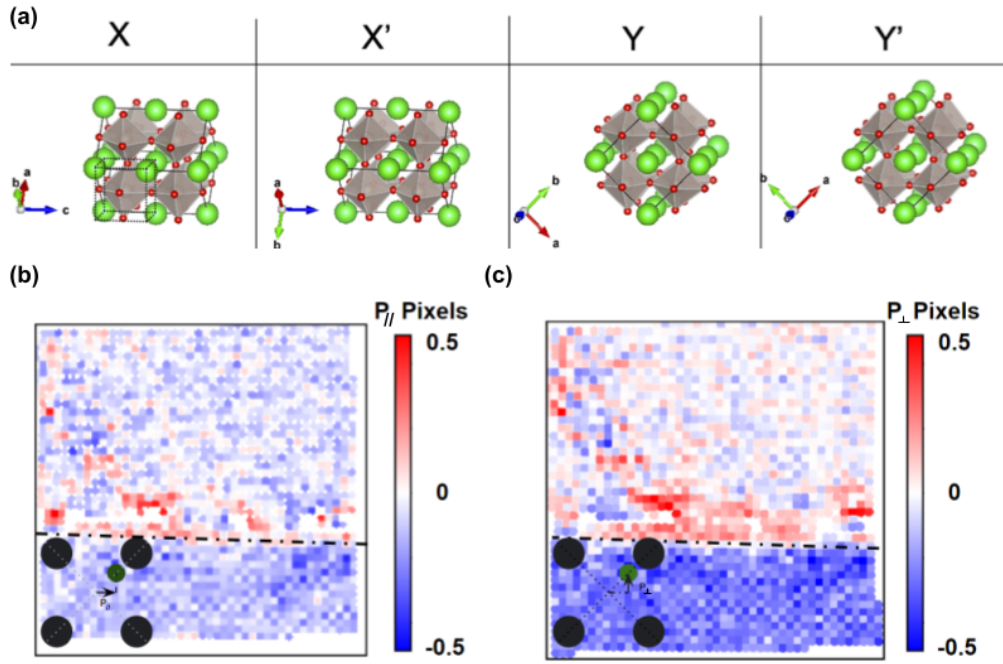


**Figure 4.10:** polarization mapping of a NSO/SBO sample. (a) schematic of the transformation from orthorhombic to cubic. The transformation induces a tilt of the octahedra which may appear as a uniform polarization on the TEM analysis. (b) the in-plane and (c) out-of-plane components of the polarization mapped on the TEM image.

$$tetra = \frac{\overline{A_0 A_2}}{\overline{A_0 A_1}} \quad (4.4)$$

The different variables are then mapped on the TEM image by attributing the values of the variables of a matrix to the position of the  $A_0$  atom. The tetragonality was enforced to be 1 on average in the NSO (110) substrate, as NSO along this direction is pseudo-cubic. On panel (b) of figure 4.9 we can observe tetragonality seems to deviate from unity close to the interface as well as in some zones located further away from the interface. However, further away from the interface most of the thin film seems to be cubic. From this analysis, we deduce the possible existence of an interfacial strained layer in which the onset of tetragonality could explain the existence of ferroelectricity in our heterostructures.

To confirm this hypothesis, we map the polarization on the TEM image. Panels (b) and (c) of figure 4.10 present maps of the in-plane and out-of-plane polarization at the interface of SBO and NSO. First, we note that the in-plane polarization is close to being uniform, except at the interface and in some zones in the leftmost part of the TEM image. Then, we note that the out-of-plane polarization is non-zero in the NSO substrate. This can be justified by the orthorhombic structure of NSO along its (001) axis. As illustrated by panel (a) of figure 4.10 the transformation from orthorhombic to pseudo-cubic results in a slightly tilted oxygen octahedra (configuration X and X') with respect to the Nd cation cage [209]. This appears as a net dipole value in the out-of-plane polarization map due to the definition we chose for the polarization. However, it does not physically result in a macroscopic polarization as the oxygen octahedra remains located at the center of the cationic cage.

We then note that the out-of-plane polarization appears to be non-zero in the SBO layers close to the interface, as well as in some zones located on the leftmost part of the TEM image. This non homogeneous onset of polarization regions could explain the weak ferroelectric behavior of our SBO samples. Provided that

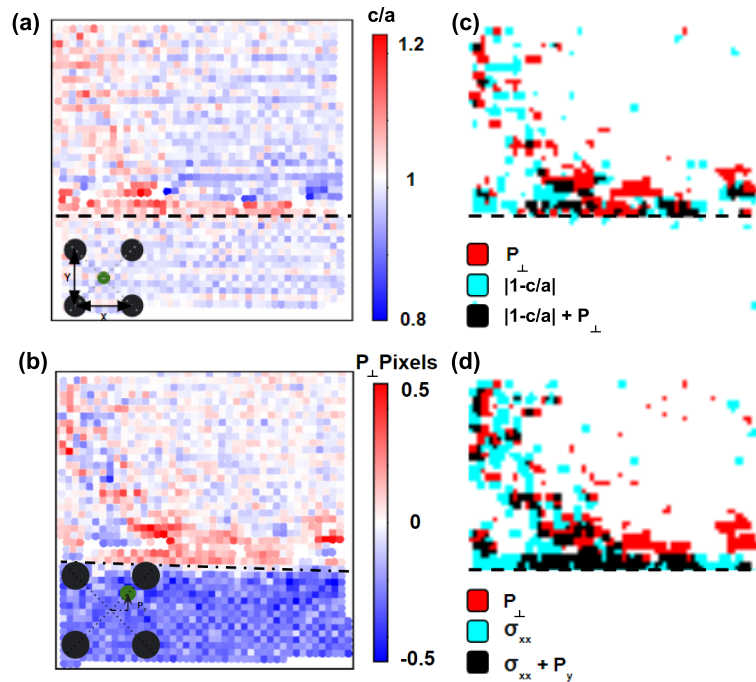


**Figure 4.11:** Correlation between the tetragonality and the strain. (a) tetragonality color map of SBO grown on NSO and (b) outward polarization map color map on the same sample. (c) superposition of the zone of high tetragonality and of high out-of-plane polarization. Regions are situated in the same vicinity but do not superpose perfectly and (d) same analysis done with in-plane strain and out-of-plane polarization.

the polarization regions can be switched, they only make part of the SBO matrix. The rest of the SBO matrix will act as paraelectric insulator. By scanning the sample with the PFM tip, we average vertically over the whole thickness of the sample and laterally over the width of the PFM tip. All in all, this result in a weak ferroelectric like behavior in PFM. This reasoning is schematised on panel (d) of figure 4.8

Looking at the tetragonality and polarization maps, it appears that the non zero polarization regions might be overlapping with the high tetragonality zones. If this is the case, it could be an indication that SBO undergoes a strain driven phase transition to a polar phase. This would confirm the theoretical predictions of J. Varignon[90]. Motivated by this observation, we investigate the correlation between the tetragonality and the polarization.

### 4.3.2 Correlations between tetragonality and polarization

Theory predicts that at tetragonality values close to unity, *i.e.* for strain values too weak to induce a phase transition, SBO should be non polar. For higher tetragonality values, which corresponds to higher strain values, we expect a positive correlation between tetragonality and polarization[90].

However, both variables appear to only be weakly correlated. We present the correlation map of both variables on figure 4.11. If we consider a small amount of tetragonality is not sufficient to induce a phase transition and only compute correlation for "strong-enough" tetragonality, we improve the correlation coefficient. Nonetheless, the correlation remains in the weak correlation range with a Pearson correlation coefficient of 0.478 at best. We bin and binarise both the tetragonality and the polarization norm to investigate their overlapping. Such an analysis is presented on figure 4.11. We observe that both variables are present in areas close to each other. However, the overlapping, presented in black, is tenuous. We conclude that the variables are only weakly correlated.

The results of the TEM analysis are not fully conclusive in identifying the origin of the ferroelectric behavior of our heterostructures. Another set of STEM experiments on samples including an electrode and a thick enough cap could have been of great help in identifying the mechanisms behind ferroelectricity in our samples. The differences observed by XRD highlight a clear difference between the connected and unconnected samples. The lattice parameters computed by using the RSMs points towards a stronger level of strain in SBO thin films grown on thin LBSO electrodes. However, owing to their relatively weak stability over time (the samples degrade over the course of a few months) the different samples on which ferroelectricity was observed could not be used for STEM imaging.

## 4.4 Conclusion

To conclude, we optimized the growth of two different electrodes to investigate the ferroelectric properties of SBO thin films.  $(\text{SrTiO}_3)_2/\text{SrBiO}_3/\text{Ba}_{0.05}\text{Sr}_{0.05}\text{RuO}_3/\text{NdScO}_3$  heterostructures did not present any ferroelectric properties, most probably because the strain state at the interface of SBO and the electrode was not important enough to induce a strain driven phase transition. In stark contrast,  $(\text{SrTiO}_3)_8/\text{SrBiO}_3/\text{La}_{0.07}\text{Ba}_{0.93}\text{SnO}_3/\text{NdScO}_3$  heterostructures were measured to present a weak ferroelectric like behavior by PFM. Further experimental investigations of such heterostructures were hindered by the relatively low stability over time of the thin films as well as technical issues related to the growth of the LBSO electrodes.

We tried to relate the onset of a ferroelectric behavior with the possible apparition of a strain driven phase transition to a non centro symmetric crystal structure in SBO. However, the study of TEM images of SBO grown on NSO is not fully conclusive in relating the apparition of polarization with the existence of a phase transition. Nonetheless, the clear observation of polarization dipoles as well as tetragonal regions at the interface of NSO and SBO is an encouraging feature in the search of ferroelectric properties in SBO, especially considering the overall unstrained nature of the SBO thin film, as per the XRD dataset. Further investigation by TEM of SBO interfaced with an LBSO electrode could help to determine whether or not an interfacial layer undergoes such a phase transition in the heterostructures in which SBO was determined to be ferroelectric.



# Chapter 5

## Development of heterostructures based on (Al,Sc)N

The approach we presented this far was focused on the homostructural approach to the ferroelectric control on the Rashba spin textures. In parallel, we chose to investigate an heterostructural approach to the ferroelectric control of the Rashba system.

The seminal discovery of the ferroelectric of the Wurtzites (Al,Sc)N family in 2019 by Fichtner *et al.* [146] is of great interest for the ferroelectric community. They constitute an interesting building block as per their exotic ferroelectric properties as well as per their CMOS compatibility. In this chapter, we present the growth optimisation by sputtering of (Al,Sc)N and preliminary results related to their integration in heterostructures of interest for the ferroelectric control of the Rashba effect. The work presented in this chapter was performed in close collaboration with Luis Vicente-Arche and Thomas Buttens.

### 5.1 (Al,Sc)N growth optimisation

### 5.2 Plasma stability

The first step of our sputtering a growth optimisation process was to stabilise the plasma of the different targets. Unlike argon, nitrogen is reactive. As a result, it is much more difficult to stabilise the plasma in a partial pressure of N<sub>2</sub>. Out of the two plasma we are using to grow (Al,Sc)N, the harder one to stabilise is the aluminium plasma. This is easily explained by looking at the work functions of aluminium (4.06-4.26 eV) and scandium (3.5 eV). In order to stabilise the plasma, we investigated two possible solutions: introducing a partial pressure of argon into the growth chamber, which might possibly cause nitrogen vacancies, or using the aluminium target with a RF source.

#### Al DC - Sc DC

With both targets driven by DC sources, the partial pressure of argon needs to be relatively high in order to stabilise the aluminium plasma. The pressure needs to be no lower than 1.2 Pa, with an argon flow of 17 sccm and a nitrogen flow no stronger than 3 sccm. Using these conditions we determine the deposition rates of scandium nitride and aluminium nitride by X-Ray reflectivity. The XRR spectra corresponding to a aluminium to scandium ratio of 0.7:0.3 are presented on panels (a) and (c) of figure 5.1. To achieve such condition, a

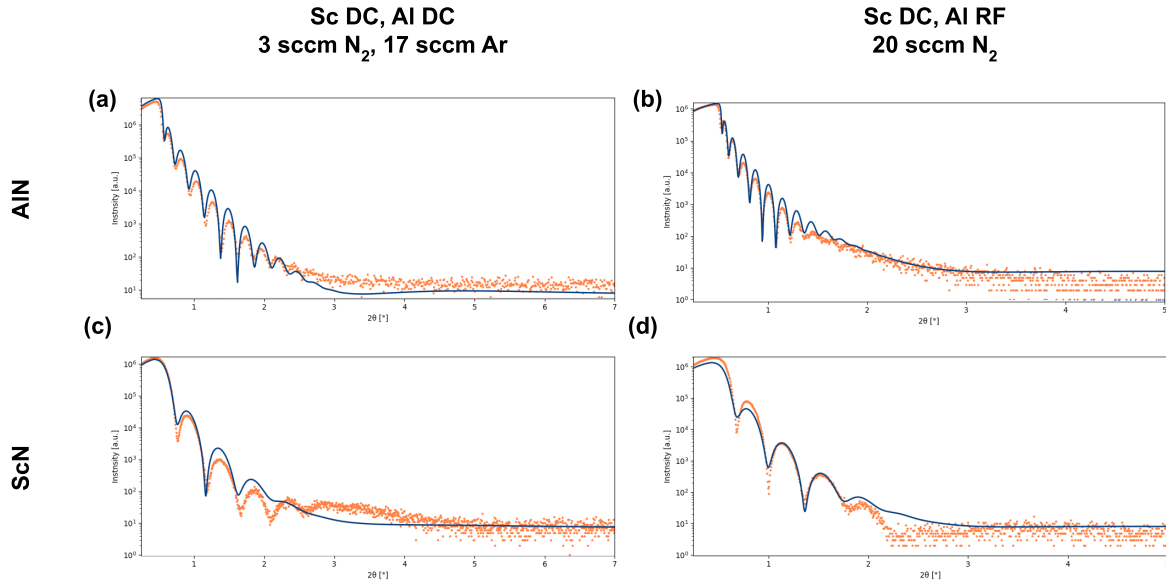


**Figure 5.1:** Growth optimisation of (Al,Sc)N: rates. Rates determined under different growth conditions.

current of 130 mA was passed through the aluminium source, while a current of 140 mA was applied to the scandium target.

We performed *in-situ* and *ex-situ* XPS measurements on pure AlN and ScN samples to investigate the chemical environment of the aluminium and scandium. The results of this study are presented on figures 5.2 and 5.3. After subtraction of a Shirley background, the peaks were fitted to a Gaussian-Lorentzian function, with a 70% Lorentzian character. The FWHM of the different peaks of a given element was enforced to be the same, and the ratio of the areas of the peaks was enforced to be 0.5 for Sc2p. First and foremost, the apparition of an oxygen peak is worrying. The samples are supposedly thick enough (> 50 nm thick samples were used in this study) to prevent any signal coming from the Si/SiO<sub>2</sub> substrate. In addition, the samples were directly transferred from the growth chamber to the XPS under high vacuum. Hence, they were never exposed to oxygen. The most likely scenario is that this oxygen signal comes from a thin layer of oxygen adsorbed at the surface. If this is the case, it in all likelihood happened during the XPS measurement. This hypothesis is further confirmed by the observation of the oxygen peak by other users. Oxygen apart, we do not observe any contamination. In addition, the peak positions are different from the peak position of their metallic counterparts which were grown under a pure argon atmosphere. The aluminium *in-situ* and *ex-situ* spectra present no difference, indicating that the aluminium fully reacted with the nitrogen to form aluminium nitride. In the case of Sc, the apparition of a scandium oxide shoulder peak in the *ex-situ* spectra indicates that the samples are reacting with the oxygen. To solve this issue, growth would have to be performed at higher nitrogen rates. However, the limitation imposed by the aluminium plasma stability makes it impossible to grow at higher nitrogen content. Hence, we decided to opt for another solution: we moved the aluminium target to the RF source.

#### Al RF - Sc DC

By using the RF source we managed to stabilise the plasma of the aluminium target with pressures no lower than 1.2 Pa, but under a pure nitrogen background pressure (20 sccm N<sub>2</sub>, no argon). Under such growth conditions, we redetermined the rates. The XRR spectra are presented on panels (b) and (d) of figure 5.1

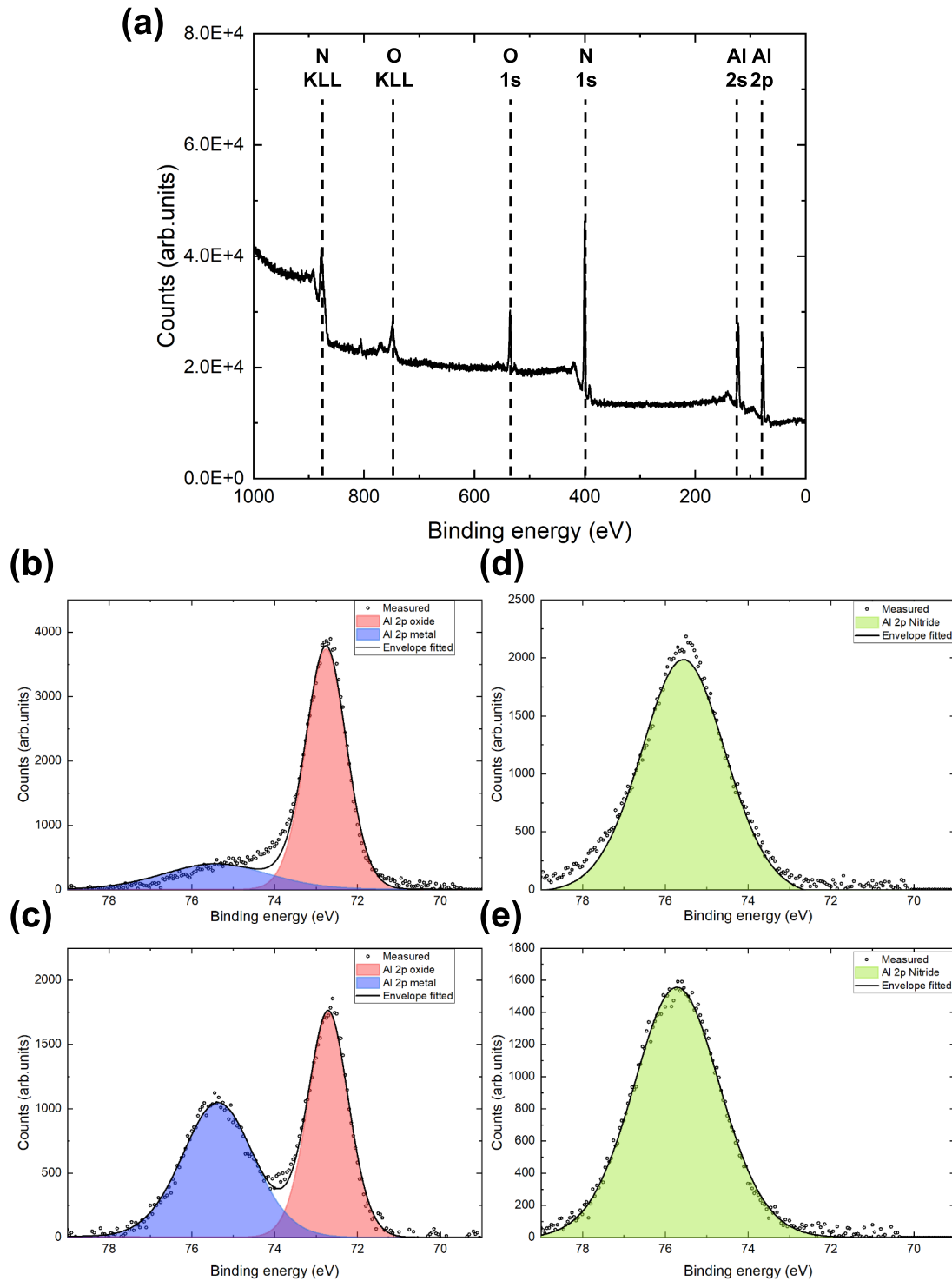


**Figure 5.2:** XPS study of aluminium based thin films grown in CONF (a) survey scan of an AlN samples. We note the presence of oxygen. (b) in-situ and (c) ex-situ aluminium thin film grown under a pure argon atmosphere. The in-situ sample presents two peaks corresponding to the purely metallic species and the sub-oxide species. The ex-situ sample also presents the two peaks, with a clear augmentation of the sub-oxide species with respect to the purely metallic species. XPS Al2p peak region of an (d) in-situ and (e) ex-situ aluminium thin film grown under a mixed atmosphere of nitrogen and argon. We observe that after exposing the thin film to the air the aluminium peak remains unchanged, indicating that aluminium fully reacted with the nitrogen.

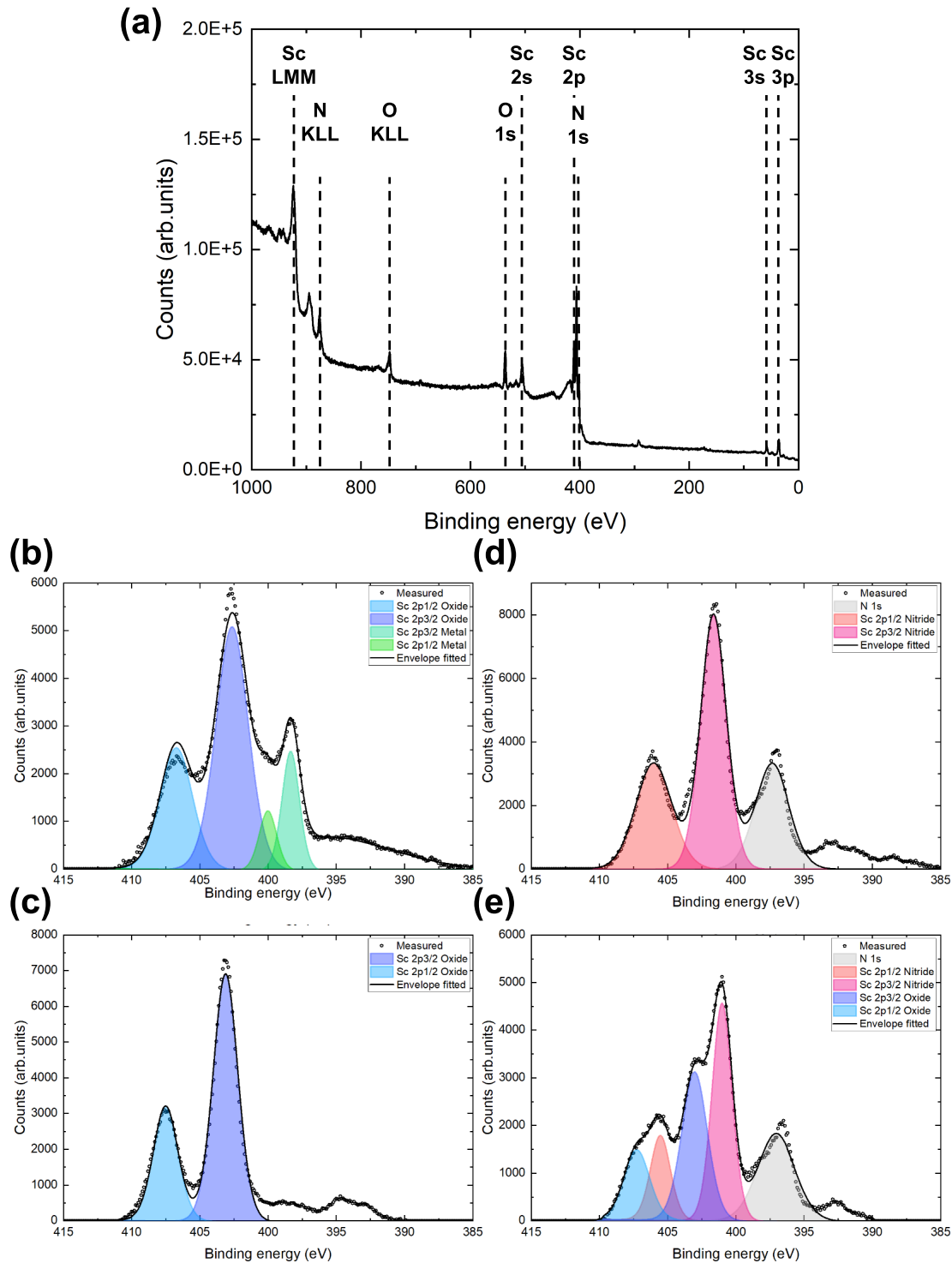


**Figure 5.3:** XPS study of scandium based thin films grown in CONF (a) survey scan of a ScN samples. We note the presence of oxygen. (b) in-situ and (c) ex-situ scandium thin film grown under a pure argon atmosphere. The in-situ sample presents two families of peaks corresponding to the purely metallic species and the suboxide species. The ex-situ sample is solely composed of oxidised scandium. XPS Sc2p peak region (d) in-situ and (e) ex-situ scandium thin film grown under a mixed atmosphere of nitrogen and argon. We note that the position of the N 1s peak hinder the observation of the metallic scandium peaks. However, we observe that after exposing the thin film to the air, some oxide sub-species appear, indicating that some scandium did not react with the nitrogen.

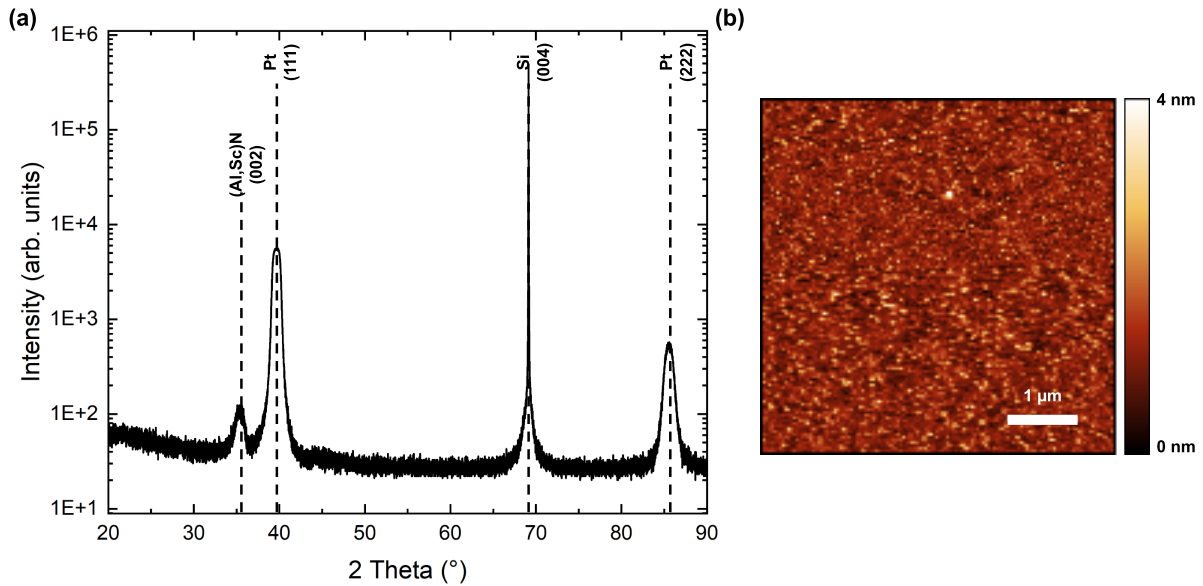


**Figure 5.4:** *Ex-situ* characterisation of (Al,Sc)N thin films (a) XRD spectrum acquired on a 150 nm thick Si/SiO<sub>2</sub>/Pt(111)/Al<sub>0.7</sub>Sc<sub>0.3</sub>N sample. The peak at 35.4 ° is characteristic of (Al,Sc)N. (b) AFM acquired on an (Al,Sc)N thin film grown on a 50 nm thick Si/SiO<sub>2</sub>/Pt(111)/Al<sub>0.7</sub>Sc<sub>0.3</sub>N sample.

Conveniently, we once again present the XRR spectra which will ultimately lead to a aluminium to scandium ratio of 0.7:0.3. On a final note, we considered reintroducing 25 % of argon during the growth, as the early reports on piezoelectrics seemed to report better out of plane orientation of the thin films with 25 % of argon with respect to growth under a full nitrogen atmosphere[143]. Other studies reported better ferroelectric properties when argon was kept out of the growth chamber[210]. Samples grown with and without 25 % argon were investigated by XRD. We concluded that not introducing argon was beneficial to grow samples with better crystal quality. To investigate the ferroelectric properties and to grow epitaxial oriented thin film of (Al,Sc)N, we grew *ex-situ* a 50 nm platinum (111) oriented bottom electrode. Using the conditions described in this paragraph at a temperature of 350 °C yields on such an electrode yields an epitaxial thin film, as indicated by the XRD spectra presented of figure 5.4. The peak at 35.4 ° is characteristic of an oriented (Al,Sc)N thin film. It is coherent with the literature for 30 % doped (Al,Sc)N thin film[211]. The XPS survey acquired on such sample was used to quantify the aluminium to scandium ratio which was computed to be Al:Sc of 71:29 ± 5 % [167].

The investigation presented in this section can be summarized by the following sample: a 150 nm Al<sub>0.7</sub>Sc<sub>0.3</sub>N thin film was grown on a Pt(111) electrode itself grown on Si/SiO<sub>2</sub>. The film was grown at 350°C, under a pressure of 1.2 Pa and with a pure nitrogen flow of 20 sccm, and was immediately capped *in-situ*. The top electrode will be discussed in the next section.

### 5.3 AlScN ferroelectric properties

To investigate the ferroelectric properties of such samples, we grew *ex-situ* a 50 nm platinum (111) oriented bottom electrode. In addition, a 20 nm top electrode of platinum was grown *in-situ*. The samples were then patterned by photo lithography to fabricate electrodes to permit the investigation of their ferroelectric properties by electrical measurements, as presented on section 2.3.5. The ferroelectric characterisation of a

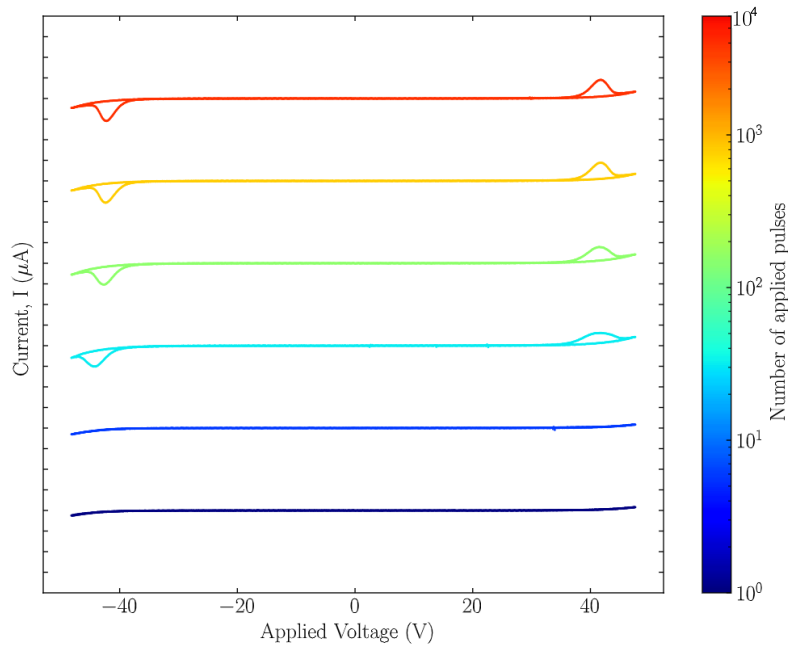


**Figure 5.5:** Endurance study of an 150 nm thick  $\text{Al}_{0.7}\text{Sc}_{0.3}\text{N}$  thin film. The thin film is ferroelectric after a wake-up process of  $\sim 40$  cycles. The maximum endurance supported by the films is of  $\sim 10^5$  cycles.

150 nm thick  $\text{Al}_{0.7}\text{Sc}_{0.3}\text{N}$  sample is presented on figure 5.5

The current loops presented in this manuscript were acquired on round electrodes with a diameter of 50  $\mu\text{m}$  by using a PUND measurement set-up, as previously described in section 2.3.4. First and foremost, we note that the very first current loops are flat, presenting no polarization switching features. The thin films need to be woken up, which is coherent with available reports regarding ferroelectric Wurtzites[31]. Next, after a wake up process of about 40 cycles, we observe the onset of polarization currents at -45 V and 45 V. These coercive voltages are in reasonable agreement with previously reported data for this specific composition and thickness[212]. In addition, we probe the endurance of our thin films. Up to  $10^4$  cycles we observe stable polarization states. The polarization loop is destroyed after cycling the sample  $10^5$  times. The wake-up effect, as well as the endurance supported by the film are in good agreement with the literature [31] [153]. Finally, we integrate the current loop to recover the full polarization hysteresis loop as presented on figure 5.6. We retrieve polarization values of  $\sim 130 \mu\text{C cm}^{-2}$ , which is on the high end of reported values[212].

To be compatible with practical applications, the switching voltage of the ferroelectric has to be reduced by one order of magnitude, in the range of some volts[19]. The key parameters to play with to reduce the voltage at which the polarisation switches are the thickness of the ferroelectric as well as the scandium doping content. As aforementioned, the scandium doping content both affects the height of the switching energy barrier (and thus the the values of the coercive fields[154]) as well as the value of the gap (and thus the appearance of leakage currents [213]). Our reasoning is that reducing the scandium content will increase the polarization switching voltages at a given thickness, but might be favorable in scaling the samples down as it might contribute to reducing the effect of leakage in thinner samples. This might ultimately result in lower coercive voltages. We demonstrate the effect of thickness lowering as a way to reduce the values of the coercive voltage. The electric characterisation of a 50 nm thick sample with  $\text{Al}_{0.7}\text{Sc}_{0.3}\text{N}$  composition is presented on figure 5.7. The 20 nm thick platinum top electrodes on which the measures were taken were patterned in the exact same manner as the ones on the 150 nm thick sample. The thin film is ferroelectric, with polarization values very similar to the ones of the thicker samples. The main striking difference lies in the values of the coercive fields:  $\pm 23$  V. However, the interesting value here is the coercive electric field

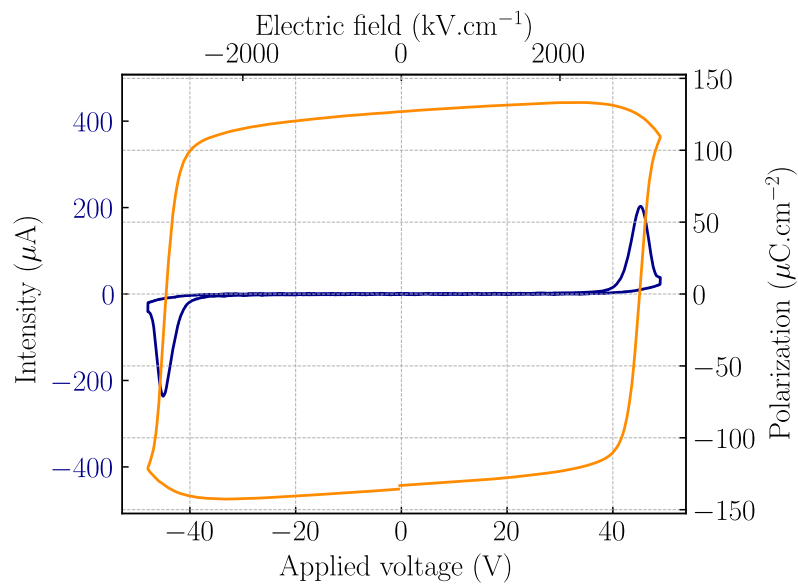


**Figure 5.6:** PUND sequence acquired on a 150 nm thick  $Al_{0.7}Sc_{0.3}N$  thin film. The current loop is presented in blue with the integrated value corresponding to the polarization presented in orange. The thin film is ferroelectric with coercive voltages at  $\pm 45V$ . The polarization inside the sample is of  $\sim 130 \mu C cm^{-2}$  which is on the higher end of values reported in the literature.

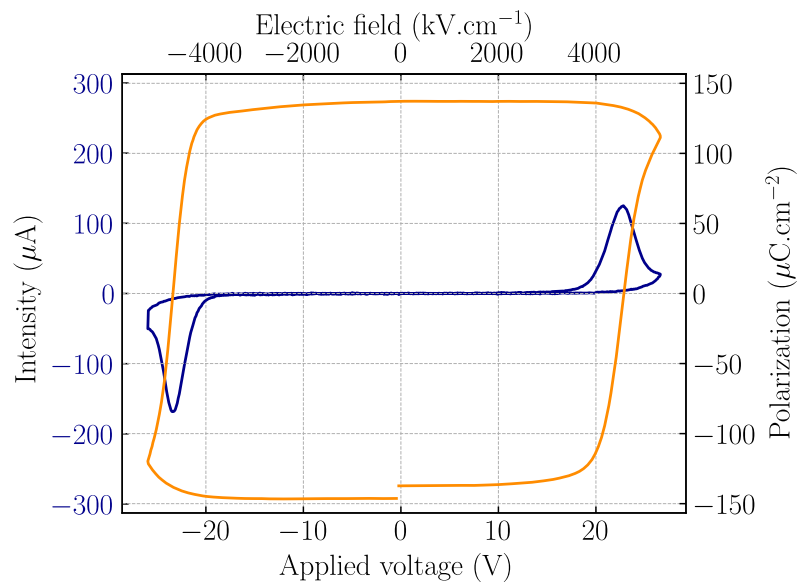


**Figure 5.7:** PUND sequence acquired on a 50 nm thick  $Al_{0.7}Sc_{0.3}N$  thin film. We observe a similar ferroelectric behavior compared to the 150 nm thick sample. The polarization currents switch at lower voltages.

which increased, from  $2.5 \text{ MV cm}^{-1}$  to  $4.5 \text{ MV cm}^{-1}$ . Such an increase is coherent with published thickness vs  $E_c$  studies which report an increase in  $E_c$  with the down scaling of the films, down to  $10 \text{ nm}$  [214]. For even thinner samples, trend is reversed [31] [215]. A thinner sample ( $20 \text{ nm}$  thick) was grown but leakage currents were too important, effectively hindering the measurement of the polarization currents. At this point, reducing the thickness of the thin film while retaining their ferroelectric properties would require diminishing the scandium content [214]. The full scandium rate to thickness ratio optimisation is still undergoing and is not presented here.

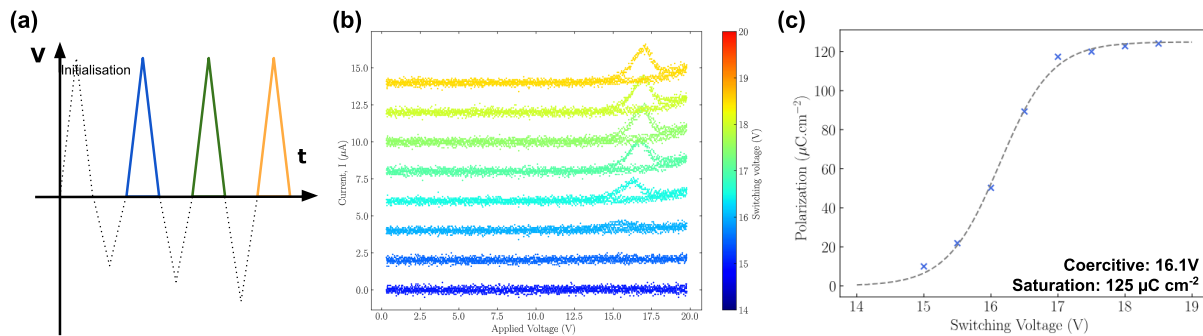


**Figure 5.8:** Partial switching study acquired with the ferrotester. (a) schematic of the wave shape applied to the sample. (b) partial switching study, the color scale encodes the value of the negative voltage applied to the thin film before "reading" with the positive pulse. (c) From this study, we deduce the value of the coercitive to be  $16.1 \text{ V}$ .

In addition, by investigating the partial switching of the ferroelectric thin film, one can get an insight on the dynamics of the polarization switching [204]. An electric partial switching study was performed on a  $42 \text{ nm}$  thick  $\text{Al}_{0.7}\text{Sc}_{0.3}\text{N}$  thin film. The voltage profile applied to the ferroelectric thin film is presented on panel (a) of figure 5.8. The result of this study is presented on panels (b) and (c) of figure 5.8. From this study we can extract a voltage coercitive value of  $16.1 \text{ V}$ . This corresponds to a coercitive ferroelectric field of  $3.3 \text{ MV cm}^{-1}$ . The value for this particular composition is on the low end of the values reported in the literature for this particular composition [212]. This is an encouraging step in fabricating low voltage-switching wurtzite ferroelectrics. This could be achieved provided that thinner samples with lower scandium content are not leaky.

Further characterisation of the polarization state was performed by PFM. The as grown thin films present a natural "up" polarization state, as displayed on panel (a) of figure 5.9. The sample presented in this study is the  $50 \text{ nm}$  thick sample with coercitives at  $\pm 23 \text{ V}$  we presented electrical characterisation of on figure 5.7. By applying a negative (positive) voltage with absolute value higher than the coercitive determined by the electrical measurement, we demonstrate we can fully switch the sample in its down (up) state, as highlighted on the most right and most left images of panel (a) of figure 5.9.

A partial switching study was performed by PFM. To do so, the sample is first fully switched to to the down

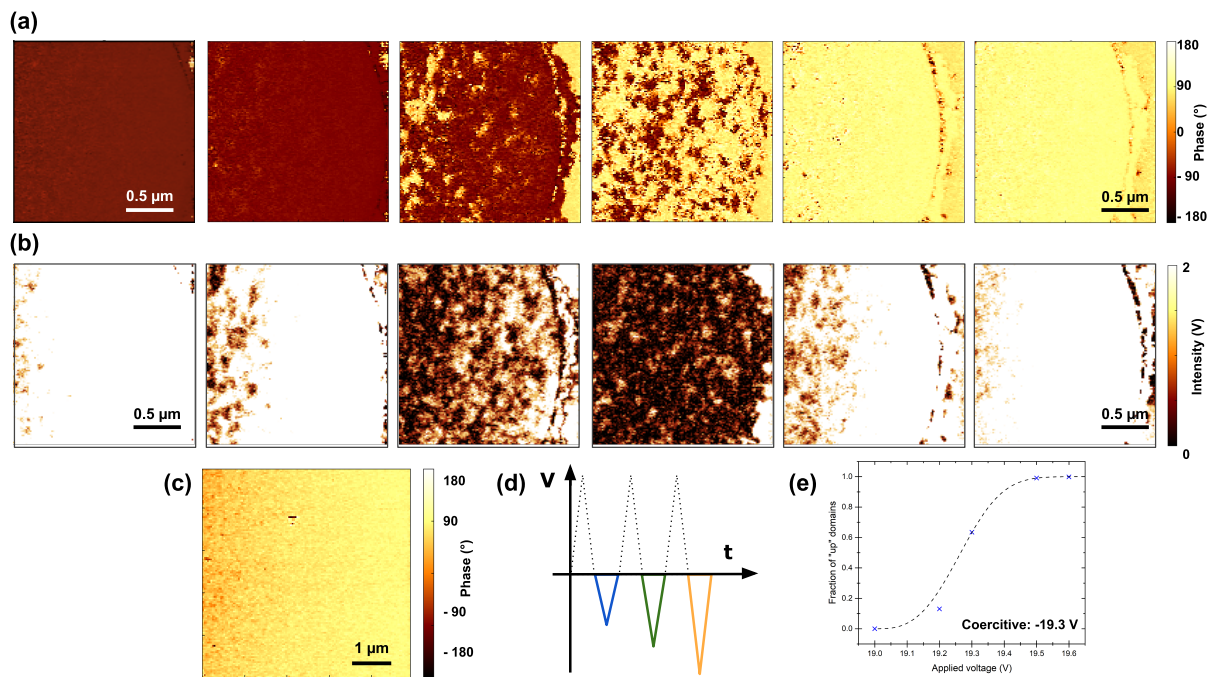


**Figure 5.9:** Partial switching study by PFM (a) PFM phase switching close to the ferroelectric coercitive voltage, (b) intensity of the PFM signal on the same image. (c) Phase imaging of the as grown sample, which presents a natural up-state. (d) bias profile applied to the sample to perform this study and (e) Determination of the coercitive voltage by binarization of the PFM phase images. We compute a coercitive voltage of 19.3 V.

state. The sample are then imaged by PFM (most-left image of panel (d) of figure 5.9). We apply a voltage with a value close to the switching voltage. By doing so, we partially switch the polarization of the thin film. We then image the sample by PFM, and repeat the process (force the thin film to its "down" state, and then partially switch it in the "up" state) while progressively increasing the positive voltage applied to the sample. At high enough voltages, all the dipoles are switched to the "up" state. The PFM images resulting from such an experiment are presented on panel (d) of figure 5.9. We observe the switching of the polarization from the "down" state to the "up" state through the nucleation of domains of opposite polarization. Due to the high density of domain walls that give zero PFM amplitude, the amplitude is strongly decreased in the mixed area (fourth and fifth image of panel (e) of figure 5.9). polarization reversal seems to occur preferentially at the center and then propagates towards the outer edges. We binarize the PFM phase images and compute the fraction of "up" domains as a function of the applied voltage. The result of this analysis is presented on panel (c) of figure 5.9. The coercitive voltage value we deduce from this analysis is of 19.8 V. Strictly speaking, the value deduced by the analysis alone is of 19.3 V, but this is not taking into account the additional AC contribution of 0.5 V peak to peak which is also applied to the PFM tip while applying the switching bias.

We note that this value is smaller than the aforementioned 23 V for the same sample. A tentative explanation might be that this difference is caused by the 5 V peak to peak AC voltage which is applied to the PFM tip while imaging the ferroelectric domains. This additional excitation might force domains which were not fully switched to do so, effectively translating the coercitive voltage to lower values.

## 5.4 Interfacing BiSb and (Al,Sc)N

Having demonstrated the ferroelectric character of our (Al,Sc)N, we propose to integrate it in heterostructures in which it will influence a Rashba spin texture in order to ultimately control spin-to-charge interconversion.

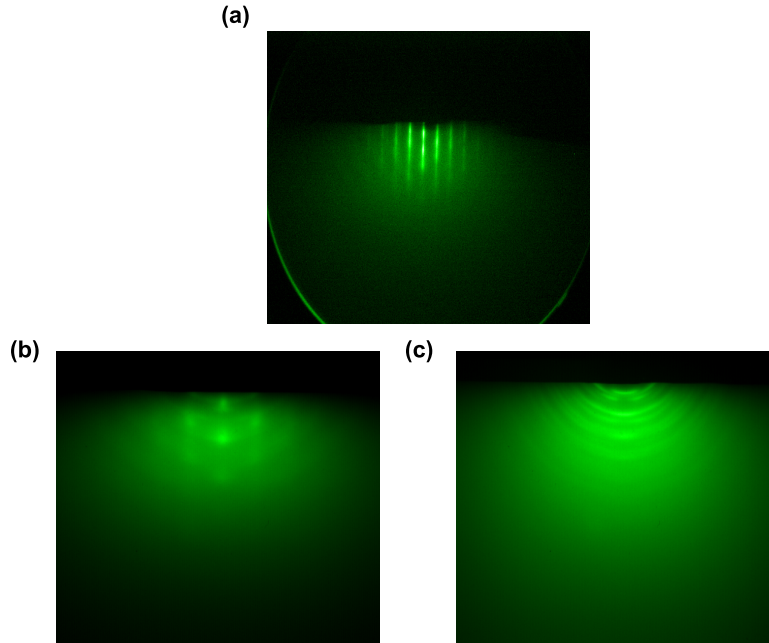


**Figure 5.10:** RHEED of BiSb/(Al,Sc)N heterostructures. (a) RHEED acquired on a 20 nm thick BiSb thin film grown on sapphire. (b) RHEED acquired on a 50 nm thick (Al,Sc)N thin film grown on Pt(111) (c) RHEED of a 20 nm thick BiSb thin film grown on said (Al,Sc)N.

As aforementioned,  $\text{Bi}_x\text{Sb}_{1-x}$  has recently been demonstrated to be an efficient spin-to-charge converter owing to its unique spin texture at the Fermi level [71]. The composition of the BiSb was not varied throughout the study presented here which was performed with  $x = 0.85$ . From this point onward, we will refer to  $\text{Bi}_{0.85}\text{Sb}_{0.15}$  as BiSb. The growth of BiSb by sputtering was optimised by Luis Moreno-Vicente Arche in the PLAS system. The heterostructures we are considering might be stacked in different orders to achieve our purposes. The two stacks we grew have the following structures:

- (i) **Pt (20 nm) /  $\text{Al}_{0.7}\text{Sc}_{0.3}\text{N}$  (42 nm) / BiSb (20 nm) / Sapphire:** In this structure, the BiSb serves as both the spin-to-charge converting layer and the bottom electrode. In such an heterostructure, the BiSb is grown on sapphire, on which it was optimised. In addition, it was recently demonstrated that non epitaxial thin films of (Al,Sc)N have better ferroelectric properties than fully epitaxial ones [31]. Hence, by growing the BiSb before the (Al,Sc)N we hope to maintain good epitaxial quality of the BiSb while maintaining good ferroelectric properties in the ferroelectric layer, maybe at the cost of the epitaxial quality of the latter. The challenges associated with growing such a structure lie in the poor stability of BiSb at temperatures higher than 300 °C, while the growth of (Al,Sc)N was optimised at 350 °C. However, it was reported that (Al,Sc)N could be grown at temperatures as low as room temperature and still present worse, but yet acceptable, ferroelectric properties [216]. We decided to grow (Al,Sc)N at 225 °C, as this is the minimal temperature at which BiSb becomes textured after annealing.
- (ii) **BiSb (20 nm) /  $\text{Al}_{0.7}\text{Sc}_{0.3}\text{N}$  (42 nm) / Pt(111) (50 nm) /  $\text{SiO}_2$  / Si:** By growing such a structure, we make sure the growth conditions of the ferroelectric thin film are optimal. In addition, the BiSb is not exposed to any other temperature step after its growth. Finally, this heterostructure has the advantage

of having the BiSb as the top layer, which might have advantages when we want to move to the investigation of the spin-to-charge interconversion properties of the stack. This is because the only subsequent growth step involves growing and patterning a spin-injection layer. However, growing the BiSb on the ferroelectric instead of sapphire has a clear effect on its crystal quality, as demonstrated by the RHEED acquired at the surface of BiSb grown on sapphire and on (Al,Sc)N presented on panels (c) and (d) of figure 5.10 respectively. A lower epitaxial quality might ultimately affect the spin-to-charge conversion properties of the topological insulator.

The two different heterostructures were grown *in-situ* in the CONF and PLAS systems and sent to Marta D. Rossell at Empa Dübendorf for TEM imaging.

### Transmission Electron Microscopy

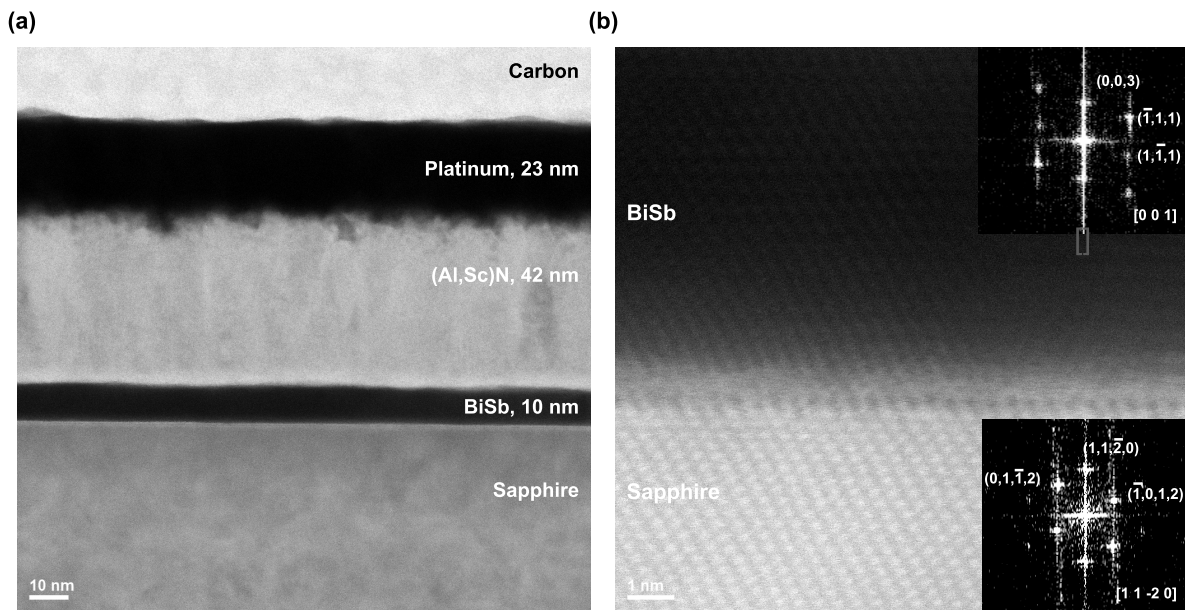


**Figure 5.11:** *Bright field (BF) STEM imaging of a heterostructure of composition Pt/Al<sub>0.7</sub>Sc<sub>0.3</sub>N/BiSb/Sapphire (a) overview image of the heterostructure and (b) a higher magnification image of the BiSb/ sapphire interface. The insets are presenting the corresponding fast fourier transform treatments of the different layers. We note that the BiSb is epitaxial with a one to one epitaxial relationship with its growth substrate.*

Electron-transparent cross-sectional samples were prepared for scanning transmission electron microscopy (STEM) investigations with a FEI Helios NanoLab 600i focused ion beam (FIB) instrument operated at accelerating voltages of 30 and 5 kV, after deposition of a 20 nm thick C protective layer. Annular dark-field (ADF) and bright-field (BF) STEM was performed with a JEOL 2200FS TEM/STEM microscope operated at 200 kV. Taking into account the CS spherical aberration of 1 mm, the probe half-convergence angle was set to 10.8 mrad and the inner half-detection angle of the annular dark-field detector was calibrated at 100 mrad. Under these operating conditions, the microscope provides a spatial resolution of approximately 1.6 Å.

A cross section image of sample (i) is presented on panel (a) of figure 5.11. The different thin films composing the heterostructures are continuous and epitaxial. It is worth noting that the BiSb layer is thinner than we originally expected, which can be explained by looking at sample (ii) and will be discussed later. The different interfaces are sharp, with the exception of the the platinum/ (Al,Sc)N interface, which shows signs of intermixing. Nonetheless, such an intermixing should not affect the ferroelectric properties of the nitride

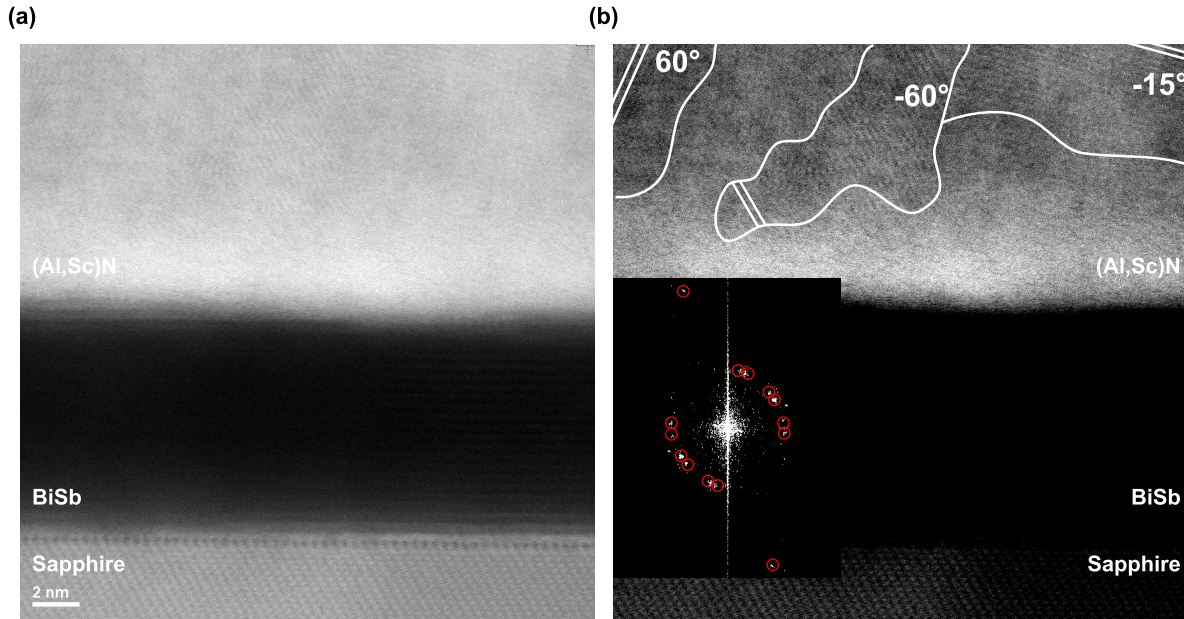


**Figure 5.12:** BF-STEM imaging of an heterostructure of composition  $Pt/Al_{0.7}Sc_{0.3}N/BiSb/Sapphire$ . (a) is a zoom in on the image presented on panel (a) of 5.11 which focuses on the  $BiSb/(Al,Sc)N$  interface (b) same image with a difference contrast which highlights the presence of multiple domains with different orientations in the  $(Al,Sc)N$ .

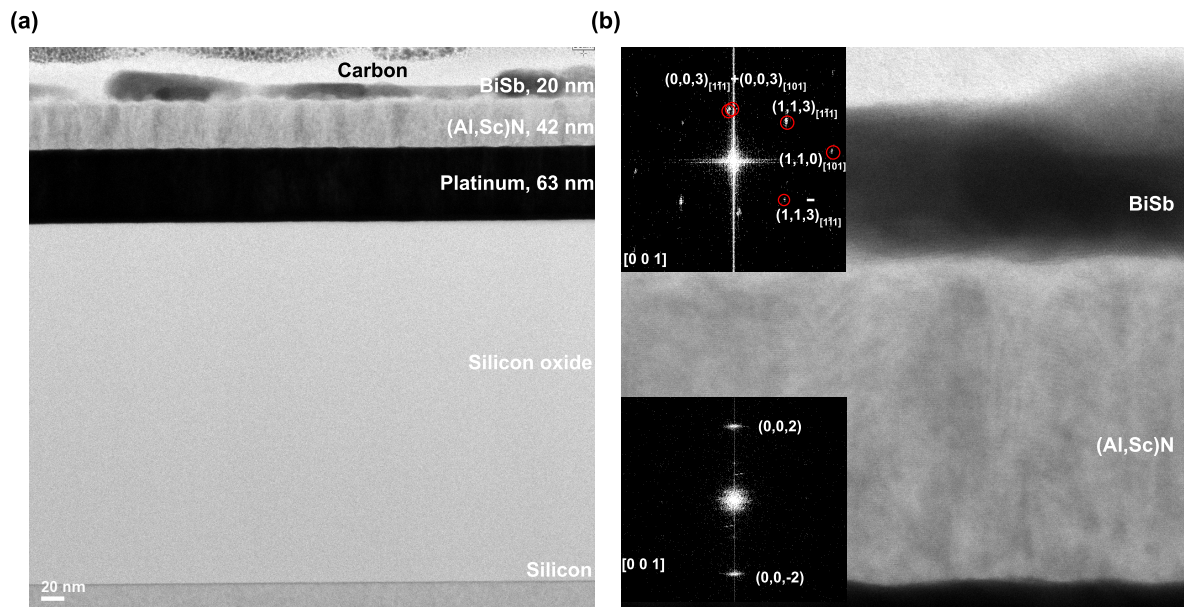


**Figure 5.13:** BF-STEM imaging of an heterostructure of composition  $BiSb/Al_{0.7}Sc_{0.3}N/Pt/SiO_2/Si$  (a) overview image of the heterostructure and (b) a higher magnification image of the  $BiSb$  and  $(Al,Sc)N$  layers. The insets are presenting the corresponding fast fourier transform treatments of the different layers.

Wurtzites close to the BiSb interface. On panel (b) of figure 5.11 we get a closer look at the sapphire/ bismuth antimony interface. The interface is sharp, presenting no sign of intermixing. We compute the fast fourrier transform (FFT) associated with the different lattice structures (inlets of panel (b) of figure 5.11). From the FFT, we determine that (0001)-BiSb grows epitaxial on sapphire with a one to one epitaxial relationship. In addition, we compute the lattice parameter of BiSb to be  $c = 12.6 \pm 0.8 \text{ \AA}$ . This is in reasonable agreements with previous reports [217] [218].

The  $\text{Al}_{0.7}\text{Sc}_{0.3}\text{N}$  grown on top of the BiSb is polycrystalline, as evidenced by the corresponding FFT signal. Several domains can be observed after enhancing the contrast of the BF-STEM image, as displayed on panel (b) of figure 5.12. The corresponding FFT signal seems to indicate the onset of a tilt of the (Al,Sc)N c-axis with respect to the BiSb (001) c-axis. The strain is accommodated at the vicinity of the interface, in a region in which the atomic position are not well defined enough to conclude on the exact relaxation mechanisms at play between the two thin films. The polycrystalline nature of the AlScN will most probably affect its ferroelectric properties, especially since the c-axis is not well defined.

Regarding the sample with composition (ii), we note that even though the (Al,Sc)N grows crystalline on the platinum, the BiSb is forming 20 nm thick islands on top the nitride. This can explain why the nominal 20 nm of BiSb grown on sapphire only resulted in a 10 nm thick film: the growth rate was most likely determined (by XRR) on a partially wetted film which was presenting a nominal thickness of 20 nm. The FFT of the nitride indicates it is highly textured along the z axis. In addition, the FFT of the BiSb islands is characteristic of a mix of two hexagonal phases forming an angle of  $30^\circ$  with each other [218]. We compute the lattice parameters of BiSb to be  $a = 4.66 \pm 0.4 \text{ \AA}$  and  $c = 12.3 \pm 0.8 \text{ \AA}$ . These values are once again in reasonable agreement with the literature [217] [218]. This particular heterostructure could be improved by ameliorating the quality of the BiSb layer. As is, a discontinuous layer of BiSb could not be used for electrical characterisation of the spin-to-charge conversion of the heterostructure. Improving the wetting of the BiSb could for example be achieved by further investigating the post annealing procedure [217] as well as considering multiple cycles of deposition / post-annealing to improve the wetting. This would in turn enhanced the BiSb coverage of the nitride surface. In addition, by using terahertz techniques it should still be possible to investigate the spin-to-charge interconversion properties of this heterostructure, and eventually probe the influence of FE switching on the spin-charge conversion response, even with a inhomogeneous coverage of the BiSb thin film.

## 5.5 Conclusion

To conclude, in this chapter we presented the growth optimization the growth of (Al,Sc)N by magnetron co-sputtering. The thin films structure were characterised by XRD, XPS and AFM, presenting good structural quality with respect to the available data in the literature [212] [213]. In addition, their ferroelectric properties were investigated by PUND measurements as well as PFM. We demonstrate ferroelectric properties at the state of the art for the composition and thickness considered, with coercive fields on the high end of reported data. Further optimisation of the down scaling of our films is still undergoing as of the writing of this manuscript. We used these thin films to demonstrate the feasibility of growing heterostructures which might be of interest to investigate the ferroelectric control of spin-charge interconversion. Such structures were characterised by RHEED and by STEM. Two different structures were investigated, each having their own perks. In the case of the structure grown on sapphire, both the bismuth antimony and the nitride are epitaxial. The Wurtzites, seems to present several domains of different orientations, which might have an effect on its ferroelectric properties. Still, its growth is epitaxial, along the z axis, and crystalline, and it did not affect the quality of the BiSb it was grown on. This heterostructure is highly interesting and should be characterised by PUND and PFM. In the case of the thin films grown on silicon, the nitride is epitaxial and textured. However, the

BiSb is forming islands on top of the Wurtzites. The islands are composed of a mix of two phases which are misorientated by  $30^\circ$  with respect to each other [218]. Nonetheless, BiSb is textured along its (001) axis. This heterostructure could benefit from more growth investigation of the BiSb layer before we proceed with further investigation regarding the ferroelectric and spin-to-charge interconversion properties, but the STEM data is encouraging.

In this chapter, we showcased the optimization of ferroelectric nitride Wurtzites, which have the potential to be paired with various layers for diverse applications. The example we presented here is focused on the ferroelectric control of the spin-charge interconversion properties in the topological insulator BiSb, but other possibilities include building Wurtzites based FE-FETS or FTJs (see section ??), which could for example find applications in the field of neuromorphics. In addition, they might also be of interest in the investigation of the electric control of magnetisation in conjunction with metallic thin films such as cobalt or aluminium.

# Chapter 6

## General conclusions and perspectives

### Conclusions

This thesis is dedicated to the development of novel material systems which are of interest for the ferroelectric control of the Rashba spin-orbit coupling and spin to charge interconversion. Two material systems were investigated. In chapter 3 we detailed the investigation of candidate FERSC SrBiO<sub>3</sub>, which had only seen little interest before. A main achievement lies in the elaboration by pulsed laser deposition of high quality thin films of SrBiO<sub>3</sub> with different strain states. The different strain states were achieved by growing epitaxial SBO on different substrates. Scanning transmission electron microscopy observations unveiled the formation of misfit dislocations in SBO when grown on SrTiO<sub>3</sub> substrates, which induces a tensile strain in the SBO thin film [190]. By growing on NdScO<sub>3</sub>, we highlighted the existence of a tetragonal interfacial layer of SBO of approximately 2-3 nm.

Inspired by the TEM observation, the growth of two candidate electrodes with adequate lattice mismatch with SrBiO<sub>3</sub> and NdScO<sub>3</sub> was optimized. This study was described in chapter 4. La<sub>0.07</sub>Ba<sub>0.93</sub>SnO<sub>3</sub> electrodes were optimised on both SrTiO<sub>3</sub> and NdScO<sub>3</sub>, while Ba<sub>0.5</sub>Sr<sub>0.5</sub>RuO<sub>3</sub> was grown on NdScO<sub>3</sub>. Out of the three systems considered (SBO/BSRO/NSO, SBO/LBSO/NSO, SBO/LBSO/STO), only one was probed to have ferroelectric like properties: SBO/LBSO/NSO. This stack was measured to be ferroelectric, with a strong imprint and with coercive fields at -2 and 5 V. The layer responsible for the ferroelectric like response acquired by PFM was identified to be SBO. Through XRD, we highlight that the SBO in this heterostructure is subjected to some level of in-plane compressive strain, which is an encouraging observation. Using advanced TEM data treatment algorithms, we tried to relate the onset of ferroelectric properties in this material system to the appearance of polarization at the interface with the substrate. We indeed observe the appearance of regions of tetragonal SBO at the interface with NSO, as well as the onset of polarization. Yet, this study is not fully conclusive in correlating the polarization to the strain in the thin films considered. Nonetheless, we must consider that this structural analysis was performed on electrode free systems. Further TEM characterisation of SBO interfaced with LBSO would be needed to draw final conclusions regarding the correlation of tetragonality and polarization in ferroelectric thin films. Further investigation of this material system was hindered by the non-reproducibility of the growth of the electrode. Recent reports of novel perovskite electrodes with large lattice constant could be of interest to probe the ferroelectric properties of SBO [191].

In chapter A we investigated CMOS-compatible heterostructures for the ferroelectric control of spin-charge interconversion. Motivated by the recent seminal discovery of ferroelectricity in doped AlN Wurtzites, the growth of Al<sub>1-x</sub>Sc<sub>x</sub>N on Pt(111) was optimised by magnetron co-sputtering. The films ferroelectric

properties were investigated by electrical and surface techniques. We demonstrated ferroelectric properties at the state of the art. Such films show great promises as they are very unique in their structure and can be interfaced with spin-orbit systems with structures very different compared to oxide ferroelectrics. We proposed to interface our ferroelectric thin films with BiSb. Pristine BiSb is a topological insulator [159] [71], but in the non-ideal scenario BiSb is more likely to present features akin to a bad metal with strong spin-orbit coupling owing to the presence of both bismuth and antimony. As such, it is a candidate system in which to probe the ferroelectric control of Rashba spin textures. BiSb was interfaced *in-situ* with the Wurtzites ferroelectrics and said heterostructures were characterised by RHEED and by TEM. In both heterostructures, the layer grown first presents a good epitaxial quality. However, when BiSb is grown on top of epitaxial (Al,Sc)N it grows columnar and with two slightly different orientations. When (Al,Sc)N is grown on epitaxial BiSb, it grows polycrystalline. Short term objectives regarding this study includes investigating the growth of a thinner Wurtzites layer. This might be necessary to enforce an epitaxial relationship between the BiSb and (Al,Sc)N, which will require more growth optimisation. This is a currently undergoing investigation. In addition, the ferroelectric properties have been probed to better understand the requirements for the nitride thin films in such heterostructure. Longer term perspectives next step of this study will be to investigate spin to charge interconversion of the different heterostructures and under different polarization states. This presupposes the growth of a spin injection layer. Fortunately, this can be done by building on the already existing expertise in the fields of spin-to-charge conversion at Laboratoire Albert Fert [71].

## Outlooks

These results on the different material systems presented in this manuscript open the route towards several appealing perspectives. Concerning the bismuthate systems, it was predicted that they could be of interest as building blocks of heterostructures in which both a 2DHG and a 2DEG would be generated [129]. This presupposes the growth of the perovskite  $\text{LaLuO}_3$ . Fortunately,  $\text{LaLuO}_3$  buffer layers were recently optimised at Laboratoire Albert for the study of antiferroelectric PZO [191]. Other methods such as the deposition of metallic thin films could be used to create a 2DEG at the surface of SBO [53]. Provided that such an interfacial state can be created, investigating the effect of polarization switching on the 2DEG, and its possible spin to charge interconversion properties could allow for a breakthrough in the field of FERSCs. A recent study reported the creation of a 2D superconducting gas at the interface of the bismuthate  $\text{BaBiO}_3$  with  $\text{EuO}$  [219], providing a potential path towards the creation of interfacial states at the surface of bismuthates. In addition, a number of computational studies highlighted the possibility that SBO might behave as a TI, owing to the presence of large spin-orbit coupling coming from the B-site bismuth atoms [133] [134]. Such an investigation would necessitate pristine SBO interfaces, which can only be obtained if SBO is kept under high vacuum. This could be achieved through the use of a vacuum suitcase. Moreover, a recent report highlighted a ferroelectric behavior in non epitaxial  $\text{BaBiO}_3$  thin films with different Ba/Bi ratios [220]. This is an encouraging result for the fields of ferroelectric bismuthates. However, using the ferroelectric behavior of these particular thin films for the means of spin to charge interconversion is rather difficult. Nonetheless, the growth of epitaxial BBO with different Bi ratio might be of interest to reproduce these results in systems in which it might theoretically be possible to induce a 2D interfacial state which might benefit from the ferroelectric properties [128]. Finally, by taking advantage of the superconducting properties of doped SBO compounds, the SBO material system is a prototypical system in which to study the interplay of superconductivity, ferroelectricity and spin-orbit coupling. Moreover, doped compounds have the added benefit of having a smaller lattice mismatch and thus of possibly being easier to induce strain on. The growth of such materials is challenging, and we present a preliminary study point of the growth of such a material in appendix .

Regarding the (Al,Sc)N Wurtzites, they are a novel system which has seen a lot of interest from the ferroelectric community but application prospects are still at their infant stage. In that regard, the CMOS compatible ferroelectric building block which they constitute, as per their low growth temperature, could be used in conjunction with different hexagonal systems. One of such examples is BiSb, with the ultimate goal of investigating the ferroelectric control of Rashba Spin textures. However, this is not the only applications they may fit in. For example, they are one of the very few ferroelectric oxygen free systems. As such, they could be interfaced with systems which are sensitive to oxidation. Examples include ultra thin metallic cobalt thin film which could benefit from being interfaced with an oxygen free ferroelectric in order to investigate the ferroelectric control of the magnetic order in a multiferroic heterostructure [221]. Finally, the favorable vertical down-scaling of ferroelectric wurtzites is of particular interest in developing a new generation of ultra-thin ferroelectric based electronic devices [144] [158]. Recent papers reporting sub-10 nm (Al,Sc)N thin films with high polarization are encouraging in that prospect [214] [215] [31] [222]. Thinning down the size of the thin films grown by PVD in our sputtering set ups is thus of critical importance and will be one of the main focus of the investigation that will be continued after the end of this thesis. Critically, Wurtzites ferroelectric with a thickness of the order of magnitude of a few nanometers could be used to create CMOS compatible ferroelectric tunnel junction devices. This would greatly accelerate the applicative development of FTJs [223]. To conclude, (Al,Sc)N shows great prospects on the growth side as the materials properties have to be further improved before moving to applications [212], as well as on the application side as it can be already be used as is for fundamental research on multiferroic heterostructures or spin-to-charge interconversion.





In the work presented in this manuscript, strain was investigated through the means of epitaxy. Strain can also take different forms, such as chemical strain. We mentioned in section [1.5.5](#) that potassium doped SBO was superconducting with a  $T_c$  of 12 K. In addition, doped compounds have a smaller lattice parameter than the parent compound. Doped compounds may thus be easier to strain than their undoped counterpart. In this annex, we present a preliminary study of the growth by PLD of potassium doped SBO.

## Target ablation test

A stoichiometric target of K-Sr-Bi-O (60 % K, 40 % Sr) (Toshiba, purity 99.99 %) was used for the PLD growth with a KrF laser (Coherent, 25 ns). The target-substrate distance was kept constant at 50 mm.

An ablation test was performed on the target and is presented on [figure 1](#). Based on this study, we decided to settle for fluencies  $< 1.3 \text{ J/cm}^2$ , as the target seems to be fully melted at this fluency. Lower fluencies compared to the parent compounds were to be expected, as potassium is more volatile than Strontium.

## PLD Growths

Starting from optimised growth conditions of SBO, we tried to optimise the growth of KSBO. Based on the ablation test, we determined that fluency should be no lower than  $0.5 \text{ J/cm}^2$  and no higher than  $1.3 \text{ J/cm}^2$ . However, growth performed with fluencies lower than  $0.9 \text{ J/cm}^2$  resulted in no crystalline growth observed by XRD. The growth investigation was performed on a parameter space centered around the optimised conditions of  $\text{SrBiO}_3$ , with the exception of fluency, as explained above.

[Figure 2](#) presents symmetrical XRD scans acquired of thin films grown on STO. We observe the formation of different phases, that we identify as SrO, KBO and a perovskite compound with lattice parameter  $\sim 4.2 \text{ \AA}$ . This peak could be attributed SBO, but owing to the small intensity of the peak and its proximity to the (002) substrate peak, it is hard to conclude on the nature of the perovskite. We attribute the multiphase nature of the deposition to a lower sticking of potassium due to its high volatility and to a rather soft target. Highly volatile elements can be "trapped" in a thin film through the means of higher frequency growth. We investigated fluency, pressure, temperature and growth frequency without much success.

We do expect the target to play a huge role here: for a  $1.3 \text{ J/cm}^2$  fluency, KBO appears with different orientations, which could be the result of target chunks depositing directly on the target. For lower fluencies, KBO peaks are less important.

In addition, we note that increasing the fluency results in the apparition of rocksalt SrO peaks. At low

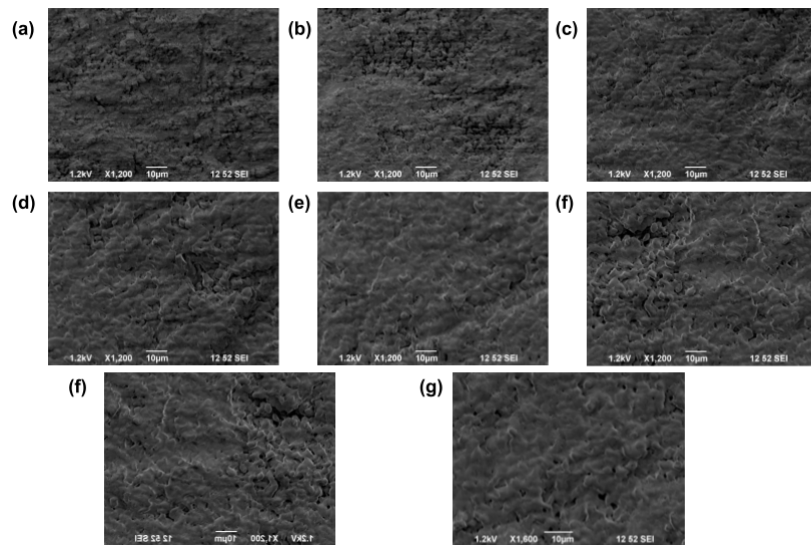


**Figure 1:** Ablation test of a KSBO target. SEM images acquired on the target ablated with fluencies of (a) 0.05 (b) 0.1 (c) 0.3 (d) 0.5 (e) 0.7 (f) 0.9 (g) 1.1 (h) 1.3  $\text{J cm}^{-2}$

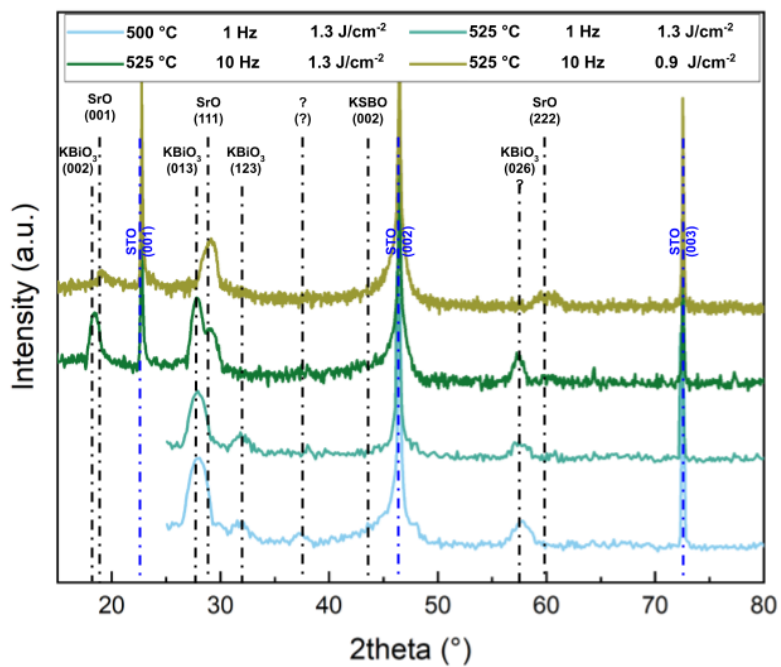


**Figure 2:** XRD characterisation of the thin films grown on STO with a KSBO target.

fluencies and high frequencies, SrO growth seems to predominate, as shown in figure 2. Based on the growth investigation of SBO presented on chapter 3, fine tuning the Oxygen partial pressure at high frequencies and low fluency may allow for the selective growth of a perovskite compound. However, this work could not be carried out in the framework of this thesis.



# $\text{La}_x\text{Ba}_{1-x}\text{SnO}_3$ : non reproducibility of the growth post laser maintenance

We described in chapter 4 the growth optimisation of different electrodes to probe the ferroelectric properties of SBO. However, after maintenance on COMAT the growth conditions had to be slightly reoptimised for the different thin films. However, we did not managed to retrieve LBSO thin films with similar quality as the ones we had prior to the maintenance. In this section, we detail the investigation which we underwent to try to retrieve proper LBSO thin films on NSO substrates.

## Initial growth conditions

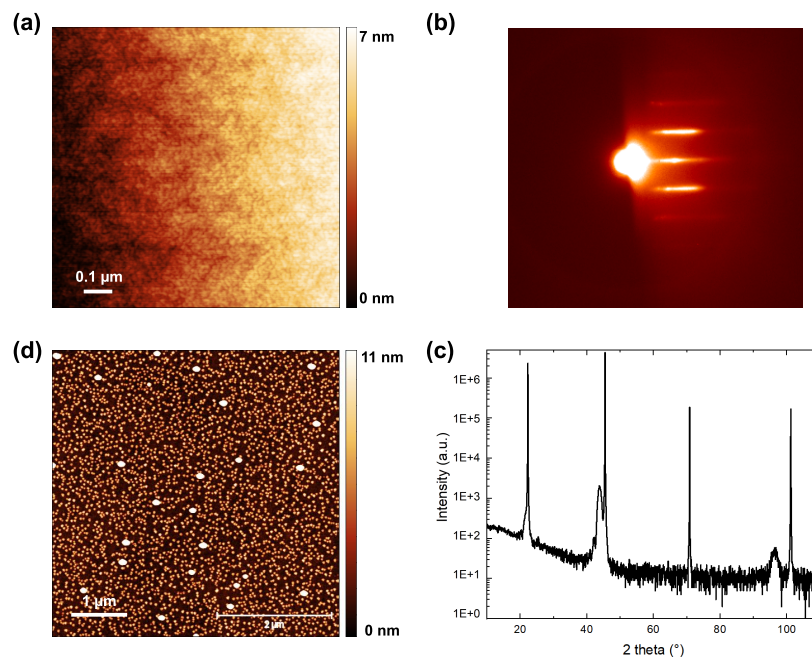


**Figure 3:** LBSO electrodes structural issue. (a) morphology of an LBSO electrode grown prior to the laser maintenance, to be compared with (b) morphology of an LBSO electrode grown after the laser maintenance. The electrode still presents acceptable RHEED and XRD; as highlighted by panels (c) and (d).

As a reminder, the initial growth condition, previously detailed in chapter 4 were the following. A stoichiometric target of  $\text{La}_{0.07}\text{Ba}_{0.93}\text{SnO}_3$  (Toshiba, purity 99.99 %) was used for the PLD growth with a KrF laser (Coherent, 25 ns). The distance between the target and substrate was kept constant at 50 mm. A repetition rate of 1 Hz was used. LBSO was previously optimised, in the same PLD chamber in which we

optimised the growth of SBO, by Jun Wang during his P.h.D. Due to a number of technical changes on the PLD optical path in between his growth optimisation and this work, growth conditions had to be re-optimised. Nonetheless, this served as a good starting point for the growth optimisation. LBSO electrodes were grown at  $830^{\circ}\text{C}$  and under a  $1.3 \cdot 10^{-1}$  mbar oxygen background pressure. The spotsize was kept at  $0.589 \text{ mm}^2$  and a fluency of  $1.3 \text{ J cm}^{-2}$ . AFM and XRD characterisation of such a films are presented on figure 4.2 and the AFM is reproduced on panel (a) of 3.

## The issue

Panel (b) of figure 3 presents the AFM of an LBSO thin film grown post laser maintenance. We observe the formation of islands. Morphology apart, RHEED and XRD of these LBSO thin films are very similar to the one acquired prior to the maintenance.

## Investigation

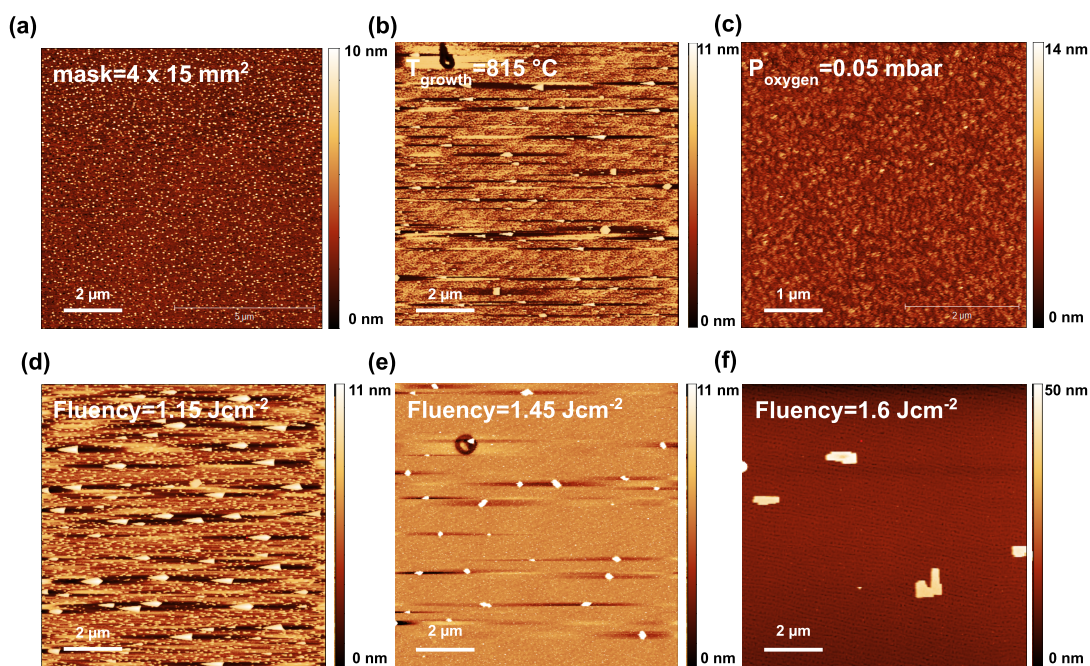


**Figure 4:** Investigation regarding the LBSO electrodes morphology. We investigated (a) the laser spotsize, (b) the growth temperature, (c) the oxygen background pressure and (d), (e), (f) the laser fluency. Increasing the fluency and reducing the oxygen does seem to improve the surface morphology, but we can not retrieve a morphology as good as the one we previously achieved.

To solve this issue, a number of growth parameter we explored, mainly focusing on laser parameters. The main results of the investigation are presented on figure 4. Changing the growth temperature does not affect the morphology of the thin films. Reducing the oxygen pressure does change the morphology, effectively reducing the size and shapes of the islands. This is a clear improvement, but we do not fully recover the same morphology as before. Increasing the fluency results in a lower nucleation rate but larger islands. Finally, increasing the spotsize by increasing the size of the mask does result in smaller islands. The result of this investigation point towards increasing the mask size as well as the fluency, while maybe further reducing the oxygen background pressure. The investigation is still ongoing.

The growth conditions that previously were previously still produced thin film with pristine morphology on STO. Hence, we inferred that growing an STO buffer layer could possibly solve our issue.

### Buffer layer

The result of a thin film grown on an STO buffer layer are presented on figure 5. The introduction of a buffer layer did not solve the issue related to the morphology of LBSO.

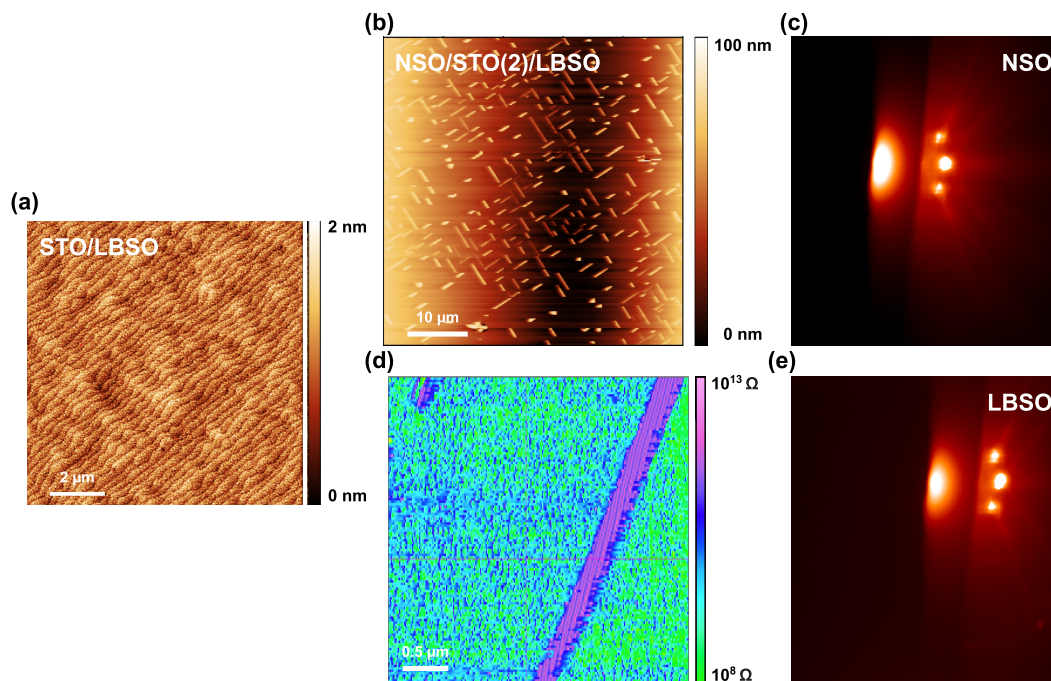


**Figure 5:** Introducing an STO buffer layer. (a) morphology of an STO/LBSO thin film post growth maintenance, (b) morphology of an LBSO thin film after introducing an STO buffer layer. The islands are insulating, as highlighted by panel (d). (e) the RHEED acquired on the LBSO thin film at the end of growth is characteristic of a 2D thin film, probably because the RHEED beam is not scanning over any islands.



# SBO ablation test

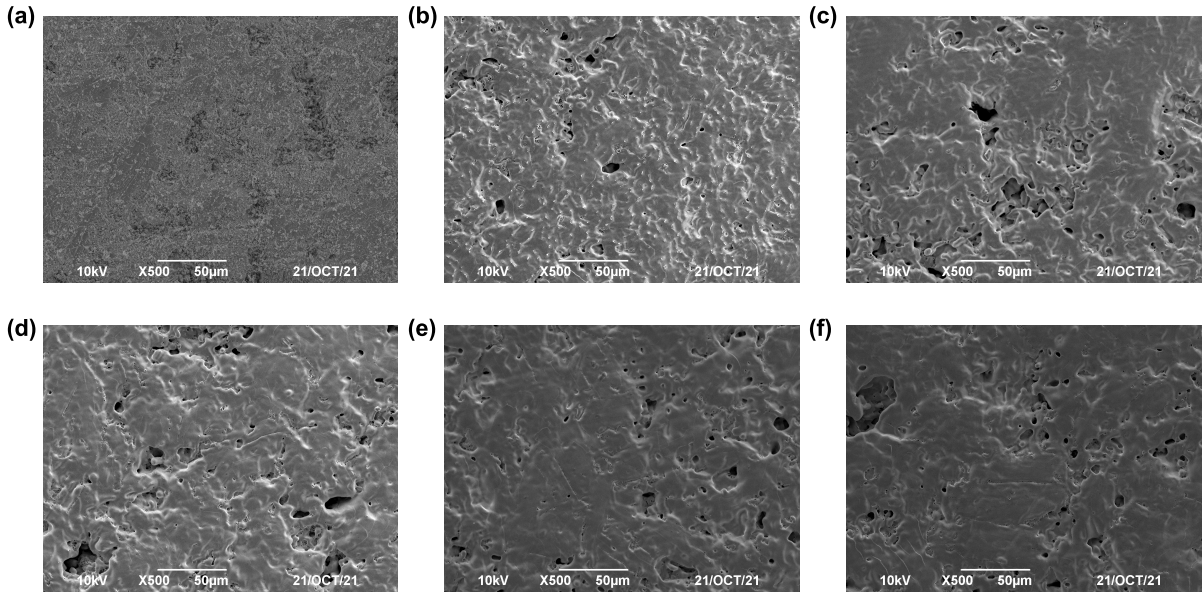


**Figure 6:** Ablation test of the SBO target. SEM images acquired on the target ablated with fluencies of (a) 0 (unablated) (b) 1.2 (c) 1.4 (d) 1.8 (e) 2.0 (f)  $2.2 \text{ J cm}^{-2}$



# Bibliography

- [1] G. E. Moore, "Cramming more components onto integrated circuits, reprinted from electronics, volume 38, number 8, april 19, 1965, pp.114 ff.," *IEEE Solid-State Circuits Society Newsletter*, vol. 11, p. 33–35, Sept. 2006.
- [2] R. Rhyner and M. Luisier, "Minimizing self-heating and heat dissipation in ultrascaled nanowire transistors," *Nano Letters*, vol. 16, pp. 1022–1026, Jan. 2016.
- [3] N. Jones, "How to stop data centres from gobbling up the world's electricity," *Nature*, vol. 561, pp. 163–166, Sept. 2018.
- [4] H. Zhang, S. Shao, H. Xu, H. Zou, and C. Tian, "Free cooling of data centers: A review," *Renewable and Sustainable Energy Reviews*, vol. 35, pp. 171–182, July 2014.
- [5] S. Manipatruni, D. E. Nikonov, and I. A. Young, "Beyond CMOS computing with spin and polarization," *Nature Physics*, vol. 14, pp. 338–343, Apr. 2018.
- [6] D. E. Nikonov and I. A. Young, "Benchmarking of beyond-CMOS exploratory devices for logic integrated circuits," *IEEE Journal on Exploratory Solid-State Computational Devices and Circuits*, vol. 1, pp. 3–11, Dec. 2015.
- [7] A. Soumyanarayanan, N. Reyren, A. Fert, and C. Panagopoulos, "Emergent phenomena induced by spin–orbit coupling at surfaces and interfaces," *Nature*, vol. 539, p. 509–517, Nov. 2016.
- [8] S. Manipatruni, D. E. Nikonov, C.-C. Lin, T. A. Gosavi, H. Liu, B. Prasad, Y.-L. Huang, E. Bon-turim, R. Ramesh, and I. A. Young, "Scalable energy-efficient magnetoelectric spin–orbit logic," *Nature*, vol. 565, pp. 35–42, Dec. 2018.
- [9] V. Edelstein, "Spin polarization of conduction electrons induced by electric current in two-dimensional asymmetric electron systems," *Solid State Communications*, vol. 73, pp. 233–235, Jan. 1990.
- [10] P. Gambardella and I. M. Miron, "Current-induced spin–orbit torques," *Philosophical Transactions of the Royal Society A: Mathematical, Physical and Engineering Sciences*, vol. 369, pp. 3175–3197, Aug. 2011.
- [11] J. C. R. Sánchez, L. Vila, G. Desfonds, S. Gambarelli, J. P. Attané, J. M. D. Teresa, C. Magén, and A. Fert, "Spin-to-charge conversion using rashba coupling at the interface between non-magnetic materials," *Nature Communications*, vol. 4, Dec. 2013.
- [12] K. Yamauchi, P. Barone, and S. Picozzi, "Bulk rashba effect in multiferroics: A theoretical prediction for BiCoO<sub>3</sub>," *Physical Review B*, vol. 100, Dec. 2019.
- [13] S. Picozzi, "Ferroelectric rashba semiconductors as a novel class of multifunctional materials," *Frontiers in Condensed Matter Physics*, 2014.

- [14] J. Varignon, L. Vila, A. Barthélémy, and M. Bibes, "A new spin for oxide interfaces," *Nature Physics*, vol. 14, pp. 322–325, Apr. 2018.
- [15] J. Chen, K. Wu, W. Hu, and J. Yang, "High-throughput inverse design for 2D ferroelectric rashba semiconductors," *Journal of the American Chemical Society*, vol. 144, p. 20035–20046, Oct. 2022.
- [16] D. C. Vaz, C.-C. Lin, J. J. Plombon, W. Y. Choi, I. Groen, I. C. Arango, A. Chuvilin, L. E. Hueso, D. E. Nikonov, H. Li, P. Debashis, S. B. Clendenning, T. A. Gosavi, Y.-L. Huang, B. Prasad, R. Ramesh, A. Vecchiola, M. Bibes, K. Bouzehouane, S. Fusil, V. Garcia, I. A. Young, and F. Casanova, "Voltage-based magnetization switching and reading in magnetoelectric spin-orbit nanodevices," 2023.
- [17] Y. H. Chu, Q. Zhan, C.-H. Yang, M. P. Cruz, L. W. Martin, T. Zhao, P. Yu, R. Ramesh, P. T. Joseph, I. N. Lin, W. Tian, and D. G. Schlom, "Low voltage performance of epitaxial bifeo<sub>3</sub> films on si substrates through lanthanum substitution," *Applied Physics Letters*, vol. 92, Mar. 2008.
- [18] P. Noël, F. Trier, L. M. V. Arche, J. Bréhin, D. C. Vaz, V. Garcia, S. Fusil, A. Barthélémy, L. Vila, M. Bibes, and J.-P. Attané, "Non-volatile electric control of spin–charge conversion in a SrTiO<sub>3</sub> rashba system," *Nature*, vol. 580, pp. 483–486, Apr. 2020.
- [19] A. Fert, R. Ramesh, V. Garcia, F. Casanova, and M. Bibes, "Electrical control of magnetism by electric field and current-induced torques," 2023.
- [20] M. Bibes, L. Vila, J.-P. Attané, P. Noël, and D. C. Vaz, "Dispositif électronique, porte numérique, composant analogique et procédé de génération d'une tension.," 2018.
- [21] J. Bréhin, L. M. V. Arche, S. Varotto, S. Mallik, J.-P. Attané, L. Vila, A. Barthélémy, N. Bergeal, and M. Bibes, "Gate-voltage switching of nonreciprocal transport in oxide-based rashba interfaces," *Physical Review Applied*, vol. 20, Oct. 2023.
- [22] S. Gnewuch and E. E. Rodriguez, "The fourth ferroic order: Current status on ferrotoroidic materials," *Journal of Solid State Chemistry*, vol. 271, p. 175–190, Mar. 2019.
- [23] C. H. Ahn, K. M. Rabe, and J.-M. Triscone, "Ferroelectricity at the nanoscale: Local polarization in oxide thin films and heterostructures," *Science*, vol. 303, p. 488–491, Jan. 2004.
- [24] S. Clima, D. J. Wouters, C. Adelman, T. Schenk, U. Schroeder, M. Jurczak, and G. Pourtois, "Identification of the ferroelectric switching process and dopant-dependent switching properties in orthorhombic HfO<sub>2</sub>: A first principles insight," *Applied Physics Letters*, vol. 104, Mar. 2014.
- [25] M. Pešić, F. P. G. Fengler, L. Larcher, A. Padovani, T. Schenk, E. D. Grimley, X. Sang, J. M. LeBeau, S. Slesazek, U. Schroeder, and T. Mikolajick, "Physical mechanisms behind the field-cycling behavior of HfO<sub>2</sub> -based ferroelectric capacitors," *Adv. Funct. Mater.*, vol. 26, pp. 4601–4612, July 2016.
- [26] K. Budd, S. Dey, and D. Payne, "Sol-gel processing of PbTiO<sub>3</sub>, PbZrO<sub>3</sub>, PZT, and PLZT thin films.," in *British Ceramic Proceedings* (B. Steele, ed.), pp. 107–121, Inst of Ceramics, 1985.
- [27] D. Wang, J. Zheng, P. Musavigharavi, W. Zhu, A. C. Foucher, S. E. Trolrier-McKinstry, E. A. Stach, and R. H. Olsson, "Ferroelectric switching in sub-20 nm aluminum scandium nitride thin films," *IEEE Electron Device Letters*, vol. 41, p. 1774–1777, Dec. 2020.
- [28] F. P. G. Fengler, M. Pešić, S. Starschich, T. Schneller, C. Künneth, U. Böttger, H. Mulaosmanovic, T. Schenk, M. H. Park, R. Nigon, P. Muralt, T. Mikolajick, and U. Schroeder, "Domain pinning: Comparison of hafnia and PZT based ferroelectrics," *Advanced Electronic Materials*, vol. 3, Mar. 2017.

- [29] Y. A. Genenko, J. Glaum, M. J. Hoffmann, and K. Albe, "Mechanisms of aging and fatigue in ferroelectrics," *Materials Science and Engineering: B*, vol. 192, p. 52–82, Feb. 2015.
- [30] M. H. Park, Y. H. Lee, T. Mikolajick, U. Schroeder, and C. S. Hwang, "Review and perspective on ferroelectric HfO<sub>2</sub>-based thin films for memory applications," *MRS Communications*, vol. 8, p. 795–808, Aug. 2018.
- [31] G. Schönweger, N. Wolff, M. R. Islam, M. Gremmel, A. Petraru, L. Kienle, H. Kohlstedt, and S. Fichtner, "In-grain ferroelectric switching in sub-5 nm thin Al<sub>0.74</sub>Sc<sub>0.26</sub>N films at 1 v," *Advanced Science*, vol. 10, June 2023.
- [32] A. Devonshire, "Theory of ferroelectrics," *Advances in Physics*, vol. 3, p. 85–130, Apr. 1954.
- [33] J. Nitta, T. Akazaki, H. Takayanagi, and T. Enoki, "Gate control of spin-orbit interaction in an inverted In<sub>0.53</sub>Ga<sub>0.47</sub>As/In<sub>0.52</sub>Al<sub>0.48</sub>As heterostructure," *Physical Review Letters*, vol. 78, p. 1335–1338, Feb. 1997.
- [34] J. Luo, H. Munekata, F. F. Fang, and P. J. Stiles, "Effects of inversion asymmetry on electron energy band structures in GaSb/InAs/GaSb quantum wells," *Physical Review B*, vol. 41, p. 7685–7693, Apr. 1990.
- [35] S. LaShell, B. A. McDougall, and E. Jensen, "Spin splitting of an au(111) surface state band observed with angle resolved photoelectron spectroscopy," *Physical Review Letters*, vol. 77, p. 3419–3422, Oct. 1996.
- [36] A. Varykhalov, D. Marchenko, M. R. Scholz, E. D. L. Rienks, T. K. Kim, G. Bihlmayer, J. Sánchez-Barriga, and O. Rader, "Ir(111) surface state with giant rashba splitting persists under graphene in air," *Physical Review Letters*, vol. 108, Feb. 2012.
- [37] Y. M. Koroteev, G. Bihlmayer, J. E. Gayone, E. V. Chulkov, S. Blügel, P. M. Echenique, and P. Hofmann, "Strong spin-orbit splitting on bi surfaces," *Physical Review Letters*, vol. 93, July 2004.
- [38] C. R. Ast, J. Henk, A. Ernst, L. Moreschini, M. C. Falub, D. Pacilé, P. Bruno, K. Kern, and M. Gioni, "Giant spin splitting through surface alloying," *Physical Review Letters*, vol. 98, May 2007.
- [39] A. D. Caviglia, M. Gabay, S. Gariglio, N. Reyren, C. Cancellieri, and J.-M. Triscone, "Tunable rashba spin-orbit interaction at oxide interfaces," *Physical Review Letters*, vol. 104, Mar. 2010.
- [40] P. D. C. King, R. C. Hatch, M. Bianchi, R. Ovsyannikov, C. Lupulescu, G. Landolt, B. Slomski, J. H. Dil, D. Guan, J. L. Mi, E. D. L. Rienks, J. Fink, A. Lindblad, S. Svensson, S. Bao, G. Balakrishnan, B. B. Iversen, J. Osterwalder, W. Eberhardt, F. Baumberger, and P. Hofmann, "Large tunable rashba spin splitting of a two-dimensional electron gas in Bi<sub>2</sub>Se<sub>3</sub>," *Physical Review Letters*, vol. 107, Aug. 2011.
- [41] D. Di Sante, P. Barone, R. Bertacco, and S. Picozzi, "Electric control of the giant rashba effect in bulk GeTe," *Advanced Materials*, vol. 25, p. 509–513, Oct. 2012.
- [42] A. Ohtomo and H. Y. Hwang, "A high-mobility electron gas at the LaAlO<sub>3</sub>/SrTiO<sub>3</sub> heterointerface," *Nature*, vol. 427, p. 423–426, Jan. 2004.
- [43] N. Nakagawa, H. Y. Hwang, and D. A. Muller, "Why some interfaces cannot be sharp," *Nature Materials*, vol. 5, p. 204–209, Jan. 2006.
- [44] S. Thiel, G. Hammerl, A. Schmehl, C. W. Schneider, and J. Mannhart, "Tunable quasi-two-dimensional electron gases in oxide heterostructures," *Science*, vol. 313, pp. 1942–1945, Sept. 2006.

- [45] M. Basletic, J.-L. Maurice, C. Carrétéro, G. Herranz, O. Copie, M. Bibes, É. Jacquet, K. Bouzehouane, S. Fusil, and A. Barthélémy, "Mapping the spatial distribution of charge carriers in  $\text{LaAlO}_3/\text{SrTiO}_3$  heterostructures," *Nature Materials*, vol. 7, pp. 621–625, June 2008.
- [46] Y. Z. Chen, N. Bovet, F. Trier, D. V. Christensen, F. M. Qu, N. H. Andersen, T. Kasama, W. Zhang, R. Giraud, J. Dufouleur, T. S. Jespersen, J. R. Sun, A. Smith, J. Nygård, L. Lu, B. Büchner, B. G. Shen, S. Linderoth, and N. Pryds, "A high-mobility two-dimensional electron gas at the spinel/perovskite interface of  $\gamma\text{-Al}_2\text{O}_3/\text{SrTiO}_3$ ," *Nature Communications*, vol. 4, Jan. 2013.
- [47] C. Chen, J. Avila, E. Frantzeskakis, A. Levy, and M. C. Asensio, "Observation of a two-dimensional liquid of fröhlich polarons at the bare  $\text{SrTiO}_3$  surface," *Nature Communications*, vol. 6, Oct. 2015.
- [48] T. C. Rödel, F. Fortuna, S. Sengupta, E. Frantzeskakis, P. L. Fèvre, F. Bertran, B. Mercey, S. Matzen, G. Agnus, T. Maroutian, P. Lecoeur, and A. F. Santander-Syro, "Universal fabrication of 2d electron systems in functional oxides," *Advanced Materials*, vol. 28, pp. 1976–1980, Jan. 2016.
- [49] D. C. Vaz, P. Noël, A. Johansson, B. Göbel, F. Y. Bruno, G. Singh, S. McKeown-Walker, F. Trier, L. M. Vicente-Arche, A. Sander, S. Valencia, P. Bruneel, M. Vivek, M. Gabay, N. Bergeal, F. Baumberger, H. Okuno, A. Barthélémy, A. Fert, L. Vila, I. Mertig, J.-P. Attané, and M. Bibes, "Mapping spin-charge conversion to the band structure in a topological oxide two-dimensional electron gas," *Nature Materials*, vol. 18, pp. 1187–1193, Sept. 2019.
- [50] L. Moreno Vicente-Arche, *Quantum oxide heterostructures for spin-charge interconversion*. Theses, Université Paris-Saclay, Apr. 2022.
- [51] S. Mallik, G. C. Ménard, G. Saïz, I. Gilmutdinov, D. Vignolles, C. Proust, A. Gloter, N. Bergeal, M. Gabay, and M. Bibes, "From low-field sondheimer oscillations to high-field very large and linear magnetoresistance in a  $\text{SrTiO}_3$ -based two-dimensional electron gas," *Nano Letters*, vol. 22, pp. 65–72, Dec. 2021.
- [52] P. Lomker, T. C. Rodel, T. Gerber, F. Fortuna, E. Frantzeskakis, P. L. Fèvre, F. Bertran, M. Muller, and A. F. Santander-Syro, "Two-dimensional electron system at the magnetically tunable  $\text{EuO}/\text{SrTiO}_3$  interface," *Physical Review Materials*, vol. 1, Nov. 2017.
- [53] L. M. Vicente-Arche, S. Mallik, M. Cosset-Cheneau, P. Noël, D. C. Vaz, F. Trier, T. A. Gosavi, C.-C. Lin, D. E. Nikonov, I. A. Young, A. Sander, A. Barthélémy, J.-P. Attané, L. Vila, and M. Bibes, "Metal/ $\text{SrTiO}_3$  two-dimensional electron gases for spin-to-charge conversion," *Physical Review Materials*, vol. 5, June 2021.
- [54] J. Bréhin, F. Trier, L. M. Vicente-Arche, P. Hemme, P. Noël, M. Cosset-Chéneau, J.-P. Attané, L. Vila, A. Sander, Y. Gallais, A. Sacuto, B. Dkhil, V. Garcia, S. Fusil, A. Barthélémy, M. Cazayous, and M. Bibes, "Switchable two-dimensional electron gas based on ferroelectric  $\text{Ca:SrTiO}_3$ ," *Phys. Rev. Mater.*, vol. 4, p. 041002, Apr 2020.
- [55] J. Bréhin, Y. Chen, M. D'Antuono, S. Varotto, D. Stornaiuolo, C. Piamonteze, J. Varignon, M. Salluzzo, and M. Bibes, "Coexistence and coupling of ferroelectricity and magnetism in an oxide two-dimensional electron gas," *Nature Physics*, Mar. 2023.
- [56] S. Mallik, B. Göbel, H. Witt, L. M. Vicente-Arche, S. Varotto, J. Bréhin, G. Ménard, G. Saïz, D. Tamsaout, A. F. Santander-Syro, F. Fortuna, F. Bertran, P. Le Fèvre, J. Rault, I. Boventer, I. Mertig, A. Barthélémy, N. Bergeal, A. Johansson, and M. Bibes, "Electronic band structure of superconducting  $\text{KTaO}_3$  (111) interfaces," *APL Mater.*, vol. 11, Dec. 2023.

- [57] E. Lesne, Y. Fu, S. Oyarzun, J. C. Rojas-Sánchez, D. C. Vaz, H. Naganuma, G. Sicoli, J.-P. Attané, M. Jamet, E. Jacquet, J.-M. George, A. Barthélémy, H. Jaffrès, A. Fert, M. Bibes, and L. Vila, "Highly efficient and tunable spin-to-charge conversion through rashba coupling at oxide interfaces," *Nature Materials*, vol. 15, pp. 1261–1266, Aug. 2016.
- [58] K. V. Shanavas, Z. S. Popović, and S. Satpathy, "Theoretical model for rashba spin-orbit interaction in d electrons," *Physical Review B*, vol. 90, Oct. 2014.
- [59] S. Hurand, A. Jouan, C. Feuillet-Palma, G. Singh, J. Biscaras, E. Lesne, N. Reyren, A. Barthélémy, M. Bibes, J. E. Villegas, C. Ulysse, X. Lafosse, M. Pannetier-Lecoœur, S. Caprara, M. Grilli, J. Lesueur, and N. Bergeal, "Field-effect control of superconductivity and rashba spin-orbit coupling in top-gated LaAlO<sub>3</sub>/SrTiO<sub>3</sub> devices," *Scientific Reports*, vol. 5, Aug. 2015.
- [60] D. C. Vaz, F. Trier, A. Dyrdal, A. Johansson, K. Garcia, A. Barthélémy, I. Mertig, J. Barnaś, A. Fert, and M. Bibes, "Determining the Rashba parameter from the bilinear magnetoresistance response in a two-dimensional electron gas," *Physical Review Materials*, vol. 4, p. 071001, July 2020. Publisher: American Physical Society.
- [61] M. Salluzzo, J. C. Cezar, N. B. Brookes, V. Bisogni, G. M. D. Luca, C. Richter, S. Thiel, J. Mannhart, M. Huijben, A. Brinkman, G. Rijnders, and G. Ghiringhelli, "Orbital reconstruction and the two-dimensional electron gas at the LaAlO<sub>3</sub> / SrTiO<sub>3</sub> interface," *Physical Review Letters*, vol. 102, Apr. 2009.
- [62] S. Varotto, A. Johansson, B. Göbel, L. M. Vicente-Arche, S. Mallik, J. Bréhin, R. Salazar, F. Bertran, P. L. Fèvre, N. Bergeal, J. Rault, I. Mertig, and M. Bibes, "Direct visualization of Rashba-split bands and spin/orbital-charge interconversion at KTaO<sub>3</sub> interfaces," *ArXiv*, p. 2207.08698, 2022. arXiv:2207.08698 [cond-mat, physics:physics].
- [63] H. Zhang, X. Yan, X. Zhang, S. Wang, C. Xiong, H. Zhang, S. Qi, J. Zhang, F. Han, N. Wu, B. Liu, Y. Chen, B. Shen, and J. Sun, "Unusual electric and optical tuning of KTaO<sub>3</sub>-based two-dimensional electron gases with 5d orbitals," *ACS Nano*, vol. 13, p. 609–615, Jan. 2019.
- [64] L. M. Vicente-Arche, J. Bréhin, S. Varotto, M. Cosset-Cheneau, S. Mallik, R. Salazar, P. Noël, D. C. Vaz, F. Trier, S. Bhattacharya, A. Sander, P. Le Fèvre, F. Bertran, G. Saiz, G. Ménard, N. Bergeal, A. Barthélémy, H. Li, C. Lin, D. E. Nikonov, I. A. Young, J. E. Rault, L. Vila, J. Attané, and M. Bibes, "Spin-Charge Interconversion in KTaO<sub>3</sub> 2D Electron Gases," *Advanced Materials*, p. 2102102, Sept. 2021.
- [65] P. D. C. King, R. H. He, T. Eknapakul, P. Buaphet, S.-K. Mo, Y. Kaneko, S. Harashima, Y. Hikita, M. S. Bahramy, C. Bell, Z. Hussain, Y. Tokura, Z.-X. Shen, H. Y. Hwang, F. Baumberger, and W. Meevasana, "Subband structure of a two-dimensional electron gas formed at the polar surface of the strong spin-orbit perovskite KTaO<sub>3</sub>," *Physical Review Letters*, vol. 108, Mar. 2012.
- [66] K. Zou, S. Ismail-Beigi, K. Kisslinger, X. Shen, D. Su, F. J. Walker, and C. H. Ahn, "LaTiO<sub>3</sub>/KTaO<sub>3</sub> interfaces: A new two-dimensional electron gas system," *APL Materials*, vol. 3, Mar. 2015.
- [67] A. H. Al-Tawhid, D. P. Kumah, and K. Ahadi, "Two-dimensional electron systems and interfacial coupling in LaCrO<sub>3</sub>/KTaO<sub>3</sub> heterostructures," *Applied Physics Letters*, vol. 118, May 2021.
- [68] N. Wadehra, R. Tomar, R. M. Varma, R. K. Gopal, Y. Singh, S. Dattagupta, and S. Chakraverty, "Planar hall effect and anisotropic magnetoresistance in polar-polar interface of LaVO<sub>3</sub>-KTaO<sub>3</sub> with strong spin-orbit coupling," *Nature Communications*, vol. 11, Feb. 2020.

- [69] C. L. Kane and E. J. Mele, "Quantum spin hall effect in graphene," *Physical Review Letters*, vol. 95, Nov. 2005.
- [70] B. A. Bernevig, T. L. Hughes, and S.-C. Zhang, "Quantum spin hall effect and topological phase transition in HgTe quantum wells," *Science*, vol. 314, p. 1757–1761, Dec. 2006.
- [71] E. Rongione, L. Baringthon, D. She, G. Patriarche, R. Lebrun, A. Lemaître, M. Morassi, N. Reyren, M. Mićica, J. Mangeney, J. Tignon, F. Bertran, S. Dhillon, P. Le Fèvre, H. Jaffrès, and J. George, "Spin-momentum locking and ultrafast spin-charge conversion in ultrathin epitaxial  $\text{bi}_{1-x}\text{sb}_x$  topological insulator," *Advanced Science*, vol. 10, Apr. 2023.
- [72] M. Z. Hasan and C. L. Kane, "Colloquium: Topological insulators," *Reviews of Modern Physics*, vol. 82, p. 3045–3067, Nov. 2010.
- [73] Z. Zhong, L. Si, Q. Zhang, W.-G. Yin, S. Yunoki, and K. Held, "Giant switchable rashba effect in oxide heterostructures," *Advanced Materials Interfaces*, 2015.
- [74] Y. Song, D. Zhang, B. Xu, K. Chang, and C.-W. Nan, "Electrical control of large rashba effect in oxide heterostructures," 2019.
- [75] M. Fang, Y. Wang, H. Wang, Y. Hou, E. Vetter, Y. Kou, W. Yang, L. Yin, Z. Xiao, Z. Li, L. Jiang, H. N. Lee, S. Zhang, R. Wu, X. Xu, D. Sun, and J. Shen, "Tuning the interfacial spin-orbit coupling with ferroelectricity," *Nature Communications*, vol. 11, May 2020.
- [76] X. Xu, L. Zhang, L. Zou, M. Li, and H. Wang, "Regulating interfacial spin hall conductivity with ferroelectricity," *The Journal of Physical Chemistry Letters*, vol. 13, p. 3310–3316, Apr. 2022.
- [77] Y. Jiang, E. Parsonnet, A. Qualls, W. Zhao, S. Susarla, D. Pesquera, A. Dasgupta, M. Acharya, H. Zhang, T. Gosavi, C.-C. Lin, D. E. Nikonov, H. Li, I. A. Young, R. Ramesh, and L. W. Martin, "Enabling ultra-low-voltage switching in  $\text{BaTiO}_3$ ," *Nature Materials*, vol. 21, p. 779–785, May 2022.
- [78] J. Sinsheimer, S. J. Callori, B. Bein, Y. Benkara, J. Daley, J. Coraor, D. Su, P. W. Stephens, and M. Dawber, "Engineering polarization rotation in a ferroelectric superlattice," *Physical Review Letters*, vol. 109, Oct. 2012.
- [79] H. Mirhosseini, I. V. Maznichenko, S. Abdelouahed, S. Ostanin, A. Ernst, I. Mertig, and J. Henk, "Toward a ferroelectric control of rashba spin-orbit coupling: Bi on  $\text{BaTiO}_3(001)$  from first principles," *Physical Review B*, vol. 81, Feb. 2010.
- [80] T. Aull, I. V. Maznichenko, S. Ostanin, E. Şaşıoğlu, and I. Mertig, "Externally controlled and switchable two-dimensional electron gas at the rashba interface between ferroelectrics and heavy **d** metals," *Physical Review Research*, vol. 3, Nov. 2021.
- [81] C. Rinaldi, S. Varotto, M. Asa, J. Sławińska, J. Fujii, G. Vinai, S. Cecchi, D. Di Sante, R. Calarco, I. Vobornik, G. Panaccione, S. Picozzi, and R. Bertacco, "Ferroelectric control of the spin texture in GeTe," *Nano Letters*, vol. 18, p. 2751–2758, Jan. 2018.
- [82] S. Varotto, L. Nessi, S. Cecchi, J. Sławińska, P. Noël, S. Petrò, F. Fagiani, A. Novati, M. Cantoni, D. Petti, E. Albisetti, M. Costa, R. Calarco, M. B. Nardelli, M. Bibes, S. Picozzi, J.-P. Attané, L. Vila, R. Bertacco, and C. Rinaldi, "Room-temperature ferroelectric switching of spin-to-charge conversion in germanium telluride," *Nature Electronics*, vol. 4, pp. 740–747, Oct. 2021.

- [83] M. Sakano, M. S. Bahramy, A. Katayama, T. Shimojima, H. Murakawa, Y. Kaneko, W. Malaeb, S. Shin, K. Ono, H. Kumigashira, R. Arita, N. Nagaosa, H. Y. Hwang, Y. Tokura, and K. Ishizaka, "Strongly spin-orbit coupled two-dimensional electron gas emerging near the surface of polar semiconductors," *Physical Review Letters*, vol. 110, Mar. 2013.
- [84] S. V. Eremeev, I. P. Rusinov, I. A. Nechaev, and E. V. Chulkov, "Rashba split surface states in BiTeBr," *New J. Phys.*, vol. 15, p. 075015, July 2013.
- [85] K. Ishizaka, M. S. Bahramy, H. Murakawa, M. Sakano, T. Shimojima, T. Sonobe, K. Koizumi, S. Shin, H. Miyahara, A. Kimura, K. Miyamoto, T. Okuda, H. Namatame, M. Taniguchi, R. Arita, N. Nagaosa, K. Kobayashi, Y. Murakami, R. Kumai, Y. Kaneko, Y. Onose, and Y. Tokura, "Giant rashba-type spin splitting in bulk BiTeI," *Nature Materials*, vol. 10, p. 521–526, June 2011.
- [86] L. G. D. da Silveira, P. Barone, and S. Picozzi, "Rashba-dresselhaus spin-splitting in the bulk ferroelectric oxide BiAlO<sub>3</sub>," *Physical Review B*, vol. 93, June 2016.
- [87] L. L. Tao and J. Wang, "Strain-tunable ferroelectricity and its control of rashba effect in KTaO<sub>3</sub>," *Journal of Applied Physics*, vol. 120, Dec. 2016.
- [88] R. Arras, J. Gosteau, H. J. Zhao, C. Paillard, Y. Yang, and L. Bellaiche, "Rashba-like spin-orbit and strain effects in tetragonal PbTiO<sub>3</sub>," *Phys. Rev. B*, vol. 100, p. 174415, Nov 2019.
- [89] H. Djani, A. C. Garcia-Castro, W.-Y. Tong, P. Barone, E. Bousquet, S. Picozzi, and P. Ghosez, "Rationalizing and engineering rashba spin-splitting in ferroelectric oxides," *Nature Quantum Materials*, 2019.
- [90] J. Varignon, J. Santamaria, and M. Bibes, "Electrically switchable and tunable rashba-type spin splitting in covalent perovskite oxides," *Phys. Rev. Lett.*, vol. 122, p. 116401, Mar 2019.
- [91] B. Zhou, "Ferroelectric rashba semiconductors, AgBiP<sub>2</sub>X<sub>6</sub> (X = S, Se and Te), with valley polarization: an avenue towards electric and nonvolatile control of spintronic devices," *Nanoscale*, vol. 12, no. 9, p. 5533–5542, 2020.
- [92] G. Krizman, T. Zakusylo, L. Sajeev, M. Hajlaoui, T. Takashiro, M. Rosmus, N. Olszowska, J. J. Kołodziej, G. Bauer, O. Caha, and G. Springholz, "A novel ferroelectric rashba semiconductor," *Advanced Materials*, vol. n/a, no. n/a, p. 2310278.
- [93] A. Narayan, "Class of rashba ferroelectrics in hexagonal semiconductors," *Physical Review B*, vol. 92, Dec. 2015.
- [94] A. Stroppa, D. Di Sante, P. Barone, M. Bokdam, G. Kresse, C. Franchini, M.-H. Whangbo, and S. Picozzi, "Tunable ferroelectric polarization and its interplay with spin-orbit coupling in tin iodide perovskites," *Nat. Commun.*, vol. 5, p. 5900, Dec. 2014.
- [95] M. Isarov, L. Z. Tan, M. I. Bodnarchuk, M. V. Kovalenko, A. M. Rappe, and E. Lifshitz, "Rashba effect in a single colloidal CsPbBr<sub>3</sub> perovskite nanocrystal detected by magneto-optical measurements," *Nano Lett.*, vol. 17, pp. 5020–5026, Aug. 2017.
- [96] P. Bhumla, D. Gill, S. Sheoran, and S. Bhattacharya, "Origin of rashba spin splitting and strain tunability in ferroelectric bulk CsPbF<sub>3</sub>," *J. Phys. Chem. Lett.*, vol. 12, pp. 9539–9546, Oct. 2021.
- [97] H. J. Zhao, P. Chen, C. Paillard, R. Arras, Y.-W. Fang, X. Li, J. Gosteau, Y. Yang, and L. Bellaiche, "Large spin splittings due to the orbital degree of freedom and spin textures in a ferroelectric nitride perovskite," *Phys. Rev. B.*, vol. 102, July 2020.

- [98] L. L. Tao, T. R. Paudel, A. A. Kovalev, and E. Y. Tsymbal, "Reversible spin texture in ferroelectric  $\text{hfo}_2$ ," *Physical Review B*, vol. 95, June 2017.
- [99] L. L. Tao and E. Y. Tsymbal, "Persistent spin texture enforced by symmetry," *Nature Communications*, vol. 9, July 2018.
- [100] M. C. Choi and S. Y. Park, "Hybrid improper ferroelectricity in a-cation ordered perovskite  $\text{BaSrBi}_2\text{O}_6$ ," *Journal of the Korean Physical Society*, vol. 81, pp. 790–795, Sept. 2022.
- [101] S. Griffitt, M. Spaić, J. Joe, Z. W. Anderson, D. Zhai, M. J. Krogstad, R. Osborn, D. Pelc, and M. Greven, "Local inversion-symmetry breaking in a bismuthate high- $T_c$  superconductor," *Nature Communications*, vol. 14, Feb. 2023.
- [102] P. A. Fleury, J. F. Scott, and J. M. Worlock, "Soft phonon modes and the 110°K phase transition in  $\text{SrTiO}_3$ ," *Physical Review Letters*, vol. 21, p. 16–19, July 1968.
- [103] J. F. Scott, "Soft-mode spectroscopy: Experimental studies of structural phase transitions," *Reviews of Modern Physics*, vol. 46, p. 83–128, Jan. 1974.
- [104] J. Varignon, "Origin of superconductivity in hole doped  $\text{SrBiO}_3$  bismuth oxide perovskite from parameter-free first-principles simulations," *npj Computational Materials*, vol. 9, Mar. 2023.
- [105] G. M. Dalpian, Q. Liu, J. Varignon, M. Bibes, and A. Zunger, "Bond disproportionation, charge self-regulation, and ligand holes in s- p and in d-electron  $\text{ABX}_3$  perovskites by density functional theory," *Physical Review B*, vol. 98, Aug. 2018.
- [106] M. Kim, G. M. McNally, H.-H. Kim, M. Oudah, A. S. Gibbs, P. Manuel, R. J. Green, R. Sutarto, T. Takayama, A. Yaresko, U. Wedig, M. Isobe, R. K. Kremer, D. A. Bonn, B. Keimer, and H. Takagi, "Superconductivity in  $(\text{Ba}, \text{K})\text{SbO}_3$ ," *Nature Materials*, vol. 21, pp. 627–633, Feb. 2022.
- [107] S. H. Chang, "Superconducting antimonates," *Nature Materials*, vol. 21, p. 612–613, May 2022.
- [108] R. K. Patel, K. Patra, S. K. Ojha, S. Kumar, S. Sarkar, A. Saha, N. Bhattacharya, J. W. Freeland, J.-W. Kim, P. J. Ryan, P. Mahadevan, and S. Middey, "Hole doping in a negative charge transfer insulator," *Communications Physics*, vol. 5, Aug. 2022.
- [109] M. Takano, J. Kawachi, N. Nakanishi, and Y. Takeda, "Valence state of the Fe ions in  $\text{Sr}_{1-x}\text{La}_x\text{FeO}_3$ ," *Journal of Solid State Chemistry*, vol. 39, p. 75–84, Aug. 1981.
- [110] T. Mizokawa, D. I. Khomskii, and G. A. Sawatzky, "Spin and charge ordering in self-doped mott insulators," *Physical Review B*, vol. 61, p. 11263–11266, May 2000.
- [111] A. W. Sleight, "Bismuthates:  $\text{BaBiO}_3$  and related superconducting phases," *Physica C: Superconductivity and its Applications*, vol. 514, pp. 152–165, July 2015.
- [112] E. Climent-Pascual, N. Ni, S. Jia, Q. Huang, and R. J. Cava, "Polymorphism in  $\text{BaPb}_{1-x}\text{Bi}_x\text{O}_3$  at the superconducting composition," *Physical Review B*, vol. 83, May 2011.
- [113] W. Fu, D. Visser, and D. IJdo, "High-resolution neutron powder diffraction study on the structure of  $\text{BaPbO}_3$ ," *Solid State Communications*, vol. 134, pp. 647–652, June 2005.
- [114] A. Sleight, J. Gillson, and P. Bierstedt, "High-temperature superconductivity in the  $\text{BaPb}_{1-x}\text{Bi}_x\text{O}_3$  systems," *Solid State Communications*, vol. 17, pp. 27–28, July 1975.
- [115] S. Sarkar, R. Raghunathan, S. Chowdhury, R. J. Choudhary, and D. M. Phase, "The mystery behind dynamic charge disproportionation in  $\text{BaBiO}_3$ ," *Nano Letters*, vol. 21, pp. 8433–8438, Sept. 2021.

- [116] S. M. Kazakov, C. Chaillout, P. Bordet, J. J. Capponi, M. Nunez-Regueiro, A. Rysak, J. L. Tholence, P. G. Radaelli, S. N. Putilin, and E. V. Antipov, "Discovery of a second family of bismuth-oxide-based superconductors," *Nature*, vol. 390, pp. 148–150, Nov. 1997.
- [117] D. G. Hinks, B. Dabrowski, J. D. Jorgensen, A. W. Mitchell, D. R. Richards, S. Pei, and D. Shi, "Synthesis, structure and superconductivity in the  $\text{Ba}_{1-x}\text{K}_x\text{BiO}_{3-y}$  system," *Nature*, vol. 333, pp. 836–838, June 1988.
- [118] A. Taraphder, H. R. Krishnamurthy, R. Pandit, and T. V. Ramakrishnan, "Negative- $u$  extended hubbard model for doped barium bismuthates," *Physical Review B*, vol. 52, pp. 1368–1388, July 1995.
- [119] Z. P. Yin, A. Kutepov, and G. Kotliar, "Correlation-enhanced electron-phonon coupling: Applications of  $gw$  and screened hybrid functional to bismuthates, chloronitrides, and other high- $t_c$  superconductors," *Physical Review X*, vol. 3, May 2013.
- [120] C. Wen, H. Xu, Q. Yao, R. Peng, X. Niu, Q. Chen, Z. Liu, D. Shen, Q. Song, X. Lou, Y. Fang, X. Liu, Y. Song, Y. Jiao, T. Duan, H. Wen, P. Dudin, G. Kotliar, Z. Yin, and D. Feng, "Unveiling the superconducting mechanism of  $\text{Ba}_{0.51}\text{K}_{0.49}\text{BiO}_3$ ," *Physical Review Letters*, vol. 121, Sept. 2018.
- [121] T. Bazhurov, S. Coh, S. G. Louie, and M. L. Cohen, "Importance of oxygen octahedra tilts for the electron-phonon coupling in  $k$ -doped  $\text{BaBiO}_3$ ," *Physical Review B*, vol. 88, Dec. 2013.
- [122] S. D. Napoli, C. Helman, A. M. Llois, and V. Vildosola, "Two-dimensional superconductivity driven by interfacial electron-phonon coupling in a  $\text{BaPbO}_3/\text{BaBiO}_3$  bilayer," *Physical Review B*, vol. 103, May 2021.
- [123] V. Vildosola, F. Guller, and A. M. Llois, "Mechanism to generate a two-dimensional electron gas at the surface of the charge-ordered semiconductor  $\text{BaBiO}_3$ ," *Physical Review Letters*, vol. 110, May 2013.
- [124] A. Gozar, G. Logvenov, V. Y. Butko, and I. Bozovic, "Surface structure analysis of atomically smooth  $\text{BaBiO}_3$  films," *Physical Review B*, vol. 75, May 2007.
- [125] C. Ferreyra, F. Marchini, P. Granell, F. Golmar, C. Albornoz, F. Williams, A. Leyva, and D. Rubi, "Growth of (100)-highly textured  $\text{BaBiO}_3$  thin films on silicon," *Thin Solid Films*, vol. 612, p. 369–372, Aug. 2016.
- [126] C. Ferreyra, F. Guller, F. Marchini, U. Lüders, C. Albornoz, A. G. Leyva, F. J. Williams, A. M. Llois, V. Vildosola, and D. Rubi, "Tuning the electronic properties at the surface of  $\text{BaBiO}_3$  thin films," *AIP Advances*, vol. 6, June 2016.
- [127] J. S. Oh, M. Kim, G. Kim, H. G. Lee, H. K. Yoo, S. Sinn, Y. J. Chang, M. Han, C. Jozwiak, A. Bostwick, E. Rotenberg, H.-D. Kim, and T. W. Noh, "Evidence for absence of metallic surface states in  $\text{BiO}_2$ -terminated  $\text{BaBiO}_3$  thin films," *Current Applied Physics*, vol. 18, p. 658–662, June 2018.
- [128] R. L. Bouwmeester and A. Brinkman, " $\text{BaBiO}_3$ —from single crystals towards oxide topological insulators," *Reviews in Physics*, vol. 6, p. 100056, June 2021.
- [129] A. Khazraie, I. Elfimov, K. Foyevtsova, and G. A. Sawatzky, "Potential superconducting interfaces in polar  $\text{ABO}_3/\text{ba}(\text{sr})\text{BiO}_3$  heterostructures," *Physical Review B*, vol. 101, Jan. 2020.
- [130] B. Hadjarab, S. Saadi, A. Bouguelia, and M. Trari, "Physical properties and photoelectrochemical characterization of  $\text{SrRuO}_{3-\delta}$ ," *physica status solidi (a)*, vol. 204, pp. 2369–2380, July 2007.
- [131] B. Yan, M. Jansen, and C. Felser, "A large-energy-gap oxide topological insulator based on the superconductor  $\text{BaBiO}_3$ ," *Nature Physics*, vol. 9, p. 709–711, Sept. 2013.

- [132] G. Li, B. Yan, R. Thomale, and W. Hanke, "Topological nature and the multiple dirac cones hidden in bismuth high-*t<sub>c</sub>* superconductors," *Scientific Reports*, vol. 5, May 2015.
- [133] G. Trimarchi, X. Zhang, A. J. Freeman, and A. Zunger, "Structurally unstable  $A^{iii}BiO_3$  perovskites are predicted to be topological insulators but their stable structural forms are trivial band insulators," *Phys. Rev. B*, vol. 90, p. 161111, Oct 2014.
- [134] B. Khamari, R. Kashikar, and B. R. K. Nanda, "Topologically invariant double dirac states in bismuth-based perovskites: Consequence of ambivalent charge states and covalent bonding," *Phys. Rev. B*, vol. 97, p. 045149, Jan 2018.
- [135] M. Zapf, M. Stübinger, L. Jin, M. Kamp, F. Pfaff, A. Lubk, B. Büchner, M. Sing, and R. Claessen, "Domain matching epitaxy of  $BaBiO_3$  on  $SrTiO_3$  with structurally modified interface," *Applied Physics Letters*, vol. 112, p. 141601, Apr. 2018.
- [136] T. Makita and H. Abe, "Control of crystal orientation for  $BaBiO_3$  thin film on  $SrTiO_3(100)$  substrate using  $BaO$  buffer layer," *Japanese Journal of Applied Physics*, vol. 36, 02 1997.
- [137] D. Mijatovic, G. Rijnders, H. Hilgenkamp, D. H. Blank, and H. Rogalla, "Growth studies of  $Ba_{1-x}(K_x)BiO_{3-\delta}$  thin films by pulsed-laser deposition," *Physica C: Superconductivity*, vol. 372-376, pp. 596–599, Aug. 2002.
- [138] K. Inumaru, H. Miyata, and S. Yamanaka, "Partial suppression of structural distortion in epitaxially grown  $BaBiO_3$ ," *Physical Review B*, vol. 78, Oct. 2008.
- [139] R. L. Bouwmeester, K. de Hond, N. Gauquelin, J. Verbeeck, G. Koster, and A. Brinkman, "Stabilization of the perovskite phase in the  $y-bi-o$  system by using a  $BaBiO_3$  buffer layer," *physica status solidi (RRL) – Rapid Research Letters*, vol. 13, p. 1800679, Mar. 2019.
- [140] L. Jin, M. Zapf, M. Stübinger, M. Kamp, M. Sing, R. Claessen, and C.-L. Jia, "Atomic-scale interface structure in domain matching epitaxial  $BaBiO_3$  thin films grown on  $SrTiO_3$  substrates," *physica status solidi (RRL) – Rapid Research Letters*, vol. 14, p. 2000054, Mar. 2020.
- [141] F. Li, B. A. Davidson, R. Sutarto, H. Shin, C. Liu, I. Elfimov, K. Foyevtsova, F. He, G. A. Sawatzky, and K. Zou, "Epitaxial growth of perovskite  $SrBiO_3$  film on  $SrTiO_3$  by oxide molecular beam epitaxy," *Physical Review Materials*, vol. 3, Oct. 2019.
- [142] C. Caliendo and P. Imperatori, "High-frequency, high-sensitivity acoustic sensor implemented on ALN/Si substrate," *Applied Physics Letters*, vol. 83, pp. 1641–1643, Aug. 2003.
- [143] W. Wang, P. M. Mayrhofer, X. He, M. Gillinger, Z. Ye, X. Wang, A. Bittner, U. Schmid, and J. K. Luo, "High performance AlScN thin film based surface acoustic wave devices with large electromechanical coupling coefficient," *Applied Physics Letters*, vol. 105, Sept. 2014.
- [144] J. Su, F. Niekil, S. Fichtner, L. Thormaehlen, C. Kirchhof, D. Meyners, E. Quandt, B. Wagner, and F. Lofink, "AlScN-based MEMS magnetoelectric sensor," *Applied Physics Letters*, vol. 117, Sept. 2020.
- [145] S. Calderon, J. Hayden, S. M. Baksa, W. Tzou, S. Trolier-McKinstry, I. Dabo, J.-P. Maria, and E. C. Dickey, "Atomic-scale polarization switching in wurtzite ferroelectrics," *Science*, vol. 380, pp. 1034–1038, June 2023.
- [146] S. Fichtner, N. Wolff, F. Lofink, L. Kienle, and B. Wagner, "AlScN: A III-V semiconductor based ferroelectric," *Journal of Applied Physics*, vol. 125, Mar. 2019.

- [147] H. Wang, N. Adamski, S. Mu, and C. G. Van de Walle, "Piezoelectric effect and polarization switching in  $\text{Al}_{1-x}\text{Sc}_x\text{N}$ ," 2021.
- [148] W. Zhu, J. Hayden, F. He, J.-I. Yang, P. Tipsawat, M. D. Hossain, J.-P. Maria, and S. Trolier-McKinstry, "Strongly temperature dependent ferroelectric switching in  $\text{AlN}$ ,  $\text{Al}_{1-x}\text{Sc}_x\text{N}$ ,  $\text{Al}_{1-x}\text{B}_x\text{N}$  thin films," *Applied Physics Letters*, vol. 119, Aug. 2021.
- [149] D. Wang, P. Wang, B. Wang, and Z. Mi, "Fully epitaxial ferroelectric  $\text{ScGaN}$  grown on  $\text{GaN}$  by molecular beam epitaxy," *Applied Physics Letters*, vol. 119, Sept. 2021.
- [150] A. M. Saitta and F. Decremps, "Unifying description of the wurtzite-to-rocksalt phase transition in wide-gap semiconductors: the effect of  $d$  electrons on the elastic constants," *Physical Review B*, vol. 70, July 2004.
- [151] K. Yazawa, D. Drury, A. Zakutayev, and G. L. Brennecke, "Reduced coercive field in epitaxial thin film of ferroelectric wurtzite  $\text{Al}_{0.7}\text{Sc}_{0.3}\text{N}$ ," *Applied Physics Letters*, vol. 118, Apr. 2021.
- [152] K. Yazawa, J. S. Mangum, P. Gorai, G. L. Brennecke, and A. Zakutayev, "Local chemical origin of ferroelectric behavior in wurtzite nitrides," *Journal of Materials Chemistry C*, vol. 10, no. 46, pp. 17557–17566, 2022.
- [153] F. He, W. Zhu, J. Hayden, J. Casamento, Q. Tran, K. Kang, Y. Song, B. A. Akgun, J. I. Yang, P. Tipsawat, G. Brennecke, S. Choi, T. N. Jackson, J.-P. Maria, and S. Trolier-McKinstry, "Frequency dependence of wake-up and fatigue characteristics in ferroelectric  $\text{Al}_{0.93}\text{B}_{0.07}\text{N}$  thin films," *Acta Materialia*, p. 119678, Jan. 2024.
- [154] P. Wang, D. Wang, N. M. Vu, T. Chiang, J. T. Heron, and Z. Mi, "Fully epitaxial ferroelectric  $\text{ScAlN}$  grown by molecular beam epitaxy," *Applied Physics Letters*, vol. 118, May 2021.
- [155] C. Joseph, G. Ved, L. Hyunjea, N. Kazuki, M. Takuya, D. Benyamin, A. M. Javad, W. John, S. Yu-Tsun, M. D. A. L. Amit, Huili, Xing, and D. Jena, "Ferroelectricity in polar  $\text{ScAlN}/\text{GaN}$  epitaxial semiconductor heterostructures," 2021.
- [156] J. Ligl, S. Leone, C. Manz, L. Kirste, P. Doering, T. Fuchs, M. Prescher, and O. Ambacher, "Metalorganic chemical vapor phase deposition of  $\text{AlScN}/\text{GaN}$  heterostructures," *Journal of Applied Physics*, vol. 127, May 2020.
- [157] B.-T. Lin, W.-H. Lee, J. Shieh, and M.-J. Chen, "Ferroelectric  $\text{AlN}$  ultrathin films prepared by atomic layer epitaxy," in *Behavior and Mechanics of Multifunctional Materials XIII* (H. E. Naguib, ed.), SPIE, mar 2019.
- [158] X. Liu, D. Wang, K.-H. Kim, K. Katti, J. Zheng, P. Musavigharavi, J. Miao, E. A. Stach, R. H. Olsson, and D. Jariwala, "Post-CMOS compatible aluminum scandium nitride/2d channel ferroelectric field-effect-transistor memory," *Nano Letters*, vol. 21, pp. 3753–3761, Apr. 2021.
- [159] S. Singh and A. H. Romero, "Giant tunable rashba spin splitting in a two-dimensional  $\text{BiSb}$  monolayer and in  $\text{BiSb}/\text{AlN}$  heterostructures," *Physical Review B*, vol. 95, Apr. 2017.
- [160] G. Koster, B. L. Kropman, G. J. H. M. Rijnders, D. H. A. Blank, and H. Rogalla, "Quasi-ideal strontium titanate crystal surfaces through formation of strontium hydroxide," *Applied Physics Letters*, vol. 73, pp. 2920–2922, Nov. 1998.

- [161] J. E. Kleibeuker, G. Koster, W. Siemons, D. Dubbink, B. Kuiper, J. L. Blok, C.-H. Yang, J. Ravichandran, R. Ramesh, J. E. ten Elshof, D. H. A. Blank, and G. Rijnders, "Atomically defined rare-earth scandate crystal surfaces," *Advanced Functional Materials*, vol. 20, pp. 3490–3496, Aug. 2010.
- [162] R. Dirsyte, J. Schwarzkopf, G. Wagner, R. Fornari, J. Lienemann, M. Busch, and H. Winter, "Thermal-induced change in surface termination of DyScO<sub>3</sub>(110)," *Surface Science*, vol. 604, pp. L55–L58, Oct. 2010.
- [163] H. N. Lee, S. S. Ambrose Seo, W. S. Choi, and C. M. Rouleau, "Growth control of oxygen stoichiometry in homoepitaxial SrTiO<sub>3</sub> films by pulsed laser epitaxy in high vacuum," *Scientific Reports*, vol. 6, Jan. 2016.
- [164] C. Yu, A. S. Sokolov, P. Kulik, and V. G. Harris, "Stoichiometry, phase, and texture evolution in pld-grown hexagonal barium ferrite films as a function of laser process parameters," *Journal of Alloys and Compounds*, vol. 814, p. 152301, Jan. 2020.
- [165] R. Groenen, J. Smit, K. Orsel, A. Vailionis, B. Bastiaens, M. Huijben, K. Boller, G. Rijnders, and G. Koster, "Research update: Stoichiometry controlled oxide thin film growth by pulsed laser deposition," *APL Materials*, vol. 3, July 2015.
- [166] C. R. Brundle and B. V. Crist, "X-ray photoelectron spectroscopy: A perspective on quantitation accuracy for composition analysis of homogeneous materials," *Journal of Vacuum Science & Technology A*, vol. 38, no. 4, p. 041001, 2020.
- [167] A. G. Shard, "Practical guides for x-ray photoelectron spectroscopy: Quantitative XPS," *Journal of Vacuum Science and Technology A: Vacuum, Surfaces, and Films*, vol. 38, July 2020.
- [168] N. Laanait, M. Ziatdinov, Q. He, and A. Borisevich, "Identifying local structural states in atomic imaging by computer vision," *Advanced Structural and Chemical Imaging*, vol. 2, Nov. 2016.
- [169] Y. Wang, U. Salzberger, W. Sigle, Y. E. Suyolcu, and P. A. van Aken, "Oxygen octahedra picker: A software tool to extract quantitative information from STEM images," *Ultramicroscopy*, vol. 168, pp. 46–52, Sept. 2016.
- [170] M. Nord, P. E. Vullum, I. MacLaren, T. Tybell, and R. Holmestad, "Atomap: a new software tool for the automated analysis of atomic resolution images using two-dimensional gaussian fitting," *Advanced Structural and Chemical Imaging*, vol. 3, Feb. 2017.
- [171] D. H. Agarwal, P. M. Bhatt, A. M. Pathan, H. Patel, and U. S. Joshi, "Development of portable experimental set-up for AFM to work at cryogenic temperature," in *AIP Conference Proceedings*, AIP, 2012.
- [172] A. Z. Simões, T. B. Onofre, and F. Moura, "Characterization of ferroelectric calcium modified lead zirconate titanate films by piezoresponse force microscopy," *Journal of Advanced Microscopy Research*, vol. 5, pp. 129–136, Aug. 2010.
- [173] C. F. Chirila, V. Stancu, G. A. Boni, I. Pasuk, L. Trupina, L. D. Filip, C. Radu, I. Pintilie, and L. Pintilie, "Author correction: Controlling polarization direction in epitaxial Pb(Zr<sub>0.2</sub>Ti<sub>0.8</sub>)O<sub>3</sub> films through nb (n-type) and fe (p-type) doping," *Scientific Reports*, vol. 12, June 2022.
- [174] S. V. Kalinin, A. N. Morozovska, L. Q. Chen, and B. J. Rodriguez, "Local polarization dynamics in ferroelectric materials," *Reports on Progress in Physics*, vol. 73, p. 056502, Apr. 2010.

- [175] C. B. Sawyer and C. H. Tower, "Rochelle salt as a dielectric," *Physical Review*, vol. 35, p. 269–273, Feb. 1930.
- [176] J. F. Scott, "Ferroelectrics go bananas," *Journal of Physics: Condensed Matter*, vol. 20, p. 021001, Dec. 2007.
- [177] A. Loidl, S. Krohns, J. Hemberger, and P. Lunkenheimer, "Bananas go paraelectric," *Journal of Physics: Condensed Matter*, vol. 20, p. 191001, Apr. 2008.
- [178] D. G. Schlom, L.-Q. Chen, C. J. Fennie, V. Gopalan, D. A. Muller, X. Pan, R. Ramesh, and R. Uecker, "Elastic strain engineering of ferroic oxides," *MRS Bulletin*, vol. 39, pp. 118–130, Feb. 2014.
- [179] H. Béa, B. Dupé, S. Fusil, R. Mattana, E. Jacquet, B. Warot-Fonrose, F. Wilhelm, A. Rogalev, S. Petit, V. Cros, A. Anane, F. Petroff, K. Bouzehouane, G. Geneste, B. Dkhil, S. Lisenkov, I. Ponomareva, L. Bellaiche, M. Bibes, and A. Barthélémy, "Evidence for room-temperature multiferroicity in a compound with a giant axial ratio," *Physical Review Letters*, vol. 102, May 2009.
- [180] I. C. Infante, S. Lisenkov, B. Dupé, M. Bibes, S. Fusil, E. Jacquet, G. Geneste, S. Petit, A. Courtial, J. Juraszek, L. Bellaiche, A. Barthélémy, and B. Dkhil, "Bridging multiferroic phase transitions by epitaxial strain in BiFeO<sub>3</sub>," *Physical Review Letters*, vol. 105, July 2010.
- [181] P. Chen, N. J. Podraza, X. S. Xu, A. Melville, E. Vlahos, V. Gopalan, R. Ramesh, D. G. Schlom, and J. L. Musfeldt, "Optical properties of quasi-tetragonal BiFeO<sub>3</sub> thin films," *Applied Physics Letters*, vol. 96, p. 131907, Mar. 2010.
- [182] H. M. Christen, J. H. Nam, H. S. Kim, A. J. Hatt, and N. A. Spaldin, "Stress-induced  $r$ - $m_a$ - $m_c$ - $t$  symmetry changes in BiFeO<sub>3</sub> films," *Physical Review B*, vol. 83, Apr. 2011.
- [183] D. A. Tenne, P. Turner, J. D. Schmidt, M. Biegalski, Y. L. Li, L. Q. Chen, A. Soukiassian, S. Trolier-McKinstry, D. G. Schlom, X. X. Xi, D. D. Fong, P. H. Fuoss, J. A. Eastman, G. B. Stephenson, C. Thompson, and S. K. Streiffer, "Ferroelectricity in ultrathin BaTiO<sub>3</sub> films: Probing the size effect by ultraviolet raman spectroscopy," *Physical Review Letters*, vol. 103, Oct. 2009.
- [184] A. Grünebohm, M. Marathe, and C. Ederer, "*Ab initio* phase diagram of BaTiO<sub>3</sub> under epitaxial strain revisited," *Applied Physics Letters*, vol. 107, p. 102901, Sept. 2015.
- [185] S. K. Streiffer, J. A. Eastman, D. D. Fong, C. Thompson, A. Munkholm, M. V. R. Murty, O. Auciello, G. R. Bai, and G. B. Stephenson, "Observation of nanoscale 180° stripe domains in ferroelectric PbTiO<sub>3</sub> thin films," *Physical Review Letters*, vol. 89, July 2002.
- [186] D. D. Fong, G. B. Stephenson, S. K. Streiffer, J. A. Eastman, O. Auciello, P. H. Fuoss, and C. Thompson, "Ferroelectricity in ultrathin perovskite films," *Science*, vol. 304, pp. 1650–1653, June 2004.
- [187] R. J. Zeches, M. D. Rossell, J. X. Zhang, A. J. Hatt, Q. He, C.-H. Yang, A. Kumar, C. H. Wang, A. Melville, C. Adamo, G. Sheng, Y.-H. Chu, J. F. Ihlefeld, R. Erni, C. Ederer, V. Gopalan, L. Q. Chen, D. G. Schlom, N. A. Spaldin, L. W. Martin, and R. Ramesh, "A strain-driven morphotropic phase boundary in BiFeO<sub>3</sub>," *Science*, vol. 326, pp. 977–980, Nov. 2009.
- [188] S. A. Lee, H. Jeong, S. Woo, J.-Y. Hwang, S.-Y. Choi, S.-D. Kim, M. Choi, S. Roh, H. Yu, J. Hwang, S. W. Kim, and W. S. Choi, "Phase transitions via selective elemental vacancy engineering in complex oxide thin films," *Sci. Rep.*, vol. 6, p. 23649, Apr. 2016.

- [189] T. Gagnidze, H. Ma, C. Cancellieri, G.-L. Bona, and F. L. Mattina, "Structural properties of ultrathin SrO film deposited on SrTiO<sub>3</sub>," *Science and Technology of Advanced Materials*, vol. 20, pp. 456–463, May 2019.
- [190] G. Verdierre, N. Gauquelin, D. Jannis, Y. A. Birkhölzer, S. Mallik, J. Verbeeck, M. Bibes, and G. Koster, "Epitaxial growth of the candidate ferroelectric rashba material SrBiO<sub>3</sub> by pulsed laser deposition," *APL Materials*, vol. 11, p. 031109, Mar. 2023.
- [191] P. Dufour, *Structural and physical properties of antiferroic oxide thin films*. PhD thesis, 2023. Thèse de doctorat dirigée par Garcia, Vincent et Maroutian, Thomas Physique université Paris-Saclay 2023.
- [192] G. Koster, L. Klein, W. Siemons, G. Rijnders, J. S. Dodge, C.-B. Eom, D. H. A. Blank, and M. R. Beasley, "Structure, physical properties, and applications of SrRuO<sub>3</sub> thin films," *Reviews of Modern Physics*, vol. 84, pp. 253–298, Mar. 2012.
- [193] M. Cuoco and A. Di Bernardo, "Materials challenges for SrRuO<sub>3</sub>: From conventional to quantum electronics," *APL Materials*, vol. 10, Sept. 2022.
- [194] S. Pandya, G. A. Velarde, R. Gao, A. S. Everhardt, J. D. Wilbur, R. Xu, J. T. Maher, J. C. Agar, C. Dames, and L. W. Martin, "Understanding the role of ferroelastic domains on the pyroelectric and electrocaloric effects in ferroelectric thin films," *Advanced Materials*, vol. 31, Dec. 2018.
- [195] K. Ellmer, "Past achievements and future challenges in the development of optically transparent electrodes," *Nature Photonics*, vol. 6, pp. 809–817, Nov. 2012.
- [196] H. Ohta, M. Orita, M. Hirano, H. Tanji, H. Kawazoe, and H. Hosono, "Highly electrically conductive indium–tin–oxide thin films epitaxially grown on yttria-stabilized zirconia (100) by pulsed-laser deposition," *Applied Physics Letters*, vol. 76, pp. 2740–2742, May 2000.
- [197] H. J. Kim, U. Kim, H. M. Kim, T. H. Kim, H. S. Mun, B.-G. Jeon, K. T. Hong, W.-J. Lee, C. Ju, K. H. Kim, and K. Char, "High mobility in a stable transparent perovskite oxide," *Applied Physics Express*, vol. 5, p. 061102, May 2012.
- [198] X. Luo, Y. S. Oh, A. Sirenko, P. Gao, T. A. Tyson, K. Char, and S.-W. Cheong, "High carrier mobility in transparent Ba<sub>1-x</sub>La<sub>x</sub>SnO<sub>3</sub> crystals with a wide band gap," *Applied Physics Letters*, vol. 100, p. 172112, Apr. 2012.
- [199] H. J. Kim, U. Kim, T. H. Kim, J. Kim, H. M. Kim, B.-G. Jeon, W.-J. Lee, H. S. Mun, K. T. Hong, J. Yu, K. Char, and K. H. Kim, "Physical properties of transparent perovskite oxides(La,Ba)SnO<sub>3</sub> with high electrical mobility at room temperature," *Physical Review B*, vol. 86, Oct. 2012.
- [200] J. Wang, *Oxide Electrodes for Pb(Zr<sub>0.52</sub>Ti<sub>0.48</sub>)O<sub>3</sub> Capacitors*. PhD thesis.
- [201] M. Zhu, P. Komissinskiy, A. Radetinac, M. Vafaei, Z. Wang, and L. Alff, "Effect of composition and strain on the electrical properties of LaNiO<sub>3</sub> thin films," *Applied Physics Letters*, vol. 103, p. 141902, Sept. 2013.
- [202] G. Kim, M. Neumann, M. Kim, M. D. Le, T. D. Kang, and T. W. Noh, "Suppression of three-dimensional charge density wave ordering via thickness control," *Physical Review Letters*, vol. 115, Nov. 2015.
- [203] H. Weaver, "Dielectric properties of single crystals of SrTiO<sub>3</sub> at low temperatures," *Journal of Physics and Chemistry of Solids*, vol. 11, pp. 274–277, Oct. 1959.

- [204] H. Yamada, V. Garcia, S. Fusil, S. Boyn, M. Marinova, A. Gloter, S. Xavier, J. Grollier, E. Jacquet, C. Carrétéro, C. Deranlot, M. Bibes, and A. Barthélémy, "Giant electroresistance of super-tetragonal BiFeO<sub>3</sub>-based ferroelectric tunnel junctions," *ACS Nano*, vol. 7, p. 5385–5390, May 2013.
- [205] Y. S. Kim, D. J. Kim, T. H. Kim, T. W. Noh, J. S. Choi, B. H. Park, and J.-G. Yoon, "Observation of room-temperature ferroelectricity in tetragonal strontium titanate thin films on SrTiO<sub>3</sub> (001) substrates," *Applied Physics Letters*, vol. 91, July 2007.
- [206] T. Li, S. Deng, H. Liu, S. Sun, H. Li, S. Hu, S. Liu, X. Xing, and J. Chen, "Strong room-temperature ferroelectricity in strained SrTiO<sub>3</sub> homoepitaxial film," *Advanced Materials*, vol. 33, p. 2008316, Apr. 2021.
- [207] J. H. Haeni, P. Irvin, W. Chang, R. Uecker, P. Reiche, Y. L. Li, S. Choudhury, W. Tian, M. E. Hawley, B. Craigo, A. K. Tagantsev, X. Q. Pan, S. K. Streiffer, L. Q. Chen, S. W. Kirchoefer, J. Levy, and D. G. Schlom, "Room-temperature ferroelectricity in strained SrTiO<sub>3</sub>," *Nature*, vol. 430, p. 758–761, Aug. 2004.
- [208] Z. Liao, M. Huijben, Z. Zhong, N. Gauquelin, S. Macke, R. J. Green, S. Van Aert, J. Verbeeck, G. Van Tendeloo, K. Held, G. A. Sawatzky, G. Koster, and G. Rijnders, "Controlled lateral anisotropy in correlated manganite heterostructures by interface-engineered oxygen octahedral coupling," *Nature Materials*, vol. 15, p. 425–431, Mar. 2016.
- [209] C. Lichtensteiger, C.-P. Su, I. Gaponenko, M. Hadjimichael, L. Tovaglieri, P. Paruch, A. Gloter, and J.-M. Triscone, "Nanoscale domain engineering in SrRuO<sub>3</sub> thin films," *APL Materials*, vol. 11, Oct. 2023.
- [210] S. Yasuoka, T. Shimizu, A. Tateyama, M. Uehara, H. Yamada, M. Akiyama, Y. Hiranaga, Y. Cho, and H. Funakubo, "Effects of deposition conditions on the ferroelectric properties of Al<sub>1-x</sub>Sc<sub>x</sub>N thin films," *J. Appl. Phys.*, vol. 128, Sept. 2020.
- [211] K. Yazawa, J. S. Mangum, P. Gorai, G. L. Brennecka, and A. Zakutayev, "Local chemical origin of ferroelectric behavior in wurtzite nitrides," *J. Mater. Chem. C Mater. Opt. Electron. Devices*, vol. 10, no. 46, pp. 17557–17566, 2022.
- [212] K.-H. Kim, I. Karpov, R. H. Olsson, and D. Jariwala, "Wurtzite and fluorite ferroelectric materials for electronic memory," *Nature Nanotechnology*, vol. 18, pp. 422–441, Apr. 2023.
- [213] D. H. Lee, Y. Lee, Y. H. Cho, H. Choi, S. H. Kim, and M. H. Park, "Unveiled ferroelectricity in well-known non-ferroelectric materials and their semiconductor applications," *Advanced Functional Materials*, vol. 33, June 2023.
- [214] R. Mizutani, S. Yasuoka, T. Shiraishi, T. Shimizu, M. Uehara, H. Yamada, M. Akiyama, O. Sakata, and H. Funakubo, "Thickness scaling of (Al<sub>0.8</sub>Sc<sub>0.2</sub>)N films with remanent polarization beyond 100 μC cm<sup>-2</sup> around 10 nm in thickness," *Applied Physics Express*, vol. 14, p. 105501, Sept. 2021.
- [215] S. Yasuoka, R. Mizutani, R. Ota, T. Shiraishi, T. Shimizu, S. Yasui, Y. Ehara, K. Nishida, M. Uehara, H. Yamada, M. Akiyama, Y. Imai, O. Sakata, and H. Funakubo, "Enhancement of crystal anisotropy and ferroelectricity by decreasing thickness in (Al, Sc)N films," *Journal of the Ceramic Society of Japan*, vol. 130, p. 436–441, July 2022.
- [216] S.-L. Tsai, T. Hoshii, H. Wakabayashi, K. Tsutsui, T.-K. Chung, E. Y. Chang, and K. Kakushima, "Room-temperature deposition of a poling-free ferroelectric AlScN film by reactive sputtering," *Applied Physics Letters*, vol. 118, Feb. 2021.

- [217] T. Fan, M. Tobah, T. Shirokura, N. Huynh Duy Khang, and P. Nam Hai, "Crystal growth and characterization of topological insulator BiSb thin films by sputtering deposition on sapphire substrates," *Japanese Journal of Applied Physics*, vol. 59, p. 063001, June 2020.
- [218] L. Baringthon, *Élaboration et caractérisation de phases topologiques de l'alliage  $Bi_{1-x}Sb_x$  pour la conversion spin charge*. PhD thesis, 2022. Thèse de doctorat dirigée par George, Jean-Marie Le Fèvre, Patrick et Lemaître, Aristide Physique université Paris-Saclay 2022.
- [219] W. Qiao, J. Zhao, Y. Chen, S. Cao, W. Xing, R. Cai, L. Guo, T. Qian, X. C. Xie, and W. Han, "Observation of quasi-two-dimensional superconductivity at the EuO-BaBiO<sub>3</sub> interface," *Physical Review B*, vol. 109, Feb. 2024.
- [220] G. Acero, H. Moreno, P. Ortega, M. Ramirez, M. Ponce, F. Moura, and A. Simões, "Unveiling the polar properties on barium bismuthate perovskite thin films with distinct Ba/Bi ratios," *Journal of Alloys and Compounds*, vol. 974, p. 172871, Feb. 2024.
- [221] Z. Ren, M. Wang, P. Liu, Q. Liu, K. Wang, G. Jakob, J. Chen, K. Meng, X. Xu, J. Miao, and Y. Jiang, "Spin logical and memory device based on the nonvolatile ferroelectric control of the perpendicular magnetic anisotropy in PbZr<sub>0.2</sub>Ti<sub>0.8</sub>O<sub>3</sub>/Co/Pt heterostructure," *Advanced Electronic Materials*, vol. 6, Apr. 2020.
- [222] L. Chen, C. Liu, H. K. Lee, B. Varghese, R. W. F. Ip, M. Li, Z. J. Quek, Y. Hong, W. Wang, W. Song, H. Lin, and Y. Zhu, "Demonstration of 10 nm ferroelectric Al<sub>0.7</sub>Sc<sub>0.3</sub>N-based capacitors for enabling selector-free memory array," *Materials*, vol. 17, p. 627, Jan. 2024.
- [223] V. Garcia and M. Bibes, "Ferroelectric tunnel junctions for information storage and processing," *Nature Communications*, vol. 5, July 2014.

# Appendix A

## Résumé de la thèse en français

Alors que la spintronique classique s'est traditionnellement appuyée sur les métaux ferromagnétiques comme générateurs et détecteurs de spin, les effets de couplage spin-orbite permettent désormais de générer et de détecter efficacement des courants de spin à partir de courants de charge dans des architectures exemptes de matériaux ferromagnétiques. Cependant, les systèmes existants capables d'obtenir cette interconversion spin/charge ne possèdent pas le caractère non volatil des matériaux ferromagnétiques. La non volatilité de l'état ferroïque est une condition nécessaire pour le stockage et le traitement de données. Les recherches présentées dans cette thèse visent à développer des systèmes dans lesquels il sera possible de combiner les avantages du couplage spin-orbite de type Rashba (RSOC) pour une interconversion efficace entre les courants de spin et de charge avec une autre famille de systèmes ferroïques, les ferroélectriques.

Le RSOC apparaît dans les systèmes dont la symétrie d'inversion est brisée, et est plus fort en présence d'éléments lourds qui tendent à avoir un couplage spin orbite important. Les ferroélectriques rompent intrinsèquement la symétrie d'inversion et pourraient donc abriter du RSOC. En prime, la commutation de la polarisation du ferroélectrique via un champ électrique devrait pouvoir changer le signe du RSOC, et ce faisant la polarité avec laquelle le matériau interconvertirait les courants de spin en courant de charge via l'effet Edelstein. De plus, les ferroélectriques peuvent accumuler (ou réduire) de très grandes densités de porteurs dans les matériaux adjacents et ainsi générer des champs électriques à l'interface qui dépendent de la direction de la polarisation du matériau ferroélectrique. En utilisant cet effet, il est donc possible de créer un RSOC interfacial qui devrait également être commutable par l'action d'un champ électrique, permettant ainsi un contrôle électrique et non volatil de l'interconversion spin/charge. L'interfaciabilité de la ferroélectricité et du couplage spin-orbite peut se faire de trois façons:

(i) Dans des gazs 2D d'électrons créés à l'interface entre un ferroélectrique et un autre matériau (2DEG). Il a été démontré qu'il est possible de transférer des propriétés de ferroélectricité aux électrons gaz. En présence d'éléments lourds, les électrons du 2DEG sont à la fois soumis à un fort couplage et à un champ de brisure de symétrie normal à leur direction de propagation. Ils sont donc soumis à un effet Rashba modulable par la ferroélectricité. Ce résultat a été démontré dans un gaz 2D créé à la surface de  $\text{SrTiO}_3$  sur lequel une couche d'aluminium a été déposée par pulvérisation cathodique pour créer un gaz 2D. Un état ferroélectrique peut être induit dans  $\text{SrTiO}_3$  en dessous de 50 K, ce qui a permis la démonstration de la modulation du coefficient Rashba du gaz. Néanmoins, il est important de noter que ces mesures ne sont possibles qu'en dessous de 50 K, ne permettant pas leur implémentation dans des procédés industriels.

(ii) dans des matériaux monophasés qui présentent à la fois des propriétés ferroélectriques et un fort couplage spin-orbite. Ces matériaux sont aussi connus sous le nom de "FerroElectric Rasha Semi Conductors

(FERSCs)". Le premier membre de cette famille, dont les propriétés ont été prédites en 2014, est le GeTe. C'est aussi le seul matériau de cette famille qui a été étudié expérimentalement. Néanmoins, les mauvaises propriétés ferroélectriques de ce matériau, liées à son faible gap, induisent de forts courants de fuites et empêchent son utilisation pour une conversion de courants de spin vers des courant de charge avec un bon rendement. Différents matériaux ont été prédit comme FERSC, parmi lesquels  $\text{SrBiO}_3$ , dont nous avons prédit qu'il deviendrait ferroélectrique avec un RSOC commutable si il était soumis à une forte contrainte en compression, et ce à température ambiante. La première partie expérimentale de ce manuscrit porte sur l'optimisation de la croissance de ce matériau par ablation à laser pulsé, tandis que la deuxième partie expérimentale se concentre sur la caractérisation de ses propriétés ferroélectriques.

(iii) Dans des systèmes multicouches, combinant un matériau ferroélectrique et un matériau à fort couplage spin-orbite. De nombreux systèmes ont été étudiés, le plus probant ( i.e. celui pour lequel la différence entre les coefficients Rashba dans les deux états de polarisation du ferroélectrique est la plus importante) est un système multicouche composé de  $\text{PbZr}_x\text{Ti}_{1-x}\text{O}_3$  (PZT), un ferroélectrique dont les propriétés sont bien connues, et de Pt (111). Dans de tels systèmes, il est possible de renverser le signe du coefficient Rashba dans la platine en changeant le signe de la polarisation dans le PZT. Néanmoins, ces systèmes présentent un certain nombre de défauts. Premièrement, leurs coefficients d'interconversion spin-charge ne sont pas assez élevés pour permettre une utilisation à faible énergie. De plus, ces systèmes ne sont que modérément compatibles avec les technologies existantes de par leur maille élémentaire cubique. Dans le cadre du travail mené durant cette thèse, nous avons conçu et caractérisé un système multicouches combinant un membre de la famille des wurtzites ferroélectriques, le (Al,Sc)N, avec le BiSb, dont les propriétés pourraient être modulées à l'aide de la ferroélectricité. Les mailles élémentaires des différents constituants de cette multicouche faisant partie du système hexagonal, ces couches sont fortement compatibles avec les technologies existantes. De plus, (Al,Sc)N est déjà utilisé à un niveau industriel, notamment en tant que matériau constituant d'antennes 4G et 5G. A ce titre, la possibilité de croître ce matériau à grande échelle a déjà été démontrée, ce qui lui confère un intérêt supplémentaire. La troisième partie expérimentale de cette thèse présente une étude d'optimisation de croissance de couches minces de (Al,Sc)N par pulvérisation cathodique, ainsi qu'une démonstration de la faisabilité de croître in-situ les systèmes multicouches susmentionnés sans forte altération de leurs propriétés cristallographiques.

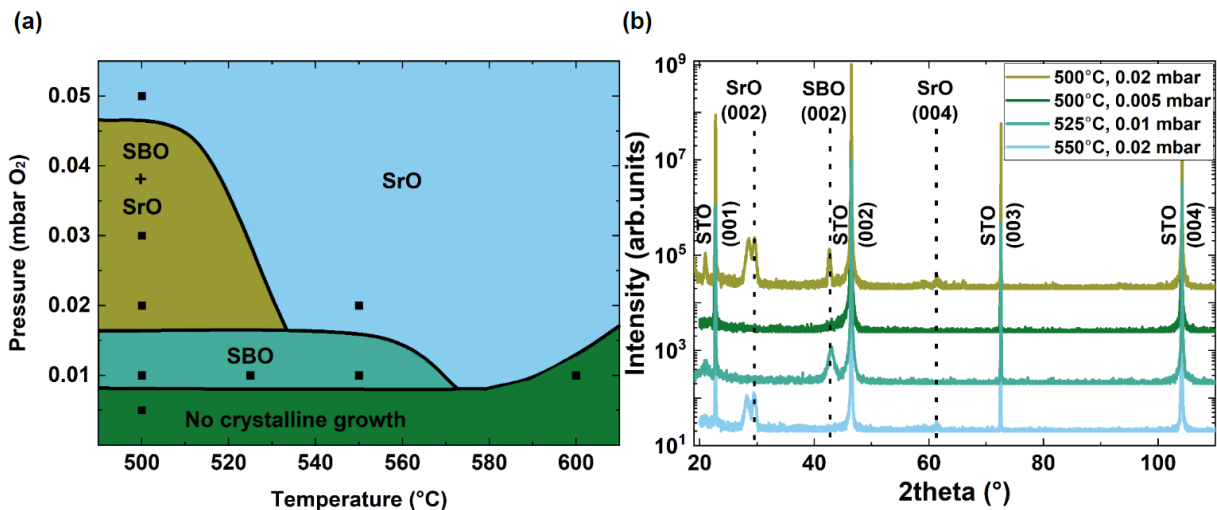
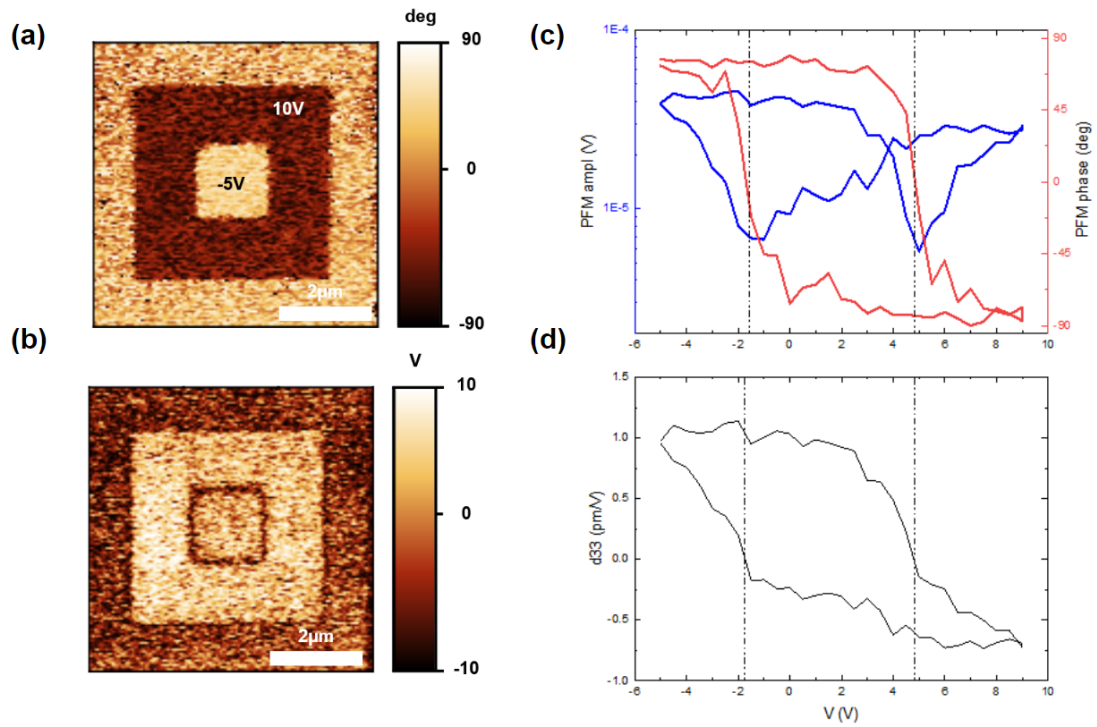


Figure A.1: Diagramme de phase pour la croissance de SBO sur STO.

Dans le premier chapitre expérimental de cette thèse, nous présentons une étude de croissance du matériau  $\text{SrBiO}_3$ .  $\text{SrBiO}_3$  fait partie de la famille des bismuthates. Ces matériaux ont une maille pérovskite, avec un

formule générique  $ABO_3$ , et comporte un atome de bismuth sur le site B. Ils ont été étudiés sous forme de céramiques dans les années 70 pour leurs propriétés de supraconducteurs à haute température ( par exemple  $T_c = 32$  K pour  $Ba_{1-x}K_xBiO_3$  ). Néanmoins, la possibilité de les croître sous forme de couches minces n'a été que très peu étudiée. Le premier objectif de cette thèse était donc d'optimiser la croissance de  $SrBiO_3$ , et d'étudier la possibilité d'induire une transition de phase vers une phase ferroélectrique à l'aide de contraintes épitaxiales. Pour ce faire, nous avons, dans un premier temps, commencé par optimiser nos croissances sur du  $SrTiO_3$ , un substrat bien connu et disponible en grande quantité. La forte différence entre les paramètres de maille ( plus de 8 %) devrait résulter en des couches de  $SrBiO_3$  relaxées. Lors de notre étude de croissance, nous avons pu constater que nos couches se décomposaient à l'air libre. Ce constat a été effectué à l'aide de mesures de diffraction aux rayons Xs ainsi que à l'aide de diffraction d'électrons *in-situ*. Pour palier à ce problème, nous avons commencé par introduire une couche protectrice. Nous avons déterminé que 1 monocouche atomique de  $SrTiO_3$  était suffisante pour empêcher la dégradation de nos couches d'intérêt. Nous avons ensuite optimisé la croissance de nos couches et avons pu construire un diagramme de phase, fonction de la pression et de la température de croissance. Les conditions optimales de croissance sont les suivantes:  $T = 525$  °C,  $P_{O_2} = 10^{-2}$  mbar,  $J = 1.9$  J/cm<sup>-2</sup>,  $f = 1$  Hz. Le recuit de ces couches a aussi été optimisé, le procédé optimal étant le suivant: à la fin de la croissance, de l'oxygène est introduit dans la chambre de croissance jusqu'à atteindre une pression de 100 mbar. Les couches (de  $SrBiO_3$  protégées par une monocouche atomique de  $SrTiO_3$ ) sont ensuite refroidies, à 25 °C/min, jusqu'à ce qu'elles atteignent une température de 300 °C. Les couches restent alors 20 min à cette température sous l'atmosphère susmentionnée, après quoi elles sont refroidies jusqu'à température ambiante à 25 °C/min. La mesure de diffraction d'électrons RHEED *in-situ* permet de suivre la croissance des couches minces monocouche par monocouche. Les couches sont ensuite caractérisées par diffraction aux rayons Xs (DRX), par microscopie à force atomique (AFM) et par spectroscopie aux rayons Xs (XPS). Les résultats de mesures XPS prouvent que nos couches sont uniquement constituées de Sr, de Bi et de O. Ces trois constituants sont présents avec un rapport de 1:1:3, ce qui est le rapport stoechiométrique attendu pour les couches que nous avons fait croître. Les mesures de DRX indiquent que les films minces ont une structure perovskite orientée (001) avec un paramètre de maille hors plan de  $4.25 \pm 0.05$  Angstrom, ce qui est en bon accord avec les données publiées dans d'autres rapports traitant de ce matériau. Les mesures de RHEED et de cartes d'espace réciproque semblent indiquer que le paramètre de maille dans le plan de nos mailles est de  $4.3 \pm 0.05$  Angstrom, ce qui voudrait dire que les couches sont soumises à une contrainte en tension, ce qui est contre intuitif étant donné que le  $SrTiO_3$  a un paramètre de maille plus petit que celui de  $SrBiO_3$ . Pour comprendre l'origine de cette contrainte en tension, nous avons collaboré avec Nicolas Gauquelin, de l'Université d' Anvers. Dans le cadre de cette collaboration, des couches de  $SrBiO_3$  sur  $SrTiO_3$  ont été imagées par microscopie électronique à balayage. A l'aide de ces mesures et de leur analyse, effectuée à l'aide d'un programme Python construit à l'aide du package "atomap", nous avons pu déterminer que à l'interface entre la couche mince et son substrat la contrainte se relaxe grâce à deux mécanismes distincts: (i) l'introduction de deux monocouches de SrO avec une structure cristalline cubique à faces centrées du type sel gemme. (ii) la formation de dislocations d'inadaptation périodiques. La formation de ces dislocations, présentent toutes les 10 mailles élémentaires de  $SrBiO_3$  pour 11 mailles élémentaires de  $SrTiO_3$ , induit dans la couche mince une contrainte en tension de telle façon que  $10x_{a_{SBO}} = 11x_{a_{STO}}$ .

Nous avons ensuite tenté d'induire une contrainte épitaxiale dans nos films en changeant le substrat. Le substrat que nous avons le plus longuement étudié est le  $NdScO_3$  (110). Ce matériau possède un paramètre de maille pseudo cubique de 4.01 Angstrom, ce qui permettrait d'induire une contrainte en compression de 5 % dans le  $SrBiO_3$ . Cette contrainte correspond à celle à laquelle il a été prédit que le  $SrBiO_3$  subirait une transition de phase vers une phase ferroélectrique. Les conditions de croissance pour le  $SrBiO_3$  sur ce nouveau substrat sont identiques à celles susmentionnées pour la croissance sur  $SrTiO_3$ . Les mesures des différents paramètres de maille par DRX et par diffraction RHEED indiquent que les couches sont relaxées ( les paramètres de



**Figure A.2:** Ferroélectricité dans des multicouches de SBO/LBSO/NSO. (a) Phase et (b) amplitude du signal PFM. La mesure du cycle ferroélectrique présenté en (c) permet d'extraire le coefficient piezoélectrique (d).

maille sont  $a=b=c= 4.26 \pm 0.05$  Angstrom ). Néanmoins, les images de microscopie électronique à balayage semblent indiquer qu'une couche interfaciale de quelques monocouches d'épaisseur ( 5 ou 6 ) se formerait à en dessous les dislocations qui relaxent la contrainte. A l'aide du programme susmentionné, nous avons pu mettre en évidence que dans cette couche la maille élémentaire du  $\text{SrBiO}_3$  n'était pas cubique. De plus, en regardant la position du cation centrale de la structure perovskite, il est possible d'inférer sur la présence de dipôles dans nos mailles. La présence de dipôle est un pré requis strict de la ferroélectricité. Nous avons montré que dans la couche interfaciale susmentionnée, il y avait des signes de polarisation. Ces résultats de MEB semblent indiquer l'existence d'une épaisseur non nulle à l'interface avec le substrat qui serait à la fois tétragonale et polaire. Nous supposons que cette couche pourrait être ferroélectrique.

Pour pouvoir tester les propriétés ferroélectriques de nos couches, il nous a fallu optimiser la croissance d'électrodes basses avec un paramètre de maille adéquat. Nous avons identifié trois systèmes d'intérêt: des substrats de  $\text{SrTiO}_3$  dopé à 0.05 % avec du Nb, et deux couches minces: le  $\text{Ba}_{0.5}\text{Sr}_{0.5}\text{RuO}_3$  (BSRO) et le  $\text{La}_{0.07}\text{Ba}_{0.93}\text{SnO}_3$  (LBSO). Dans un premier temps, les croissance SBO sur Nb-STO nous ont permis de démontrer que le SBO était bien isolant, à l'aide de méthodes d'imagerie à force atomique avec une pointe conductive. Dans un second temps, nous avons optimisé la croissance de BSRO sur les substrats de STO et de LBSO sur les substrats de NSO. La croissance de couches minces sur ces deux électrodes a ensuite été faite avec le même procédé expérimental que celui précédemment décrit. Les mesures de DRX ont révélé que dans la multicouche SBO/BSRO/STO, le SBO était soumis à un faible état de contrainte en tension. Ces multicouches ont été étudiées par microscopie à force atomique piézoélectrique (PFM). Cette méthode de pointe permet d'imager les domaines piézoélectriques dans un matériau et d'ainsi remonter à ses propriétés ferroélectriques. Les multicouches de SBO/BSRO/STO n'ont donné aucun signal probant au PFM, nous en avons donc conclu que le SBO était bel et bien paraélectrique. Dans les multicouches SBO/LBSO/NSO, les mesures de DRX et de diffraction RHEED semblent indiquer un état de contrainte en compression du film. Ce résultat est d'autant plus encourageant que les couches relaxées épitaxiées sur NSO semblaient déjà

présenter une épaisseur critique soumise à un certain niveau de contrainte. On peut donc espérer que pour des couches contraintes, ce niveau de compression à l'échelle nanoscopique soit d'autant plus important. Dans ces multicouches ci, contrairement à celles précédemment considérées, nous avons pu observer un signal PFM clair, caractéristique d'un comportement ferroélectrique. Au vu des différents résultats obtenus par DRX, par PFM et STEM, nous en avons donc conclu que les couches de SBO épitaxiées sur une électrode de LBSO sur NSO étaient ferroélectriques, et que ces propriétés ferroélectriques étaient dues à une transition de phase induite par une contrainte compressive. Nous notons que la mesure par STEM d'une de ces multicouches auraient pu nous aider à confirmer nos résultats. Néanmoins, la durée de vie des couches étant limitée, ces mesures n'ont pas pu être effectuées. De plus, dans le but d'utiliser ces multicouches pour effectuer de conversion spin-charge, il serait intéressant d'induire un état de conduction à la surface de ce matériau. La création d'un tel état pourrait à terme permettre de démontrer la faisabilité du contrôle par ferroélectricité du couplage Rashba dans ce système.

Dans un second temps, nous avons développé un système multicouches à base de (Al,Sc)N et de BiSb. L'optimisation de la croissance de (Al,Sc)N a été effectuée par co-pulvérisation cathodique sur une couche de 20 nm de Pt(111) sur SiO<sub>2</sub>/Si. Au terme de cette étude, présentée dans le chapitre A nous avons obtenu des couches de (Al,Sc)N que nous avons caractérisées à l'aide de DRX, d'XPS et de MTEB. Les propriétés cristallographiques de nos couches sont similaires à celles de films dont les propriétés ont été publiées dans des articles de revues scientifiques. De plus, nous avons caractérisé les propriétés ferroélectriques de nos films à l'aide d'un système 4 pointes et de PFM. Les propriétés mesurées sont en accord avec celles disponibles dans la littérature, avec notamment un champ coercitif de 4000 kV/cm pour une couche de 50 nm d'épaisseur et un doping de 30 %. De plus, nous aussi pu démontrer la faisabilité de la croissance de multicouches de (Al,Sc)N/ BiSb. BiSb est un isolant topologique dans lequel il a été démontré qu'il était possible d'effectuer de la conversion spin-charge. Nos multicouches ont été caractérisées par MEB. Ces caractérisation ont permis de démontrer que dans la monocouche (Al,Sc)N/BiSb/Sapphire les différentes couches étaient continues, et que la couche de BiSb étaient monocristalline tandis que celle de (Al,Sc)N était polycristalline mais néanmoins orientée selon l'axe normal à l'interface. La suite du projet, qui est en cours, sera de caractériser l'effet d'un renversement de la porisation de (Al,Sc)N sur les propriétés de conversion spin-charge du BiSb.

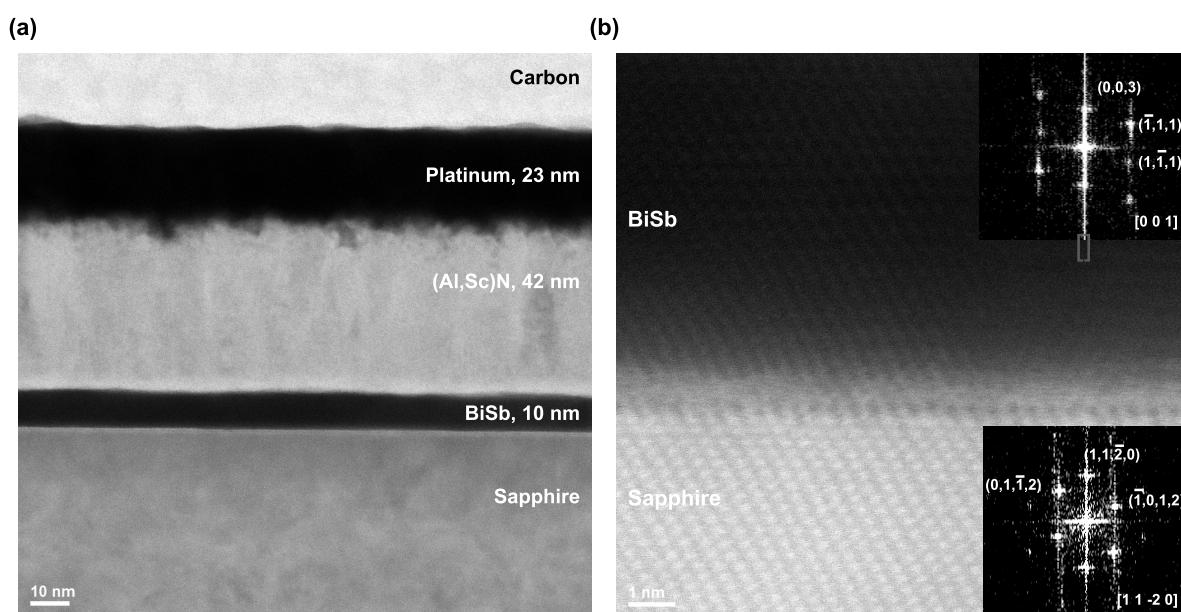


**Figure A.3:** Caractérisation par MEB des multicouches de (Al,Sc)N/BiSb//Sapphire.

En conclusion, dans le travail présenté dans cette nous avons pu développer et caractériser deux systèmes ferroélectriques Rashba: (i) un matériau monophasé,  $\text{SrBiO}_3$ , dont nous avons prédit qu'il deviendrait ferroélectrique avec un RSOC commutable si il était soumis à une forte contrainte en compression (ii) un système multicouches combinant un membre de la famille des wurtzites ferroélectriques, le  $(\text{Al,Sc})\text{N}$ , avec le  $\text{BiSb}$ , dont les propriétés pourraient être modulées à l'aide de la ferroélectricité.

**Titre :** Développement de nouveaux matériaux pour le contrôle ferroélectrique du couplage Rashba spin-orbit et de l'interconversion spin-charge

**Mots clés :** Rashba, Oxydes, Ferroélectriques, Wurtzites

**Résumé :** Alors que la spintronique classique s'est traditionnellement appuyée sur les métaux ferromagnétiques comme générateurs et détecteurs de spin, les effets de couplage spin-orbite permettent désormais de générer et de détecter efficacement des courants de spin à partir de courants de charge dans des architectures exemptes de matériaux ferromagnétiques. Cependant, les systèmes existants capables d'obtenir cette interconversion spin/charge ne possèdent pas le caractère non volatil des matériaux ferromagnétiques. La non volatilité de l'état ferroïque est une condition nécessaire pour le stockage et le traitement de données. Les recherches présentées dans cette thèse visent à développer des systèmes dans lesquels il sera possible de combiner les avantages du couplage spin-orbite de type Rashba (RSOC) pour une interconversion efficace entre les courants de spin et de charge avec une autre famille de systèmes ferroïques, les ferroélectriques. Le RSOC apparaît dans les systèmes dont la symétrie d'inversion est brisée, et est plus fort en présence d'éléments lourds. Les ferroélectriques rompent intrinsèquement la symétrie d'inversion et pourraient donc abriter du RSOC. En prime, la commutation de la polarisation du ferroélectrique via un champ

électrique devrait pouvoir changer le signe du RSOC, et ce faisant la polarité avec laquelle le matériau interconvertirait les courants de spin en courant de charge via l'effet Edelstein. De plus, les ferroélectriques peuvent accumuler (ou réduire) de très grandes densités de porteurs dans les matériaux adjacents et ainsi générer des champs électriques à l'interface qui dépendent de la direction de la polarisation du matériau ferroélectrique. En utilisant cet effet, il est donc possible de créer un RSOC interfacial qui devrait également être commutable par l'action d'un champ électrique, permettant ainsi un contrôle électrique et non volatil de l'interconversion spin/charge. Dans le cadre du travail mené durant cette thèse, nous avons conçu et caractérisé deux types d'hétérostructures de couches minces ferroélectriques dans le but d'observer à terme du RSOC commutable : (i) un matériau monophasé,  $\text{SrBiO}_3$ , dont nous avons prédit qu'il deviendrait ferroélectrique avec un RSOC commutable si il était soumis à une forte contrainte en compression; (ii) un système multicouches combinant un membre de la famille des wurtzites ferroélectriques, le  $(\text{Al},\text{Sc})\text{N}$ , avec le  $\text{BiSb}$ , dont les propriétés pourraient être modulées à l'aide de la ferroélectricité.

**Title :** Development of new material systems for the ferroelectric control of Rashba spin-orbit coupling and spin-charge interconversion

**Keywords :** Rashba, Oxides, Ferroelectrics, Wurtzites

**Abstract :** While classical spintronics has traditionally relied on ferromagnetic metals as spin generators and spin detectors, spin-orbit effects now make it possible to efficiently generate and detect spin currents from charge currents in architectures free from ferromagnets. However, existing materials able to achieve this spin/charge interconversion do not possess the non-volatile character of ferromagnets required for non-volatile data storage and processing. In the work presented in this thesis, we tried to develop material systems in which it would be possible to combine the advantages of Rashba-type spin-orbit coupling (RSOC) for efficient interconversion between spin and charge currents with another family of ferroic systems, ferroelectrics. RSOC appears in systems with broken inversion symmetry, and is stronger in the presence of heavy elements. Ferroelectrics intrinsically break inversion symmetry and could thus harbour RSOC. As a bonus, switching the polarization of the ferroelectric with an electric field should switch

the sign of the RSOC and thus the polarity with which the material would interconvert spin into charge via the Edelstein effect. In addition, ferroelectrics can accumulate or deplete very large carrier densities in adjacent materials and thus generate interfacial electric fields that would depend on the ferroelectric polarization direction. This would result in an interfacial RSOC that should also be tunable, allowing for a non-volatile electrical control of spin/charge interconversion.

In the framework of this thesis, we investigated the growth and characterisation of two types of ferroelectric thin film heterostructures which should present switchable RSOC : (i) a single phase material,  $\text{SrBiO}_3$ , that we predicted to become ferroelectric with switchable RSOC at compressive strain; (ii) an interface system combining the novel family of ferroelectrics, the wurtzites  $(\text{Al,Sc})\text{N}$ , with  $\text{BiSb}$ , a topological insulator whose spin-charge interconversion properties could be modulated through the means of ferroelectricity.